

Alma Mater Studiorum – Università di Bologna

DOTTORATO DI RICERCA IN

Ingegneria Elettronica, Telecomunicazioni
e Tecnologie dell' Informazione

Ciclo XXXII

Settore Concorsuale: 09/F1 - Campi Elettromagnetici

Settore Scientifico Disciplinare: ING-INF/02 - Campi Elettromagnetici

Digital Signal Processing Techniques Applied to Radio over Fiber Systems

Presentata da: Engr. Muhammad Usman Hadi

Coordinatore Dottorato

Prof. Ing. Alessandra Costanzo

Supervisore

Prof. Ing. Giovanni Tartarini

Co-Supervisore

Prof. Ing. Pier Andrea Traverso

Esame finale anno 2020

ABSTRACT

Radio over Fiber (RoF) is a pertinent technology to deal with exorbitant requirement of bandwidth in multivariate wireless services both for outdoor and indoor scenarios and is regarded as a significant technology for building centralized/cloud radio access network (C-RAN) due to its inherent capillary properties.

The dissertation aims to analyze different Radio over Fiber systems for the front-haul applications. Particularly, analog radio over fiber (A-RoF) are simplest and suffer from nonlinearities, therefore, mitigating such nonlinearities through digital predistortion are studied. In particular for the long haul A-RoF links, direct digital predistortion technique (DPDT) is proposed which is based on the behavioral model of the link which can be applied to reduce the impairments of A-RoF systems due to the combined effects of frequency chirp of the laser source and chromatic dispersion of the optical channel. Then, indirect learning architecture (ILA) based structures namely memory polynomial (MP), generalized memory polynomial (GMP) and decomposed vector rotation (DVR) models are employed to perform adaptive digital predistortion with low complexities. Distributed feedback (DFB) laser and vertical cavity surface emitting lasers (VCSELs) in combination with single mode/multi-mode fibers have been linearized with different quadrature amplitude modulation (QAM) formats for single and multichannel cases. Finally, a feedback adaptive DPD compensation is proposed.

Then, there is still a possibility to exploit the other realizations of RoF namely digital radio over fiber (D-RoF) system where signal is digitized and transmits the digitized bit streams via digital optical communication links. The proposed solution is robust and immune to nonlinearities up-to 70 km of link length. It is shown that efficient D-RoF links can be obtained with a relatively low amount of analog to digital converter (ADC) resolution bits.

Lastly, in light of disadvantages coming from A-RoF and D-RoF, it is still possible to take only the advantages from both methods and implement a more recent form known as Sigma Delta Radio over Fiber (S-DRoF) system. Second Order Sigma Delta Modulator and Multi-stage-noise-shaping (MASH) based Sigma Delta Modulator are proposed. The workbench has been evaluated for 20 MHz LTE signal with 256 QAM modulation. Finally, the 6x2 GSa/s sigma delta modulators are realized on FPGA to show a real time demonstration of S-DRoF system. The demonstration shows that S-DRoF is a competitive competitor for 5G sub-6GHz band applications.

Keywords: **Radio over Fiber** **Direct Digital Predistortion Technique** **Digital Predistortion Technique**
Nonlinearities **Generalized Memory Polynomial** **Decomposed Vector Rotation Model**

ACKNOWLEDGEMENTS

In the name of Almighty Allah, the most gracious the most merciful who gave me courage and strength to finish my project successfully. My prayers are upon his Messenger Prophet Mohammad (peace be upon him) who is our role model in every business of life and who urges to seek knowledge from cot to the grave. My foremost expression of submission and gratitude goes to Allah Almighty without whose grace and mercy; this work would never be possible even in the slightest.

I would like to express my sincere gratitude to my supervisor, Prof. Giovanni Tartarini, for giving me the opportunity to commence my PhD studies. It is his trust and guidance that always motivated me in shaping my research and also his encouragement and support during difficult times. I would also extend my appreciation to my co supervisor Prof. Pier Andrea Traverso for their guidance and support during my PhD. I am also obliged and thankful to my Co-supervisors in ESIEE Paris, France Prof. Jean-Luc Polleux and Prof. Genevieve Baudoin for their guidance and advice during my period abroad. Special thanks to Dott. Jacopo Nanni for standing through thick and thin during my stay in Lab and Bologna. Thanks to all the current and former members of my lab for their kind support and for providing a pleasant environment.

No acknowledgment would ever adequately express my obligation to my parents Dr. Abdul Hadi and Salma Hadi for their endless support, love, prayers and good wishes to see me prospering. These are their sacrifices and encouragements for my better education and career which make me what I am today. Above all I would like to thank my wife Mareya for her love and constant support, for all the late nights and early mornings, and for keeping me sane. Thank you for being my muse, editor, proofreader, and sounding board. But most of all, thank you for being my best friend. I owe you everything.

Finally, I would like to thank my dear friends Dr. Awais, Dr. Danish Rehman, Dr. Ghulam Murtaza, Engrs. Saqib Iqbal, Faizan Afzal, Jan Muhammad and many others for their encouragement, fun times and cooperation to complete my research. I would thank Dr. Hyun Jung, Dr. Nelofar Aslam and Prof. Kiran Khurshid for fruitful collaborations in my PhD.

TABLE OF CONTENTS

ABSTRACT.....	ii
LIST OF TABLES.....	xiii
LIST OF ACRONYMS.....	xiv
CHAPTER 1 INTRODUCTION.....	1
1.1 Introduction.....	1
1.2 Radio over Fiber Architectures.....	3
1.3 Aims of the Thesis.....	6
1.4 Thesis Outline.....	7
CHAPTER 2 LINEARIZATION METHODS FOR ANALOG RADIO OVER FIBER	
TRANSMISSION SYSTEMS.....	14
2.1 Introduction.....	14
2.2 Operating Principles.....	24
2.3 Parameters to evaluate DPD linearization on signals.....	25
2.4 DPD Models.....	26
2.4.1 Memoryless Model.....	27
2.4.2 Models Derived from Volterra Series.....	27
2.4.2.1 Memory Polynomial Model.....	28
2.4.2.2 Generalized Memory Polynomial Model.....	29
2.4.2.3 Orthogonal Polynomial Model.....	29
2.4.3 Decomposed Vector Rotation Model.....	30
2.4.4 Neural Network Models.....	31
2.5 DPD Identification.....	32
2.5.1 Indirect Learning Architecture.....	32
2.5.2 Direct Learning Architecture.....	34
2.6 Conclusions.....	37
CHAPTER 3 DIRECT DIGITAL PREDISTORTION FOR COMPENSATION OF	
NONLINEARITIES IN RADIO OVER FIBER LINKS.....	48
3.1 Introduction.....	48
3.2 Proposed Approach.....	50

3.2.1	Directly Modulated Laser	52
3.2.2	Fiber Compensation	54
3.2.3	Approximations Applied to the Model	55
3.3	Numerical Results and Discussion.....	57
3.3.1	Evaluation of Intermodulation Distortion for Dual RF Tone	58
3.3.2	Evaluation of LTE Signal as an Input Test Signal.....	61
3.3.2.1	ACLR Results for LTE Signal	61
3.3.2.2	EVM Results for LTE Signal	63
3.4	Behavior of Predistorter in Presence of Adiabatic Chirp	64
3.5	Feasibility of the Proposed Predistorter	67
3.6	Conclusion.....	67
CHAPTER 4 EXPERIMENTAL DEMONSTRATION OF DIGITAL PREDISTORTION		
FOR RADIO OVER FIBER (ROF) SYSTEMS		
72		
4.1	Experimental Demonstration of Digital Predistortion for VCSELs based RoF links ...	73
4.1.1	DPD Methodology Implied to SM-VCSEL.....	74
4.1.1.1	Modeling Methodology for SM-VCSELs based RoF links	74
4.1.1.2	Digital Predistortion Model.....	75
4.1.1.3	Estimation Algorithm	77
4.1.1.4	Experimental Setup	77
4.1.1.5	Results and Discussion.....	80
4.1.2	Linearization of MM-VCSEL-MMF based RoF systems	85
4.1.2.1	Experimental Setup	86
4.1.2.2	Results and Discussion.....	88
4.1.3	Discussion and Conclusions	91
4.2	Linearization of DFB-SSMF based RoF links	92
4.2.1	Modeling Methodology	93
4.2.2	Experimental Setup.....	95
4.2.3	Experimental Results and Discussion.....	96
4.3	Experimental Demonstration on Digital Predistortion for Multi-Channel Radio over Fiber Systems.....	100

4.3.1 Review of the developed multi-dimensional DPD models	101
4.3.2 Multi-Channel DPD for DFB based RoF System	106
4.3.2.1 Results and Discussion	108
4.3.3 Multi-Channel DPD for VCSEL based RoF System	112
4.3.3.1 Results and Discussion	113
4.4 REAL TIME SCENARIO	116
4.4.1 Modeling Approach.....	120
4.4.2 Experimental Setup	120
4.4.3 Results and Discussion.....	122
CHAPTER 5 EXPERIMENTAL EVALUATION OF DIGITAL RADIO OVER FIBER	
SYSTEM.....	131
5.1 Introduction.....	131
5.2 Background-Digital Radio over Fiber	132
5.2.1 Band Pass Sampling	133
5.3 Signal Impairments in D-RoF Link	136
5.3.1 Signal Impairments in ADC	136
5.3.1.1 Signal to Noise Ratio (SNR) degradation in ADC	137
5.3.1.2 Signal to Noise Ratio (SNR) degradation due to Quantization	138
5.3.1.3 Signal to Noise Ratio (SNR) degradation due to out of band noise aliasing.....	139
5.3.1.4 Signal to Noise Ratio (SNR) degradation due to Jitter Noise.....	140
5.3.2 Signal Impairments in DAC	142
5.3.3 Optical Link Noise	143
5.3.4 Total Link Noise.....	144
5.4 Analytical model for D-RoF systems	146
5.4.1 Performance Results.....	149
5.5 D-RoF Experimental Setup and Analytical Model Results Validation	153
5.5.1 Results and Discussion.....	155
5.6 Conclusions.....	158

CHAPTER 6 SIGMA DELTA RADIO OVER FIBER SYSTEMS AS A NEW CANDIDATE FOR FRONTHAUL APPLICATIONS	162
6.1 Introduction	162
6.2 Review of Sigma Delta Radio over Fiber System.....	163
6.3 Operation Principle.....	166
6.4 Structures of Sigma Delta Modulator ΔM	168
6.4.1 Second Order Sigma-Delta Modulator	168
6.4.1.1 System Description.....	170
6.5 Conclusion.....	186
CHAPTER 7 CONCLUSIONS/FINAL REMARKS AND FUTURE DIRECTIONS.....	190
APPENDIX A LIST OF PUBLICATIONS	197

LIST OF FIGURES

Figure 1.1: Basic C-RAN architecture showing optical fronthauls (OFHs)	2
Figure 1.2: Essential schematic illustration of A-RoF, D-RoF and SD-RoF downlinks.....	5
Figure 1.3: Comprehensive overview of the thesis	9
Figure 2.1: RoF uplink and downlink schematic	15
Figure 2.2: Summary of linearization techniques	15
Figure 2.3: DPD linearization principle for Analog MFH	24
Figure 2.4: Multilayer Neural Network Model	32
Figure 2.5: Indirect Learning Architecture (ILA) for system under test.....	33
Figure 2.6: Direct Learning Architecture (DLA) for system under test.....	35
Figure 3.1: Block scheme representing the collocation.....	50
Figure 3.2: Functional Block scheme representing the collocation of the proposed predistorter block.....	51
Figure 3.3: Comparison between values of ACLR (for Dual Sinusoidal RF Tone), for varying length z for $M_{IM} = 10\%$ and $M_{IM} = 30\%$, with and without the application of the proposed predistortion technique.	60
Figure 3.4: Comparison between Absolute Improvement in ACLR (for Dual Sinusoidal Tone), for varying length z and for varying input power.....	60
Figure 3.5: Comparison between values of ACLR (for LTE Signal), for varying length z for $M_{IM} = 10\%$ and $M_{IM} = 30\%$, with and without the application of the proposed predistortion technique.	62
Figure 3.6: Comparison between Absolute Improvement in ACLR (for LTE Signal), for varying length z and for varying input power.	62
Figure 3.7: Comparison between the EVM values (for LTE Signals), for varying length $z = 0 -$ 50 km for $M_{IM} = 10\%$ and 30% , with and without the application of the proposed predistortion technique.	63
Figure 3.8: Comparison between the values of ACLR (for LTE Signal), for varying % of Adiabatic Chirp for fixed length $z = 50$ km for $M_{IM} = 30\%$, $f_c = 2.14$ GHz, with and without the application of the proposed predistortion technique.....	64

Figure 3.9: The Effectiveness of predistortion in suppressing spectral regrowth, with and without correction.....	65
Figure 3.10: Comparison between the EVM values (for LTE Signals), for varying % of Adiabatic Chirp for fixed length $z=50$ km for $M_{IM} = 30\%$, with and without the application of the proposed predistortion technique	66
Figure 4.1: DPD identification for RoF utilizing ILA.....	75
Figure 4.2: Experimental evaluation comprising of DPD training and application phase.....	78
Figure 4.3: L-I-V characterization utilized in the evaluation of DPD experiments for SM-VCSEL.	80
Figure 4.4: Normalized Mean Square Error results with varying values of memory depth Q and Nonlinearity Order K	81
Figure 4.5: ACPR outcomes vs. input RF power. ($Q=1,2$, $R=1$ and $K=3$ for MP & GMP).	82
Figure 4.6: PSD evaluation of output signal without and with DPD (MP/GMP) 0 dBm for 1 Km SSMF with SM-VCSEL having: (a) $Q=1$, $R=1$, $K=3$ and (b) $Q=2$, $R=1$, $K=3$	83
Figure 4.7: ACPR results vs. varying input signal power using ($Q=2$ and $K=3$ for GMP) for SM-VCSEL with SSMF.....	83
Figure 4.8: (a) AM-AM and (b) AM-PM plots for SM-VCSEL at 1 Km of SSMF for 0 dBm of input RF power with and without DPD.....	84
Figure 4.9: EVM results vs. varying input signal power using ($Q=2$ and $K=3$ for GMP) for SM-VCSEL with SSMF.....	85
Figure 4.10: Experimental evaluation comprising of DPD training and application phase.....	87
Figure 4.11: L-I-V characterization of DPD experiments for MM-VCSEL.....	88
Figure 4.12: PSD comparison between MP and GMP.....	89
Figure 4.13: ACPR results vs. varying input signal power using ($Q=2$ and $K=3$ for GMP) for MM-VCSEL with MMF.	90
Figure 4.14: EVM results vs. varying input signal power using ($Q=2$ and $K=3$ for GMP) for MM-VCSEL with MMF.	90
Figure 4.15: DPD schematic showing RoF system utilizing Indirect Learning Architecture...	93
Figure 4.16: Schematic of Experimental testbed.....	96
Figure 4.17: Normalized Mean Square Error results for different K and Q	97

Figure 4.18: ACPR for varying input power for MP/GMP/DVR	97
Figure 4.19: PSD for 0 dBm in the different considered cases.....	98
Figure 4.20: EVM for varying input power for MP/GMP/DVR.....	98
Figure 4.21: Effect of DVR-based DPD on AM/AM and AM/PM curves for DFB based RoF links	99
Figure 4.22: Schematic for Dual Channel DPD methodology for RoF System.....	101
Figure 4.23: Experimental Setup for DFB based RoF link DPD (Training and Testing phase)	107
Figure 4.24: ACPR improvement for DFB in channel 1 and 2 with using GMP and DVR. (a) represents channel 1 with GMP. (b) represents channel 2 with GMP. (c) represents channel 1 with DVR and (d) represents DVR with channel 2.....	109
Figure 4.25: ACPR improvement for DFB in channel 1 and 2 with using GMP and DVR with varying RF input power.....	110
Figure 4.26: EVM improvement for DFB RoF link in channel 1 and 2 with using GMP and DVR with varying RF input power	111
Figure 4.27: Spectral Regrowth of input, output and corrected channels for DFB based RoF link.....	112
Figure 4.28: Experimental setup for MM-VCSEL based MMF for DPD training and testing phase.....	113
Figure 4.30: ACPR improvement for MM-VCSEL-MMF based RoF link in channel 1 and 2 with using GMP and DVR with varying RF input power	115
Figure 4.31: Spectral Regrowth for MM-VCSEL based MMF RoF link for both channels ..	115
Figure 4.32: EVM performance for corrected and uncorrected both channels for DVR and GMP architectures	116
Figure 4.33: First possible realization of an adaptive predistortion scheme.	118
Figure 4.34: Second possible realization of an adaptive predistortion scheme.....	119
Figure 4.35: Block diagram of the training phase of the proposed DPD technique for a RoF system using Indirect Learning Architecture.	120
Figure 4.36: Block diagram of the experimental bench.....	121

Figure 4.37: ACPR improvement with proposed DPD technique for varying orders of nonlinearity order (K_{GMP}) and memory depth (Q_{GMP}) at 0 dBm of input power.	122
Figure 4.38: Comparison of Output signal without DPD and with DPD for back to back (0 m length) and 75 m MMF at 0 dBm input signal power	123
Figure 4.39: Comparison of Output signal without DPD and with DPD for back to back (0 m length) and 75 m length at 0 dBm input signal power	124
Figure 4.40: EVM comparison for DPD and without DPD for varying P_{IN}	124
Figure 5.1: Block diagram of D-RoF system	132
Figure 5.2: Spectrum of the signal along its sampled version.....	135
Figure 5.3: Schematic illustration of (a) Frequency spectrum of the bandpass sampled LTE signal (b) Original Bandwidth, of the same LTE signal, including guard bands.	136
Figure 5.4: Schematic illustrating functions of the ADC	137
Figure 5.5: Schematic illustration of analog input mapping to digital output code	138
Figure 5.6: Schematic explaining the effect of jitter	141
Figure 5.7: Schematic for DAC.....	143
Figure 5.8: Block diagram of noise sources at different stages of the D-RoF link	144
Figure 5.9: Block Diagram of the D-RoF link	147
Figure 5.10: Values of EVM vs RF input power are illustrated for both the Analog Channel) constellations at $P_{IN} = 5dBm$ are shown as well.	149
Figure 5.11: Values of EVM vs fiber length L are illustrated for both the Analog and the Digital RoF systems analyzed. PDSCH constellations at $L = 70 km$ are shown as well.	150
Figure 5.12: Results for SNR vs. Fiber Length	151
Figure 5.13: Results for EVM and SNR as a function of ADC Resolution	152
Figure 5.14: Eye Opening Penalty versus Fiber length.....	152
Figure 5.15: Experimental setup for D-RoF transmission.....	154
Figure 5.16: Theoretical vs Experimental SNR for varying ADC resolution bits	155
Figure 5.17: Theoretical versus experimental EVM for different numbers of ADC bits.....	156
Figure 5.18: Theoretical versus experimental EVM for varying RF input power at 30 Km. .	157
Figure 5.19: Theoretical versus experimental EOP for varying fiber lengths.....	157
Figure 6.1: Schematic illustration of (a) A-RoF, (b) D-RoF and (c) S-DRoF.	165

Figure 6.2: Frequency domain for (a) Nyquist rate ADC, (b) the aliasing effect, and (c) oversampling ADC (ΔM concept).....	166
Figure 6.3: BPF.	167
Figure 6.4: Frequency domain model of Second order ΔM structure	169
Figure 6.5: Frequency response of Second order ΔM structure	170
Figure 6.6: Simulation setup for Sigma Delta Radio over Fiber system. SDM: Sigma Delta Modulation. PPG: Pulse Pattern Generation, BPF: Band Pass Filtering.....	170
Figure 6.7: EVM performance for varying symbol rate for varying fiber lengths.....	171
Figure 6.8: EVM performance for 20 km at (a) 25 Mbd and (b) 100Mbd.....	172
Figure 6.9: EVM performance for varying symbol rate for varying fiber lengths.....	172
Figure 6.10: ACPR performance for varying RF input power and varying fiber lengths.....	173
Figure 6.11: 2 stage MASH based ΔM structure.....	174
Figure 6.12: Experimental Bench for Sigma Delta Radio over Fiber system.	176
Figure 6.13: EVM performance for varying symbol rates and fiber lengths.	176
Figure 6.14: EVM performance for varying input powers and fiber lengths.....	177
Figure 6.15: ACLR performance for varying RF input power.....	177
Figure 6.16: EOP versus Fiber length for 0 dBm of input power.....	178
Figure 6.17: Experimental test bed for real time implementation of Sigma Delta Radio over Fibre system.	180
Figure 6.18: EVM performance for varying input powers for all channels with minimum and maximum link length.....	182
Figure 6.19: (a) EVM performance for varying symbol rate lengths.....	183
Figure 6.21: ACLR vs input power for varying lengths.....	184

LIST OF TABLES

Table 2-1: Overview of the linearization techniques implied for RoF transmission.....	17
Table 3-1: Parameters utilized in the formulation of simulation results.....	59
Table 3-2: Parameters of the LTE Signal Utilized.....	61
Table 3-3: Linearization Performance for adiabatic Chirp (Minimum and Maximum Values).....	66
Table 4-1: System Parameters	79
Table 4-2: Linearization performance for proposed DPD.....	85
Table 4-3: System Parameters utilized in MM-VCSEL-MMF based RoF system	88
Table 4-4: Linearization performance for proposed DPD for MM-VCSEL-MMF.....	91
Table 4-5: Comparison among the utilized DPD models for $P_{IN}=0 \text{ dBm}$	99
Table 4-6: Linearization performance for DFB based directly- modulated RoF links.....	111
Table 4-7: Linearization performance for an input power of 0 dBm	125
Table 5-1: Summary of different noise sources, with their expression and assumptions.....	145
Table 5-2: Parameters utilized in the simulation of the Optical Link.....	148
Table 5-3: Summary of the analytical and experimental bench for D-RoF.....	158
Table 6-1: Parameters Value.....	171
Table 6-2: Performance Evaluation for 20 km at -5 dBm	173
Table 6-3: Performance Evaluation Parameters	175
Table 6-4: Performance Summary at -5 dBm for 400 Mbd	178
Table 6-5: System parameters.....	181
Table 6-6: Performance Evaluation at 0 dBm for 100 MBd	185
Table 7-1: Summary of RoF Transmission Topics Discussed in this Dissertation	192

LIST OF ACRONYMS

- ACLR** Adjacent Channel Leakage Ratio
- ACPR** Adjacent Channel Power Ratio
- ADC** Analog-to-Digital Converter
- AM** Normalized Magnitude
- ANN** Artificial Neural Network
- A-RoF** Analog Radio over Fiber
- B2B** Back-to-Back
- BBU** BaseBand Unit
- BPF** Band Pass Filter
- BTS** Base Transceiver Station
- BW** Bandwidth
- CO/BTS** Central Office / Base Transmit Station
- CPRI** Common Public Radio Interface
- CRAN** Centralized/Cloud Radio Access Network
- DAC** digital-to-analog converter
- DAS** Distributed Antenna System
- DFB** Distributed Feed-Back
- DFT** Discrete Fourier Transform
- D-MBFH** Digital Mobile Front Haul
- DPD** Digital Predistortion

DPDT Direct Digital Predistortion Technique/ Direct Predistortion Technique

D-RoF Digital Radio over Fiber

DSO Digital Signal Oscilloscope

DSP Digital Signal Processing

DVR Decomposed Vector Rotation

EAM Electro-Absorption Modulator

EEL Edge Emitting Laser

EO Eye Opening

EOH Eye Opening Height

EOP Eye Opening Penalty

EVM Error Vector Magnitude

FH Front-Haul

FFNN Feedforward neural network

FTTH Fiber-To-The-Home

FWHM Full Width Half Maximum

GMP Generalized Memory Polynomial

GSM Global System for Mobile

IF Intermediate Frequency

IMDD Intensity Modulation Direct Detection

LD Laser Diode

LMS Least Means Square

LNA Low Noise Amplifier

LTE Long Term Evolution

MFH Mobile Front-Haul
MMF Multi-Mode Fiber
MP Memory Polynomial
MQWs Multi-Quantum Wells
MZM Mach-Zehnder Modulator
NMSE Normalized Means Square Error
NN Neural Network
NSD Noise Spectral Density
NTF Noise Transfer Function
OFH Optical Front Hauls
OMI Optical Modulation Index
OTx Optical Transmitter
PAPR Peak-to-Average Power Ratio
PD Photo-Diode
PDSCH Physical Downlink Shared Channel
PIN P-doped-Intrinsic-N-doped
PM Phase Magnitude
PSD Power Spectral Density
QAM Quadrature Amplitude Modulation
QPSK quadrature phase shift keying
QW Quantum Well
RAN Radio Access Network
RAP Radio Access Point

RAU Remote Access/Antenna Unit

RF Radio Frequency

RIN Relative Intensity Noise

RLS Recursive Least Squares

RoF Radio over Fiber

RRH Remote Radio Head

RRU Remote Radio Unit

RTx Radio Transmitter

SDM Sigma Delta Modulation

S-DRoF Sigma Delta Radio over Fiber

SM Single-Mode

SMF Single-Mode Fiber

SNOM Scanning Near-field Optical Mapping

SNR Signal-to-Noise Ratio

SSMF Standard Single-Mode Fiber

STF Signal Transfer Function

UL Uplink

UMTS Universal Mobile Telecommunications Service

VCSEL Vertical Cavity Surface Emitting Laser

VNA Vector Network Analyzer

VSA Vector Signal Analyzer

VSG Vector Signal Generator

WAN Wide Area Network

WLAN Wireless Local Area Network

WiFi Wireless Fidelity

WiMAX Worldwide Interoperability for Microwave Access

WDM Wavelength Division Multiplexing

ZOH Zero Order Hold

3G Third Generation

4G Fourth Generation

5G Fifth Generation

$\Sigma \Delta M$ Sigma Delta Modulator

Chapter 1

Introduction

The contents of this chapter are taken partially from A2, where we presented the characterization and review of different Radio over Fiber systems.

1.1 Introduction

The fifth generation (5G) technology is envisaged to provide faster internet access with low latency, cost effectiveness and pervasive mobile coverage [1.1-1.3]. The increasing demand of Internet-connected smartphones, tablets and other gadgets are leading towards the explosive growth of mobile data traffic. This has made mobile fronthaul (MFH) networks as the data rate bottleneck of user experience. To enhance the capacity and coverage of mobile data networks, the next generation MFH is expected to support the coexistence of multiple mobile services from various radio access technologies (RATs), such as Long Term Evolution (LTE) signals, etc. Radio over Fiber (RoF) is a pertinent technology to deal with exorbitant requirement of bandwidth multivariate wireless services both for outdoor and indoor scenarios [1.4-1.6] and is regarded as a significant technology for the next generation networks [1.7]. In particular, RoF technology can provide an essential platform for building centralized/cloud radio access network (C-RAN) which should be able to control the centralized base band units (BBU) coming from different base stations and remote radio heads (RRHs) [1.8].

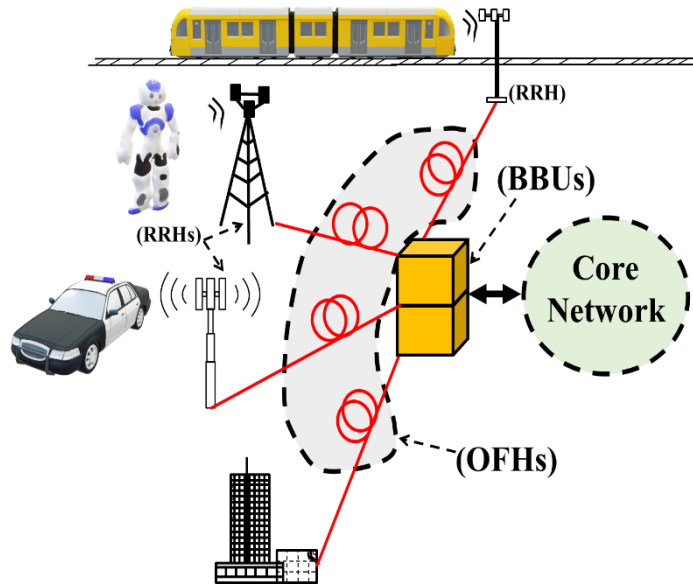


Figure 1.1: Basic C-RAN architecture showing optical fronthauls (OFHs)

The interconnectivity of these BBUs with RRHs is economically viable with the distribution network known as the ‘fronthaul’ [1.9-1.10]. The RoF technology is then a suitable candidate for the fronthauling due to its inherent capillary properties. Figure 1.1 shows the C-RAN utilizing optical front hauls (OFHs).

In addition to the advantages coming from the use of the optical fiber as a transmission channel, like extremely broad bandwidth, immunity to electromagnetic interference and large transmission distances, an additional attractive feature lies in the agnosticism of RoF systems concerning the particular transmission modulation format, which makes them intrinsically future-proof. Nonetheless, the drawbacks of these systems can be presented through the presence of distortion that can possibly lower the performances. These impairments are caused by imperfect linear behavior of laser, photo detector and optical fiber. or due to the combination of fiber chromatic dispersion and spurious phase signals generated by the laser source (also called frequency chirp) [1.11]. Similarly, since RoF transmission is based on optical subcarrier modulation, therefore, it is susceptible to nonlinear distortion.

To avoid these issues, an alternative solution can consist in the Digital Radio over Fiber (D-RoF) technique [1.12]. Transmitting digital data mitigates the non-linearity issues at both the transmitter and receiver [1.13].

Similarly, the phase relation between many RRHs does not remain steady and spectral efficiency decreases [1.14]. More recently, Delta-Sigma modulation has been proposed as a new digitization interface for a digital fronthaul link [1.15-1.16]. However, these systems require expensive, highly efficient and high sampling rate DSP circuitry to achieve the performance [1.17]. Therefore, to utilize the A-RoF technology while applying an efficient methodology to alleviate the inherent nonlinearities can represent a reasonable choice. Different topologies of RoF are discussed in the following section.

1.2 Radio over Fiber Architectures

In this section, different radio over fiber topologies are compared. The idea is to explain the differences in the topologies of the different RoF architectures. Figure 1.2 shows a possible scenario for the comparison of different RoF architectures.

The typical schematic framework of an A-RoF architecture system at the downstream link is shown in Figure 1.2. In the most typical case, the baseband signal is upconverted to an RF signal. The RF signal is then converted to an optical signal in the electrical to optical (E-O) conversion block and transmitted through the optical link. At the receiver, optical to electrical (O-E) block retrieves the received RF signal back to electrical domain. This signal is then transmitted through the antenna after performing filtering and amplification. The link explained is called in literature as Intensity Modulation Direct Detection (IM-DD) Analog Radio over Fiber (A-RoF). In particular, the intensity of optical power produced by the laser is directly modulated by the useful RF signal, while the output RF current of the photo-detector (PD) is produced by the optical power which is directly absorbed by the PD. Moreover, the transmission is performed in the analog domain, or rather, without the usage of any Analog-to-Digital Converter (ADC) to convert the RF signal in the digital domain [1.18-1.22].

However, the A-RoF is liable to noise and distortion due to nonlinearities, which, in general, are generated both, at the transmitter and receiver sides [1.23-1.26]. The other possible architecture is Digital Radio over Fiber. The architecture is similar to

A-RoF, however, after the frequency up-conversion, analog to digital (ADC) converter is present which converts the analog signal to digital one. On the other hand, Digital mobile fronthauls (D-MBFHs) based on the Digital-Radio over Fiber (D-RoF) technique are not affected by the nonlinear effects typical of A-RoF systems [1.12-1.13,1.27]. In Figure 1.2, considering the blue (D-RoF) branches, a typical D-RoF architecture can be visualized.

The common public radio interface (CPRI) that was proposed by the CPRI cooperation, Nokia, Bell Labs, Ericsson, Huawei, Orange and NEC, was adopted as the D-MBFH interface [1.28]. However, when CPRI was employed as a digitization interface developed for narrowband radio access technologies (RATs), such as UMTS (CPRI version 1 and 2), WiMAX (version 3), LTE (version 4) and GSM (version 5), due to its limited spectral efficiency, it had limited scalability. Moreover, it also requires a very high data traffic in the fronthaul network segment, implying the use of expensive high-performance analog-to-digital and digital-to-analog converters [1.14]. Therefore, an alternative solution, which can overcome these bottlenecks would be desirable.

This solution can be pursued by employing Sigma-Delta ($\Sigma\Delta$) Modulation, realizing in this way a technique which can be called Sigma-Delta Radio over Fibre ($\Sigma\Delta$ -RoF) and can combine the advantages of both A-RoF and D-RoF. An example of realization of a $\Sigma\Delta$ -RoF system can still be appreciated in Figure 1.2, considering the red ($\Sigma\Delta$ -RoF) branches. It can be observed that in the $\Sigma\Delta$ -RoF systems, the signal, before being converted to the Optical domain by the Optical Transmitter, undergoes the $\Sigma\Delta$ modulation. This operation, exploiting a highspeed digital oversampling of the modulating signal with 1-bit resolution, allows to reach a high immunity to nonlinearities. At the same time, it realizes the so-called operation of noise shaping, which places most of the noise power out of the signal bandwidth [1.29-1.32].

As shown in Figure 1.2, at the receiver end, after the optical-to-electrical conversion, performed by a photodetector, a band-pass filter (BPF) guarantees the correct digital-to-analogue conversion of the signal as well as the spectral emission requirements, by filtering the out-of-band quantization noise.

It can then be observed that the $\Sigma\Delta$ -RoF technique proves particularly convenient in the realization of the fronthaul downlink, where the transmitting section is located at the BBU, while the receiving section is at the RRH. Indeed, the cost of the $\Sigma\Delta$ modulator can in this way be shared by many users, while the RRH structure is maintained simple, without the installation of active devices. Following the same idea, solutions for the fronthaul uplink which can maintain the RRH simple configuration should be pursued, not excluding the A-RoF one [1.32].

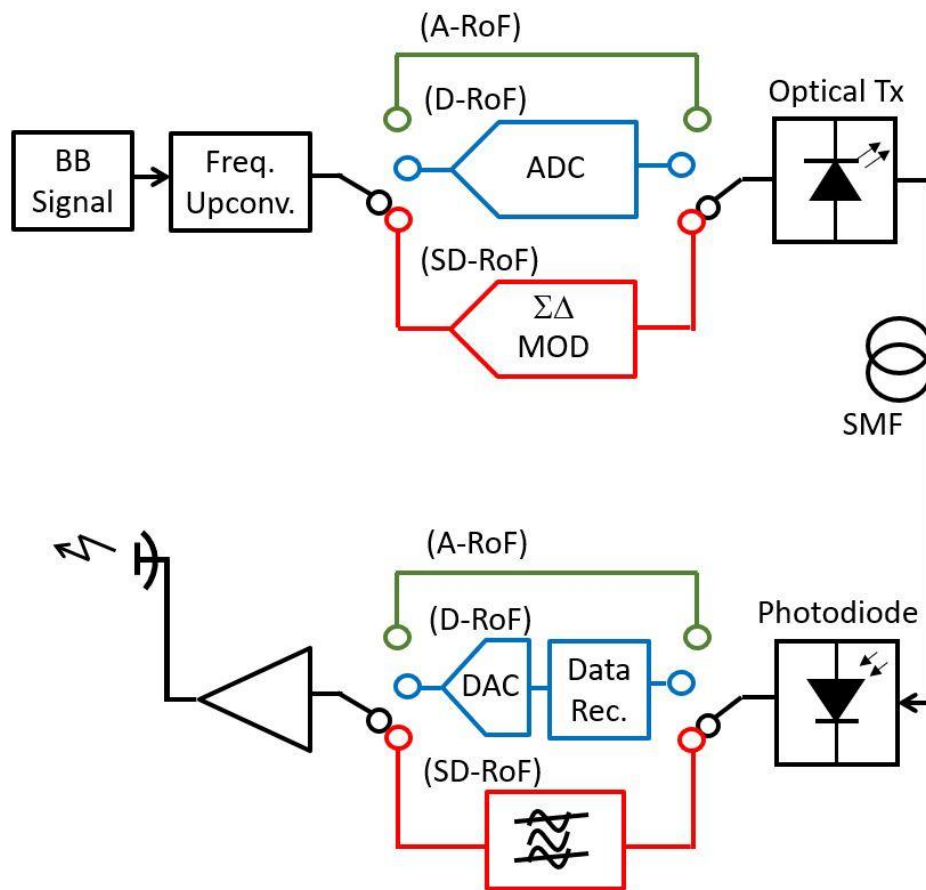


Figure 1.2: Essential schematic illustration of A-RoF, D-RoF and SD-RoF downlinks. Note that the SD-RoF scheme can also be implemented swapping the positions of the $\Sigma\Delta$ MOD block and of the Freq. Upconv. Block.

1.3 Aims of the Thesis

The main aim and contribution of this thesis are two fold. Firstly, to exploit different Radio over Fiber systems for the front-haul applications. Particularly, Analog Radio over Fiber are simplest and suffer from nonlinearities, therefore, applying linearization methods to Analog Radio over Fiber systems is studied and implemented in first half of thesis. Then, there is still a possibility to exploit the other realization of RoF namely a digital radio over fiber is discussed and designed. Lastly, in light of disadvantages coming from A-RoF and D-RoF, it is still possible to take the advantages from both methods and implement a more recent form known as Sigma Delta RoF.

The specific objectives of the thesis are listed below.

1. To develop a novel predistortion methodology that linearizes the link impairments in long haul Analog Radio over Fiber links caused due to combined effect of laser chirp and fiber dispersion.
2. To develop a novel predistortion linearization technique based on indirect learning architecture for improving the nonlinearities issue in Analog Radio over fiber links based on Vertical Capacity Surface Emitting Lasers (VCSELs) or Distributed Feedback (DFB) lasers. Linearization methodologies are shown not only for single but multi-channel scenarios as well.
3. To design and implement a Digital Radio over Fiber System for medium range length and compare its performance with Analog Radio over Fiber links.
4. To realize a Sigma Delta Radio over Fiber System which intermixes the advantages of both, A-RoF and D-RoF links. Different sigma delta modulation structures are implemented, and performance methodologies are evaluated. Particularly, a real time Sigma delta RoF link is designed where FPGA is used to implement sigma delta modulation followed by performance evaluation.

1.4 Thesis Outline

This thesis is organized into seven chapters, and its comprehensive overview is depicted in Figure 1.2.

- **Chapter 1** discusses the main context of the thesis followed by the main contributions added through this thesis. It introduces the radio over fiber (RoF) technology. A brief summary of different RoF topologies are discussed. The aim of the thesis is discussed.
- **Chapter 2** discusses the literature review of previous linearization techniques developed for Analog Radio over Fiber system. Different architectures developed in Digital predistortion are discussed. Chapter also includes the literature review of DPD identification process and DPD models that have been proposed up till now.
- **Chapter 3** proposes a predistortion technique for linearizing Analog RoF links which corrects the link impairments caused due to combined effect of laser chirp and fiber dispersion. The proposed technique is independent of the laser model which makes it salutary in terms of adapting to other possible laser models. The mathematical framework of the proposed technique and its implementation is discussed. The predistortion is applied firstly to sinusoidal signals and then to LTE standard signals. As a figure of merit, the effects of the proposed operation are reported by analysing the Adjacent Channel Leakage Ratio (ACLR) and Error Vector Magnitude (EVM) of the received signal.
- **Chapter 4** discusses linearization techniques based on indirect learning architecture. Two class of links are linearized i.e. Vertical Capacity Surface Emitting Lasers (VCSELs) and Distributed Feedback Laser (DFB) based RoF links. Volterra polynomial structures such as memory polynomial (MP) and generalized memory polynomial (GMP) methods are proposed for linearizing Radio over fiber links. Similarly, a novel demonstration is shown for dual channel transmission where each channel nonlinearities are reduced with the DPD models proposed in this chapter. Finally, a feedback approximation methodology is proposed which is a possible implementation of a digital predistorter in adaptive form.

- **Chapter 5** discusses another class of RoF system which is called as Digital Radio over Fiber system. The chapter introduces the need and importance of digital RoF system. It is discussed that Digital RoF is a good option to switch from Analog RoF to Digital RoF. Analytical model is proposed and it is shown that a better error free transmission is obtained for digital RoF as compared to Analog RoF. Then, an experimental validation of this analytical model is presented which proves that the proposed digital radio over fiber system is an optimized version that uses less number of ADC resolution bits.
- **Chapter 6** discusses another class of RoF system which is called as Sigma Digital Radio over Fiber (S-DroF) system. The chapter introduces the need and importance of Sigma delta RoF system, an auxiliary method that amalgamates the advantages of A-RoF and D-RoF. It discusses the basics of sigma delta modulator ($\Sigma \Delta M$). The need of power hungry and high-speed digital to analog converter (DAC) required in D-RoF is replaced by a $\Sigma \Delta M$. It describes the different architectures that have been proposed. The analytical model with simulation is shown and then experimental setup is discussed.
- **Chapter 7** concludes and discusses the overall findings of the thesis. It also highlights the extension of the work that can be the object of future research activity.

The comprehensive overview of the thesis is shown in Figure 1.3.

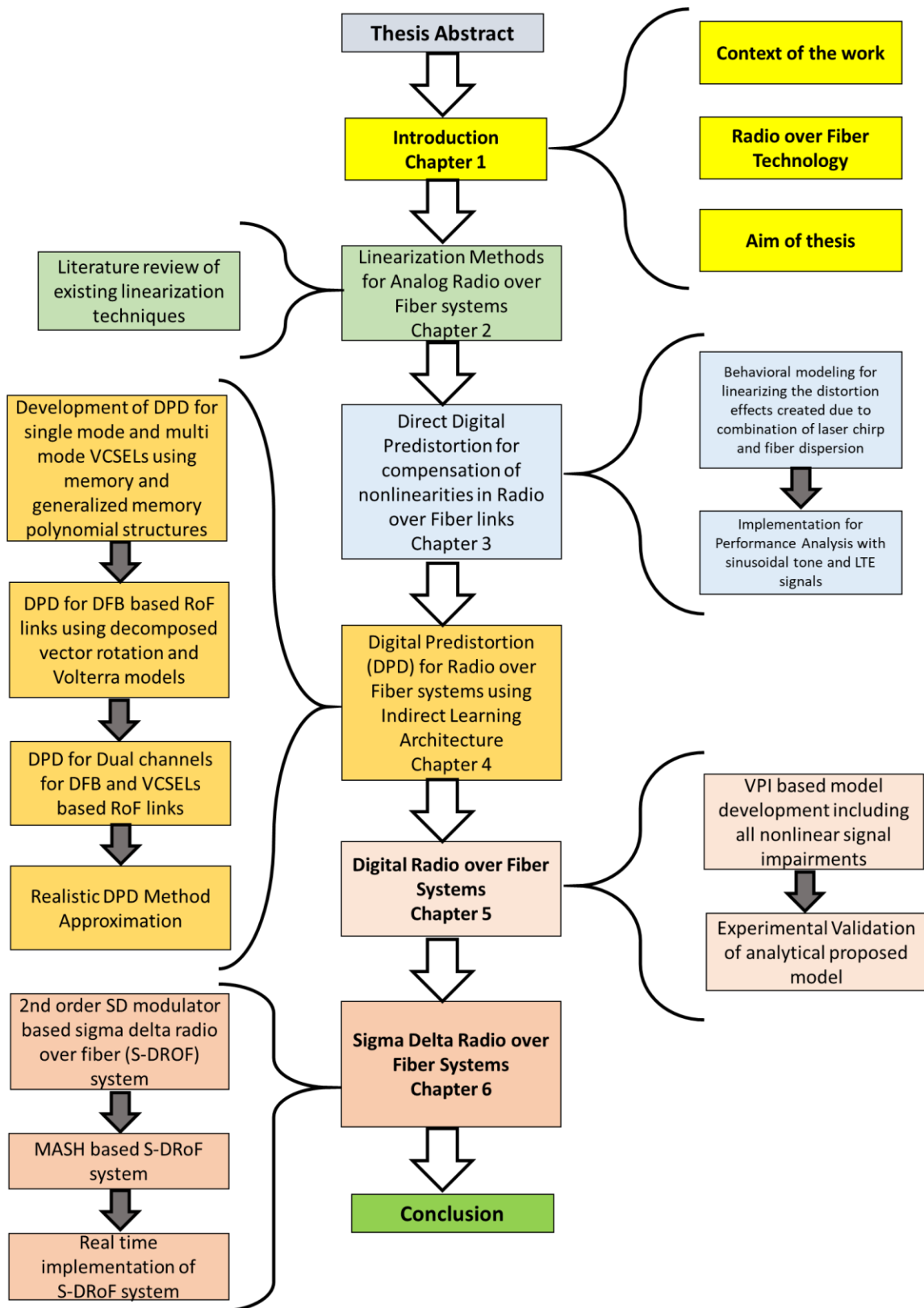


Figure 1.3: Comprehensive overview of the thesis

References

- 1.1 C. Ranaweera, E. Wong, A. Nirmalathas, C. Jayasundara and C. Lim, "5G C-RAN With Optical Fronthaul: An Analysis From a Deployment Perspective," in *Journal of Lightwave Technology*, vol. 36, no. 11, pp. 2059-2068, 1 June1, 2018.
- 1.2 China Mobile, "C-RAN the road towards green RAN (version 2.5)," White Paper, Oct 2011
- 1.3 A. Gupta et al., "A Survey of 5G Network: Architecture and Emerging Technologies," *IEEE Access*, Vol. 3, p. 1206-1232 (2015).
- 1.4 M.C. Parker, et al. "Radio-over-fibre technologies arising from the Building the future Optical Network in Europe (BONE) project," *IET Optoelectronics*, 4(6),. 247 – 259, 2010
- 1.5 D. Visani et al., "3×2N-QAM Constellation Formats for DMT Over 1-mm Core Diameter Plastic Optical Fiber", *IEEE Photonics Technology Letters*, 23, pp. 768-770 , 2011
- 1.6 M. Morant, R.Llorente, "Performance analysis of multiple radio-access provision in a multicore-fibre optical fronthaul", *Optics Communications* 436 (2019) 161–167
- 1.7 Y. Shi et al., "Ultrawideband Signal Distribution Over Large-Core POF for In-Home Networks," *IEEE/OSA J. Lightw. Technol*, vol. 30, pp. 2995-3002, Sept. 2012.
- 1.8 K. Y. Lau, "RF transport over optical fiber in urban wireless infrastructures," in *IEEE/OSA Journal of Optical Communications and Networking*, vol. 4, no. 4, pp. 326-335, April 2012.
- 1.9 Hadi, M., Jung, H., Traverso, P., et al. (2019). Digital Radio Frequency Transport over Optical Fiber for 5G Fronthaul Links. *Journal of Optical Communications*, 0(0), pp. - Apr. 2019, from doi:10.1515/joc-2019-0051

- 1.10 Hadi, M., Hadi, M., Aslam, N., et al. (2019). Experimental Demonstration of MASH Based Sigma Delta Radio over Fiber System for 5G C-RAN Downlink. *Journal of Optical Communications*, 0(0), pp. -. Retrieved 23 Feb. 2019, from doi:10.1515/joc-2019-0011
- 1.11 G. Meslener, "Chromatic dispersion induced distortion of modulated monochromatic light employing direct detection," in *IEEE Journal of Quantum Electronics*, vol. 20, no. 10, pp. 1208-1216, Oct 1984.
- 1.12 Muhammad Usman Hadi, Hyun Jung, Salman Ghaffar, Pier Andrea Traverso, Giovanni Tartarini, Optimized digital radio over fiber system for medium range communication, *Optics Communications*, Volume 443, 2019, Pages 177-185, ISSN 0030-4018, <https://doi.org/10.1016/j.optcom.2019.03.037>.
- 1.13 P. A. Gamage, A. Nirmalathas, C. Lim, D. Novak, and R. Waterhouse, "Design and analysis of digitized RF-over-fiber links," *IEEE J. Lightw. Technol.*, vol. 27, p. 2052–2061, June 2009.
- 1.14 Haddad, A.; Gagnaire, M.: Radio-over-Fiber (RoF) for mobile backhauling: A technical and economic comparison between analog and digitized RoF. *Int. Conf. Opt. Netw. Design Modeling*, pp. 132137 (2014)
- 1.15 L. Breyne, G. Torfs, X. Yin, P. Demeester and J. Bauwelinck, "Comparison Between Analog Radio-Over-Fiber and Sigma Delta Modulated RadioOver-Fiber," in *IEEE Photonics Technology Letters*, vol. 29, no. 21, pp 1808-1811, 1 Nov.1, 2017. doi: 10.1109/LPT.2017.2752284
- 1.16 Hadi, M., Aslam, N. & Jung, H. (2019). Performance Appraisal of Sigma Delta Modulated Radio over Fiber System. *Journal of Optical Communications*, 0(0), pp. -Jan. 2019, from doi:10.1515/joc-2018-0227
- 1.17 Hadi, M., Hadi, M., Aslam, N., et al. (2019). Experimental Demonstration of MASH Based Sigma Delta Radio over Fiber System for 5G C-RAN Downlink. *Journal of Optical Communications*, 0(0), pp. -. Retrieved 27 Feb. 2019, from doi:10.1515/joc-2019-0011
- 1.18 Y. Shi ; D. Visani ; C.M. Okonkwo ; H. Yang ; H.P.A. van den Boom ; G. Tartarini ; E. Tangdiongga ; A.M.J. Koonen "First demonstration of HD video distribution over large-

- core POF employing UWB for in-home networks,” 2011 Optical Fiber Communication Conference and Exposition and the National Fiber Optic Engineers Conference, pp 1-3 (2011)
- 1.19 Y. Shi et al., "Ultrawideband Signal Distribution Over Large-Core POF for In-Home Networks," in *Journal of Lightwave Technology*, vol. 30, no. 18, pp. 2995-3002, Sept.15, 2012.
- 1.20 S. Jang, G. Jo, J. Jung, B. Park, and S. Hong, "A digitized if-over fiber transmission based on low-pass delta-sigma modulation," *IEEE Photonics Technology Letters*, vol. 26, no. 24, pp. 2484–2487, Dec 2014.
- 1.21 Draa, M.; Hastings, A.; Williams, K. Comparison of photodiode nonlinearity measurement systems. *OSA Optics Expr.* 2011, 19, 12635–12645.
- 1.22 Chen, Z.; Yan, L.; Pan, W.; Luo, B.; Zou, X.; Guo, Y.; Jiang, H.; Zhou, T. SFDR enhancement in analog photonic links by simultaneous compensation for dispersion and nonlinearity. *OSA Optics Expr.* 2013, 21, 20999–21009.
- 1.23 Haas, B.M.; Murphy, T.E. A simple, linearized, phase-modulated analog optical transmission system. *IEEE Photon. Technol. Lett.* 2007, 19, 729–731.
- 1.24 Zhu, R.; Zhang, X. Linearization of Radio-Over-Fiber Systems by Using Two Lasers with Different Wavelengths. In *Proceedings of the 2014 IEEE MTT-S International Microwave Symposium (IMS)*, Tampa, FL, USA, 1–6 June 2014
- 1.25 Ghannouchi, F.; Younes, M.; Rawat, M. Distortion and impairments mitigation and compensation of single- and multi-band wireless transmitters. *IET Microw. Antennas Propag.* 2013, 7, 518–534.
- 1.26 Duan, R.; Xu, K.; Dai, J.; Cui, Y.; Wu, J.; Li, Y.; Dai, Y.; Li, J. Linearity improvement based on digital signal processing in intensity-modulated analog optical links incorporating photonic frequency down conversion. In *Proceedings of the Optical Fiber Communication Conference and Exposition*, Los Angeles, LA, USA, 6–8 March 2012

- 1.27 Christina Lim, Ampalavanapillai (Thas) Nirmalathas, Ka-Lun Lee, Dalma Novak, Rod Waterhouse, Waterhouse intermodulation distortion improvement for fiber–radio applications incorporating OSSB+C modulation in an optical integrated-access environment, *J. Lightwave Technol.* 25 (2007) 1602–1612.
- 1.28 Common Public Radio Interface (CPRI) Specification V7.0 (2015-10-09).http://www.cpri.info/downloads/CPRI_v_7_0_2015-10-09.pdf
- 1.29 Luis M. Pessoa, Joana S. Tavares, Diogo Coelho, and Henrique M. Salgado, "Experimental evaluation of a digitized fiber-wireless system employing sigma delta modulation," *Opt. Express* 22, 17508-17523 (2014)
- 1.30 L. Breyne, G. Torfs, X. Yin, P. Demeester and J. Bauwelinck, "Comparison Between Analog Radio-Over-Fiber and Sigma Delta Modulated Radio-Over-Fiber," in *IEEE Photonics Technology Letters*, vol. 29, no. 21, pp. 1808-1811, 1 Nov.1, 2017. doi: 10.1109/LPT.2017.2752284
- 1.31 I. C. Sezgin, J. Gustavsson, T. Lengyel, T. Eriksson, Z. S. He and C. Fager, "Effect of VCSEL Characteristics on Ultra-High Speed Sigma-Delta-Over-Fiber Communication Links," in *Journal of Lightwave Technology*, vol. 37, no. 9, pp. 2109-2119, 1 May1, 2019. doi: 10.1109/JLT.2019.2898270.
- 1.32 M.U..Hadi, P..A.Traverso, G.Tartarini, H. Jung, "Experimental characterization of Sigma Delta Radio over fiber system for 5G C-RAN downlink", *ICT Express* available online 21 June 2019

Chapter 2

Linearization Methods for Analog Radio over Fiber Transmission Systems

This chapter presents the literature review of previous linearization techniques developed for Analog Radio over fiber system. Then, Digital Predistortion (DPD) is discussed in detail followed by the different architectures utilized. This Chapter also includes the literature review of DPD identification process and DPD models that have been proposed up till now.

2.1 Introduction

Suppression of nonlinearities that arise in A-RoF is the key for the successful application of RoF transmission. It is important to identify the causes of these nonlinearities. In general, non-linear distortion in RoF transmission occur due to nonlinear characteristics of microwave and optical transmission in the RoF systems.

The main sources of nonlinearities in the RoF based front-haul are the following:

1. Signal Impairments of Optical Modulation at optical transmitter (OTx)
2. Nonlinearities of RF power amplification at radio transmitter (RTx)
3. Fiber Dispersion
4. Combination of laser chirp and fiber dispersion
5. Other possible components such as low noise amplifiers (LNA), photodiodes, etc.

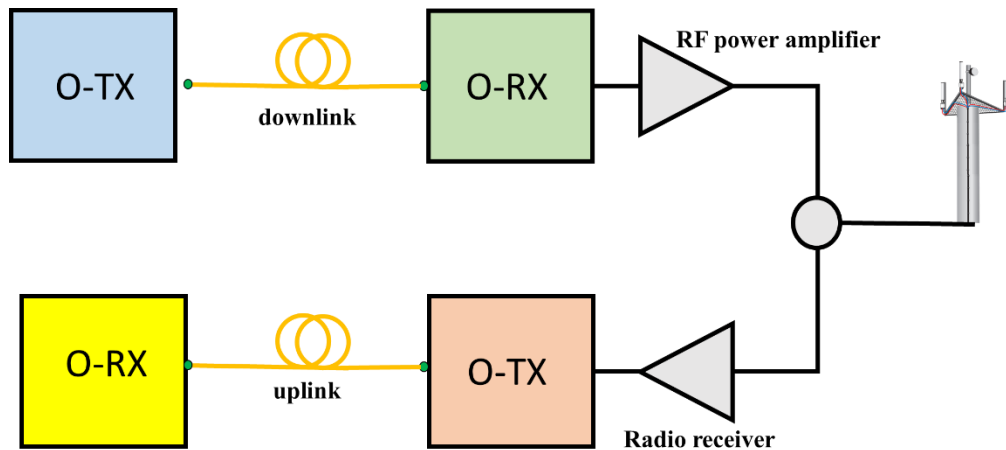


Figure 2.1: RoF uplink and downlink schematic

For RoF downlinks in Figure 2.1, the main sources of nonlinearities stem from optical subcarrier modulation at baseband unit (BBU) and RF power amplifier at remote radio head (RRH). While for RoF uplinks, the main sources of nonlinearities originate from optical subcarrier modulation at RRH. The rest of the components also introduce nonlinearities, but typically are very small compared to the above. In order to minimize the nonlinearities in RoF transmission, different methodologies have been proposed that comprises of electrical and optical linearization methods. They have been summarized in the block diagram below in Figure 2.2.

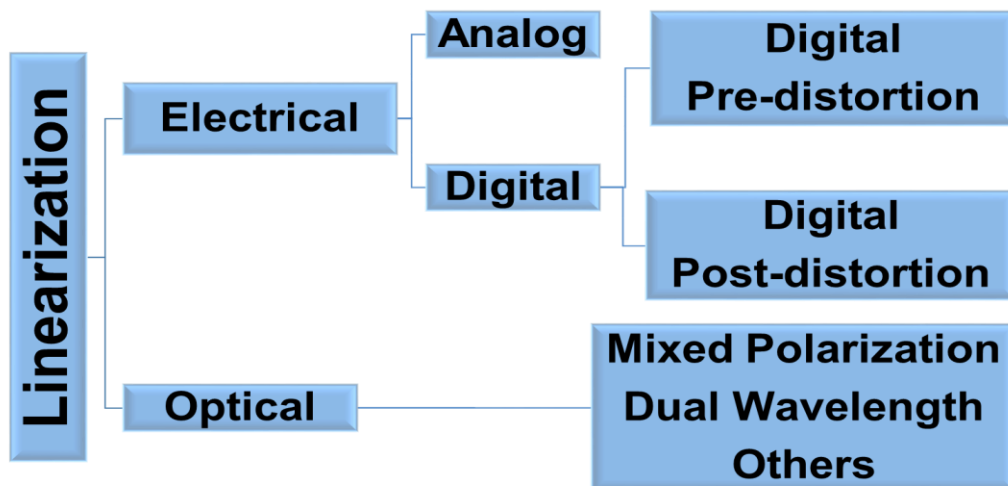


Figure 2.2: Summary of linearization techniques

The literature review of linearization techniques is presented below in Table 2.1. Major linearization techniques implied for RoF transmission are summarized.

Table 2-1: Overview of the linearization techniques implied for RoF transmission

Sr. No.	Authors	Type of linearization	Sub-category	Evaluated quantities	Linearization	Advantages	Disadvantages
1	Draa et al; Chen et al [2.18, 2.19]	Electrical	Analog Predistortion	IMD3	Complete RoF system (Laser, photodiode, LNA)	Maintenance of phase for generated IMD3 components	Difficult to have suppression of second order nonlinear distortion for large bandwidth.
2	Hass et al; Hraimel et al [2.20, 2.21]	Optical	Mixed Polarization	Second or third order nonlinear distortions	Complete RoF system	Suppression of second and third order nonlinearities	<ul style="list-style-type: none"> • RoF transmission should be polarization dependent. • Compression of linear components to some extent.
3	Zhu et al [2.22]	Optical	Dual wavelength linearization (DWL)	Second or third order nonlinear distortions	Complete RoF system	Suppression of second and third order nonlinearities	Wavelength dependent transmission i.e. suppression of nonlinear components only if wavelengths are anti-phase to each other.
4	Ghannouchi et al [2.23]	Digital	Digital Pre- distortion (DPD)	Third order nonlinearities	Power Amplifier	Wideband linearization achievable	<ul style="list-style-type: none"> • Complicated DSP required • Power consumption is huge

5	Duan et al [2.24]	Digital	DPD		ACPR, EVM	Laser	Additional accuracy with less DSP requirements	Complexity and calculation time for digital linearization is high for higher nonlinearity order and memory depth.
6	Pei et al [2.25]	Digital	DPD		ACPR	Laser/ RoF	15 dB higher suppression in ACPR	Feedback complexity.
7	Lam et al [2.26]	Digital	Digital Processing (DPP)	Post	ACPR, BER	RoF	All order nonlinear distortion components compressed significantly.	<ul style="list-style-type: none"> • High speed digitizer required. • Applicable to uplinks only. • DPP to be deployed at RRH side, which means price of the prototype has to be passed to the customer side, which is undesirable and also will add higher complexity to the RRH.

8	Hekkala et al [2.27]	Digital	DPD	ACPR, EVM	Laser only	Less complexity and overhead	<ul style="list-style-type: none"> • 0.3% improvement in EVM. • No link length considered. • DPD done using intermediate frequency. • RoF link was not composed of laser-fiber-photodiode only. Attenuators & amplifiers were used, may be the signal impairments corrected were due to these components. • Limited to sinusoid input signals
9	Hadi et al [2.28]	Digital	DPD	C/HD2, IIP3	IIP2, Combination of fiber dispersion and laser chirp	Linearizes links up to tens of km.	<ul style="list-style-type: none"> • Limited to sinusoidal (single, dual) input tones. • No EVM, ACPR shown

10	Vieira et al. [2.29]	Digital	DPD	EVM	Laser	Utilization of OFDM signal with 5 MHz bandwidth	<ul style="list-style-type: none"> • Only magnitude (AM/AM) linearization shown. • RoF link is not generic, RoF link contains 10 dB attenuator.
11	Hekkala et al. [2.30]	Digital	DPD	ACPR, BER	Laser	Utilization of OFDM signal with 12.5 MHz bandwidth	Joint compensation proposed for PA and RoF which results in reduction in improvement.
12	Mateo et al. [2.31]	Digital	DPD	EVM, ACPR	RoF system	Utilization of LTE 20 MHz signal.	<ul style="list-style-type: none"> • RoF link is not generic. Contains signal amplification by LNA and a PA. • Feedback for 10 km length is unrealistic, requires a uplink for the linearization of downlink.

13	Mateo et al. [2.32]	Digital	DPD	NMSE, ACPR	RoF system	Utilization of LTE 20 MHz with 16 QAM modulation	<ul style="list-style-type: none"> • PSD of output with and without DPD is not at the same level after normalization, DPD has reduced the bandwidth of the signal. • DFB laser has not been pushed to higher RF input powers in order to see the efficacy of the predistorter.
14	Mateo et al. [2.33]	Digital	DPD	ACPR, EVM	RoF system	Linearization considering ideal and no feedback	Results are attenuation dependent i.e. with proper attenuation using different optimization algorithms, similar results to ideal case can be obtained.
15	Roselli et al. [2.34]	Electrical	Analog predistortion	IMD3	Laser	Maintenance of phase for generated IMD3 components	Difficult application to large scale production because every single RoF transmitter requires a variant predistorter.
16	R. B. Childs et al. [2.35]	Electrical	Analog predistortion	IMD3	Laser	Accurate correction	Difficulties to synthesize arbitrary transfer functions in the time domain.

17	Veiga et al. [2.36]	Electrical	Analog predistortion	IMD3	Laser	Phase maintenance is easy	.Simultaneous correction of both, second and third order is not possible due to coupling between different paths. To compensate arbitrary bandwidth limitation in the frequency domain.
----	---------------------	------------	----------------------	------	-------	---------------------------	--------------------------------------------------------------------------------------------------------------------------------------------------------------------------------------------

Apart from the techniques summarized in Table 2.1, detailed explanation of the possible techniques is discussed. Linearization methods based on optical technologies such as feedforward [2.37-2.42], cascaded SOA and MZM [2.43-44], light injection cross modulation [2.45-2.48] and dual-parallel modulation [2.49-2.54] suffer from expensive optical components, complicated system design, and more importantly, precise control/matching requirement of amplitude, phase, or bias, which severely prevent them from real application. Predistortion technique, on the other hand, features simple and low-cost implementations, which only needs a block of predistorter before the transmitter to pre-compensate the nonlinear channel response, and can be realized in electrical domain without expensive optical components. Given the static and highly predictable nature of MFH networks, as well as the limited system budget of access networks, predistortion is considered as one of the most cost-effective solutions to linearize analog MFH.

Predistortion can be applied in either analog or digital domain. For analog predistortion, the exponential transfer characteristics of diodes and CMOS circuits can be exploited to form desired nonlinear transfer function to linearize MFH channel response.

In general, any transmission impairments can be modeled as nonlinear distortion with memory effect, where the nonlinear distortion captures the dependence of channel transfer function on input amplitudes in the time domain; whereas memory effect is contributed by the bandwidth limitation in the frequency domain. For analog predistortion, the main technical challenges are the difficulties to synthesize arbitrary transfer functions in the time domain, and to compensate arbitrary bandwidth limitation in the frequency domain.

Withal, predistortion has another form that can be carried out in digital form too. Digital predistortion first transforms the input analog signals to digital domain by ADC, and after DSP the processed signals are transformed back to analog domain by DAC. Enabled by the advancement of DSP technologies, the challenges of analog predistortion can be easily addressed. In the time domain, arbitrary transfer functions can be synthesized; in the frequency domain, arbitrary memory effects can be addressed by frequency equalization enabled by FFT/IFFT.

Some functions that are difficult or even impossible to achieve with analog diodes can be easily realized by DSP. The only constraint of digital predistortion is the processing speed, which is limited by the speed and power consumption of input/output ADC/DAC.

In this chapter, a literature review is presented for digital predistortion (DPD) techniques that linearize the analog mobile front haul. Section 2.2 discusses the operating principles of DPD. Section 2.3 presents the evaluation performance parameters

2.2 Operating Principles

The principle of DPD exploits an inverse and nonlinear profile as that of the Radio over Fiber system. Consequently, when cascaded with the RoF system, it will lead to linearization of the overall cascaded system. The principle of DPD is shown in Figure 2.3.

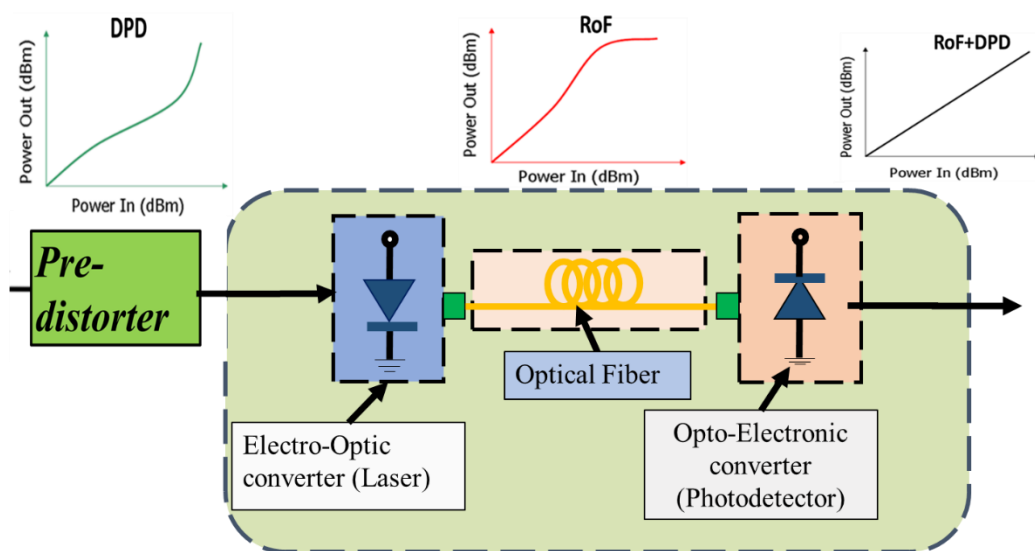


Figure 2.3: DPD linearization principle for Analog MFH

DPD should be inserted before the Electro-Optical (E/O) converter so that the over all link can be compensated. It should be noted that DPD based linearization can linearize links based on intensity modulation-direct detection (IM-DD) or coherent transmission.

2.3 Parameters to evaluate DPD linearization on signals

The performance evaluation and order of improvement in link linearization will be presented by the evaluation of parameters such as adjacent channel power ratio (ACPR), normalized mean square error (NMSE) and error vector magnitude (EVM).

The efficiency of the proposed methods is presented by the ACPR that computes the distortion components outside the useful signal bandwidth. It is expressed as [2.1]:

$$ACPR_{dBc} = 10 \log_{10} \left[\frac{\int_{ab_l}^{ab_u} S(f) df}{\int_{ub_l}^{ub_u} S(f) df} \right] \quad (2.1)$$

where ab_l and ab_u are the lower and upper frequency limits of the adjacent channel; ub_l and ub_u are the frequency bounds of useful bands. $S(f)$ denotes Power Spectral Density (PSD) of the output signal $y(n)$.

NMSE is defined as follows [2.27]:

$$NMSE_{dB} = 10 \log_{10} \left[\frac{\sum_{n=1}^N |x(n) - z_p(n)|^2}{\sum_{n=1}^N |x(n)|^2} \right] \quad (2.2)$$

The NMSE value is estimated between $z_p(n)$ and $x(n)$ of the RoF where N embodies the total signal length.

The performance of the proposed methods will be calculated additionally by the Error Vector Magnitude (EVM). It is a quantity that assesses the difference between the ‘expected’ complex value of a demodulated symbol with reference to ‘actual’ value of the received symbol. EVM can be mathematically expressed as [2.3]:

$$EVM (\%) = \sqrt{\frac{\frac{1}{M} \sum_{m=1}^M |S_m - S_{0,m}|^2}{\frac{1}{M} \sum_{m=1}^M |S_m|^2}} \quad (2.3)$$

where M is the number of symbols in the constellation, S_m is the ideal symbol of the constellation associated with the symbol “ m ” and $S_{0,m}$ is the real symbol associated with S_m . The 3GPP has set an EVM limit for LTE signals modulated by 256 quadrature amplitude modulation (QAM) format to be 3.5% [2.55].

2.4 DPD Models

The behavioral model of RoF treats RoF as a “black-box”. For DPD operation, input and output signals are required. Many mathematical models have been proposed that can be used for DPD identification. Many DPD techniques have been reported in this literature review. They can be classified into three categories: look-up table (LUT)-based DPDs [2.56, 2.57], Volterra series based DPDs [2.58-2.59] and neural network (NN)-based DPDs [2.60, 2.61]. The LUT-based DPD is simple, but its linearization performance depends on the size of the LUT.

Volterra series-based models are most widely used. One of the most commonly used models is memory polynomial (MP) that is able to counter act the non-linearities and memory effects at the same time. MP model is also called as diagonal Volterra model because the diagonal terms are non-zero while non diagonal terms are zero. Indeed, this MP model is a compromise between a memory less and full Volterra memory model. Depending on the application, scenario and order of nonlinearity, appropriate model can be chosen.

Recently, with growing interest in the complex models that have been derived from Volterra series. These models include Generalized Memory Polynomial (GMP), Dynamic Deviation Reduction (DDR) model, Laguerre Volterra model, etc. Now we discuss these models in the sections below. The DPD models can be divided in two main categories depending on the memory that they possess: Memoryless models and memory models.

In [2.60], an MP DPD based on direct learning architecture is proposed. Another MP DPD is proposed in [2.62], which is based on indirect learning architecture. The MP model is widely used because it has lower complexity than the Volterra series model and can closely mimic the nonlinear behavior of PA with memory effects. The artificial neural network (ANN) has excellent capability to accurately approximate nonlinear functions. Hence, ANN can be used to model the inverse characteristics of PA.

2.4.1 Memoryless Model

These equivalent basebands filtered models have been used extensively for modeling the DPD for power amplifiers. For low input bandwidth signal, the characteristics of PA have been modeled with memoryless model or with diagonal memory polynomial model. However, in case of RoF, memoryless models are not able to find a good linearization, therefore we have considered only memory-based models in our literature. Similarly, memoryless model defines only AM/AM conversion.

The memoryless polynomial model can be written as:

$$y(n) = \sum_{k=0}^{K-1} b_k |x(n)|^k (x(n)) \quad (2.4)$$

where $x(n)$ is baseband input and $y(n)$ is baseband output respectively. b_k is the complex valued coefficient and K is maximum order of nonlinearity.

2.4.2 Models Derived from Volterra Series

The E/O and O/E conversion can introduce memory effects which can add a limitation to the performance of DPD operation. Therefore, in order to take in to account the memory effects, Volterra series is a good choice.

The Volterra series model can be expressed in following form:

$$\check{y}(n) = \sum_{k=1}^{+\infty} \int_0^{+\infty} \dots \int_0^{+\infty} h_k(\tau_1, \dots, \tau_k) \prod_{r=1}^k \check{x}(t - \tau_r) d\tau_r \quad (2.5)$$

Where $\check{y}(n)$ is the RF output signal of the system, $\check{x}(n)$ is the RF input signal, while $h_m(\cdot)$ is the m -th order Volterra kernel. Once the RF signal is down converted to baseband, the envelope can be obtained through low pass filter. Therefore, a baseband image in discrete time with input as $\check{x}(n)$ will be:

$$y(n) = \sum_{k=0}^K \sum_{q_1=0}^{Q-1} \sum_{q_2=l_1}^{Q-1} \dots \sum_{q_{2k+1}}^{Q-1} h_{2k+1}(l_1, \dots, l_{2k+1}) \prod_{r=1}^{k+1} \tilde{x}(t - l_j) \prod_{r=k+2}^{2k+1} x^*(n - l_j) \quad (2.6)$$

where K represents the nonlinearity order and Q represents the memory depth.

Eq. 2.6 states that Volterra series model is strongly dependent on the number of terms. The complexity increases with increasing number of terms. Moreover, the identification process becomes cumbersome.

2.4.2.1 Memory Polynomial Model

Memory Polynomial (MP) model is referred as an inverse non-linear model that has been exploited previously as a powerful model for both, inverse and direct modeling of power amplifier (PA) nonlinearities. Applying this model for RoF has an additional advantage since memory less model might have problems to characterize the electro-optical (EO) conversion phenomena accurately [2.63].

The MP model is generally referred as a compromise between memoryless nonlinearity and full Volterra series due to presence of diagonal memory. The output in this case is referred as:

$$y(n) = \sum_{k=0}^{K-1} \sum_{q=0}^{Q-1} c_{kq} x(n-l) |x(n-l)|^k \quad (2.7)$$

Here K represents order of non-linearity, Q is referred as the memory depth, $y(n)$ represents the predistorter input sequence, $x(n)$ shows a baseband input signal and c_{kq} denotes the model coefficients.

2.4.2.2 Generalized Memory Polynomial Model

MP model has been effectively used for DPD, however, the performance can be improved by formulating a more general memory structure. The use of Generalized Memory Polynomial (GMP) model has been widely utilized for the linearization of PAs [2.64]. However, GMP has not been yet evaluated for RoF with varying lengths. The GMP model basis functions possess memory for both, for the diagonal terms as well as for the crossing terms i.e., $x(n - q)|x(n - r)|^{k-1}$, where $q \neq r$. The output of the post inverse block $z_p(n)$ modeled with GMP can be expressed as:

$$\begin{aligned}
 y(n) = & \sum_{k=0}^{K_a-1} \sum_{q=0}^{Q_a-1} c_{kq} x(n - q) |x(n - q)|^k \\
 & + \sum_{k=1}^{K_b} \sum_{q=0}^{Q_b-1} \sum_{r=1}^{R_b} d_{kqr} x(n - q) |x(n - q - r)|^k \\
 & + \sum_{k=1}^{K_c} \sum_{q=0}^{Q_c-1} \sum_{r=1}^{R_c} e_{kqr} x(n - q) |x(n - q + r)|^k
 \end{aligned} \tag{2.8}$$

where $y(n)$ and $x(n)$ represents the DPD output and input respectively. Similarly, c_{kq} ; d_{kqr} and e_{kqr} denotes the complex coefficients for the signal and the envelope; signal and lagging envelope and signal and leading envelope respectively.

k represents the index of nonlinearity, and q, r represents the indices of the memory. While K_a, K_b, K_c are the maximum orders of nonlinearity, Q_a, Q_b, Q_c are the memory depths, while R_b and R_c exhibits the lagging and leading delay tap lengths, respectively. GMP has been applied choosing $K_a=K_b=K_c=K$, $Q_a=Q_b=Q_c=Q$ and $R_b = R_c = R$.

2.4.2.3 Orthogonal Polynomial Model

The conventional polynomial model as in Eq. (2.7) has basis functions which are not orthogonal. The polynomial model with orthogonal basis reduces the numerical instability linked with conventional polynomial model.

The memoryless polynomial given in Eq. (2.6) is given as follows:

$$y(n) = \sum_{k=0}^{K-1} \beta_k \psi_k(x(n)) \quad (2.9)$$

Where

$$\psi_k(x) = \sum_{i=0}^k U_{ik} |x|^i x \quad (2.10)$$

And U_{ik} are the coefficients of orthogonal polynomial basis functions.

Similarly, the memory polynomial with orthogonal basis is proposed as:

$$y(n) = \sum_{k=0}^{K-1} \sum_{q=0}^{Q-1} \beta_k \psi_k(x(n-l)) \quad (2.11)$$

2.4.3 Decomposed Vector Rotation Model

The Decomposed Vector Rotation model (DVR) architecture was suggested for the linearization of Power Amplifiers (PAs) [2.65] and a comparative study for PAs was implied recently in [2.66]. DVR is an adapted version of the canonical piecewise linear (CPWL) functions to handle complex valued signal. DVR is expressed as:

$$\begin{aligned} y(n) &= \sum_{i=0}^{Q_{DVR}} a_i |x(n-i)| \\ &+ \sum_{k=1}^{K_{DVR}} \sum_{i=0}^{Q_{DVR}} a_{ki,1} \left(|x(n-i)| - \beta_k \right) e^{j\theta(n-i)} \\ &+ \sum_{k=1}^{K_{DVR}} \sum_{i=0}^{Q_{DVR}} a_{ki,21} \left(|x(n-i)| - \beta_k \right) e^{j\theta(n-i)} \cdot |x(n)| \end{aligned}$$

$$\begin{aligned}
& + \sum_{k=1}^{K_{DVR}} \sum_{i=0}^{Q_{DVR}} a_{ki,22} \left| |x(n-i)| - \beta_k \right| \cdot x(n) \\
& + \sum_{k=1}^{K_{DVR}} \sum_{i=0}^{Q_{DVR}} a_{ki,23} \left| |x(n-i)| - \beta_k \right| \cdot x(n-i) \\
& + \sum_{k=1}^{K_{DVR}} \sum_{i=0}^{Q_{DVR}} a_{ki,24} \left| |x(n-i)| - \beta_k \right| \cdot x(n-i) \\
& + \dots
\end{aligned} \tag{2.12}$$

where $x(n)$ and $y(n)$ are the input and output respectively. Similarly, β_k is the breakpoint while K_{DVR} represents elements in the partition and Q_{DVR} represents the memory depth.

2.4.4 Neural Network Models

Neural network (NN) models are also used for DPD modeling. NN is a multi-layer structure that has been developed from imitating the nervous system. It is a consolidated choice because it can be trained to learn any arbitrary nonlinear input-output relationships. Since it carries excellent capability to accurately approximate nonlinear functions, it can be used to model the inverse characteristics of the system under test.

The input signal is fed to the input layer, and the output signal is found at the output layer. Each layer is a group of neurons which have no connection between each other but have connections with the neurons of the next layer. For linearization of PA, a PD based on a multilayer perceptron is presented in [2.67]. In [2.68], a two-hidden-layer feedforward neural network (FFNN) model is proposed for PA modelling and DPD. A real-valued time delay neural network is proposed in [2.69] using only real-valued parameters and the real components of input and output signals. The multilayer NN model is shown below in Figure 2.4:

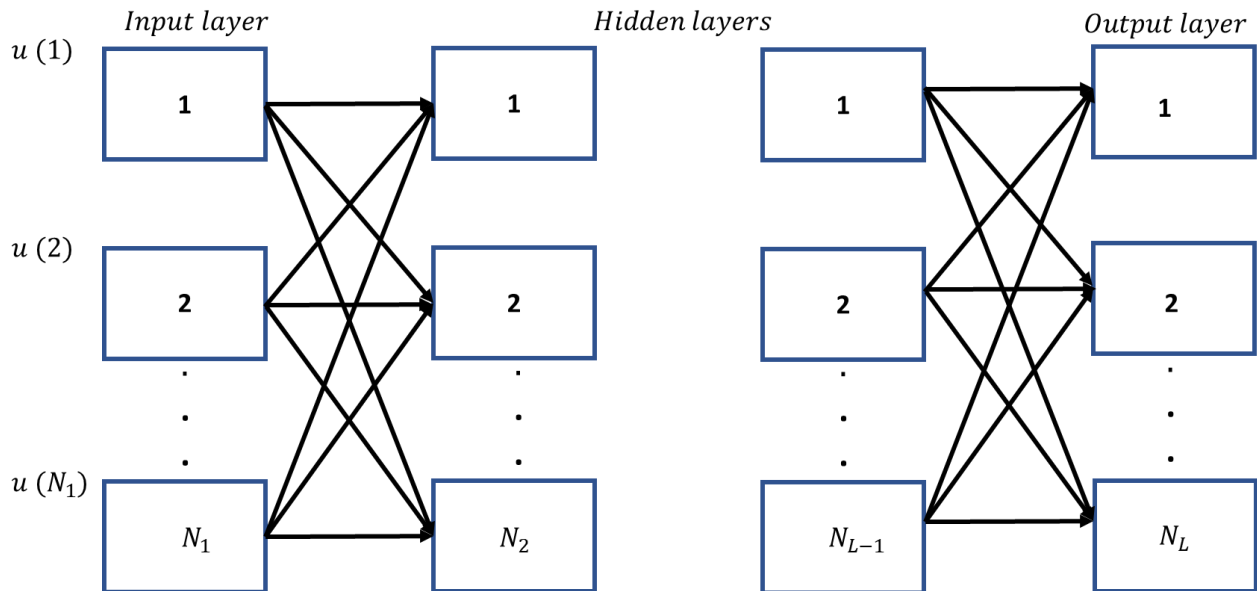


Figure 2.4: Multilayer Neural Network Model

2.5 DPD Identification

The estimation of predistortion model coefficients is referred as DPD identification which is an important aspect of digital predistortion.

There are two approaches that have been identified in literature for estimation of model coefficients: direct learning architecture (DLA) and indirect learning architecture (ILA) [2.60, 2.62].

In DLA, the DPD operation is directly identified with the input/output signals of the system while in ILA, a pre distorter training block generally referred as “post-inverse” block identifies first the input and output signals and then in the second phase applies the training coefficients to the system under test as a DPD. This means that post-inverse becomes cascaded as a predistorter block after the training phase.

2.5.1 Indirect Learning Architecture

The indirect learning architecture (ILA) is shown in Figure 2.5. The DPD model identification is very important aspect which is based on the estimation of the digital predistorter model

coefficients. Since in ILA, there is no need of model assumption, post-inverse (post-distorter) can be used as pre-inverse (pre-distorter) and allows for linear estimation of the coefficients, therefore it is straightforward and has been commonly used in [2.64], [2.65].

ILA can imply different techniques to identify DPD models such as least squares (LS), recursive least square (RLS) and least mean square (LMS) [2.70-2.73]. We will describe LS method since its usability is straight forward and carries less complexity.

There are number of least squares (LS) algorithm for estimation of model coefficients that take the linear weighting of nonlinear signals [2.74]. The formulation of the estimation initiates with collecting the coefficients e.g., c_{kq} , d_{kqr} and e_{kqr} in to a $R \times 1$ vector \mathbf{v} . R represents the total number of coefficients. \mathbf{v} means a signal whose time will sample over the same period. Considering (2), coefficients c_{21} denotes the signal $x(n-1)|x(n-1)|^2$. \mathbf{Z} characterizes the collection of all such vectors into a $N \times R$ matrix.

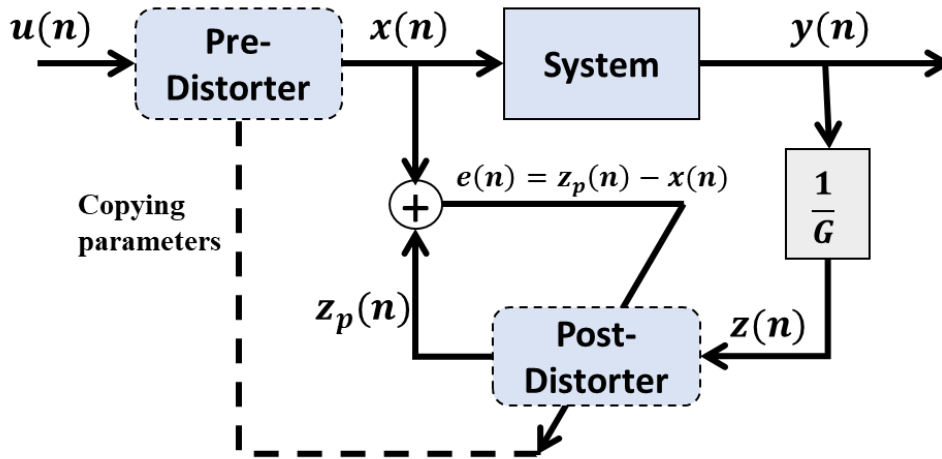


Figure 2.5: Indirect Learning Architecture (ILA) for system under test

Once the convergence condition is obtained, the output of the predistorter training block becomes: $z_p(n) = x(n)$ and hence $z(n) = u(n)$. For total samples N , the output can be written in the following way:

$$\mathbf{z}_p = \mathbf{Z}\mathbf{v} \quad (2.13)$$

Where $\mathbf{z} = [z(1), \dots, z(N)]^T$, $\mathbf{z}_p = [z_p(1), \dots, z_p(N)]^T$, while \mathbf{v} displays a $R \times 1$ vector that contains the coefficients c_{kq} , d_{kqr} and e_{kqr} . The LS solution will then become a solution for the equation expressed as:

$$[\mathbf{Z}^H \mathbf{Z}] \hat{\mathbf{v}} = \mathbf{Z}^H \mathbf{x} \quad (2.14)$$

In order to solve Eq. (2.14), many approaches have been proposed. One of them is QR factorization which is generally implied to badly conditioned matrix. $\mathbf{Z}^H \mathbf{Z}$ is generally badly conditioned matrix. Therefore, we explain below the QR factorization method:

- i. QR factorization is computed. Since $\mathbf{Z} = \mathbf{Q}\mathbf{R}$, where \mathbf{Q} is a matrix ($N \times N$) while \mathbf{R} is a $N \times R$ upper triangular matrix. There are $2N \times R^2 - \frac{2}{3} R^3$ flops in this step.
- ii. $\mathbf{Q}^H \mathbf{x}$ is computed. Here, $2NR - R$ are flops in this step.
- iii. $\mathbf{R}\hat{\mathbf{c}} = \mathbf{Q}^H \mathbf{x}$ is solved for upper triangular matrix. There are R^2 flops involved in this step.

The LS solution in (4) should minimize the cost function

$$C = \sum_{n=1}^N |z_p(n) - x(n)|^2 \quad (2.15)$$

2.5.2 Direct Learning Architecture

The direct learning architecture (DLA) is shown in Figure 2.6. The model of DPD employing DLA using nonlinear filtered x least mean square algorithm (NFxLMS) has been used in [2.75]. The coefficient κ of the basis function $\varphi_k[u(n)]$ can be updated by stochastic gradient algorithm while the gradient is represented by derivative:

$$\begin{aligned} \frac{\partial \varepsilon^2(n)}{\partial \kappa} &= 2\varepsilon^2(n) \frac{\partial \varepsilon(n)}{\partial \kappa} \\ &= -2\varepsilon^*(n) \frac{\partial z(n)}{\partial \kappa} \end{aligned} \quad (2.16)$$

where

$$\frac{\partial z(n)}{\partial \kappa} \cong \sum_{q=0}^{Q-1} \frac{\partial z(n)}{\partial x(n-q)} \varphi_k[u(n-q)] \quad (2.17)$$

Here Q is the memory depth of DPD model and $\frac{\partial z(n)}{\partial x(n-q)}$ is the derivative of nonlinear model.

Therefore, a model needs to be identified firstly.

For simplicity, $g(q, n) = \frac{\partial z(n)}{\partial x(n-q)}$; therefore Eq. 2.17 becomes:

$$\frac{\partial z(n)}{\partial \kappa} \cong \sum_{q=0}^{Q-1} g(q, n) \varphi_k[u(n-q)] \quad (2.18)$$

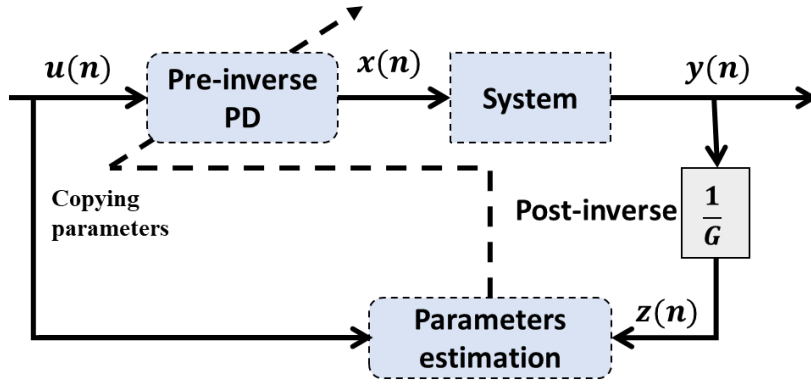


Figure 2.6: Direct Learning Architecture (DLA) for system under test

It is equivalent that each basis function $\varphi_k[u(n)]$ is filtered by an instantaneous equivalent linear (IEL) filter $\mathbf{g}(n) = [\mathbf{g}(0, n), \dots, \mathbf{g}(L-1, n)]$ [2.76]. Using this method, an NFxRLS is proposed for recursive least square (RLS) algorithm. Replacing (2.18) into (2.16), we can have:

$$\begin{aligned} \frac{\partial \varepsilon^2(n)}{\partial \kappa} &= -2\varepsilon^*(n) \frac{\partial z(n)}{\partial \kappa} \\ &= -2\varepsilon^*(n) \sum_{q=0}^{Q-1} g(q, n) \varphi_k[u(n-q)] \end{aligned}$$

$$= -2 \left[\varepsilon(n) \sum_{q=0}^{Q-1} g^*(q, n) \right]^* \varphi_k[u(n-q)] \quad (2.19)$$

A DLA estimator has been widely used to estimate DPD coefficients [2.77]. Since, there is no need to identify the PA model and coefficients errors is solved as a linear problem. The relation between the input u and the output x of the DPD can be expressed in matrix form as:

$$x = Uc \quad (2.20)$$

Where $x = [x(1) \dots x(N)]^T$, c is $R \times 1$ is coefficient vector where U is a $N \times R$ matrix of basis functions. The reference error of measurement is given as:

$$\begin{aligned} e(n) &= \frac{y(n)}{G} - u(n) \\ &= z(n) - u(n) \end{aligned} \quad (2.21)$$

The origin of the reference comes from two parts:

- The coefficients of DPD are not ideal. As the DPD model is linear with its coefficients, we can express the error generated by the coefficients error $\Delta \mathbf{c}$ by $\mathbf{U} \cdot \Delta \mathbf{c}$, where $\Delta \mathbf{c}$ is $R \times 1$ vector containing the set of coefficient errors $\Delta \mathbf{c}_i$.
- The LS error e_{LS} in the identification. In LS calculation, QR factorization is an orthogonal projection. Thus e_{LS} is orthogonal to the input signal \mathbf{U} .

$$e = e_{LS} + \mathbf{U} \cdot \Delta \mathbf{c} \quad (2.22)$$

To reduce e_{LS} , the cost function to minimize is:

$$\sigma = \sum \left| e(n) - \sum_R \Delta c_R \varphi_R[u(n)] \right|^2 \quad (2.23)$$

The LS solution of the coefficient error which minimize (2.23) is the solution for the following equation

$$U^H e = [U^H U] \Delta \mathbf{c} \quad (2.24)$$

where $e = [e(1)\dots e(N)]^T$

In this method, there is no need to calculate the inverse of the system model.

2.6 Conclusions

The chapter reviews the methodologies implied for linearization of analog radio over fiber systems. Table 2.1 presents a comparative overview of different linearization techniques. Each methodology is discussed w.r.t advantages and disadvantages that it carries. The concept of digital predistortion based linearization is discussed as the most advantageous technique. The motivation of applying DPD and methodologies are discussed in detail. The most important class of models utilized is the volterra based polynomial methods. DPD identification methods are presented.

It has been shown that initially volterra based methods were widely employed for the linearization of PAs. Later, these models were adapted for RoF too. It has been shown that it is also possible to go out of the “Volterra Box” and utilize other models such as DVR, DDR and ANN. Their tradeoffs have been discussed in light of literature review.

The main contributions of this dissertation are thoroughly presented in the following chapters.

References

- 2.1 M. U. Hadi et al., "Experimental evaluation of digital predistortion for VCSEL-SSMF-based Radio-over-Fiber link," 2018 International Topical Meeting on Microwave Photonics (MWP), Toulouse, France, 2018, pp. 1-4.
- 2.2 A. Gupta et al., "A Survey of 5G Network: Architecture and Emerging Technologies," IEEE Access, Vol. 3, p. 1206-1232 (2015).
- 2.3 Muhammad Usman Hadi, Hyun Jung, Salman Ghaffar, Pier Andrea Traverso, Giovanni Tartarini, Optimized digital radio over fiber system for medium range communication, Optics Communications, Volume 443, 2019, Pages 177-185, ISSN 0030-4018, <https://doi.org/10.1016/j.optcom.2019.03.037>.
- 2.4 K. Y. Lau, "RF transport over optical fiber in urban wireless infrastructures," in IEEE/OSA Journal of Optical Communications and Networking, vol. 4, no. 4, pp. 326-335, April 2012.
- 2.5 Y. Shi ; D. Visani ; C.M. Okonkwo ; H. Yang ; H.P.A. van den Boom ; G. Tartarini ; E. Tangdiongga ; A.M.J. Koonen "First demonstration of HD video distribution over large-core POF employing UWB for in-home networks," 2011 Optical Fiber Communication Conference and Exposition and the National Fiber Optic Engineers Conference, pp 1-3 (2011)
- 2.6 Y. Shi et al., "Ultrawideband Signal Distribution Over Large-Core POF for In-Home Networks," in Journal of Lightwave Technology, vol. 30, no. 18, pp. 2995-3002, Sept.15, 2012.
- 2.7 Hadi, M., Aslam, N. & Jung, H. (2019). Performance Appraisal of Sigma Delta Modulated Radio over Fiber System. Journal of Optical Communications, 0(0), pp. -Jan. 2019, from [doi:10.1515/joc-2018-0227](https://doi.org/10.1515/joc-2018-0227)
- 2.8 Hadi, M., Jung, H., Traverso, P., et al. (2019). Digital Radio Frequency Transport over Optical Fiber for 5G Fronthaul Links. Journal of Optical Communications, 0(0), pp. - Apr. 2019, from [doi:10.1515/joc-2019-0051](https://doi.org/10.1515/joc-2019-0051)

- 2.9 Hadi, M., Hadi, M., Aslam, N., et al. (2019). Experimental Demonstration of MASH Based Sigma Delta Radio over Fiber System for 5G C-RAN Downlink. *Journal of Optical Communications*, 0(0), pp. -. Retrieved 23 Feb. 2019, from doi:10.1515/joc-2019-0011
- 2.10 J. Nanni et al., "VCSEL-Based Radio-Over-G652 Fiber System for Short-/Medium-Range MFH Solutions," *IEEE/OSA J. Lightw. Technol.*, vol. 36, pp. 4430-4437, Oct.1, 2018.
- 2.11 G. Meslener, "Chromatic dispersion induced distortion of modulated monochromatic light employing direct detection," in *IEEE Journal of Quantum Electronics*, vol. 20, no. 10, pp. 1208-1216, Oct 1984.
- 2.12 P. A. Gamage, A. Nirmalathas, C. Lim, D. Novak, and R. Waterhouse, "Design and analysis of digitized RF-over-fiber links," *IEEE J. Lightw. Technol.*, vol. 27, p. 2052–2061, June 2009.
- 2.13 Haddad, A.; Gagnaire, M.: Radio-over-Fiber (RoF) for mobile backhauling: A technical and economic comparison between analog and digitized RoF. *Int. Conf. Opt. Netw. Design Modeling*, pp. 132137 (2014)
- 2.14 L. Breyne, G. Torfs, X. Yin, P. Demeester and J. Bauwelinck, "Comparison Between Analog Radio-Over-Fiber and Sigma Delta Modulated RadioOver-Fiber," in *IEEE Photonics Technology Letters*, vol. 29, no. 21, pp 1808-1811, 1 Nov.1, 2017. doi: 10.1109/LPT.2017.2752284
- 2.15 Hadi, M., Aslam, N. & Jung, H. (2019). Performance Appraisal of Sigma Delta Modulated Radio over Fiber System. *Journal of Optical Communications*, 0(0), pp. -Jan. 2019, from doi:10.1515/joc-2018-0227
- 2.16 Hadi, M., Hadi, M., Aslam, N., et al. (2019). Experimental Demonstration of MASH Based Sigma Delta Radio over Fiber System for 5G C-RAN Downlink. *Journal of Optical Communications*, 0(0), pp. -. Retrieved 27 Feb. 2019, from doi:10.1515/joc-2019-0011
- 2.17 S. Jang, G. Jo, J. Jung, B. Park, and S. Hong, "A digitized if-over fiber transmission based on low-pass delta-sigma modulation," *IEEE Photonics Technology Letters*, vol. 26, no. 24, pp. 2484–2487, Dec 2014.

- 2.18 Draa, M.; Hastings, A.; Williams, K. Comparison of photodiode nonlinearity measurement systems. *OSA Optics Expr.* 2011, 19, 12635–12645.
- 2.19 Chen, Z.; Yan, L.; Pan, W.; Luo, B.; Zou, X.; Guo, Y.; Jiang, H.; Zhou, T. SFDR enhancement in analog photonic links by simultaneous compensation for dispersion and nonlinearity. *OSA Optics Expr.* 2013, 21, 20999–21009.
- 2.20 Haas, B.M.; Murphy, T.E. A simple, linearized, phase-modulated analog optical transmission system. *IEEE Photon. Technol. Lett.* 2007, 19, 729–731.
- 2.21 Hraimel, B.; Zhang, X. Characterization and compensation of AM-AM and AM-PM distortion in mixed polarization radio over fiber systems. In *Proceedings of the 2012 IEEE MTT-S International Microwave Symposium (IMS)*, Montreal, QC, Canada, 1–3 June 2012
- 2.22 Zhu, R.; Zhang, X. Linearization of Radio-Over-Fiber Systems by Using Two Lasers with Different Wavelengths. In *Proceedings of the 2014 IEEE MTT-S International Microwave Symposium (IMS)*, Tampa, FL, USA, 1–6 June 2014
- 2.23 Ghannouchi, F.; Younes, M.; Rawat, M. Distortion and impairments mitigation and compensation of single- and multi-band wireless transmitters. *IET Microw. Antennas Propag.* 2013, 7, 518–534.
- 2.24 Duan, R.; Xu, K.; Dai, J.; Cui, Y.; Wu, J.; Li, Y.; Dai, Y.; Li, J. Linearity improvement based on digital signal processing in intensity-modulated analog optical links incorporating photonic frequency down conversion. In *Proceedings of the Optical Fiber Communication Conference and Exposition*, Los Angeles, LA, USA, 6–8 March 2012
- 2.25 Vieira, L.; Gomes, N.J.; Nkansah, A.; van Dijk, F. Behavioral modeling of radio-over-fiber links using memory polynomials. In *Proceedings of the 2010 IEEE Topical Meeting on Microwave Photonics (MWP)*, Montreal, QC, Canada, 5–9 October 2010; pp. 85–88.
- 2.26 Pei, Y.; Xu, K.; Li, J.; Zhang, A.; Dai, Y.; Ji, Y.; Lin, J. Complexity-reduced digital predistortion for subcarrier multiplexed radio over fiber systems transmitting sparse multi-band RF signals. *OSA Optics Expr.* 2013, 21, 3708–3714.

- 2.27 Atso Hekkala, Mikko Hiivala, Mika Lasanen, Jari Perttu, Luis C. Vieira, Nathan J. Gomes, Anthony Nkansah, "Predistortion of Radio Over Fiber Links: Algorithms Implementation and Measurements", *Circuits and Systems I: Regular Papers IEEE Transactions on*, vol. 59, no. 3, pp. 664-672, 2012.
- 2.28 F. Fuochi, M. U. Hadi, J. Nanni, P. A. Traverso, G. Tartarini, "Digital predistortion technique for the compensation of nonlinear effects in radio over fiber links", 2016 IEEE 2nd International Forum on Research and Technologies for Society and Industry Leveraging a better tomorrow (RTSI), pp. 1-6, 2016.
- 2.29 L. C. Vieira, N. J. Gomes and A. Nkansah, "An experimental study on digital predistortion for radio-over-fiber links," *Asia Communications and Photonics Conference and Exhibition*, Shanghai, 2010, pp. 126-127. doi: 10.1109/ACP.2010.5682803
- 2.30 A. Hekkala, M. Lasanen, L. C. Vieira, N. J. Gomes and A. Nkansah, "Architectures for Joint Compensation of RoF and PA with Nonideal Feedback," 2010 IEEE 71st Vehicular Technology Conference, Taipei, 2010, pp. 1-5. doi: 10.1109/VETECS.2010.5493871
- 2.31 C. Mateo, P. L. Carro, P. García-Dúcar, J. de Mingo and Í. Salinas, "Experimental evaluation of the feedback loop effects in digital predistortion of a radio-over-fiber system," 2017 Ninth International Conference on Ubiquitous and Future Networks (ICUFN), Milan, 2017, pp. 1039-1041. doi: 10.1109/ICUFN.2017.7993958
- 2.32 C. Mateo, J. Clemente, P. Garcia-Ducar, P. L. Carro, J. de Mingo and I. Salinas, "Digital predistortion of a full-duplex Radio-over-Fiber mobile fronthaul link with feedback loop," 2017 13th International Wireless Communications and Mobile Computing Conference (IWCMC), Valencia, 2017, pp. 1425-1430. doi: 10.1109/IWCMC.2017.7986493
- 2.33 C. Mateo, P. L. Carro, P. García-Dúcar, J. de Mingo and Í. Salinas, "Minimization of Feedback Loop Distortions in Digital Predistortion of a Radio-Over-Fiber System With Optimization Algorithms," in *IEEE Photonics Journal*, vol. 9, no. 3, pp. 1-14, June 2017, Art no. 7904414. doi: 10.1109/JPHOT.2017.2706364

- 2.34 Roselli, L., Borgioni, V., Zepparelli, F., Ambrosi, F., Comez, M., Faccin, P., Casini, A.: Analog laser predistortion for multiservice radio-over-fiber systems. *IEEE J. Lightw. Technol.* 37(5), 1211-1223 (2003)
- 2.35 R. B. Childs, V. A. O'Byrne, V.A., Multichannel AM video transmission using a high-power Nd:YAG laser and linearized external modulator," *Journal on Selected Areas in Communications*, vol. 8, no. 7, pp. 1369-1376, 1990.
- 2.36 B. Hraimel and X. Zhang, Low-cost broadband predistortion-linearized singledrive x-cut Mach-Zehnder modulator for radio-over-fiber systems," *Photonics Technology Letters*, vol. 24, no. 18, pp. 1571-1573, 2012
- 2.37 L. S. Fock, R. S. Tucker, Reduction of distortion in analogue modulated semiconductor lasers by feedforward compensation," *Electronics Letters*, vol. 27, no. 8, pp. 669-671, 1991.
- 2.38 L. S. Fock, R. S. Tucker, Simultaneous reduction of intensity noise and distortion in semiconductor lasers by feedforward compensation," *Electronics Letters*, vol. 27, no. 14, pp. 1297-1299, 1991.
- 2.39 L. S. Fock, A. Kwan, and R. S. Tucker, Reduction of semiconductor laser intensity noise by feedforward compensation: experiment and theory," *Journal of Lightwave Technology*, vol. 10, no. 12, pp. 1919-1925, 1992.
- 2.40 D. Hassin and R. Vahldieck, Feedforward linearization of analog modulated laser diodes-theoretical analysis and experimental verification," *IEEE Transactions on Microwave Theory and Techniques*, vol. 41, no. 12, pp. 2376-2382, 1993.
- 2.41 B. Buxton, R. Vahldieck, Noise and intermodulation distortion reduction in an optical feedforward transmitter," *IEEE Microwave Theory and Techniques Society (MTT-S) International Microwave Symposium (IMS) 1994*, paper WE3F-47, pp. 1105-1108.

- 2.42 T. Iwai, K. Sato, K. Suto, Signal distortion and noise in AM-SCM transmission systems employing the feedforward linearized MQW-EA external modulator," *Journal of Lightwave Technology*, vol. 13, no. 8, pp. 1606-1612, 1995.
- 2.43 S.-Y. Lee, B.-J. Koo, H.-D. Jung, and S.-K. Han, Reduction of chromatic dispersion effects and linearization of dual-drive Mach-Zehnder modulator by using semiconductor optical amplifier in analog optical links," *European Conference on Optical Communication (ECOC) 2002*, paper P3.32.
- 2.44 D.-H. Jeon, H.-D. Jung, and S.-K. Han, Mitigation of dispersion-induced effects using SOA in analog optical transmission," *Photonics Technology Letters*, vol. 14, no. 8, pp. 1166-1168, 2002.
- 2.45 T. Ismail, J. E. Mitchell, A. J. Seeds, Linearity enhancement of a directly modulated uncooled DFB laser in a multi-channel wireless-over-fibre system," *IEEE Microwave Theory and Techniques Society (MTT-S) International Microwave Symposium (IMS) 2005*, pp. 7-10. 151
- 2.46 T. Ismail, C.-P. Liu, J. E. Mitchell, and A. J. Seeds, High-dynamic-range wireless-over-fiber link using feedforward linearization," *Journal of Lightwave Technology*, vol. 25, no. 11, pp. 3274-3282, 2007.
- 2.47 S.-H. Lee, J.-M. Kang, I.-H. Choi, and S.-K. Han, Linearization of DFB laser diode by external light-injected cross-gain modulation for radio-over-fiber link," *Photonics Technology Letters*, vol. 18, no. 14, pp. 1545-1547, 2006.
- 2.48 C. Sun, D. Liu, B. Xiong, Y. Luo, J. Wang, Z. Hao, Y. Han, L. Wang, H. Li, Modulation characteristics enhancement of monolithically integrated laser diodes under mutual injection locking," *Journal of Selected Topics in Quantum Electronics*, vol. 21, no. 6, pp. 628-635, 2015.
- 2.49 S. K. Korotky and R. M. De Ridder, Dual parallel modulation schemes for low-distortion analog optical transmission," *IEEE Journal of Selected Areas in Communications*, vol. 8, no. 7, pp. 1377-1381, 1990.

- 2.50A. Djupsjobacka, A linearization concept for integrated-optic modulators," *Photonics Technology Letters*, vol. 4, no. 8, pp. 869-872, 1992.
- 2.51J. L. Brooks, R. A. Becker, Implementation and evaluation of a dual parallel linearization system for AM-SCM video transmission," *Journal of Lightwave Technology*, vol. 11, no. 1, pp. 34-41, 1993.
- 2.52 H.-D. Jung, S.-K. Han, Dynamic nonlinearity reduction of DFB-LD by dual parallel modulation," *IEEE Lasers and Electro-Optics Society (LEOS) Annual Meeting 2000*, vol. 1, pp. 74-75, paper MH2.
- 2.53 H.-D. Jung, S.-K. Han, Nonlinear distortion suppression in directly modulated DFB-LD by dual-parallel modulation," *Photonics Technology Letters*, vol. 14, no. 7, pp. 980-982, 2002.
- 2.54T. M. F. Alves and A. V. T. Cartaxo, Transmission of OFDM-UWB radio signals in IM-DD optical fiber communication systems employing optimized dual parallel mach-zehnder modulators," *Journal of Optical Communications and Networking*, vol. 5, no. 2, pp. 159-171, 2013.
- 2.55 3GPP TS36.101 V12.6.0, Evolved Universal Terrestrial Radio Access (E-UTRA) User Equipment (UE) Radio Transmission and Reception (Release 12), December 2014
- 2.56 Gilabert, P.L., and Montoro, G.: 'Look-up table implementation of a slow envelope dependent digital predistorter for envelope tracking power amplifiers', *IEEE Microw. Compon. Lett.*, 2012, 22, (2), pp. 97–99
- 2.57 Feng, X., Feuvrie, B., Descamps, A.S., and Wang, Y.: 'A digital predistortion technique based on non-uniform MP model and interpolated LUT for linearizing PAs with memory effects', *Electron. Lett.*, 2014, 50, (24), pp. 1882–1884
- 2.58 Cabarkapa, M., Neskovic, N., Neskovic, A., and Budimir, D.: 'Adaptive nonlinearity compensation technique for 4G wireless transmitters', *Electron. Lett.*, 2012, 48, (20), pp. 1308–1309

- 2.59 Ding, L., Zhou, G.T., Morgan, D.R., Ma, Z., Kenney, J.S., Kim, J., and Giardina, C.R.: ‘A robust digital baseband predistorter constructed using memory polynomials’, IEEE Trans. Commun., 2004, 52, (1), pp. 159–165
- 2.60 Naskas, N., and Papananos, Y.: ‘Neural-network-based adaptive baseband predistortion method for RF power amplifiers’, IEEE Trans. Circuits Syst. II, Exp. Briefs, 2004, 51, (11), pp. 619–623
- 2.61 Mkaem, F., and Boumaiza, S.: ‘Physically inspired neural network model for RF power amplifier behavioral modeling and digital predistortion’, IEEE Trans. Microw. Theory Tech., 2011, 59, (4), pp. 913–923
- 2.62 Ding, L., Zhou, G.T., Morgan, D.R., Ma, Z., Kenney, J.S., Kim, J., and Giardina, C.R.: ‘A robust digital baseband predistorter constructed using memory polynomials’, IEEE Trans. Commun., 2004, 52, (1), pp. 159–165
- 2.63 M.U. Hadi, J. Nanni, O. Venard, G. Baudoin, J. Polleux, P.A. Traverso, G. Tartarini "Linearity Improvement of VCSELs based Radio over Fiber Systems utilizing Digital Predistortion", Advances in Science, Technology and Engineering Systems Journal, vol. 4, no. 3, pp. 156-163 (2019).
- 2.64 D. Morgan, Z. Ma, J. Kim, M. Zierdt, and J. Pastalan, “A generalized memory polynomial model for digital predistortion of rf power amplifiers,” Signal Processing, IEEE Transactions on, vol. 54, no. 10, pp. 3852–3860, Oct. 2006.
- 2.65 A. Zhu, “Decomposed Vector Rotation-Based Behavioral Modeling for Digital Predistortion of RF Power Amplifiers,” IEEE Trans. Microw. Theory Tech., 63(2), 737-744, 2015
- 2.66 C. Kantana, et al., "Comparison of GMP and DVR models," 2018 INMMIC, Brive La Gaillarde, 2018, pp. 1-3
- 2.67 Naskas, N., and Papananos, Y.: ‘Neural-network-based adaptive baseband predistortion method for RF power amplifiers’, IEEE Trans. Circuits Syst. II, Exp. Briefs, 2004, 51, (11), pp. 619–623

- 2.68 Mkadem, F., and Boumaiza, S.: ‘Physically inspired neural network model for RF power amplifier behavioral modeling and digital predistortion’, *IEEE Trans. Microw. Theory Tech.*, 2011, 59, (4), pp. 913–923
- 2.69 T. Liu, S. Boumaiza, and F. Ghannouchi, “Dynamic behavioral modeling of 3g power amplifiers using real-valued time-delay neural networks,” *Microwave Theory and Techniques, IEEE Transactions on*, vol. 52, no. 3, pp. 1025–1033, March 2004.
- 2.70 L. Ding, G. Zhou, D. Morgan, Z. Ma, J. Kenney, J. Kim, and C. Giardina, “A robust digital baseband predistorter constructed using memory polynomials,” *Communications, IEEE Transactions on*, vol. 52, no. 1, pp. 159–165, Jan. 2004
- 2.71 C. Eun and E. Powers, “A new volterra predistorter based on the indirect learning architecture,” *Signal Processing, IEEE Transactions on*, vol. 45, no. 1, pp. 223–227, Jan 1997.
- 2.72 M. Abi Hussein, V. Bohara, and O. Venard, “On the system level convergence of ILA and DLA for digital predistortion,” in *Wireless Communication Systems (ISWCS), 2012 International Symposium on*, Aug 2012, pp. 870–874
- 2.73 M. Hussein, V. Bohara, and O. Venard, “Multi-stage digital predistortion based on indirect learning architecture,” in *Acoustics, Speech and Signal Processing (ICASSP), 2013 IEEE International Conference on*, May 2013, pp. 6093–6097.
- 2.74 M. Schoukens and K. Tiels, “Identification of nonlinear block-oriented systems starting from linear approximations: A survey,” *CoRR*, vol. abs/1607.01217, 2016. [Online]. Available: <http://arxiv.org/abs/1607.01217>
- 2.75 Y. H. Lim, Y. S. Cho, I. W. Cha, and D. H. Youn, “An adaptive nonlinear prefilter for compensation of distortion in nonlinear systems,” *Signal Processing, IEEE Transactions on*, vol. 46, no. 6, pp. 1726–1730, Jun 1998.
- 2.76 D. Zhou and V. E. DeBrunner, “Novel adaptive nonlinear predistorters based on the direct learning algorithm,” *Signal Processing, IEEE Transactions on*, vol. 55, no. 1, pp. 120–133, Jan. 2007.

2.77R. N. Braithwaite, "Closed-loop digital predistortion (dpd) using an observation path with limited bandwidth," *IEEE Transactions on Microwave Theory and Techniques*, vol. 63, no. 2, pp. 726–736, Feb 2015.

Chapter 3

Direct Digital Predistortion for compensation of nonlinearities in Radio over Fiber links

Some contents of this chapter are taken from J2, C2 and C3, where we presented the characterization of digital predistortion method based on behavioral model.

This chapter proposes a predistortion technique for linearizing Analog RoF links which corrects the link impairments caused due to combined effect of laser chirp and fiber dispersion. The proposed technique is independent of the laser model which makes it salutary in terms of adapting to other possible laser models. The mathematical framework of the proposed technique and its implementation is discussed. The predistortion is applied firstly to sinusoidal signals and then to LTE standard signals. As a figure of merit, the effects of the proposed operation are reported by analysing the Adjacent Channel Leakage Ratio (ACLR) and Error Vector Magnitude (EVM) of the received signal.

3.1 Introduction

In order to manage the ever-increasing demand for larger transmission bandwidth, the Analog Radio-over-Fiber (A-RoF) technology is a viable solution which has found application in the distribution of both wired and wireless services within various scenarios, utilizing as transmission channel different types of silica fibers, as Single Mode [3.1], Multimode [3.2] or Multi-Core [3.3], or also utilizing Polymeric Plastic optical fibers [3.4].

The A-RoF technology plays a major role in the realization of the physical layer of 3G and 4G systems and is expected to form the cornerstone of the future fifth generation of wireless networks [3.5-3.7]. In addition to the advantages coming from the use of the optical fiber as a transmission channel, like extremely broad bandwidth, immunity to electromagnetic interference and large

transmission distances, an additional attractive feature lies in the agnosticism of RoF systems concerning the particular transmission modulation format, which makes them intrinsically future-proof.

Nonetheless, the drawbacks of these systems can be presented through the presence of distortion that can possibly lower the performances. These impairments are caused by imperfect linear behavior of laser, photo detector and optical fiber. One primary drawback of these systems is the signal susceptibility to the combination of fiber chromatic dispersion and spurious phase signals generated by the laser source (also called frequency chirp) [3.8].

To subdue the nonlinearities in A-RoF transmission, various solutions have been proposed, which include analog and digital electrical techniques [3.9-3.13]

Analog predistortion method was addressed in [3.9] where the nonlinearities of the laser source were compensated. The drawback of the said methodology is difficult application on large scale production because every single RoF transmitter requires a variant predistorter. Digital Predistortion linearization technique using memory polynomials was discussed in [3.10], while a trained predistorter based on Volterra series has been applied to Non Linear RoF link [3.11-3.14]. Similarly, the Digital Predistortion technique based on canonical pecewise-linear (CPWL) function was proposed for intensity modulated/direct detection RoF system [3.15]. More recently, Digital Predistortion based on memory and generalized memory polynomial was proposed for VCSELs based radio over fiber links [3.16-3.17].

All the techniques apply the distortion compensation considering the RoF systems as “black box”. However, to guarantee the accuracy of the digital linearization performed, memory length and order of nonlinearity has to increase which leads to high complexity of the predistortion process. This factor can reduce the application of this linearization method substantially. Similarly, there exists a simpler possibility where one can identify the source of nonlinear behavior and directly compensate it without any feedback. One of these cases is based on the behavioral modeling of the whole link in which predistorter is used to compensate the nonlinearity of the RoF link [3.18]. In this case, knowing physical macroscopic quantities of the A-RoF components it is possible to compensate for nonlinearities generated by laser chirp and fiber dispersion.

In this chapter, the above mentioned “direct” predistortion is theoretically studied and implemented. The predistortion is applied firstly to sinusoidal signals and then to LTE standard signals. As a figure of merit, the effects of the proposed operation are reported by analyzing the Adjacent Channel Leakage Ratio (ACLR) and Error Vector Magnitude (EVM) of the received signal. ACLR and EVM are utilized as performance parameters. The proposed technique is independent of the Laser model which makes it salutary in terms of adapting to other possible laser models.

The chapter is organized as follows. Section 3.2 gives the brief description related to the mathematical modeling of the proposed predistorter. In Section 3.3, simulation results for the proposed predistorter are presented and briefly discussed. Section 3.4 discusses the predistorter behavior in the presence of adiabatic chirp while Section 3.5 talks about feasibility of the proposed distorter. Finally, Section 3.6 concludes the chapter.

3.2 Proposed Approach

A conventional directly modulated A-RoF link, including the proposed predistorter is shown in Figure 3.1. In detail, the RoF link is composed of a laser transmitter, a standard optical fiber cable, and a photodiode, which converts the optical power in the electric current. The combined effect of laser chirp and fiber chromatic dispersion leads to signal degeneration in RoF links [3.8-3.19].

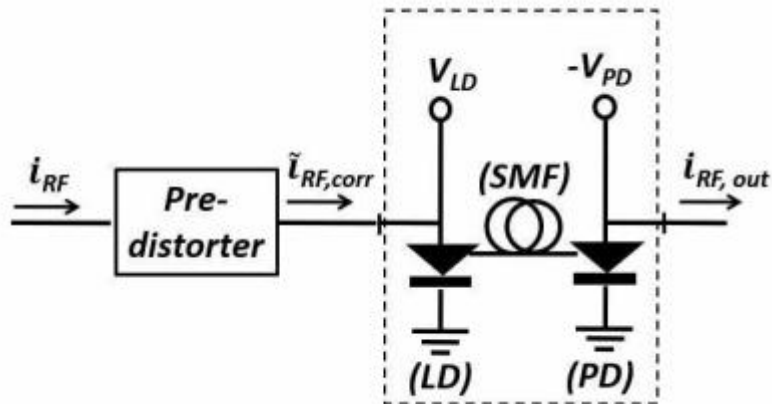


Figure 3.1: Block scheme representing the collocation of the proposed predistorter block. The dashed rectangle encases Radio over Fiber link schematized through its essential components. LD: Laser diode; SMF: Single Mode Fiber; PD: Photo Diode.

The idea behind the proposed predistortion technique is that in the absence of fiber chromatic dispersion, the only presence of laser chirp would not determine any nonlinear effect. Thus, the predistorter is then used to digitally generate an opposite dispersion to compensate the nonlinearity of the RoF link. The functional scheme of the Predistorter block is shown in Figure 3.2.

The proposed approach, in the beginning, converts the analog RF modulating current to a digital one by means of an Analog to Digital Converter (ADC). Then it works with the samples $I(t_n)$ to predict a modulated optical field $E(t_n)$ by exploiting an appropriate laser model. $E(t_n)$ becomes the input of the “Fiber Compensation” block whose output is a corrected modulated optical field $E_{corr}(t_n)$ which would theoretically not be affected by the fiber dispersion effect.

To obtain $E_{corr}(t_n)$, the field $E(t_n)$ is convolved with the conjugate of the fiber pulse response. Subsequently, the input current correction block calculates, through an inverse function of the Laser model, the corrected samples of current, $i_{corr}(t_n)$, that, once utilized as a laser input signal, should result in an electric field as close as possible to $E_{corr}(t_n)$. Through a Digital to Analog Converter (DAC), the current is finally brought back to analog form and modulates the injection current of the laser source of the real RoF link.

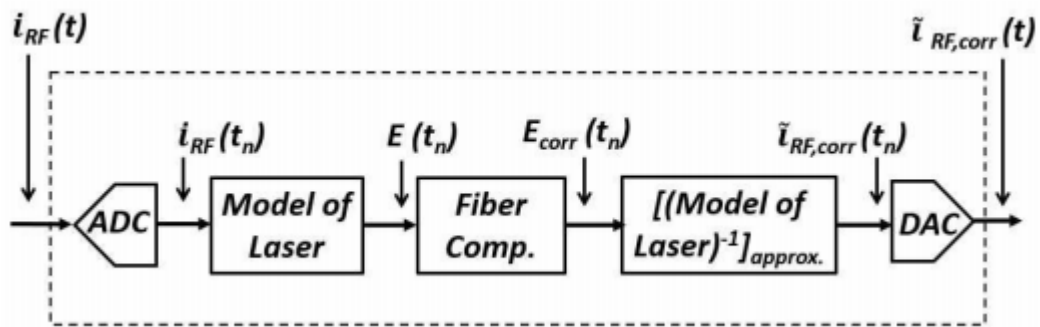


Figure 3.2: Functional Block scheme representing the collocation of the proposed predistorter block.

Referring again to the functional scheme of Figure 2, the mathematical framework is now discussed in detail.

3.2.1 Directly Modulated Laser

The Electrical field $E(t)$ produced by a directly modulated Laser Diode (LD) exhibits Intensity Modulation (IM) as a desired result together with an additional undesired Frequency Modulation (FM) known as frequency chirping. Such field is described by the following expression:

$$E(t) = E_0 \sqrt{1 + M_{IM} i_{RF}(t)}. e^{j[\omega_o t + \Delta\theta(t)]} \quad (3.1)$$

In Eq 3.1, E_0 is the field amplitude without RF modulation, M_{IM} is the Optical Modulation Index also often indicated as OMI defined as [3.20]:

$$M_{IM} = \frac{\sqrt{2 \langle (P(t) - P_o)^2 \rangle}}{P_o} \quad (3.2)$$

where $P(t) = P_o [1 + M_{IM} i_{RF}(t)]$ describes the instantaneous optical power and the operator $\langle \langle \cdot \rangle \rangle$ denotes that the time average of (\cdot) is performed.

In turn, the quantity $P_o = \eta(I_{bias} - I_{th})$ is the portion of the optical power due to the only bias current I_{bias} , while I_{th} is the threshold current of the laser and η represents its slope-efficiency. The increase in RF power leads to increase in M_{IM} , while biasing is kept fixed. With $i_{RF}(t)$, it is indicated the current that modulates the laser source, which, as a consequence of the definition given by Eq. 3.2 obeys to the normalization $\langle (i_{RF}(t))^2 \rangle = \frac{1}{2}$. Note that in the particular case when the RF current which modulates the laser is just a sinusoidal tone given by $I_{RF,M} \cos(\omega_{RF} t)$, it is $P(t) = \eta(I_{bias} - I_{th} + I_{RF,M} \cos(\omega_{RF} t))$ where $M_{IM} = \frac{I_{RF,M}}{I_{bias} - I_{th}}$ and $i_{RF}(t) = \cos(\omega_{RF} t)$. Moreover, ω_o is the angular emission frequency of the laser source while $\Delta\theta(t)$ represents the instantaneous phase deviation of the optical carrier due to the mentioned chirp phenomenon.

The concept of instantaneous change in the optical frequency is given in [3.21]. This concept can be employed to determine the instantaneous phase deviation. The instantaneous change in optical frequency is given as

$$\Delta f(t) = \frac{\alpha LW}{4\pi} \left[\frac{1}{P(t)} \frac{dP(t)}{dt} + \kappa P(t) \right] \quad (3.3)$$

In Eq.3.3, αLW is the Henry linewidth enhancement factor. Whereas, κ is the adiabatic chirp scaling factor of the laser source utilized. In Eq. 3.3, $\frac{1}{P(t)} \frac{dP(t)}{dt}$ represents transient chirp while $\kappa P(t)$ represents adiabatic chirp.

Since $\Delta\theta(t) = \int 2\pi\Delta f(t) dt$, the instantaneous phase deviation comes out to be:

$$\Delta\theta(t) = \frac{\alpha LW}{2} \ln(P(t)) + \frac{\alpha LW}{2} \kappa \int P(t) dt \quad (3.4)$$

In Eq. 3.4, by substituting the instantaneous optical power $P(t)$, a more meaningful expression can be obtained in the following way:

$$\Delta\theta(t) = \frac{\alpha LW}{2} [M_{IM} \cdot i_{RF}(t)] \frac{\alpha LW}{2} \kappa M_{IM} P_o \int i_{RF}(t) dt \quad (3.5)$$

The RF modulating current $i_{RF}(t)$ is a pass-band signal and can therefore be written as:

$$i_{RF}(t) = I(t) \cos(\omega_c t) - Q(t) \sin(\omega_c t) \quad (3.6)$$

where $I(t)$ and $Q(t)$ are the In-Phase and Quadrature baseband signals respectively and ω_c is the RF carrier frequency. With the help of this expression for $i_{RF}(t)$, the instantaneous phase deviation becomes as follows:

$$\Delta\theta(t) = \frac{\alpha LW}{2} M_{IM} \cdot [I(t) \cos(\omega_c t) - Q \sin(\omega_c t)] + \frac{\alpha LW}{2\omega_c} \kappa M_{IM} P_o [I(t) \sin(\omega_c t) + Q(t) \cos(\omega_c t)] \quad (3.7)$$

In Eq. 3.6, the term $I(t) \sin(\omega_c t) + Q(t) \cos(\omega_c t)$ can be referred as $i_{RF}(t)$ and $\frac{I_{RF}'(t)}{\omega_c}$ becomes the integral of the signal $i_{RF}(t)$. It is then:

$$\Delta\theta(t) = \frac{\alpha LW}{2} M_{IM} \cdot i_{RF}(t) + \frac{\alpha LW}{2\omega_c} \kappa M_{IM} P_o \frac{I_{RF}'(t)}{\omega_c} \quad (3.8)$$

and, consequently,

$$\begin{aligned} \Delta\theta(t) &= \frac{\alpha LW}{2} M_{IM} \cdot i_{RF}(t) + \frac{\alpha LW}{2\omega_c} \kappa M_{IM} P_o \int i_{RF}(t) \\ &= K_t i_{RF}(t) + K_f \int i_{RF}(t) \end{aligned} \quad (3.9)$$

where K_t and K_f represent the transient and adiabatic chirp coefficients respectively. Therefore, the expression in Eq. 3.1 becomes

$$E(t) = E_0 \sqrt{1 + M_{IM} i_{RF}(t)} \cdot e^{j(\omega_o t + [K_t i_{RF}(t)] + [K_f \int i_{RF}(t) dt])} \quad (3.10)$$

3.2.2 Fiber Compensation

The ‘‘Fiber Compensation’’ block receives $E(t)$ as an input. The corresponding time impulse response is obtained considering the fiber pulse response:

$$h(t, z) = \sqrt{\frac{\pi}{j\gamma}} \cdot e^{\frac{j\pi^2 t^2}{\gamma}} \text{ and } \gamma = \frac{Dz \lambda_o}{2\omega_o} (2\pi)^2 \quad (3.11)$$

In Eq. 3.10, D is the second order dispersion ($\frac{sec}{m^2}$), z is the fiber's length (m), λ_o is the optical wavelength, $\omega_o = 2\pi f_o$ where f_o is the optical frequency. The corrected field $E_{corr}(t)$ is then found by the convolution operation of the input field $E(t)$ with the conjugate of the fiber pulse response. This corrected field $E_{corr}(t)$ would entirely compensate the Fiber dispersion effect. It can therefore be written as:

$$E_{corr}(t) = E(t) \otimes h^*(t) \quad (3.12)$$

3.2.3 Approximations Applied to the Model

As explained above, the aim of the digital predistortion technique is to eliminate the chromatic dispersion effect which operates on the phase of the electric field emitted by the laser. The proposed approach starts from the consideration that an appropriate current $i_{RF,corr}$ given in input to the laser would assure that the optical field “generated” by the laser is $E_{corr}(t)$ given by Eq. 3.11. This means that it is possible to write:

$$E_{corr}(t) = |E_{corr}(t)| e^{j\angle E_{corr}(t)} = g[i_{RF,corr}(t)] \quad (3.13)$$

$$= E_{corr,0} \sqrt{1 + M_{IM} i_{RF,corr}(t)}. e^{j(\omega_0 t + [K_t i_{RF,corr}(t)] + [K_f \int i_{RF,corr}(t) dt])} \quad (3.14)$$

where $g[.]$ is the function describing the relationship between the field emitted by the laser and its input modulating RF current. In order to determine $i_{RF,corr}(t)$ it is then necessary to perform the operation symbolically expressed by:

$$i_{RF,corr}(t) = g^{-1}[E_{corr}(t)] \quad (3.15)$$

An approximation is at this point applied to the resolution of Eq. 3.15, namely it is taken:

$$i_{RF,corr}(t) = g^{-1}[E_{corr}(t)] \sim \frac{1}{K_t} [\angle E_{corr}(t) - \omega_0 t] = \tilde{i}_{corr}(t) \quad (3.16)$$

Aim of this approximation is to simplify the model and allow the application of the correction in a straightforward way. Indeed, as can be seen from Eq. 3.14 the relationship given between Eq. 3.15 is rigorously valid only when $M_{IM} \ll 1$ and $K_f \int i_{RF,corr}(t) dt \ll K_t i_{RF,corr}(t)$, i.e. when the power of the RF modulating signal exhibits low values and when the transient chirp effect prevails over the adiabatic one.

After the $\tilde{i}_{corr}(t)$ is computed, the electric field emitted by laser source and coupled at the fiber input section leads to following expression:

$$E_{TX}(t, z = 0) = E_{corr,0} \sqrt{1 + M_{IM} \tilde{i}_{corr}} \cdot e^{j(\omega_0 t + [K_t \tilde{i}_{corr}(t)] + [K_f \int \tilde{i}_{corr}(t) dt])} \quad (3.17)$$

Eq. 3.17 takes into account that in general, in addition to transient chirp, the real laser will also exhibit the adiabatic chirp [3.22]. The propagation of the field E_{TX} is modeled in the frequency domain, by taking its Fast Fourier Transform $\mathcal{E}_{TX}(\omega, z = 0)$ and multiplying it by a fiber transfer function which is given as follows in the Eq. 3.18:

$$\mathcal{H}(\omega, z) = 10^{-\frac{\alpha_{loss} z}{20}} \times e^{-j\beta|\omega_0 z} \times e^{-j\left.\frac{\partial\beta}{\partial\omega}\right|_{\omega_0}(\omega-\omega_0)z} \times e^{-j\left.\frac{1}{2}\frac{\partial^2\beta}{\partial\omega^2}\right|_{\omega_0}(\omega-\omega_0)^2 z} \quad (3.18)$$

In Eq. 3.18, α_{loss} represents the field attenuation coefficient expressed in $\left[\frac{dB}{km}\right]$, β represents the propagation constant of the fundamental mode propagating in the fiber. $\left.\frac{\partial\beta}{\partial\omega}\right|_{\omega_0}$ is its group delay per unit length, $\frac{\partial^2\beta}{\partial\omega^2} = -\frac{D\lambda_0}{\omega_0}$ is the chromatic dispersion coefficient expressed in $\frac{sec^2}{m}$.

The second and the third factors at the right hand side (RHS) of Eq. 3.18 respectively introduce just a phase delay and a group delay to the $E_{TX}(t, z = 0)$ given by Eq. 3.17, which do not determine nonlinearities in the RF signal received. Moreover, the first factor at the RHS of Eq. 3.18 practically represents an attenuation coefficient, since α_{loss} can be regarded as constant in the bandwidth considered. The square of this coefficient multiplies the powers of both the desired RF signal and the undesired RF disturbances due to the studied nonlinearities. Since all the figures of merit studied in the following depend on the ratio between these two powers, this attenuation coefficient does not practically influence the results obtained in the present simulations.

For the purpose of the present study Eq. 3.19 can then be simplified to the following Fiber transfer function:

$$H(\omega, z) = e^{j\left(Dz\frac{\lambda_0}{2\omega_0}2\pi(\omega-\omega_0)^2\right)} \quad (3.19)$$

whose Inverse Fourier Transform is actually the pulse response of the optical fiber span introduced in Eq. 3.11

Note that the mentioned simplification on the term $10^{-\frac{\alpha_{loss} z}{20}}$ is here possible because, with the aim to study in detail the impairments due to the system nonlinearities, the presence of a noise

floor at the receiver side has not been taken into account in the simulations performed. However, the maximum link distance considered has been chosen as 50 km, in order to focus the study on realistic applicative scenarios.

The output electric field is then estimated through the product between the Inverse Fourier transform of $\mathcal{E}_{TX}(\omega, z = 0)$ and $H(\omega, z)$. The following expression of output field $E_{TX}(t, z = L)$ is achieved:

$$E_{TX}(t, z = L) = \mathcal{F}^{-1}[\mathcal{F}(\mathcal{E}_{TX}(\omega, z = 0)) \cdot H(\omega, z)] \quad (3.20)$$

This output electric field is then finally used to compute the received RF current assuming a square law detection using common photodiode (PD). Hence, the photo-detected current becomes:

$$i_{out}(t) = \mathcal{R}|E_{TX}(t, z = L)|^2 \quad (3.21)$$

where \mathcal{R} represents the responsivity of the Photodiode.

Note also that Eq. 3.1 and Eq. 3.21 imply that the power vs current characteristic of the laser and the current vs power characteristic of the photodiode exhibit linear behaviors. This assumption is due to the fact that aim of the proposed method is to counterbalance the combined effect of laser chirp and chromatic dispersion, which is the prevailing cause of nonlinearity in directly modulated RoF links with lengths of tens of km. For this reason, other possible causes of nonlinearities have not been included in the numerical model.

3.3 Numerical Results and Discussion

In the following sub-sections, the proposed Direct Predistortion Technique (DPDT) has been utilized to carry out numerical simulation for the two sinusoidal RF tone and LTE signal as a test signal. The technique developed has been implemented on MATLAB. The results of evaluated quantities for the said test signals are discussed in detail.

Firstly, the case is considered when only the transient chirp is present in the directly modulated laser, i.e. when the approximation given by Eq. 3.16 can be reasonably accepted.

In addition, with the aim to show that the solution proposed features a general applicability, Sec. 3.3 studies also the case when only the adiabatic chirp is present, allowing to appreciate that also in this case a beneficial effect is present on the global system performance. The analysis of these two extreme situations is motivated by the fact that in the majority of applicative situations one of the two types of chirp prevails over the other, and can be considered to be the only one determining the frequency modulation of the field emitted by the laser [3.23].

3.3.1 Evaluation of Intermodulation Distortion for Dual RF Tone

The predistorter simulation efficacy is evaluated initially with a signal composed by a couple of sinusoidal RF tones having frequencies f_{RF1} and f_{RF2} , namely $i_{RF}(t) = \cos(\omega_{RF1}t) + \cos(\omega_{RF2}t)$ with $\omega_{RF1} = 2\pi f_{RF1}$ and $\omega_{RF2} = 2\pi f_{RF2}$. The nonlinearities considered of the RoF link have been those related to the generation of an undesired component at the frequency $2f_{RF1} - f_{RF2}$ at the receiver side.

To evaluate the model, initially a pure dual tone RF sinusoidal signal is utilized. This allows to test the proposed model and approach without increasing the complexity of the input radio signal. In this case, the frequency of modulating RF tones f_{RF1} and f_{RF2} is considered to be 1 GHz and 1.01 GHz respectively. An optical fiber of G.652 type is utilized which exhibits a chromatic dispersion coefficient $D = \frac{16.10^{-6}\text{sec}}{\text{m}^2}$ for the operating wavelength of $\lambda = 1.55\ \mu\text{m}$. Similarly to what has been assumed for laser and photodiode characteristics, also the possible nonlinearities coming from the optical fiber have assumed to be negligible with respect to the prevailing effect of laser chirp and fiber chromatic dispersion. Note however that the system considered utilizes a single wavelength where a sub-carrier modulation is performed. The only detriment could then come from the Self Phase Modulation phenomenon, which, due to the typical values of the optical powers involved in these systems (few dBm) can be regarded as negligible Table 3.1 lists the main parameters utilized in the simulations.

Optical Link Component	Parameters Values
Laser and PD	$I_{bias} = 70 \text{ mA}$ $I_{th} = 5 \text{ mA}$ $M_{IM} = 10,30 \%$ $K_t = 110 \left(\frac{1}{\text{mA}}\right)$ $\mathcal{R} = 1 \left(\frac{\text{mA}}{\text{mW}}\right)$
Fiber (ITU-T G.652)	Dispersion= $16 \frac{\text{ps}}{\text{nm km}}$ $z = 0\text{-}50 \text{ km}$ Attenuation= $0.2 \frac{\text{dB}}{\text{km}}$
Signal	$f_{RF1} = 1 \text{ GHz}$ $f_{RF2} = 1.01 \text{ GHz}$

Table 3-1: Parameters utilized in the formulation of simulation results

The results for the dual sinusoidal RF tone are presented in Figure 3.3. P_{IMD} indicates the third order intermodulation power received at the frequency $2f_{RF2} - f_{RF1}$ and $P_{C,OUT}$ the power received at one of the two carrier frequencies (e.g. f_{RF1}). The ratio $\frac{P_{IMD}}{P_{C,OUT}}$ is reported as a function of the RoF link length for two possible values of M_{IM} ($M_{IM}=10\%$ and $M_{IM} = 30\%$). The intermodulation distortion is reported in this way and not using the typical third order input or output intercept points, because the ratio $\frac{P_{IMD}}{P_{C,OUT}}$ corresponds to the Adjacent Channel Leakage Ratio i.e. ACLR which will be one of the quantities utilized with reference to realistic LTE signals.

The amount by which each signal modulates the optical transmitter is measured by M_{IM} . Typically, increasing M_{IM} is expected to lead to higher signal distortion due to the corresponding higher value of RF modulating power for a given I_{bias} of the laser.

Indeed, the curves for 10% of M_{IM} exhibit lower values of $\frac{P_{IMD}}{P_{C,OUT}}$ as compared to 30% of M_{IM} . At the same time, in both, a noticeable improvement due to the proposed correction can be noticed. For example, for $M_{IM} = 10\%$, at a distance of 50 km, the predistorted corrected curve exhibits $\frac{P_{IMD}}{P_{C,OUT}} = -97.08 \text{ dBc}$ (as compared to uncompensated value of -82.78 dBc) while for

30% of M_{IM} , at 50 km, the compensated corrected curve has a value of -70.09 dBc (as compared to the uncompensated value of -59.80 dBc).

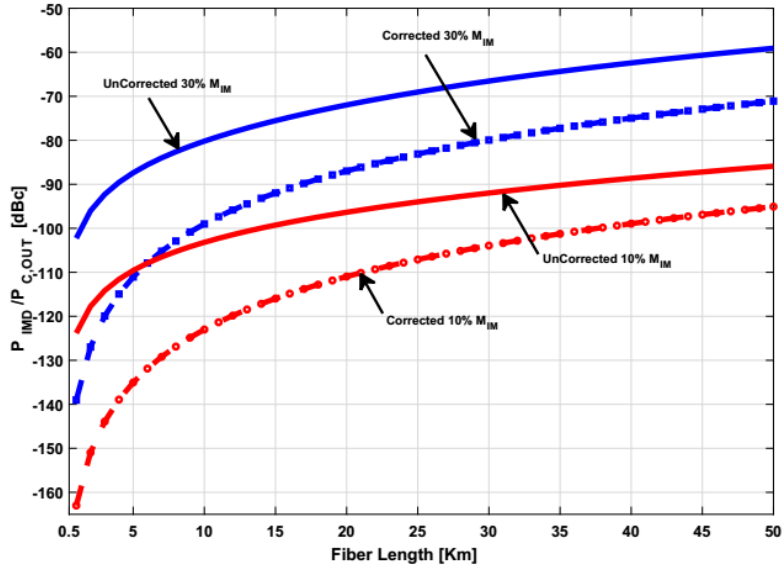


Figure 3.3: Comparison between values of ACLR (for Dual Sinusoidal RF Tone), for varying length z for $M_{IM} = 10\%$ and $M_{IM} = 30\%$, with and without the application of the proposed predistortion technique.

In order to summarize the results for the sinusoidal tone, Figure 3.4 presents a comparison between absolute improvement in ACLR, varying length and input power P_{IN} . It can be seen that improvement due to proposed Direct predistortion technique is also significant at higher lengths.

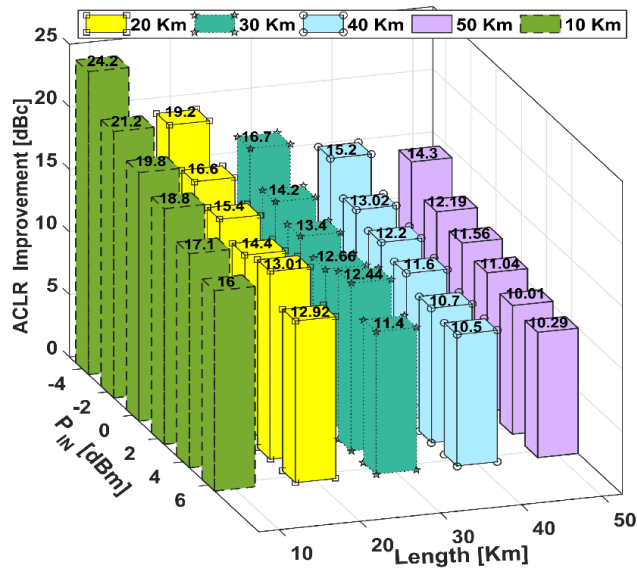


Figure 3.4: Comparison between Absolute Improvement in ACLR (for Dual Sinusoidal Tone), for varying length z and for varying input power P_{IN} .

3.3.2 Evaluation of LTE Signal as an Input Test Signal

As mentioned above, the model is now evaluated with reference to a realistic LTE standard signal. Tests are performed by generating a LTE signal of 3.84 MHz bandwidth having 64 QAM modulation format. The signal is modeled through a locally developed software which complies with the release 13.4 of the LTE standard (3GPP Release 13). The parameters of the LTE signal in base band are summarized in Table 3-2.

Parameter	Values
Nominal Channel Bandwidth (B_{ch})	3 MHz
Useful Channel Bandwidth (B_{chu})	2.7 MHz
Sampling Frequency (F_s)	3.84 MHz
Frame Duration (T_{frame})	10 ms
Subframe duration ($\Delta T_{subframe}$)	1 ms
FFT size	256

Table 3-2: Parameters of the LTE Signal Utilized

3.3.2.1 ACLR Results for LTE Signal

In the following subsection, the results of the simulations are discussed. The first quantity to be evaluated is the Adjacent Channel Leakage Ratio (ACLR). In Figure 3.5, the behavior of ACLR is reported as a function of fiber link length for $f_c = 2.14 \text{ GHz}$ for two possible values of the optical modulation index M_{IM} . The parameters used in this case for RoF components are the same of Table 3-1.

As expected, also in this case higher the M_{IM} , higher is the distortion generated (see the uncorrected curve in Figure 3.5). The interesting fact is that the improvement in ACLR is still significant taking into account high distances. For example, at $z=50 \text{ km}$ for $M_{IM} = 10\%$. ACLR is lowered by 25.2 dBc for the corrected curve as compared to the uncompensated ACLR value. Similarly, $M_{IM} = 30\%$, the uncompensated value of ACLR is -53.15 dBc while this value is lowered to -70.9 dBc for the compensated case.

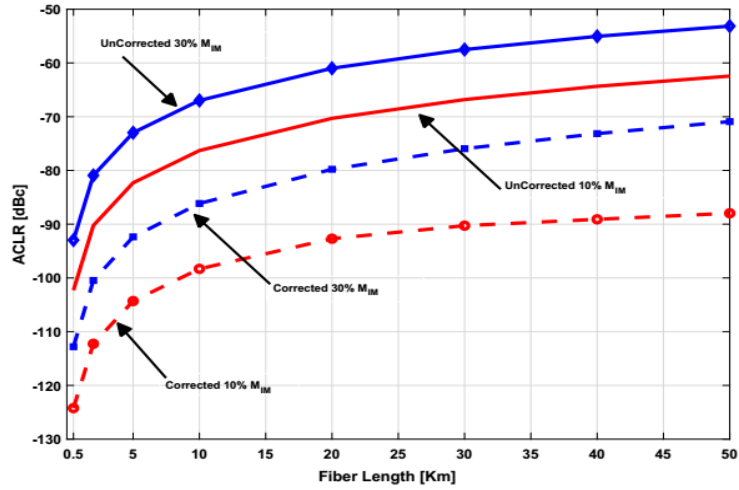


Figure 3.5: Comparison between values of ACLR (for LTE Signal), for varying length z for $M_{IM} = 10\%$ and $M_{IM} = 30\%$, with and without the application of the proposed predistortion technique.

Moreover, ACLR improvement has been evaluated for all proposed conditions and the numerical results have been summarized in Figure 3.6

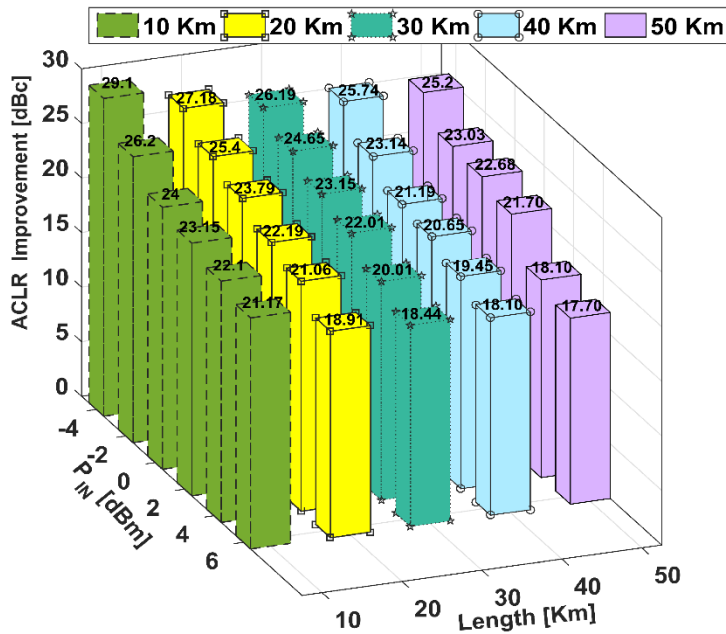


Figure 3.6: Comparison between Absolute Improvement in ACLR (for LTE Signal), for varying length z and for varying input power P_{IN} .

3.3.2.2 EVM Results for LTE Signal

The effect of the proposed correction is now evaluated with respect to the EVM. EVM is evaluated through a locally developed software. The software is based on an EVM characterization bench for Frequency Division Duplexing (FDD) downlink LTE frame transmission based on the release 13.4 of the standard. The entire frame of 10 ms is generated using a software developed in MATLAB. The program also creates the samples followed by the creation of the modulating signals and up-converts them to a RF carrier frequency. It is then launched into the Radio-over-Fiber link model whose characterization has already been explained in the Section 3.1. After the signal propagates through the A-RoF link, the signal undergoes post processing that comprises of down conversion and down sampling respectively. The software is realized ad-hoc for LTE frame, and is able to synchronize the frame, equalize the channel and extract the EVM for each physical and logical channel. Tests were performed generating an LTE signal of 3.84 MHz. To see the effect of transient chirp for LTE signals on EVM, a test is done where EVM is reported for respective lengths up to 50 Km. The trend in Figure 3.7 formalizes that EVM improvement can be seen for 10 and 30 % of M_{IM} values. This endorses that the proposed predistorter improves the EVM by further lowering it from the uncorrected value.

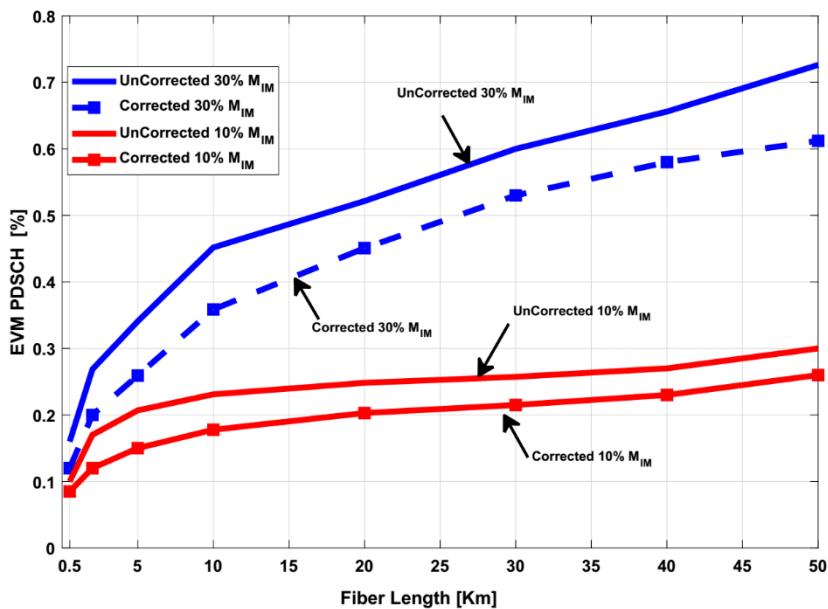


Figure 3.7: Comparison between the EVM values (for LTE Signals), for varying length $z = 0 - 50$ Km for $M_{IM} = 10\%$ and 30% , with and without the application of the proposed predistortion technique.

3.4 Behavior of Predistorter in Presence of Adiabatic Chirp

As shown in Section 3.1.3, the proposed predistortion technique aims on the compensation of the transient chirp. However, in many practical cases, especially using Distributed Feedback (DFB) lasers, the adiabatic chirp component generally prevails [3.24]. In order to evaluate this situation, the electric field $E_{TX}(t)$ from Eq. 3.17 can be expressed as follows:

$$E_{TX}(t, z = 0) = E_{corr,0} \sqrt{1 + M_{IM} \tilde{i}_{corr}} \cdot e^{j(\omega_0 t + [K_f \int \tilde{i}_{corr}(t) dt])}$$

In order to evaluate the effect of adiabatic chirp on the trend of ACLR and on its correction, K_f is varied from 30 to 440 $\frac{MHz}{mA}$, length is fixed to 50 km and $M_{IM} = 30\%$.

The results reported in Figure 3.7 affirms that increase in adiabatic chirp produces the distortion that worsens the ACLR to a point where the need of predistortion becomes critical. For instance, for the adiabatic chirp of 300 $\frac{MHz}{mA}$, the uncorrected ACLR value of -21 dBc is compensated to a relative lower value of -35 dBc. This means that proposed predistorter is able to correct the adiabatic chirp as well.

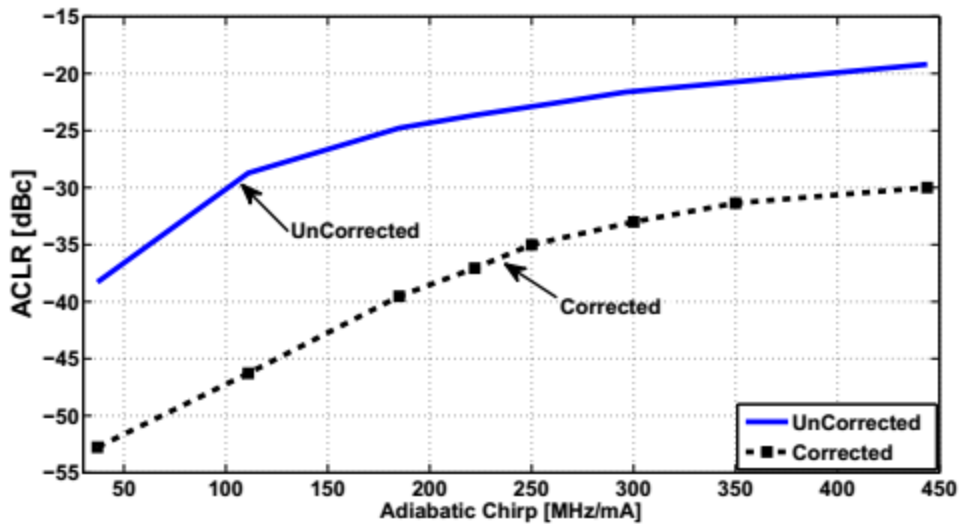


Figure 3.8: Comparison between the values of ACLR (for LTE Signal), for varying % of Adiabatic Chirp for fixed length $z = 50$ km for $M_{IM} = 30\%$, $f_c = 2.14$ GHz, with and without the application of the proposed predistortion technique

Lengths up to 50 km are introduced to show the behavior of the improvement due to the proposed procedure from the point of view of the numerical simulation. The inclusion of optical amplifier

is not envisaged in the model of RoF since the amplification will amplify the transmission and the adjacent channel in the same proportion and the ratio of the channels will have no effect. The effectiveness of proposed predistorter is further confirmed by analyzing the power spectral densities (PSD) of the output signal with and without linearization process. It can be observed that Proposed predistortion technique results in spectral regrowth reduction (see Figure 3.9).

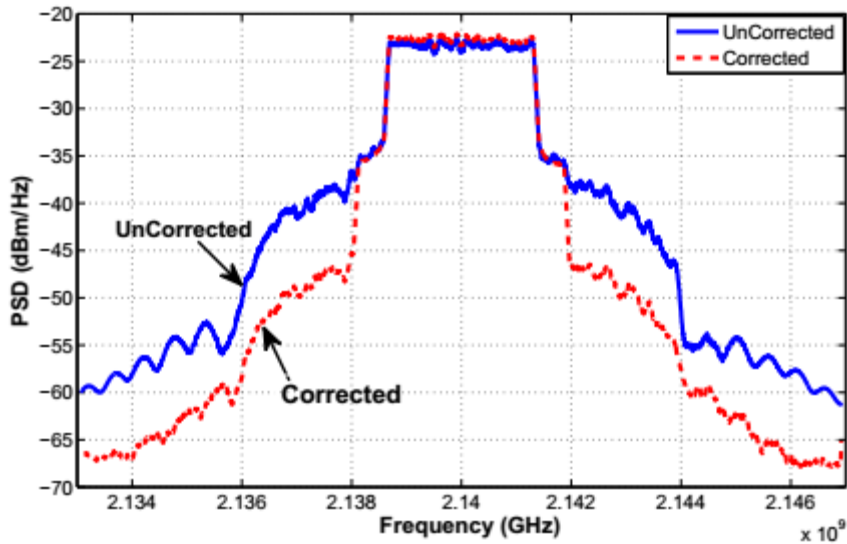


Figure 3.9: The Effectiveness of predistortion in suppressing spectral regrowth, with and without correction. $K_f = 220 \frac{MHz}{mA}$, $z = 50$ km for $M_{IM} = 30\%$.

To see the effect of adiabatic chirp for LTE signals on EVM, a test is done where length is fixed to be 50 Km and adiabatic chirp is varied from 30 to $440 \frac{MHz}{mA}$. The trend in Figure 3.10 substantiates that higher the % of the adiabatic chirp, higher is the EVM value, e.g. at $330 \frac{MHz}{mA}$, contribution of the adiabatic chirp, the corrected EVM is 2.010 % as compared to 3.64 % for uncorrected EVM. In order to highlight the EVM improvement by the proposed predistorter, the comparison between the constellation of received Physical Downlink Shared Channel (PDSCH) with and without correction. There is an appreciable improvement in the received constellation

of PDSCH for the corrected case as compared to the uncorrected case. This validates that the proposed predistorter improves the EVM.

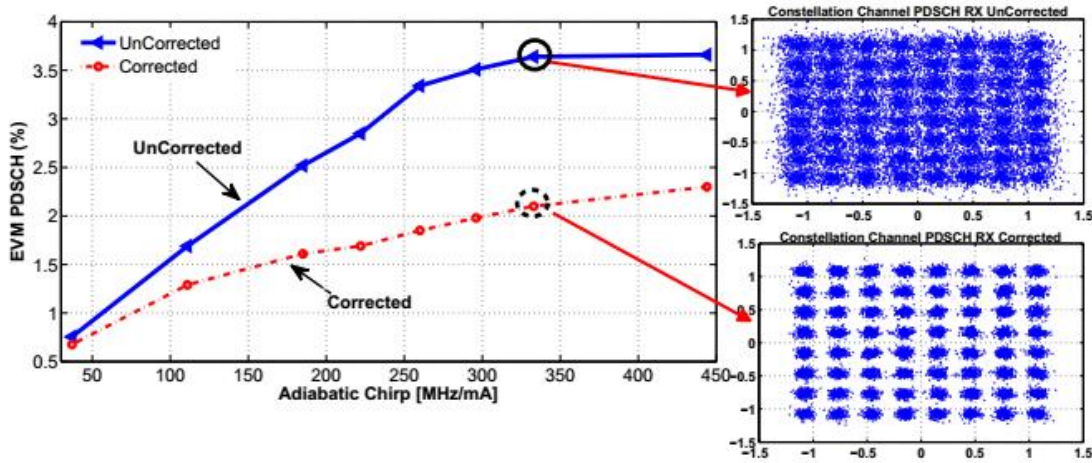


Figure 3.10: Comparison between the EVM values (for LTE Signals), for varying % of Adiabatic Chirp for fixed length $z=50$ km for $M_{IM} = 30\%$, with and without the application of the proposed predistortion technique

A comparative overview of LTE signals for minimum and maximum adiabatic chirps at 50 km is gathered in Table 3-3. For $33 \frac{\text{MHz}}{\text{mA}}$ of K_f , with the proposed DPDT, ACLR is -52.77 dBc and without the DPDT, the value is -38.29 dBc, with an improvement of 14.48 dB. However, EVM results reveal that with the DPDT, its value is 0.60 %, whereas without the DPDT, it is 0.81 %. Similarly, for $450 \frac{\text{MHz}}{\text{mA}}$ of K_f , the improvement with DPDT is 10.1 dB in terms of ACLR and EVM is reduced from 3.7 % to 2.2 % i.e. reduction in EVM is 40 % of its uncorrected value.

Setup	ACLR (dBc)	EVM (%)
$K_f = 33 \frac{\text{MHz}}{\text{mA}}$		
w/o DPDT	-38.29	0.81
with DPDT	-52.77	0.60
$K_f = 450 \frac{\text{MHz}}{\text{mA}}$		
w/o DPDT	-19.9	3.7
with DPDT	-30	2.2

Table 3-3: Linearization Performance for adiabatic Chirp (Minimum and Maximum Values)

3.5 Feasibility of the Proposed Predistorter

As far as realization is concerned, a primary role is played by the ADC, which constitutes the first block of the predistorter (see again Figure 3.2) and converts the analog input signal to a digital signal that can be processed either in a DSP or in a FPGA. As it is established that cost of an ADC is closely related with performance capabilities, higher is the sampling rate of an ADC, higher is its cost. Note however, that the sampling rate is related to the bandwidth of the modulating signal. Increasing the order of the modulation scheme (e.g. 256 QAM instead of 64 QAM) would not require an ADC with higher sampling rate. In any case, bandpass sampling theory could be employed to appreciably reduce the sampling rate, without any replica overlapping, as proposed by various authors in different fashions [3.25-3.27]. In this view, for the presented application, use of ADC08DJ3200 6.4-GSPS Single-Channel from Texas Instruments is envisaged.

3.6 Conclusion

A numerical predistortion technique, based on a rigorous mathematical simulation model, is proposed which aims to improve the performance of the RoF link. The nonlinearity compensation technique evaluates the inter-modulation related quantities like ACLR and EVM of signals under test. The performed simulations gives a quantitative idea of its beneficial effects. When adiabatic chirp is considered, the simulated results guarantee “at present” a significant reduction of ACLR by 14 dBc for K_f of 220 MHz/mA when length is 50 km and MIM is 30%. Similarly, EVM is reduced from 2.95 to 1.6% with the proposed technique. The simulation program can be a helpful tool for the design of cost-effective RoF link. The proposed approach is advantageous as it compensates the disturbance caused by the phase of the field and it is adaptable to other laser models. Higher levels of practical realizability are featured by the proposed technique with respect to other Digital Predistortion solutions, while maintaining good degrees of nonlinearities compensation. The realization of the predistortion system is anticipated, since it can be realized using Field Programmable Gate Arrays of typical characteristics.

References

- 3.1 Wake, D., Nkansah, A., Gomes, N.J.: Radio over fiber link design for next generation wireless systems. *IEEE/OSA J. Lightwave Technol.* 28(16), 2456–2464 (2010)
- 3.2 Alcaro, G., Visani, D., Tarlazzi, L., Faccin, P., Tartarini, G.: Distortion mechanisms originating from modal noise in radio over multimode fiber links. *IEEE Trans. Microw. Theory Tech.* 60(1), 185–194 (2012)
- 3.3 Morant, M., Llorente, P.: Performance analysis of multiple radio-access provision in a multicore-fibre optical fronthaul. *Opt. Commun.* 436, 161–167 (2019)
- 3.4 Visani, D., Okonkwo, C.M., Shi, Y., Yang, H., van den Boom, H.P.A., Tartarini, G., Tangdiongga, E., Koonen, A.M.J.: 3x2N-QAM constellation formats for DMT over 1-mm core diameter plastic optical fiber. *IEEE Photonics Technol. Lett.* 23, 768–770 (2011)
- 3.5 Kabonzo, F.M., Dilshad, M.U.: Impact of radio over fiber technology for integrated 5G front and backhaul applications. In: 2017 IEEE 2nd advanced information technology, electronic and automation control conference (IAEAC), Chongqing, pp. 1077–1081 (2017)
- 3.6 Thomas, V.A., El-Hajjar, M., Hanzo, L.: Performance improvement and cost reduction techniques for radio over fiber communications. *IEEE Commun. Surv. Tutor.* 17(2), 627–670 (2015)
- 3.7 Nanni, J., Polleux, J., Algani, C., Rusticelli, S., Perini, F., Tartarini, G.: VCSEL-based radio-over-G652 fiber system for short-/medium-range MFH solutions. *J. Lightwave Technol.* 36(19), 4430–4437 (2018)
- 3.8 Meslener, G.J.: Chromatic dispersion induced distortion of modulated monochromatic light employing direct detection. *IEEE J. Quantum Electron.* QE 20, 1208–1216 (1984)
- 3.9 Vieira, L.C., Gomes, N.J., Nkansah, A., Van Dijk, F.: Behavioral modeling of radio-over-fiber links using memory polynomials. In: 2010 IEEE international topical meeting on microwave photonics, Montreal, QC, pp. 85–88 (2010)

- 3.10 Roselli, L., Borgioni, V., Zepparelli, F., Ambrosi, F., Comez, M., Faccin, P., Casini, A.: Analog laser predistortion for multiservice radio-over-fiber systems. *IEEE J. Lightwave Technol.* 37(5), 1211–1223 (2003)
- 3.11 Zhu, R., Zhang, X.: Broadband predistortion circuit design for electro-absorption modulator in radio over fiber system. In: Proceedings of the optical fiber communications conference and exhibition (OFC), San Francisco, CA, USA (2014)
- 3.12 Huang, H.T., Lin, C.T., Chiang, S.C., Lin, B.J., Shih, P.T.B., Ng'oma, A.: Volterra nonlinearity compensator for I/Q imbalanced mm-wave OFDM RoF systems. In: 2015 International topical meeting on microwave photonics (MWP). pp. 1–4 (2015)
- 3.13 Fuochi, F., Hadi, M.U., Nanni, J., Traverso, P.A., Tartarini, G.: Digital predistortion technique for the compensation of nonlinear effects in radio over fiber links. In: 2016 IEEE 2nd international forum on research and technologies for society and industry leveraging a better tomorrow (RTSI), pp. 1–6 (2016)
- 3.14 Hadi, M.U., Nanni, J., Traverso, P.A., Tartarini, G., Venard, O., Baudoin, G., Polleux, J.L.: Experimental evaluation of digital predistortion for VCSEL-SSMF-based Radio-over-Fiber link, In: 2018 International topical meeting on microwave photonics (MWP), Toulouse, France, pp. 1–4 (2018)
- 3.15 Mateo, C., Carro, P.L., García-Dúcar, P., De Mingo, J., Salinas, I.: Radio-over-fiber linearization with optimized genetic algorithm CPWL model. *Opt. Express* 25(4), 3694–3708 (2017)
- 3.16 Hadi, M.U., Traverso, P.A., Tartarini, G., Venard, O., Baudoin, G., Polleux, J.L.: Digital predistortion for linearity improvement of VCSEL-SSMF-based radio-over-fiber links. *IEEE Microw. Wirel. Compon. Lett.* 29(2), 155–157 (2019a)
- 3.17 Hadi, M.U., Nanni, J., Traverso, P.A., Tartarini, G., Venard, O., Baudoin, G., Polleux, J.L.: Linearity improvement of VCSELs based radio over fiber systems utilizing digital predistortion. *Adv. Sci. Technol. Eng. Syst. J.* 4(4), 156–163 (2019f)

- 3.18 Shafik, R.A., Rahman, M.S., Islam, A.R.: On the extended relationships among EVM, BER and SNR as performance metrics. In: 2006 International conference on electrical and computer engineering, Dhaka, pp. 408–411 (2006)
- 3.19 Tartarini, G., Faccin, P.: Efficient characterization of harmonic and intermodulation distortion effects in dispersive radio over fiber systems with direct laser modulation. *Microw. Opt. Technol. Lett.* 46(2), 114–117 (2005)
- 3.20 Visani, D., Tartarini, G., Tarlazzi, L., Faccin, P.: Transmission of UMTS and WIMAX signals over cost-effective radio over fiber systems. *IEEE Microw. Wirel. Compon. Lett.* 19(12), 831–833 (2009)
- 3.21 Koch, T.L., Linke, R.A., Hanzo, L.: Effect of nonlinear gain reduction on semiconductor laser wavelength chirping. *Am. Inst. Phys. Appl. Phys. Lett.* 48, 613–615 (1986)
- 3.22 Wei, C.C.: Small-signal analysis of OOFDM signal transmission with directly modulated laser and direct detection. *Opt. Lett.* 36, 151–153 (2011)
- 3.23 Nanni, J., Barbiroli, M., Fuschini, F., Masotti, D., Polleux, J.-L., Algani, C., Tartarini, G.: Chirp evaluation of semiconductor DFB lasers through a simple Interferometry-based (IB) technique. *Appl. Opt. (OSA)* 55(28), 7788–7795 (2016)
- 3.24 Villafranca, A., Lasobras, J., Garces, I.: Precise characterization of the frequency chirp in directly modulated DFB lasers. In: Spanish conference on electron devices, pp. 173–176 (2007)
- 3.25 Betta, G., Capriglione, D., Ferrigno, L., Miele, G.: Innovative methods for the selection of bandpass sampling rate in cost-effective RF measurement instruments. *Meas. J. Int. Meas. Confed.* 43(8), 985–993 (2010)
- 3.26 Braithwaite, R.N.: Wide bandwidth adaptive digital predistortion of power amplifiers using reduced order memory correction. In: Microwave symposium digest, IEEE MTT-S international, pp. 1517–1520 (2008)
- 3.27 Liu, Y., Yan, J.J., Dabag, H.T., Asbeck, P.M.: Novel technique for wideband digital predistortion of power amplifiers with an under-sampling ADC. *IEEE Trans. Microw.*

Theory Tech. 62(11), 2604– 2617 (2014)

Chapter 4

Experimental demonstration of Digital Predistortion for Radio over Fiber (RoF) Systems

The contents of this chapter are taken from [J3],[J8]-[J9], [C1]- [C3] and [A1] where we presented the characterization of digital predistortion method for Analog Radio over Fiber Systems.

The utilization of Analog Radio over Fiber System is prone to nonlinearities. In previous chapter, we discussed a digital predistortion method based on behavioral model of radio over fiber system that compensates the nonlinearities due to combined effect of laser chirp and fiber dispersion. In this chapter, DPD based methods are discussed for the short range RoF links where laser nonlinearities are the primary source of nonlinearity.

The chapter is organized as follows.

1. The first part discusses the experimental demonstration of DPD technique to VCSELs based RoF links. Here, the DPD application is discussed separately for Single mode VCSELs and Multi-Mode VCSELs respectively for varying link lengths.
2. The second part discusses DPD technique implied to DFB based RoF links. DPD efficacy is discussed by comparing MP, GMP and DVR models.
3. The third part discusses a Multi-channel DPD methodology implied to both, VCSELs and DFB based RoF links.

The chapter is organized as follows:

Sec 4.1 discusses DPD methodology implied to VCSELs while Sec. 4.2 explains DPD methodology for DFB based RoF links. Sec. 4.3 includes the demonstration of DPD for multichannel carriers applied to both, VCSELs and DFB based RoF links. Sec. 4.4 introduces the

concept of real time implementation of the proposed DPD method and Sec. 4.5 concludes the chapter.

4.1 Experimental Demonstration of Digital Predistortion for VCSELs based RoF links

In this section, we will discuss the developed methodology that has been applied to class of links which utilizes VCSELs for fronthaul applications. The section will first introduce the significance of VCSELs for short link applications followed by the need of DPD in such scenario. Then, we discuss the developed method and its demonstration for single mode and multi-mode VCSELs. Finally, conclusions are drawn for this section.

While considering the short-medium reach networks, OFHs based on the RoF technology can be realized utilizing Standard Single mode Fiber (SSMF) or also Multimode Fiber (MMF) [4.1]. In both cases, a possible solution which keeps low levels cost and power consumption can be obtained utilizing Vertical Cavity Surface Emitting Lasers also known as VCSELs which emit in the first optical window (wavelength $\lambda=850$ nm) as the optical source.

While the use of VCSELs operating at short wavelengths is a relatively consolidated choice finding application e.g. in combinations with Plastic Optical Fibers within in-building networks [4.2-4.3] or in combination with MMFs within data centers [4.4], care must be taken in front of the possible impairments due to the multimodal behavior of SSMFs that operate at the 850 nm [4.5]. The presence of multimodal behavior would indeed be absent if expensive VCSELs operating at $1.3 \mu\text{m}$ and $1.55 \mu\text{m}$ were utilized, in which the major SSMF-related impairments could just be ascribed to optical nonlinear effects and/or to chromatic dispersion [4.4-4.6]. However, appropriate countermeasures have been proposed, which can prevent this last impairment cause to be critical [4.7-4.8].

Besides the cited OFH, VCSEL-based RoF systems can be found in multivariate scenarios, being utilized for radio astronomic signal transmission [4.9], multi service indoor wireless signal distribution [4.10], or machine learning detection [4.11].

In all these cases, a cardinal issue is represented by the impairments of the opto-electronic devices and particularly the whole VCSEL based Radio over Fiber system. Such nonlinearities, that arise due to relatively stable causes like nonlinear attributes coming from laser diode and perhaps from photodiode [4.12]. These nonlinearities can also arise due to little dynamics of

VCSELs [4.13], e.g., when high Peak-to-Average Power Ratio (PAPR) signals are transmitted and can have an important role especially for multi-channel transmission. They indeed can cause high in and out of band distortion, which leads to higher interference among near channels.

In this section, we apply DPD based linearization to VCSELs based RoF links, particularly, the linearization is applied to Single Mode (SM)-VCSELs and Multi-Mode (MM) VCSELs. The novelty of the work presented is summarized as follows:

1. A novel evaluation is performed by considering the SM VCSEL-based RoF system, not only in B2B configuration, but equipped with SSMF spans of different lengths;
2. Moreover, also Multimode (MM) VCSEL-based RoF systems are analyzed, utilizing different lengths of MMFs;
3. In addition, the DPD technique is evaluated based on Memory Polynomials (MP) and Generalized Memory Polynomial (GMP), where GMP in general shows an improved effectiveness with respect to MP;
4. The DPD is trained and tested near to threshold to check the efficacy of the proposed technique.

As a performance index evaluation, the link linearity improvements are observed by calculating the Adjacent Channel Power Ratio (ACPR), Normalized Mean Square Error (NMSE), spectral regrowth, Normalized Magnitude (AM/AM) and Normalized phase (AM/PM). The characterization has been done for two different VCSELs to show linearization. Firstly, In Section 4.1.1, the DPD methodology is discussed for SM-VCSEL. 4.1.2, modeling methodology is highlighted for MM-VCSELs based RoF links while in Section 4.1.3, conclusions are drawn.

4.1.1 DPD Methodology Implied to SM-VCSEL

In this section, DPD for SM-VCSELs will be considered only. The detailed modeling methodology is discussed followed by experimental setup and results and discussion.

4.1.1.1 Modeling Methodology for SM-VCSELs based RoF links

The architecture of the predistortion technique is shown in Figure 4.1 which utilizes Indirect Learning Architecture for the estimation of PD training coefficients [4.14-4.17]. Since the

statistic of the waveform will remain the same over time, therefore, it can be assumed that system nonlinearity is not time varying and the training of the predistortion can be applied in an off-line practice. This will not only reduce the expenditures and over heads of the predistorter but also avoids the need of an identification algorithm. The identification of DPD is performed in one step. Hence, a linear estimation of PD coefficients results in straightforward identification.

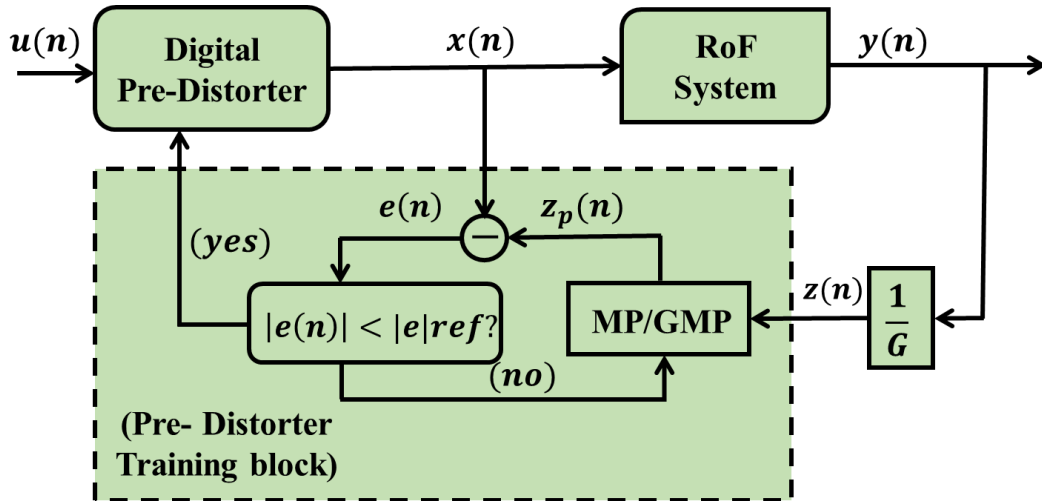


Figure 4.1: DPD identification for RoF utilizing ILA

At first, the training phase calculates the predistorter coefficients. At this point, the RoF system output $y(n)$, becomes input $z(n)$ to the Pre-Distorter Training block which is defined as $z(n) = \frac{y(n)}{G}$ where G denotes the gain of the system. The coefficients appraisal can be made using least-squares-based algorithm and is described in Sec. 2.5.1. The convergence point of the training is achieved by minimizing the error function. Eventually, the computed training coefficients are employed to the predistorter referred as Digital Pre-Distorter in Figure 4.2. The predistorter models utilized are derived from the classical Volterra series.

4.1.1.2 Digital Predistortion Model

A. Memory Polynomial (MP) Model

Memory Polynomial (MP) model is referred as an inverse non-linear model that has been exploited previously as a powerful model for both, inverse and direct modeling of power amplifier (PA) nonlinearities. Applying this model for RoF has an additional advantage since memory less model might have problems to characterize the electro-optical (EO) conversion phenomena

accurately. The MP model is generally referred as a compromise between memoryless nonlinearity and full Volterra series due to presence of diagonal memory. The output in this case is referred as:

$$z_p(n) = \sum_{k=0}^{K-1} \sum_{q=0}^{Q-1} c_{kq} z(n-q) |z(n-q)|^k \quad (4.1)$$

Here K represents order of non-linearity, Q is referred as the memory depth, z represents the predistorter input sequence and c_{kq} denotes the model coefficients.

B. Generalized Memory Polynomial (GMP) Model

The use of Generalized Memory Polynomial (GMP) model has been widely utilized for the linearization of PAs [4.18]. However, GMP has not been yet evaluated for RoF with varying lengths. The GMP model basis functions possess memory for both, for the diagonal terms as well as for the crossing terms i.e., $x(n-q)|x(n-r)|^{k-1}$, where $q \neq r$. The output of the post inverse block $z_p(n)$ modeled with GMP can be expressed as:

$$\begin{aligned} z_p(n) = & \sum_{k=0}^{K_a-1} \sum_{q=0}^{Q_a-1} c_{kq} z(n-q) |z(n-q)|^k \\ & + \sum_{k=1}^{K_b} \sum_{q=0}^{Q_b-1} \sum_{r=1}^{R_b} d_{kqr} z(n-q) |z(n-q-r)|^k \\ & + \sum_{k=1}^{K_c} \sum_{q=0}^{Q_c-1} \sum_{r=1}^{R_c} e_{kqr} z(n-q) |z(n-q+r)|^k \end{aligned} \quad (4.2)$$

where $z_p(n)$ and $z(n)$ represents the DPD output and input respectively. Similarly, c_{kq} ; d_{kqr} and e_{kqr} denotes the complex coefficients for the signal and the envelope; signal and lagging envelope and signal and leading envelope respectively. k represents the index of nonlinearity, and q, r represents the indices of the memory. While K_a, K_b, K_c are the maximum orders of nonlinearity, Q_a, Q_b, Q_c are the memory depths, while R_b and R_c exhibits the lagging and leading delay tap lengths, respectively. GMP has been applied choosing $K_a=K_b=K_c=K$, $Q_a=Q_b=Q_c=Q$ and $R_b = R_c = R$.

The main objective of the predistorter is to minimize the error ($e(n) = z_p(n) - x(n)$) between the $z_p(n)$ and the input x of the RoF system.

4.1.1.3 Estimation Algorithm

There are number of least squares (LS) algorithm for estimation of model coefficients that take the linear weighting of nonlinear signals [4.18-4.21]. The formulation of the estimation initiates with collecting the coefficients e.g., c_{kq} , d_{kqr} and e_{kqr} in to a $R \times 1$ vector \mathbf{v} . R represents the total number of coefficients. \mathbf{v} means a signal whose time will sample over the same period. Considering (2), coefficients c_{21} denotes the signal $x(n-1)|x(n-1)|^2$. \mathbf{Z} characterizes the collection of all such vectors into a $N \times R$ matrix. Once the convergence condition is obtained, the output of the predistorter training block becomes: $z_p(n) = x(n)$ and hence $z(n) = u(n)$. For total samples N , the output can be written in the following way:

$$\mathbf{z}_p = \mathbf{Z}\mathbf{v} \quad (4.3)$$

Where $\mathbf{z} = [z(1), \dots, z(N)]^T$, $\mathbf{z}_p = [z_p(1), \dots, z_p(N)]^T$, while \mathbf{v} displays a $R \times 1$ vector that contains the coefficients c_{kq} , d_{kqr} and e_{kqr} . The LS solution will then become a solution for the equation expressed as:

$$[\mathbf{Z}^H \mathbf{Z}] \hat{\mathbf{v}} = \mathbf{Z}^H \mathbf{x} \quad (4.4)$$

The LS solution in (4) should minimize the cost function

$$C = \sum_{n=1}^N |z_p(n) - x(n)|^2 \quad (4.5)$$

The advanced variations to Volterra series in form of MP, GMP and others increases the effectiveness of predistortion. However, this advanced variation can come into existence by increasing the memory depth and nonlinearity order. However, this will extortionate the computational complexity and this has to be weighed against other simpler expediencies. Moreover, the performance would generally be more efficient if the predistortion model has higher number of coefficients. This means that while selecting the model and its complexity, a smart tradeoff between complexity and performance can be made accordingly.

4.1.1.4 Experimental Setup

The experimental test bed utilized for demonstrating and validating the proposed DPD technique is shown in Figure 4.2. The baseband LTE signal of 5-MHz with 64 QAM modulation format is

emulated through a domestic software on MATLAB compliant with 3GPP release TS 36.104 V15.2.0 [4.22]. The signal is oversampled at 38.4 MSa/s. After this, the sampled sequence of signals passes through the DPD block, which is then RF-transformed at 800 MHz by a Vector Signal Generator (VSG) (see Figure 4.2) and is then sent to the optical link. The signal at the output of the RoF is then down-converted to baseband by a Rohde and Schwarz Vector Spectrum Analyzer (VSA) which provides this down converted baseband received signal for post processing to PC workbench. VSA has frequency range between 2 Hz and 8 GHz.

A Single Mode VCSEL (Optowell), that operate at 850-nm, which is followed by a fiber span (SSMF) and a PIN photodiode, having 2.5 GHz bandwidth and responsivity factor of 0.6 A/W constitutes the RoF link. The SSMF for varying lengths has been utilized so that the effect of length on the DPD technique can be observed.

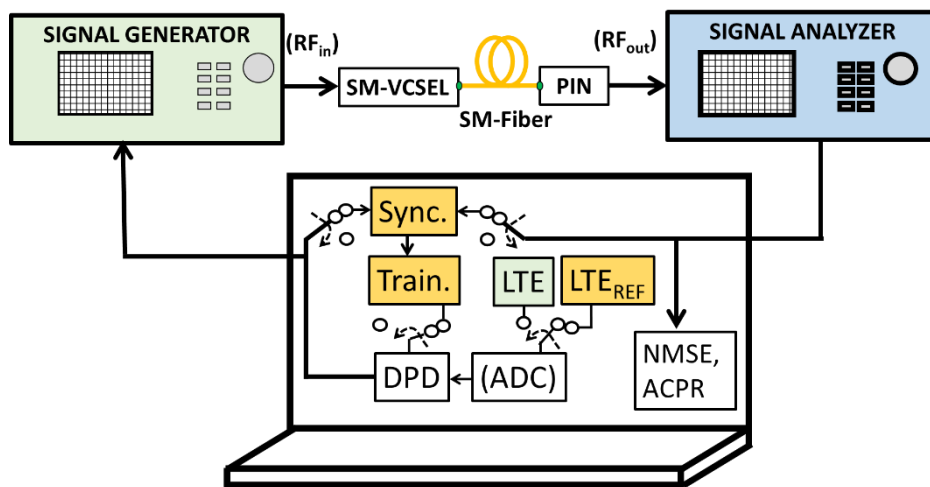


Figure 4.2: Experimental evaluation comprising of DPD training and application phase.

The process of predistortion is carried out in two steps. The first step is referred as a training phase. In training phase, the parameter identification for predistorter is carried out as referred in Figure 4.2. During the training phase, reference LTE frames are utilized (see LTE_{REF} block in Figure 4.2). Primarily, input and output signals are synchronized i.e. time aligned (see Sync. in Figure 4.2). This block finds the time delay estimation by utilizing the Synchronization Signals (Primary and Secondary) accessible in the LTE framework.

Then, the predistorter coefficients are procured through the PD models utilized (see Train. in Figure 4.2). In the second step i.e. the testing phase, the training coefficients obtained in previous step are utilized to apply DPD in MATLAB. This means that all switches are turned to opposite position in Figure 4.2 and the testing is done for LTE frames followed by sampling, pre-distortion, and then uploaded to the Vector Signal Generator (VSG). Finally, they are channelized through the optical link and performance metrics are compared with the one without predistortion. It must be noted that the DPD testing and validation is not only evaluated for the reference LTE signals that were used not only for training, but also for generalized LTE frames. Details of parameters utilized is given in Table 4-1.

Optical Link Component	Parameters Values
Laser	SM-VCSEL Wavelength= 850 nm $I_{Bias} = 4 \text{ mA}$ $I_{Threshold} = 2 \text{ mA}$ RIN = -130 dB/Hz
SSMF Fiber	Maximum Length = 1.5 Km Attenuation = $2.5 \frac{\text{dB}}{\text{km}}$
Photo- detector	Responsivity = 0.6 A/W Bandwidth = 2.5 GHz

Table 4-1: System Parameters

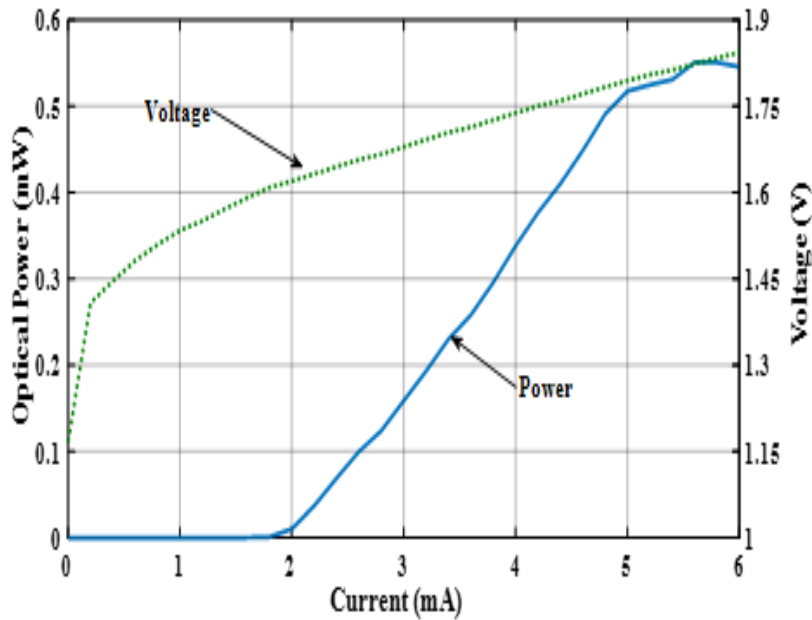


Figure 4.3: L-I-V characterization utilized in the evaluation of DPD experiments for SM-VCSEL.

4.1.1.5 Results and Discussion

The efficacy of the linearization method is appraised and brought into discussion in this section. A primary attention should be given while selecting the parameters of the predistorter such as memory depth (Q) and nonlinearity order (K).

The L-I-V characteristic curve of SM-VCSEL utilized is illustrated in Figure 4.3. In SM-VCSEL, the maximum saturation current (I_s) is 5 mA while threshold current (I_{th}) is 2 mA. The bias point (I_{bias}) is chosen at 4 mA.

The predistorter complexity is dependent upon the model and order of Q and K chosen. In order to show the trend of this fact, Figure 4.4 elaborates the experimental NMSE results for different choices of Q and K using both models.

The evaluation in Figure 4.4 has been done for varying orders of Q (0, 1, 2 & 3) and non-linearity K (3, 4, 5 & 6) by applying a higher RF input power (0 dBm). It can be perceived that GMP results in higher reduction of NMSE in comparison to MP at lower orders of K . From this initial finding, the optimal values $Q = 1,2$ and $K = 3$ are chosen, resulting from a tradeoff between performance achieved and complexity required to the system.

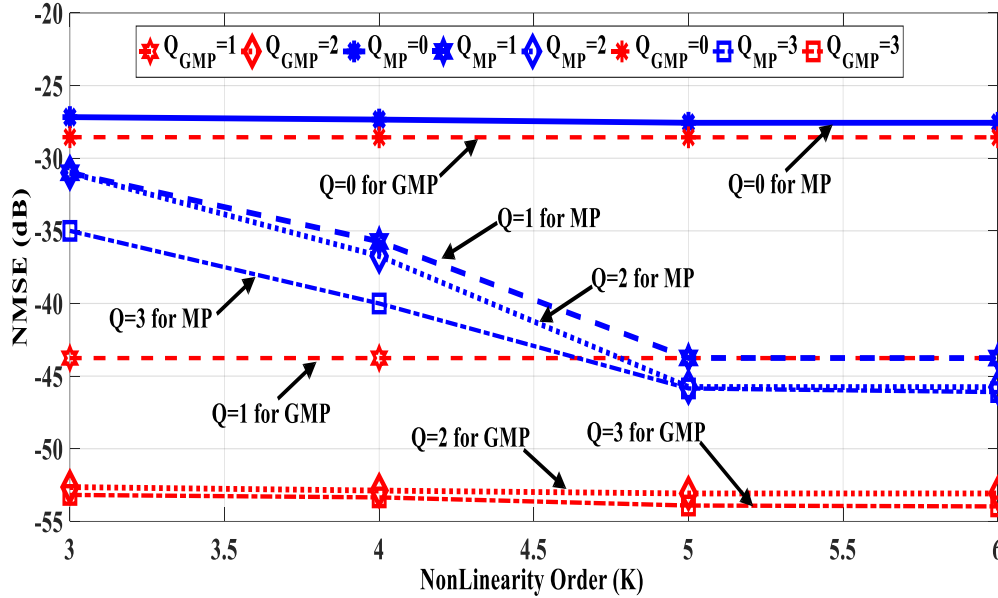


Figure 4.4: Normalized Mean Square Error results with varying values of memory depth Q and Nonlinearity Order K .

In addition to NMSE, to show the effect of increasing complexity of the proposed distorter, keeping the value of $R = 1$ fixed, Figure 4.5 represents the ACPR for MP ($Q = 1, 2$ and $K = 3$) and GMP ($Q = 1, 2$ and $K = 3$) for 1 Km of SSMF. It is perceived that ACPR for MP model doesn't satisfies 3GPP ACPR requirement for MP (both $Q = 1, 2$ and $K = 3$) after -5 dBm of input power. While, GMP with $Q = 1$ and $K = 3$ satisfies the requirement, however, it is exactly on the borderline at 0 dBm of RF input power.

Considering GMP with $Q = 2$ and $K = 3$, the ACPR is well below the requirement set by 3GPP, hence the higher complexity enhances the performance. This demonstration shows that the performance can be enhanced at the cost of higher complexity of the PD model.

Similarly, the Power Spectral Density (PSD) of the received sequence is analyzed when both models are implemented. The length is fixed to 1 km and RF input power is 0 dBm. The results have been arranged for comparison of MP and GMP with same order of K and Q .

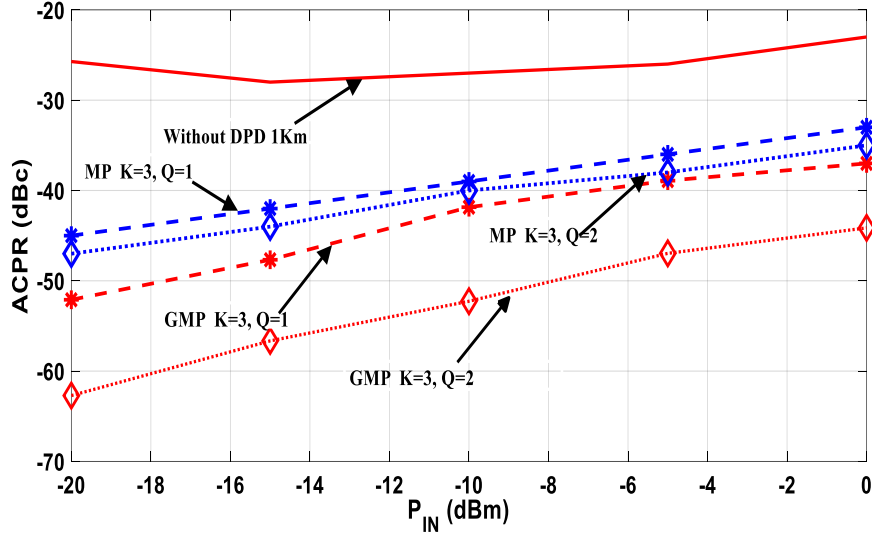


Figure 4.5: ACPR outcomes vs. input RF power. ($Q=1,2, R=1$ and $K=3$ for MP & GMP).

Consider Figure 4.6(a), the DPD for received output signal is demonstrated for both models by fixing $K=3$ and $Q=1$. It is noticeable that GMP has higher reduction in spectral regrowth reduction as compared to MP. Then, in order to highlight the effect of increasing the complexity order, the PSD of GMP and MP are compared for $K=3$ and $Q=2$ in Figure 4.6 (b). This shows that DPD for $K=3$ and $Q=2$ is stronger as compared to $K=3$ and $Q=1$ due to which spectral regrowth reduction in latter case is higher. Similarly, GMP for $K=3$ and $Q=2$ results in ACPR of -44 dBc as compared to -37 dBc when GMP is utilized for ($K=3$ and $Q=1$). This substantiates that GMP has better ACPR reduction than MP. This conclusion seems justified due to the fact that GMP carries memory not only in the diagonal but also in the crossing terms. In light of this discussion and results in the Figure 4.4, 4.5 and 4.6, GMP with optimal values $Q = 2$ and $K = 3$ keeping $R = 1$ fixed have been selected from a tradeoff between performance achieved and complexity required to the system.

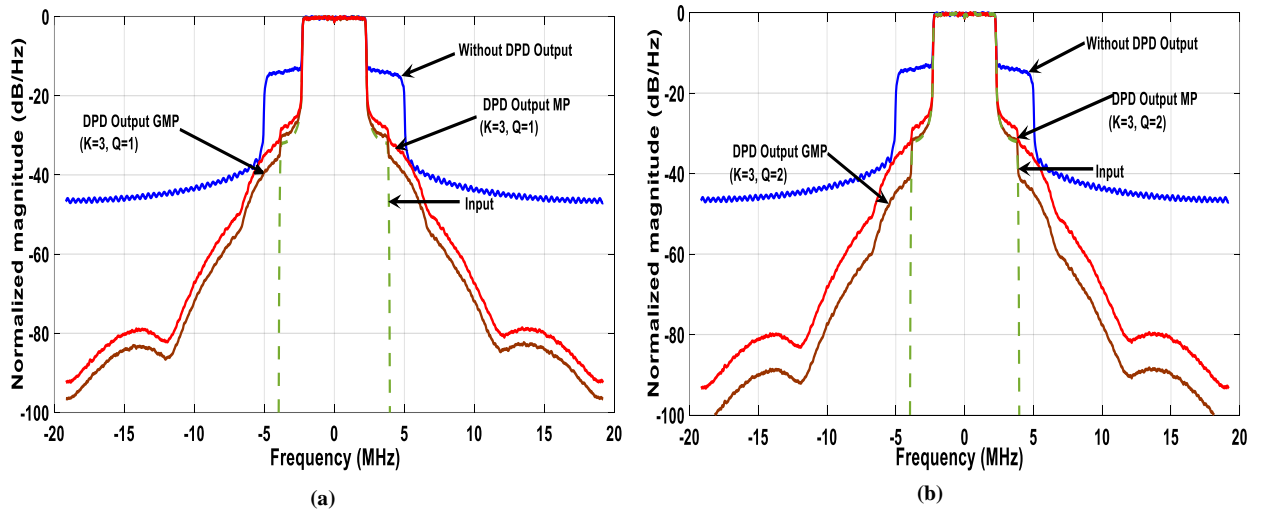


Figure 4.6: PSD evaluation of output signal without and with DPD (MP/GMP) 0 dBm for 1 Km SSMF with SM-VCSEL having: (a) $Q=1$, $R=1$, $K=3$ and (b) $Q=2$, $R=1$, $K=3$.

In Figure 4.7, the ACPR experimental outcomes for several RF input powers (P_{in}) are reported for SM-VCSEL with SSMF. There are three different cases discussed: Patch cord (back to back), 1 km fiber length and 1.5 km fiber length case. By increasing the length of the fiber, the leakages in adjacent channels rise and therefore the worsening occurs with higher lengths. By employing linearization, it can be seen that fiber length with different lengths have different linearization profiles. For instance, let's consider 1.5 km length case, the ACPR without linearization at 0 dBm is -18 dBc, and with linearization employed, it is reduced by 22 dBc to -40 dBc.

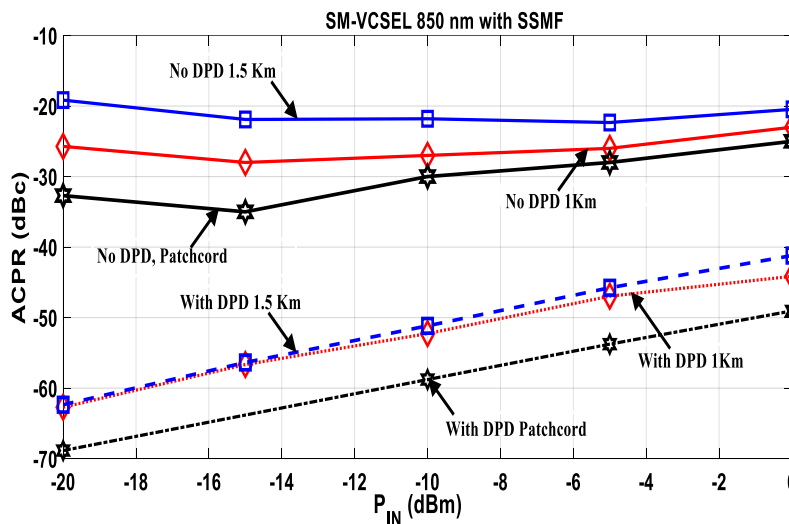


Figure 4.7: ACPR results vs. varying input signal power using ($Q=2$ and $K=3$ for GMP) for SM-VCSEL with SSMF.

It can be deduced from the trend in Figure 4.8 that the proposed DPD technique linearizes the length cases as well. Indeed, linearizing the laser nonlinearity is primary aim of the short link lengths, however, in addition to an optical channel consisting in a fiber patch cord (few meters of length), the proposed technique works efficiently for longer fiber lengths.

It must be put into evidence that linearization method has been evaluated for conditions which are very critical such as high PAPR and I_{bias} close to the threshold with optimal values of K and Q . If these critical conditions are relaxed, this will lead to better linearization performance of the predistorter.

Figure 4.8 represents the AM-AM and AM-PM statistics with and without the linearization employed for the RoF link consisting of 1 Km SSMF and SM-VCSEL. In Figure 4.8 (a), The normalized magnitude with respect to output is shown for the case with and without DPD. With DPD, the curve is a straight line. Similarly, It can be seen in Figure 4.8 (b) that after DPD, the AM/PM is now a straight line and the phase difference is reduced to within 2 degrees.

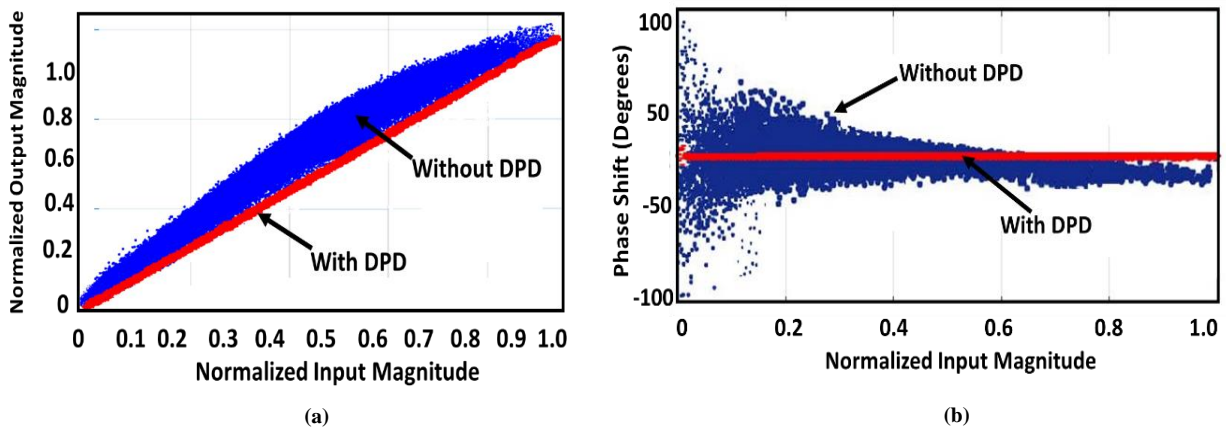


Figure 4.8: (a) AM-AM and (b) AM-PM plots for SM-VCSEL at 1 km of SSMF for 0 dBm of input RF power with and without DPD.

Figure 4.9 shows the EVM computation of SM-VCSEL for 1 km length utilizing MP and GMP for $K = 3, Q = 2$. It is understandable that EVM reduction with GMP is higher than MP.

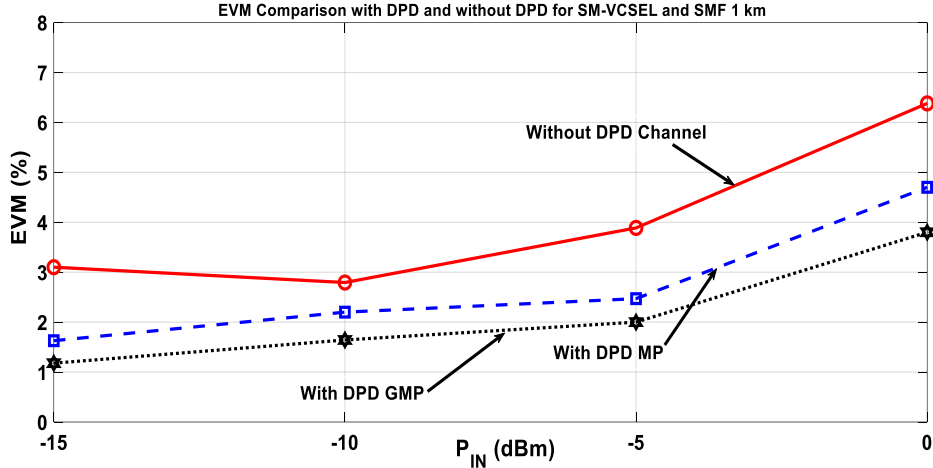


Figure 4.9: EVM results vs. varying input signal power using ($Q=2$ and $K=3$ for GMP) for SM-VCSEL with SSMF.

Table 4.2 reports the results of the proposed technique, referred to 1 km of link length with 0 dBm. The results are summarized for MP and GMP with $K=3$ and $Q=2$ in terms of ACPR and NMSE. The suggested technique linearizes the SM-VCSEL link and MM-VCSEL. Indeed, Table 4.2 suggests that linearization with GMP is better than MP for link length of 1 km (SM for SM-VCSEL). The reduction in ACPR and NMSE for SM-VCSEL is 22 and 20 dB respectively.

Table 4-2: Linearization performance for proposed DPD ($P_{IN}=0$ dBm, Link length= 1 km)

<i>Model</i>	<i>SM-VCSEL</i>		
	<i>NMSE (dB)</i>	<i>ACPR (dBc)</i>	<i>EVM (%)</i>
<i>Without DPD</i>	-19.86	-20	6.8
<i>With GMP (K=3, Q=2)</i>	-41.548	-44	4.7
<i>With MP (K=3, Q=2)</i>	-31.25	-35	3.4

4.1.2 Linearization of MM-VCSEL-MMF based RoF systems

It was explained in the introduction of Sec. 4.1 that the use of VCSELs operating at short wavelengths is a relatively consolidated choice finding applications in multi variate scenarios. Not only SM-VCSELs but also MM-VCSELs have applications in realistic scenarios e.g. in combination with MMFs within data centers [4.4].

However, all these systems are prone to impairments of the opto-electronic devices. These nonlinearities can also arise due to little dynamics of VCSELs, e.g., when high Peak-to-Average Power Ratio (PAPR) signals are transmitted and can have an important role especially for multi-channel transmission. They indeed can cause high in and out of band distortion, which leads to higher interference among near channels. Therefore, it is necessary to linearize these links and diminish the non-linearities.

In this section, we will discuss in detail the linearization method implied for MM-VCSEL-MMF based RoF systems.

4.1.2.1 Experimental Setup

Figure 4.10 shows a block diagram of the experimental testbed used for the validation of the proposed DPD technique for MM-VCSEL. A MM-VCSEL, operating at 850-nm wavelength, is followed by a MMF and a PIN photodiode, with responsivity of 0.6 A/W and 2.5-GHz bandwidth. The baseband LTE 5-MHz signals, emulated according to 3GPP Release 13 through a local MATLAB software with 64 QAM format, are oversampled (ADC in Figure 4.10) at a rate of 38.4 MSa/s. The sampled signals pass through the DPD block, are RF-converted (800 MHz) by an Agilent N5182B MXG X-Series Signal Generator (see Figure 4.10) and sent to the optical link.

In the DPD training phase, reference LTE frames are utilized (LTE_{REF} block in Figure 4.10), the input and output sequences are first synchronized in time (Sync. block in Figure 4.10). This is accomplished through an in-house developed algorithm, which finds the cross-correlation for time delay estimation, by capitalizing the Primary Synchronization Signals and Secondary Synchronization Signals present in the LTE frame. The DPD coefficients are then obtained (Train. block in Figure 4.10) through an in-house developed MATLAB program.

In the DPD testing phase (Figure 4.10 with all switches turned to opposite position), different LTE frames are sampled, predistorted, uploaded to the Signal Generator and transmitted through the optical link. ACPR and NMSE are then evaluated and compared to the corresponding case when no DPD is applied. It is worth noticing that the DPD is tested not only for the ref signals that were used for training, but also for general LTE frames.

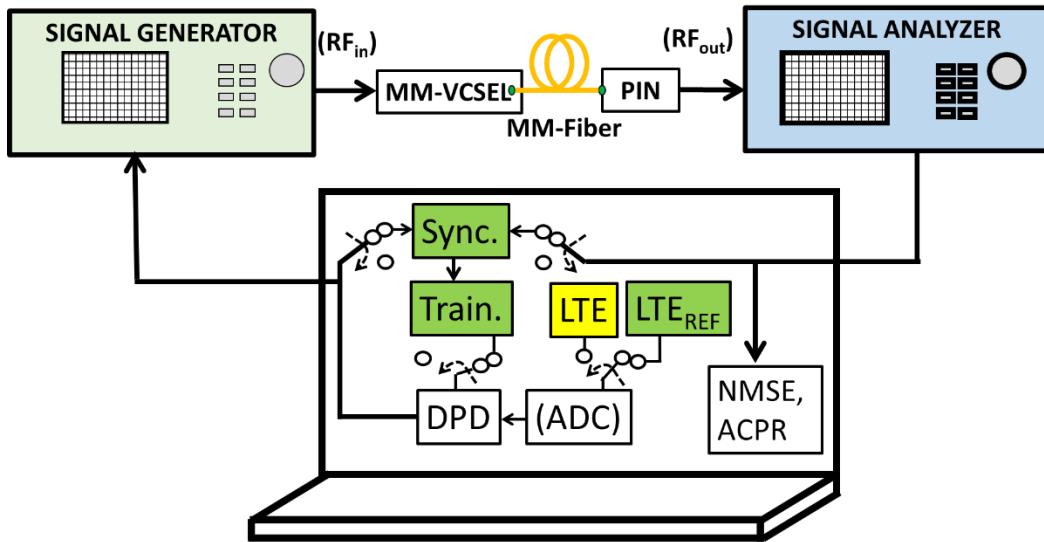


Figure 4.10: Experimental evaluation comprising of DPD training and application phase.

The reason performing the test with reference to the MM-VCSEL-MMF based RoF configurations is related to the fact that, according to the particular applicative context, may make it preferable with respect to the SM-VCSEL-SMF based RoF systems. Indeed, the SM-VCSEL-SSMF based link can indeed feature convenience in terms of cost and flexibility, because of the lower cost per meter of SSMF with respect to MMF, and because of the huge transmission bandwidth of the SSMF. The MM-VCSEL-MMF based link can take advantage of a typically higher dynamic range and emitted/coupled power of the MM-VCSEL over MMF with respect to the SM-VCSEL over SSMF case.

Table 4.3 contains the parameters utilized in the experimental bench in Sec. 4.1.2.1.

Table 4-3: System Parameters utilized in MM-VCSEL-MMF based RoF system

Optical Link Component	Parameters Values
Laser	MM-VCSEL Wavelength= 850 nm $I_{Bias} = 4 \text{ mA}$ $I_{Threshold} = 0.8 \text{ mA}$ RIN = -125 dB/Hz
Fiber	MMF Maximum Length = 1 km Attenuation = $2.5 \frac{\text{dB}}{\text{km}}$
Photo- detector	Responsivity = 0.6 A/W Bandwidth = 2.5 GHz

4.1.2.2 Results and Discussion

The efficacy of the linearization method is discussed and brought into discussion in this section. As discussed previously, primary attention should be given while selecting the parameters of the predistorter such as memory depth (Q) and nonlinearity order (K). The L-I-V characteristic curve of MM-VCSEL utilized are illustrated in Figure 4.11. In MM-VCSEL, the maximum saturation current (I_s) is 8 mA and threshold current (I_{th}) is 0.8 mA. The bias point (I_{bias}) is chosen to be 4 mA. The signals having higher PAPR will give rise to higher distortions owing to small dynamics.

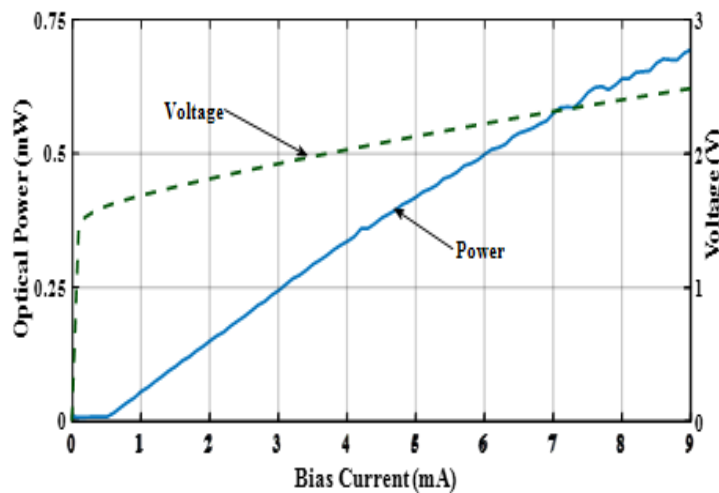


Figure 4.11: L-I-V characterization utilized in the evaluation of DPD experiments for MM-VCSEL.

The PAPR of signal utilized is 9.1 dB. In Figure 4.12, the PSD of MM-VCSEL for 1 km utilizing $K = 3, Q = 2$ is shown. Since GMP results in better reduction than MP, we have shown results with GMP only for simplicity.

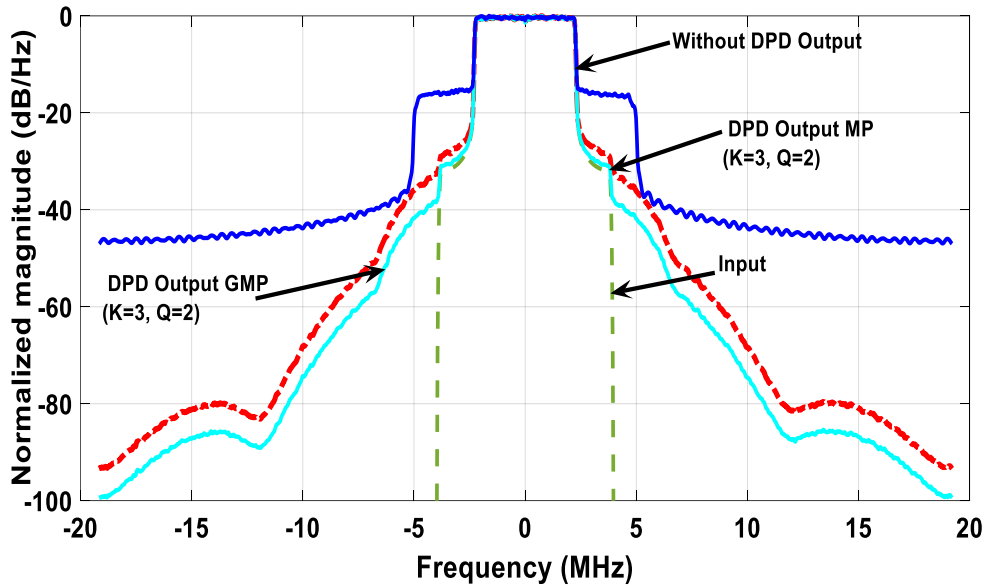


Figure 4.12: PSD comparison between MP and GMP using DPD experiments for MM-VCSEL.

In Figure 4.13, the ACPR of MM-VCSEL with four different lengths is shown up to 1 km. For instance, 1 km length, the uncorrected ACPR at 0 dBm is around -22 dBc while the linearization results in a significant reduction to -36 dBc. It can be seen from the trend in Figure 4.13 that the proposed DPD technique linearizes the length cases as well. Indeed, linearizing the laser nonlinearity is primary aim of the short link lengths, however, in addition to an optical channel consisting in a fiber patch cord (few meters of length), the proposed technique works efficiently for longer fiber lengths.

It must be put into evidence that linearization method has been evaluated for conditions which are very critical such as high PAPR and I_{bias} close to the threshold with optimal values of K and Q . We have chosen the biasing point of VCSEL by intention so that it can be shown that DPD is operational even for critical conditions. Indeed, if these critical conditions are relaxed, this will lead to better linearization performance of the predistorter.

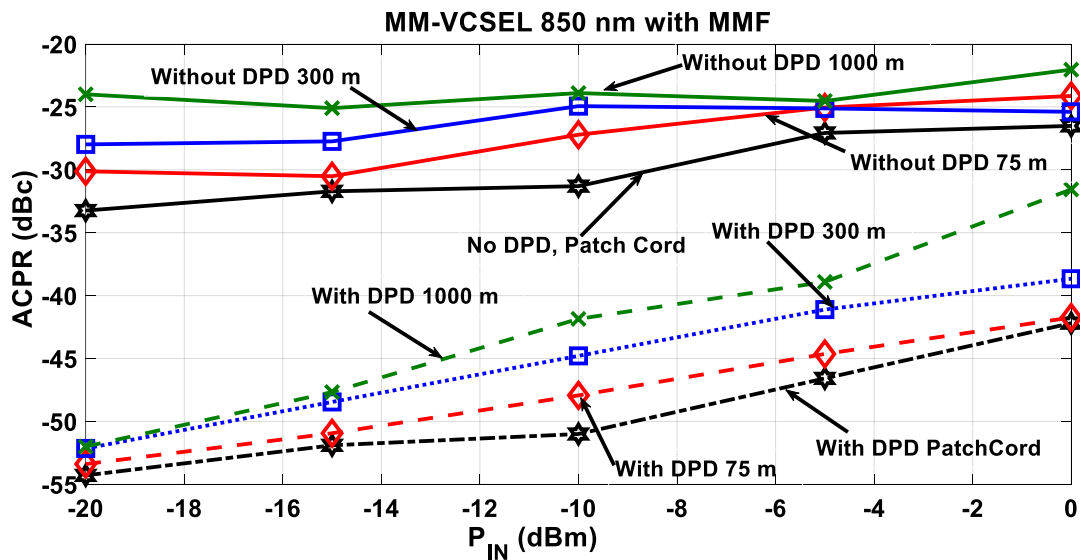


Figure 4.13: ACPR results vs. varying input signal power using ($Q=2$ and $K=3$ for GMP) for MM-VCSEL with MMF.

Similarly order of linearization in terms of EVM is expressed in Figure 4.14. It is visible that MM-VCSEL-MMF at 1 km can be linearized well in the limits by utilizing MP/GMP architecture, though, GMP surpasses the linearization from MP.

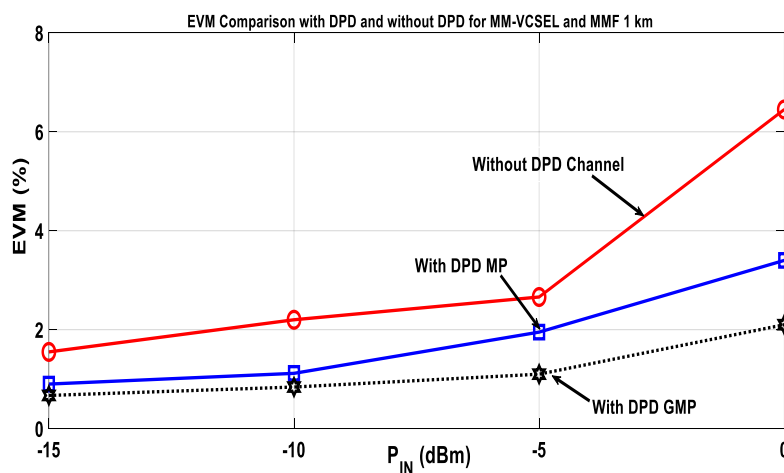


Figure 4.14: EVM results vs. varying input signal power using ($Q=2$ and $K=3$ for GMP) for MM-VCSEL with MMF.

Table 4.4 reports the results of the proposed technique, referred to 1 km of link length with 0 dBm. The results are summarized for MP and GMP with $K=3$ and $Q=2$ in terms of ACPR and NMSE.

<i>Model</i>	<i>MM-VCSEL</i>		
	<i>NMSE (dB)</i>	<i>ACPR (dBc)</i>	<i>EVM (%)</i>
<i>Without DPD</i>	-17.63	-22.04	6.45
<i>With GMP (K=3, Q=2)</i>	-33.18	-36	2.1
<i>With MP (K=3, Q=2)</i>	-30.14	-29	3.4

Table 4-4: Linearization performance for proposed DPD for MM-VCSEL-MMF

$$(P_{IN}= 0 \text{ dBm, Link length}= 1 \text{ km})$$

The reduction in ACPR and NMSE for MM-VCSEL 14 and 16 dB respectively. The improvement for MM-VCSEL is different from SM-VCSEL (see sec. 4.1.1.5) because the nonlinearities of two lasers are different. It should be noted that MM-VCSEL can achieve higher linearization by selecting appropriate sets of coefficients.

4.1.3 Discussion and Conclusions

The time devoted to the periodical re-training of the Digital Predistortion system would in any case remain negligible with respect to the time of normal operation of the RoF system, still allowing its adoption in real applicative scenarios. Similarly, it is possible to utilize an additional photodiode in a base station and feedback the laser nonlinearities and approximating that laser is the main cause of nonlinearity in the RoF link.

Note also that the proposed predistortion method can be applied also to LTE signals of larger bandwidth. The polynomial models nonetheless would require higher values of K & Q with respect to the case presented.

Considering the LTE signal bandwidth and higher modulation format, they would result in a higher PAPR of the transmitted RF signal [4.23]. At the same time, the increase in bandwidth also

determines a correspondent increase in the overall base-band memory of the system to be taken into account by the model.

The polynomial models proposed can still be applied in these operating conditions. They nonetheless would require higher values of the K & Q with respect to the case presented in the submitted work. These requirements would impact the cost of the DPD implementation, which would be higher due to the higher sampling rate of ADCs, and higher computing capabilities of FPGAs.

This section proposed a Digital Pre-Distortion mechanism for linearizing VCSEL based RoF links with different characteristics specifically link lengths. The proposed technique demonstrates a digital predistorter based on MP and GMP. The experiments have been prosecuted for systems based on SM-VCSEL followed by SSMF and on MM-VCSEL followed by MMF. The signal transmitted was a 5-MHz Bandwidth 64 QAM LTE signals and different link lengths have been considered. The performance has been explored in terms of ACPR and NMSE showing that for a link length up to 1 *km*, both SM-VCSEL and MM-VCSEL can be linearized in good proportion. Particularly, utilizing SM-VCSEL, GMP results in 22 *dBs* of reduction in ACPR while MM-VCSEL results in 14 *dBs* of reduction in spectral regrowth. The results testify an encouraging link performance with low complexity of the predistorter model. It has been demonstrated for the first time that GMPs achieves superior linearization as compared to MP for link lengths up to 1.5 *km*.

4.2 Linearization of DFB-SSMF based RoF links

As discussed earlier, RoF systems offer efficient and worthwhile solutions on enhancing the coverage and capacity of wireless links both in long and short-reach networks [4.24-4.26]. Besides their attractive features, such as low-loss, broad bandwidth and impunity to electromagnetic interventions, RoF systems are prone to nonlinearities. In short range networks, the nonlinearities due to the combination of fiber chromatic dispersion and laser frequency chirp are usually negligible [4.27]. However, the non-idealities owing to laser and possibly to photodiode are of paramount importance. Consequently, the quality of transmission is degraded and interference with near channels is aggravated. Orthogonal Frequency Division Modulated (OFDM) signals, like e.g. Long-Term Evolution (LTE) and fifth generation (5G) ones, are prone to such distortions ascribed to a high peak-to average power ratio (PAPR) in their signal envelope.

In order to improve the linearity of intensity modulated/direct detection (IM/DD) RoF systems, we present in this section Indirect Learning Architecture (ILA) based predistortion identification for increasing the linearization of such links. In this section, referring to Distributed Feedback (DFB) laser based RoF links, the advantages of the Decomposed Vector Rotation (DVR) technique will be shown, compared to Memory Polynomial (MP) and Generalized Memory Polynomial (GMP) methods that have been consolidated in details in Section 4.1. Section 4.1.1 discusses modeling methodology for ILA. Section 4.2.2 discusses experimental setup for the DFB based DPD method. In Section 4.2.3, the results are analyzed by means of reduction in Normalized Mean Square Error (NMSE), Adjacent Channel Power Ratio (ACPR) and Error Vector Magnitude (EVM). Section 4.2.4 concludes this section.

4.2.1 Modeling Methodology

The ILA used for the evaluation of DPD is depicted in Figure 4.15. The predistorter coefficients are computed during the training phase. The digitized baseband output of the RoF system $y(n)$ feeds the Pre-Distorter Training block through $z(n) = \frac{y(n)}{G}$. Here G represents the link gain. The coefficients estimation takes place using any least-squares-based algorithm. Once the error function $e(n)$ converges, the coefficients are passed to the Digital Pre-Distorter block.

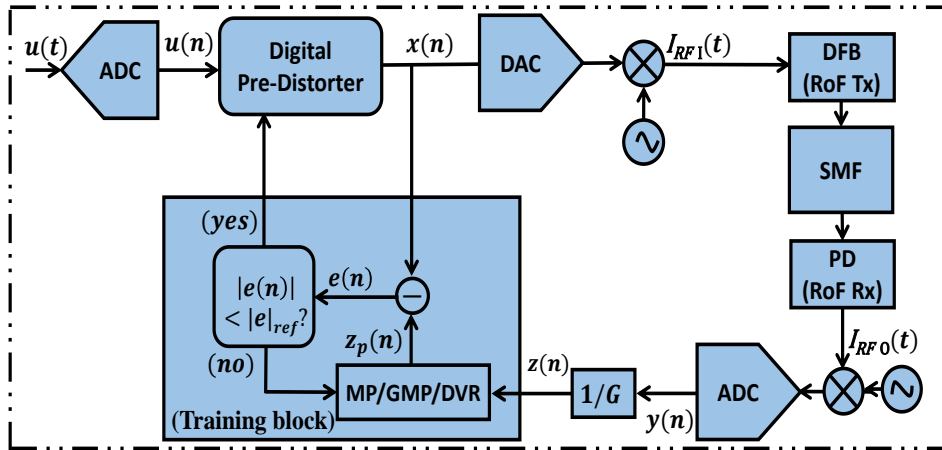


Figure 4.15: DPD schematic showing RoF system utilizing Indirect Learning Architecture

A. Decomposed Vector Rotation Model

The Decomposed Vector Rotation model (DVR) architecture was suggested for the linearization of Power Amplifiers (PAs) [4.28] and a comparative study for PAs was implied

recently in [4.29]. DVR is an adapted version of the canonical piecewise linear (CPWL) functions to handle complex valued signal. Although, generally for RoF, and DFBs in particular, the comparison between DVR and MP/GMP hasn't been so far evaluated. To find a balance between implementation complexity and performance efficiency in the RoF links, the use of a modified DVR model is here proposed, which is syncopated version of the model proposed. The truncated version considers only the linear and first order basis function. The idea is to show that the modified DVR model having low complexity is efficient enough to provide better linearization as compared to MP/GMP models for RoF link linearization. The simple version of DVR is expressed as:

$$z_p(n) = \sum_{i=0}^{Q_{DVR}} a_i |z(n-i)| + \sum_{k=1}^{K_{DVR}} \sum_{i=0}^{Q_{DVR}} a_{ki,j} \left| |z(n-i)| - \beta_k \right| e^{j\theta(n-i)} \quad (4.6)$$

where $z_p(n)$ and $z(n)$ are the DPD output and input respectively. Similarly, a_i and $a_{ki,j}$ are the model coefficients. Q_{DVR} represents the memory depth, K_{DVR} represents elements in the partition while β_k 's show thresholds that define the partition i.e. $\beta_k = \frac{k}{K_{DVR}}$ for $k = 1, 2, \dots, K_{DVR}$.

B. Memory Polynomial Model

The second predistorter model implemented is a bargain between complete memory and memoryless structure due to a diagonal memory that it possesses. The Pre-Distorter Training block output will be:

$$z_p(n) = \sum_{k=0}^{K-1} \sum_{q=0}^{Q-1} a_{kq} z(n-q) |z(n-q)|^k \quad (4.7)$$

while K shows non-linearity order, Q represents memory depth, z is the input of predistorter and a_{kq} are the model coefficients.

C. Generalized Memory Polynomial Model

Generalized Memory Polynomial architecture was recently applied to RoF based VCSELs in [4.16,4.30]. The GMP is expressed as:

$$\begin{aligned}
z_p(n) = & \sum_{k=0}^{K_a-1} \sum_{q=0}^{Q_a-1} a_{kq} z(n-q) |z(n-q)|^k \\
& + \sum_{k=1}^{K_b} \sum_{q=0}^{Q_b-1} \sum_{r=1}^{R_b} b_{kqr} z(n-q) |z(n-q-r)|^k \\
& + \sum_{k=1}^{K_c} \sum_{q=0}^{Q_c-1} \sum_{r=1}^{R_c} c_{kqr} z(n-q) |z(n-q+r)|^k
\end{aligned} \tag{4.8}$$

here $z_p(n)$ and $z(n)$ are the DPD output and input respectively. likewise, a_{kq} , b_{kqr} and c_{kqr} denotes the complex coefficients for the signal and the envelope; signal and lagging envelope and signal and leading envelope respectively. K_a, K_b, K_c are the orders of nonlinearity, Q_a, Q_b, Q_c are the memory depths, R_c symbolizes the leading and R_b denotes the lagging delay tap lengths, respectively.

In order to perform an impartial juxtaposition among the three models, once the parameters K and Q are chosen in applying the MP model, GMP and DVR models are applied choosing respectively $K_a=K_b=K_c=K$, $Q_a=Q_b=Q_c=Q$, and $K_{DVR}=K$, $Q_{DVR}=Q$.

4.2.2 Experimental Setup

The experimental testbed utilized is presented in Figure 4.16. A Multi Quantum Well (MQW) DFB laser, working at 1310-nm wavelength succeeds a Standard Single Mode Fiber (SSMF) of 1.5 km having attenuation equal to 0.4 dB/km and negligible chromatic dispersion. The optical signal detection is accomplished by a PIN photodiode. The PIN photodiode has a bandwidth of 2.5 GHz and 0.6 A/W of responsivity. The biasing current was $I_{bias} = 15 \text{ mA}$, setting the power consumption to an acceptable level, while being not too close to the threshold current $I_{th} \sim 5.5 \text{ mA}$.

The LTE baseband signal of 5 MHz with 256 QAM modulation is emulated through a domestic software on MATLAB compliant with 3GPP release TS 36.104 V15.2.0. The signal is oversampled at a scale of 38.4 MSa/s. The sampled signals pass through the DPD block and are then upconverted at 1 GHz utilizing an Agilent N5182B MXG Vector Signal Generator and then transmitted to the optical link. The signal received through the vector signal analyzer is passed through the training phase of the DPD. Firstly, the LTE reference frames are employed for synchronizing the input and output signals (Sync. block in Figure 4.16).

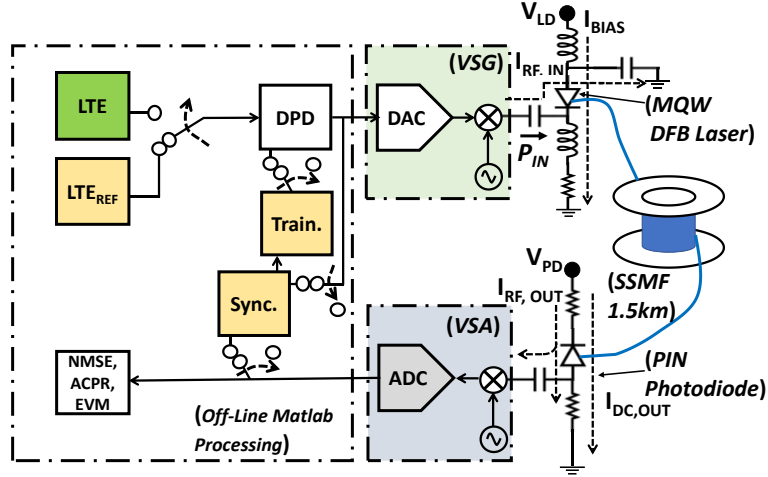


Figure 4.16: Schematic of Experimental testbed. Train. Phase (yellow units active). By changing the position of switches (green block active) DPD implemented for many LTE frames.

This block finds the time delay evaluation by utilizing the Synchronization Signals (Primary and Secondary) accessible in the LTE framework. Then, the predistorter coefficients are procured through the PD models utilized (see Train. in Figure 4.16). For the DPD validation phase (all switches move to opposite direction in Figure 4.16), testing is done for LTE frames followed by sampling, pre-distortion, and then uploaded to the Vector Signal Generator (VSG). It is noteworthy that the DPD is validated for general frames of LTE.

4.2.3 Experimental Results and Discussion

Figure 4.17 shows a comparison of experimental NMSE results using MP, GMP and DVR. In case of MP and GMP, the results have been evaluated for varying Q (1, 2 and 3) and non-linearity orders K (3, 4, 5 and 6) while for DVR, same orders of Q are evaluated for number of elements in the partitions K . The average value of RF input power is $P_{IN} = 0 \text{ dBm}$.

It is perceptible from Figure 4.17 that DVR bring about higher mitigation of NMSE as compared to MP/ GMP. Considering that higher values of Q and K lead to lower values of NMSE at the expense of an increased computational time, the average value of RF input power is $P_{IN} = 0 \text{ dBm}$. Taking into account that higher values of Q and K lead to lower values of NMSE at the expense of an increased computational time, the optimal values $Q = 2$, $K = 3$ have been selected to proceed in the comparison among the architectures.

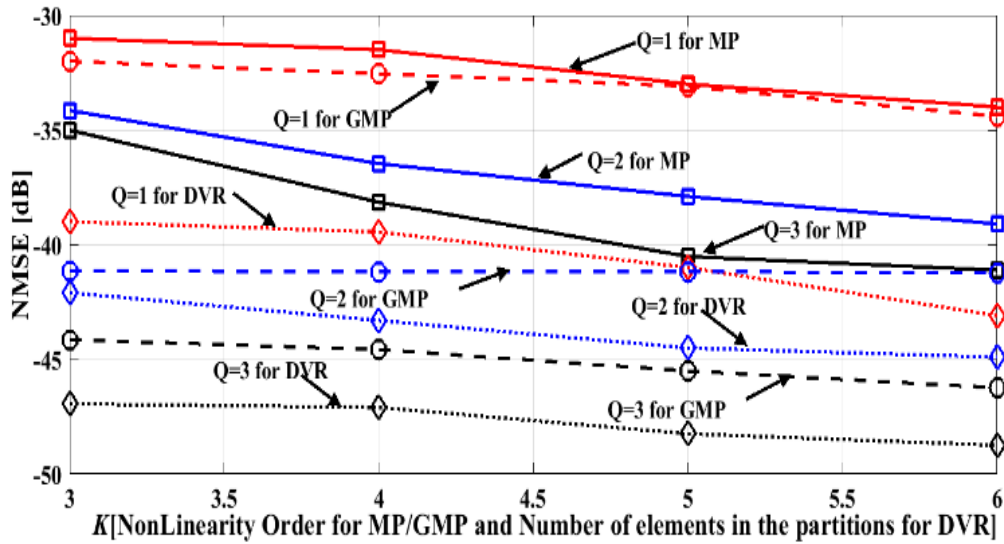


Figure 4.17: Normalized Mean Square Error results for different K and Q .

In Figure 4.18, the ACPR experimental outcomes for varying input powers with and without DPD are reported, confirming that also in terms of reducing the ACPR values; the linearization performance proves better using DVR than GMP/MP.

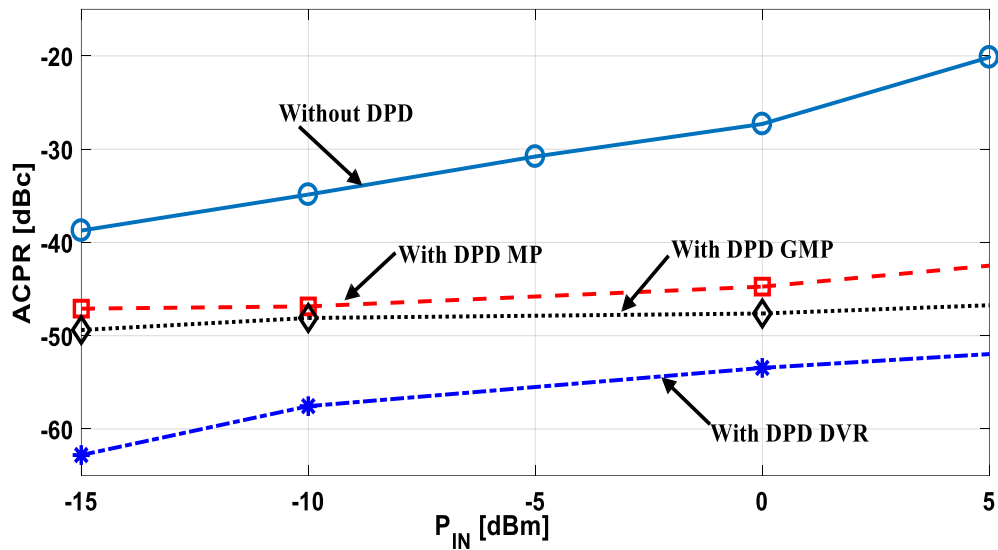


Figure 4.18: ACPR for varying input power for MP/GMP/DVR

Figure 4.19 details the Power Spectral Density (PSD) of the output signal with and without the different DPDs for $P_{IN} = 0 \text{ dBm}$. As expected, DVR results in lower spectral regrowth with respect to MP/GMP.

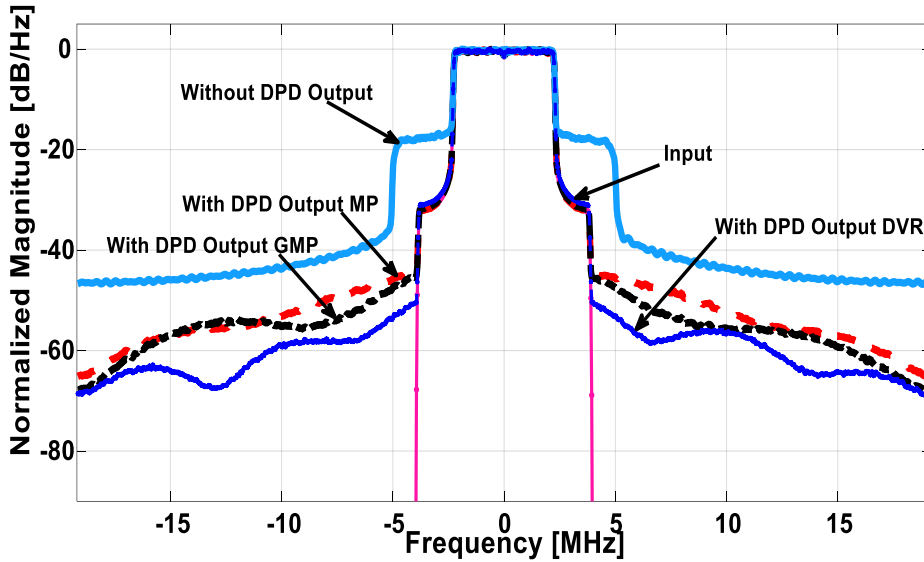


Figure 4.19: PSD for $P_{IN} = 0$ dBm in the different considered cases.

Figure 4.20 shows the EVM comparison with and without DPD by sweeping the input power. DVR results in better linearization than MP/GMP at higher RF input powers as well.

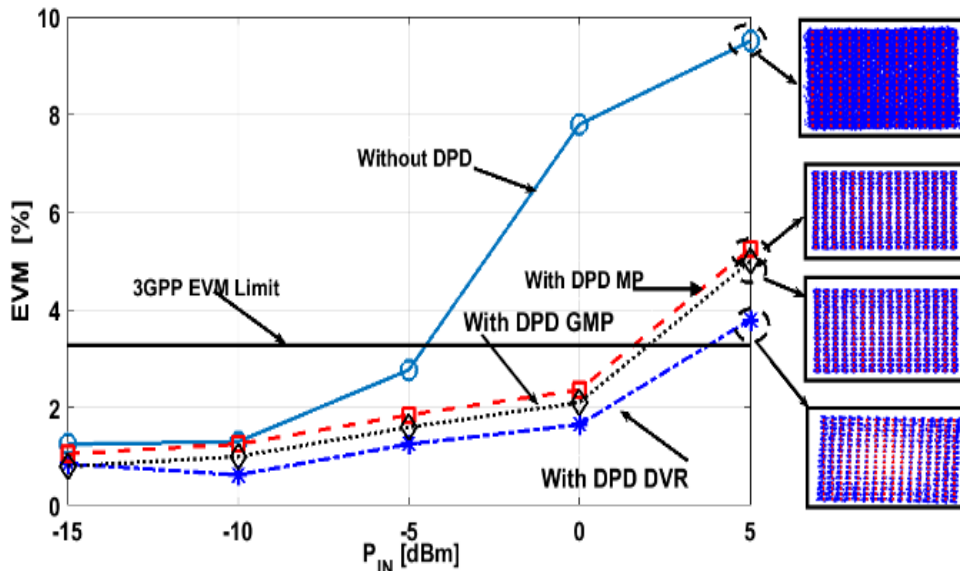


Figure 4.20: EVM for varying input power for MP/GMP/DVR

Table 4.5 summarizes quantitatively the shown experimental results for $Q = 2, K = 3$. Note that the proposed DPD is functional for longer link distances and higher bandwidth provided that model is extracted with right Q and/or K .

<i>Model</i>	<i>NMSE (dB)</i>	<i>ACPR (dBc)</i>	<i>EVM (%)</i>
No DPD	-19.10	-27.25	8.2
MP-DPD	-35.15	-44.56	2.36
GMP-DPD	-40.14	-47.62	1.9
DVR-DPD	-42.10	-53.45	1.65

Table 4-5: Comparison among the utilized DPD models for $P_{IN}=0dBm$

Finally, to further highlight the performance of the DVR model, in Figure 4.21, the comparison is presented in terms of normalized magnitude (AM/AM) and normalized phase (AM/PM) characteristics with and without its application where the AM/AM curve is linear, while the phase difference is highly reduced.

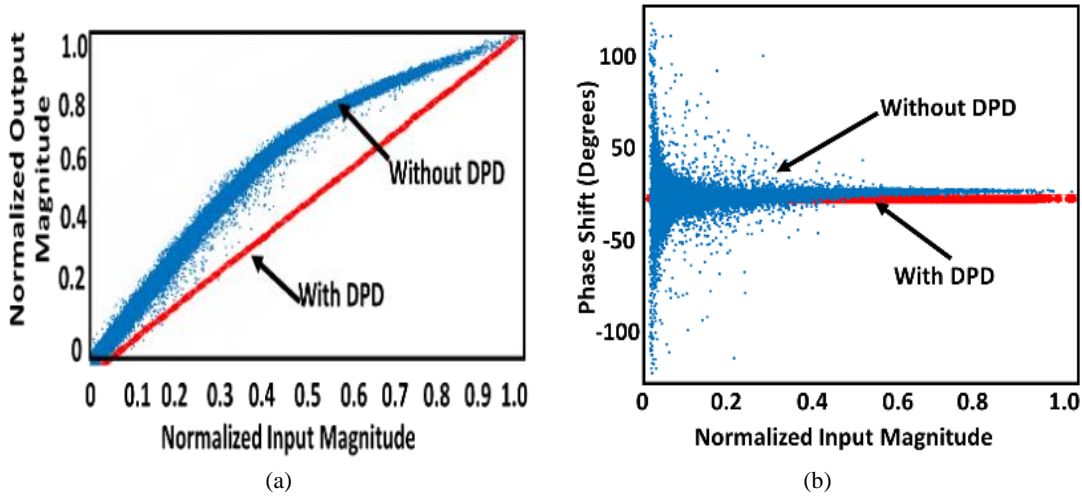


Figure 4.21: Effect of DVR-based DPD on AM/AM and AM/PM curves for DFB based RoF links

4.2.4 Conclusions

A novel evaluation has been experimentally carried out between DPD identification models for DFB based RoF links. In particular, the system performance in terms of NMSE, ACPR and EVM are estimated by means of classical MP and GMP models and with the DVR one, based on segmentation approach. For DFB based RoF links, the results establish that a promising link performance improvement is obtained already at low non-linearity order, with all the three models. It has been however shown that DVR allows to obtain a higher degree of linearization for all the considered quantities.

4.3 Experimental Demonstration on Digital Predistortion for Multi-Channel Radio over Fiber Systems

The diversity of the wireless services have been increasing within the past decade. Multi standard and multi band technologies are getting a lot of importance and preferred for wireless operations. In case of distributed antenna systems (DAS), radio over fiber (RoF) is a viable technology due to their benefits such as front haul fiber sharing, scalability and low loss transmission. The RoF technology plays a major role in the realization of the physical layer of 3G and 4G systems and is expected to form the cornerstone of the future fifth generation of wireless networks. Multi-band techniques are widely implied due to potential cost and energy saving. However, these networks are prone to inherent nonlinearities such as laser chirp, in band and cross band non-linear distortions and optical link impairments. For multi-band RoF systems, the modulation nonlinearities can result in both in-band and cross-band nonlinear distortions, which ultimately limits the link performance and radiofrequency (RF) power transmitting efficiency [4.32-4.34]. In this section, we propose a novel simplified multi-band DPD technique for such multi band RoF systems. In the proposed technique, instead of processing the multi-band RF signal as a single entity, the DPD is performed on the baseband signal of each individual RF band before frequency up-conversion and RF combination. The compensation function is synthesized for each RF band by involving the nonlinear impacts and memory effects from all existing RF bands.

The proposed technique provides the following advantages compared to the previously published techniques:

- i. The nonlinearities compensation is done for each band individually.
- ii. DPD technique has dependency over frequency offset.

This section is organized as follows. Section 4.3.1 describes and demonstrates the theoretical understanding about the principle of the proposed architecture is described comprehensively and the mathematical theory behind the proposed model is explained accordingly. Finally, Section 4.3.2 reports the measurement results and performance improvements using the proposed architecture.

4.3.1 Review of the developed multi-dimensional DPD models

The indirect learning architecture utilized for multi-channel DPD is shown in Figure 4.22. $u_i(n)$ ($i = 1, 2$) denotes the original baseband complex signal of the i^{th} band. The output of DPD block which becomes the input to RoF link is $x_i(n)$ while the output of RoF link is referred as $y_i(n)$. The digital predistorter indeed has an inverse transfer function with respect to the RoF link. G_i is the gain of the RoF link for the i^{th} band.

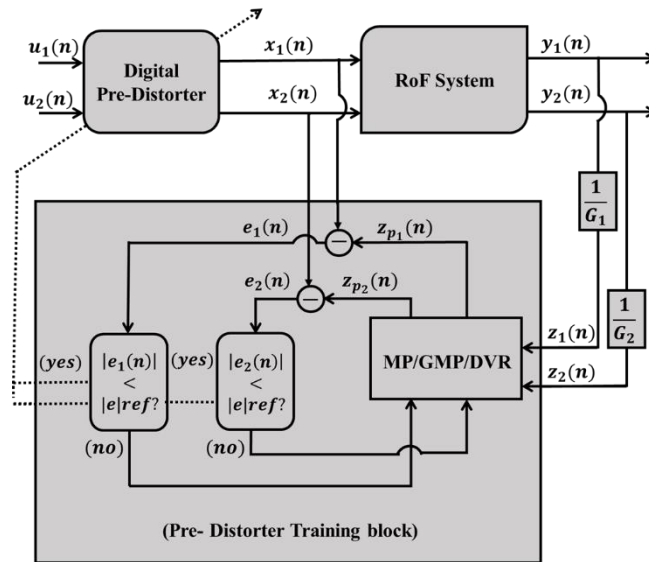


Figure 4.22: Schematic for Dual Channel DPD methodology for RoF System

We will discuss the PD models and their forms for the multi-channel cases in the following sections. As both the input signals play their part in model identification process, therefore, a new model identification model has been discussed. The model considers the dual baseband input with K as nonlinearity order and Q as memory depth.

The general form of Volterra baseband DPD is given as:

$$\begin{aligned}
y(n) &= \sum_{m_1=0}^M \lambda_{m_1}^1 x_{n-m_1} + \sum_{m_1=0}^M \sum_{m_2=m_1}^M \sum_{m_3=0}^M \lambda_{m_1 m_2 m_3}^3 x_{n-m_1} x_{n-m_2} x_{n-m_3}^* \\
&+ \sum_{m_1=0}^M \sum_{m_2=m_1}^M \sum_{m_3=m_2}^M \sum_{m_4=0}^M \sum_{m_5=m_4}^M \lambda_{m_1 m_2 m_3 m_4 m_5}^5 x_{n-m_1} x_{n-m_2} x_{n-m_3} x_{n-m_4}^* x_{n-m_5}^*
\end{aligned} \tag{4.9}$$

The form presented in Eq. (4.9) is a truncated baseband representation in time-discrete domain for any nonlinear RF PD. The monomials in the Volterra are all odd order. These monomials are product of delayed inputs and their complex-conjugates, with one decreasing complex conjugate factor. The monomials with even order contain signals that fall outside the band of interests and are filtered away [4.35].

In order to derive the Generalized Polynomial model for dual band input, let us assume that $x_1(n)$ and $x_2(n)$ are the baseband input signals at different carrier frequencies. Such signal can be represented as:

$$x_n = x_1(n)e^{j\omega_0 n} + x_2(n)e^{-j\omega_0 n} \tag{4.10}$$

Substituting (4.10), the following linear terms are obtained:

$$x_{n-m_1} = x_{1,n-m_1} e^{j\omega_0(n-m_1)} + x_{2,n-m_1} e^{-j\omega_0(n-m_1)} \tag{4.11}$$

The 3rd order terms obtained by inserting (4.11) in (4.10) is given as:

$$\begin{aligned}
&x_{n-m_1} x_{n-m_2} x_{n-m_3}^* = x_{1,n-m_1} e^{j\omega_0(n-m_1)} + x_{2,n-m_1} e^{-j\omega_0(n-m_1)} \\
&x_{1,n-m_2} e^{j\omega_0(n-m_2)} + x_{2,n-m_2} e^{-j\omega_0(n-m_2)} (x_{1,n-m_3}^* e^{j\omega_0(n-m_3)} + x_{2,n-m_3}^* e^{-j\omega_0(n-m_3)}) \\
&= e^{-j\omega_0 n} (x_{2,n-m_1} x_{2,n-m_2} x_{2,n-m_3}^* e^{j(m_1+m_2-m_3)} + x_{2,n-m_1} x_{1,n-m_2} x_{1,n-m_3}^* e^{j(m_1-m_2+m_3)} \\
&\quad + x_{1,n-m_1} x_{2,n-m_2} x_{1,n-m_3}^* e^{j(-m_1+m_2+m_3)}) \\
&\quad + e^{-3j\omega_0 n} (x_{2,n-m_1} x_{2,n-m_2} x_{1,n-m_3}^* e^{j(m_1+m_2+m_3)}) \\
&\quad + e^{3j\omega_0 n} (x_{1,n-m_1} x_{1,n-m_2} x_{2,n-m_3}^* e^{j(-m_1-m_2-m_3)}) \\
&\quad + e^{j\omega_0 n} (x_{1,n-m_1} x_{1,n-m_2} x_{1,n-m_3}^* e^{j(-m_1-m_2+m_3)} + x_{1,n-m_1} x_{2,n-m_2} x_{2,n-m_3}^* e^{j(-m_1+m_2-m_3)} \\
&\quad + x_{2,n-m_1} x_{1,n-m_2} x_{2,n-m_3}^* e^{j(m_1-m_2-m_3)})
\end{aligned} \tag{4.12}$$

The higher order terms get complicated with increasing order. However, it can be predicted from 3rd order expression that there is 1 positive and 2 negative delays in the exponent as these

are the components which occur in interesting frequency region. The complete series expression consists of the weighted sum of all terms of all orders and delays as represented in :

$$\begin{aligned}
y_n &= \sum_{m_1=0}^M a_{m_1}^{(1)} x_{1,n-m_1} \\
&+ \sum_{m_1=0}^M \sum_{m_2=m_1}^M \sum_{m_3=0}^M a_{m_1 m_2 m_3}^{(3)} (x_{1,n-m_1} x_{1,n-m_2} x_{1,n-m_3}^* e^{j(-m_1-m_2+m_3)} \\
&\quad + x_{1,n-m_1} x_{2,n-m_2} x_{2,n-m_3}^* e^{j(-m_1+m_2-m_3)} + x_{2,n-m_1} x_{1,n-m_2} x_{2,n-m_3}^* e^{j(m_1-m_2-m_3)}) \\
&+ \sum_{m_1=0}^M \sum_{m_2=m_1}^M \sum_{m_3=m_2}^M \sum_{m_4=0}^M \sum_{m_5=m_4}^M a_{m_1 m_2 m_3 m_4 m_5}^{(5)} (x_{1,n-m_1} x_{1,n-m_2} x_{1,n-m_3} x_{1,n-m_4}^* x_{1,n-m_5}^* e^{j(-m_1-m_2-m_3+m_4+m_5)} \\
&+ x_{1,n-m_1} x_{1,n-m_2} x_{2,n-m_3} x_{2,n-m_4}^* x_{1,n-m_5}^* e^{j\omega_0(-m_1-m_2+m_3-m_4+m_5)}) \\
&+ \dots
\end{aligned} \tag{4.13}$$

There is a possibility that we can simplify the complex conjugate terms. Since, we enforce that all complex-conjugate terms to have same delay as that of non-complex-conjugates. This will simplify $x_{n-m} x_{n-m}^* = |x_{n-m}|^2$. This simplification is two folded: first, allowing real valued multiplications instead of complex ones and secondly, few delays to sum over. The simplified complexity reduced form is given by:

$$\begin{aligned}
y_n &= \sum_{m_1=0}^M b_{m_1} x_{1,n-m_1} \\
&+ \sum_{m_1=0}^M \sum_{m_2=0}^M \sum_{s_1=1}^2 b_{m_1 m_2}^{(s_1)} x_{1,n-m_1} |x_{s_1,n-m_2}|^2 \\
&+ \sum_{m_1=0}^M \sum_{m_2=0}^M \sum_{m_3=0}^M \sum_{s_1=1}^2 \sum_{s_2=s_1}^2 b_{m_1 m_2}^{(s_1, s_2)} x_{1,n-m_1} |x_{s_1,n-m_2}|^2 |x_{s_2,n-m_3}|^2
\end{aligned} \tag{4.14}$$

This representation can be further simplified and reduced by restricting the allowed cross-terms between different delays and signals.

$$\begin{aligned}
y_n = & \sum_{m=0}^M \sum_{k=0,2,\dots}^P \sum_{j=0,2,\dots}^k b_{m,0}^{(k,j)} x_{1,n-m} |x_{1,n-m}|^{k-j} |x_{2,n-m}|^j \\
& + \sum_{m=0}^M \sum_{l=1}^G \sum_{k=2,4,\dots}^P \sum_{j=0,2,\dots}^k b_{m,l}^{(k,j)} x_{1,n-m} |x_{1,n-m-l}|^{k-j} |x_{2,n-m-l}|^j \\
& + \sum_{m=0}^M \sum_{l=1}^G \sum_{k=2,4,\dots}^P \sum_{j=0,2,\dots}^k b_{m,-l}^{(k,j)} x_{1,n-m-l} |x_{1,n-m}|^{k-j} |x_{2,n-m}|^j
\end{aligned} \tag{4.15}$$

This is the generalized memory polynomial for dual channel.

Similarly, if we remove totally all the cross-terms altogether, This is the structure used in [4.34-4.35] and the memory polynomial for dual band is given as:

$$y_n = \sum_{m=0}^M \sum_{k=0,2,\dots}^P \sum_{j=0,2,\dots}^k b_{m,0}^{(k,j)} x_{1,n-m} |x_{1,n-m}|^{k-j} |x_{2,n-m}|^j \tag{4.16}$$

There are of course also other complexity-reductions of the full Volterra that can be considered, such as:

- If the x_2 signal has much less power than x_1 (or vice versa), it may be useful to only include the linear effects of x_2 , since higher order terms may be insignificant.
- The memory depth of high-order terms can be reduced compared to the linear terms, since high-order, high delayed terms should be of less significance.
- Likewise, the nonlinear order of high-delayed terms can be reduced.
- In general, the general dual-input Volterra can be pruned by excluding insignificant terms in various ways.

Another model that can be applied has been recently developed by Anding Zhu in [4.28] which was applied to single input channel power amplifiers. We have also discussed in Sec. 4.2.1.A the use of DVR for linearization of DFB based RoF link. Here we discuss its usage for dual channel case.

$$y(n) = \sum_{i=0}^M a_i |x_1(n-i)|$$

$$\begin{aligned}
& + \sum_{k=1}^K \sum_{i=0}^M a_{ki,in} \left| |x_1(n-i)| - \beta_{1,k,in} \right| x_1(n-i) \\
& + \sum_{k=1}^K \sum_{i=0}^M a_{ki,cross,1} \left| |x_2(n-i)| - \beta_{2,k,cross,1} \right| x_1(n-i) \\
& + \sum_{k=1}^K \sum_{i=0}^M a_{ki,cross,2} \left| |x_1(n-i)| + |x_2(n-i)| - \beta_{2,k,cross,2} \right| x_1(n-i) \quad (4.17) \\
& + \sum_{k=1}^K \sum_{i=0}^M a_{ki,cross,3} \left| |x_1(n-i)| - |x_2(n-i)| - \beta_{2,k,cross,3} \right| x_1(n-i) \\
& + \sum_{k=1}^K \sum_{i=0}^M a_{ki,cross,4} \left| \sqrt{|x_1(n-i)|^2 + |x_2(n-i)|^2} - \beta_{2,k,cross,4} \right| x_1(n-i)
\end{aligned}$$

Here $y(n)$ represents the output while $x_1(n)$ and $x_2(n)$ shows signal input. The memory depth is represented by M while K represents the hyperplanes or number of elements in the partition. β_k represents the thresholds that define the partition. The absolute operation serves as nonlinear basis functions including both in band and cross band terms.

Coefficients Extraction

The decision to apply different models depends on robust, fast and accurate model extraction routine. DPD model extraction can be performed by utilizing ILA or DLA. As discussed in Sec. 2.5, ILA employs predistorter RoF training block (post-inverse) by using input and output signals and then transferring the training coefficients to DPD. Since this technique offers a fast convergence as compared to DLA, we will use ILA for dual channel DPD model identification. The general output signal associated with i^{th} input signal can be presented as:

$$y_1(n) = \sum_{k=0}^K \sum_{q=0}^{Q-1} \sum_{m=0}^k c_{kqm}^1 x_1(n-q) |x_1(n-q)|^{k-m} |x_2(n-q)|^m \quad (4.18)$$

and

$$y_2(n) = \sum_{k=0}^K \sum_{q=0}^{Q-1} \sum_{m=0}^k c_{kqm}^2 x_2(n-q) |x_1(n-q)|^{k-m} |x_2(n-q)|^m \quad (4.19)$$

Here $(c_{kqm}^1 c_{kqm}^2)$ are the coefficients while $x_1(n - q)$ and $x_2(n - q)$ are complex baseband signals at the frequency f_1 and f_2 . $|\dots|$ is the absolute value of the complex signals.

The representation in matrix form becomes:

$$\vec{y}_i = \mathbf{A}_{\vec{x}}^i \vec{C} \quad (4.20)$$

Here

$$\vec{C} = [c_{000}^i \ c_{100}^i \ c_{110}^i \ \dots \ c_{K \ Q-1 \ k}^i]^T \quad (4.21)$$

represents vector of polynomial coefficients.

$$\vec{y}_i = [y(n) \ \dots \ y(n + I - 1)]^T \quad (4.22)$$

represents a vector with I samples of the output signal at i th output.

while $\mathbf{A}_{\vec{x}}^i$ is represented as:

$$\mathbf{A}_{\vec{x}}^i = [\mathbf{b}_{\vec{x}}^{(0)} \ \dots \ \mathbf{b}_{\vec{x}}^{(S)} \ \dots \ \mathbf{b}_{\vec{x}}^{(Q-1)}] \quad (4.23)$$

In this Eq. (4.23),

$$\mathbf{b}_{\vec{x}}^{(S)} =$$

$$\begin{bmatrix} x_i(n - s) & x_i(n - s)|x_i(n - s)|^{k-m}|x_{ii}(n - s)|^k & x_i(n - s)|x_{ii}(n - s)|^K \\ \vdots & \vdots & \vdots \\ x_i(n - s + I - 1) & x_i(n - s + I - 1)|x_i(n - s + I - 1)|^{k-m}|x_{ii}(n - s + I - 1)|^k & x_i(n - s + I - 1)|x_{ii}(n - s + I - 1)|^K \end{bmatrix} \quad (4.24)$$

which represents the elements extracted from Eq. (4.23)

The model identification is based on indirect learning approach [4.36]. The LS algorithm is utilized to solve Eq. (4.23). The calculated coefficients are then utilized to predistort the input signals.

4.3.2 Multi-Channel DPD for DFB based RoF System

As discussed in Sec. 4.3, to illustrate the possible DPD methodology for more than one channel, we employ DPD for dual channels first to Distributed Feedback laser based RoF links. DFB based

RoF links are prone to nonlinearities such as intermodulation distortion due to inherent nonlinear behaviour of electrical to optical (E/O) converters.

The experimental setup is shown in Figure 4.23. Two independent processing cells are used, where each processing cell is responsible for the compensation of the nonlinearity associated with that particular frequency band. A Multi Quantum Well (MQW) DFB laser, working at 1310-nm wavelength succeeds a Standard Single Mode Fiber (SSMF) of 1.5 km having attenuation equal to 0.4 dB/km and negligible chromatic dispersion. The optical signal detection is accomplished by a PIN photodiode. The PIN photodiode has a bandwidth of 2.5 GHz and 0.6 A/W of responsivity. The biasing current was $I_{bias} = 15\text{ mA}$ while threshold $I_{th} = 5.5\text{ mA}$. The baseband LTE 10 MHz signals, emulated according to 3GPP Release TS 36.104 V15.2.0 through a local MATLAB software with 256 QAM format, are oversampled (ADC in Figure 4.23) at a rate of 76.8 MSa/s. The sampled signals pass through the DPD block, are RF-converted (1000 MHz) by an Agilent N5182B MXG X-Series Signal Generator (see Figure 4.23) and sent to the optical link.

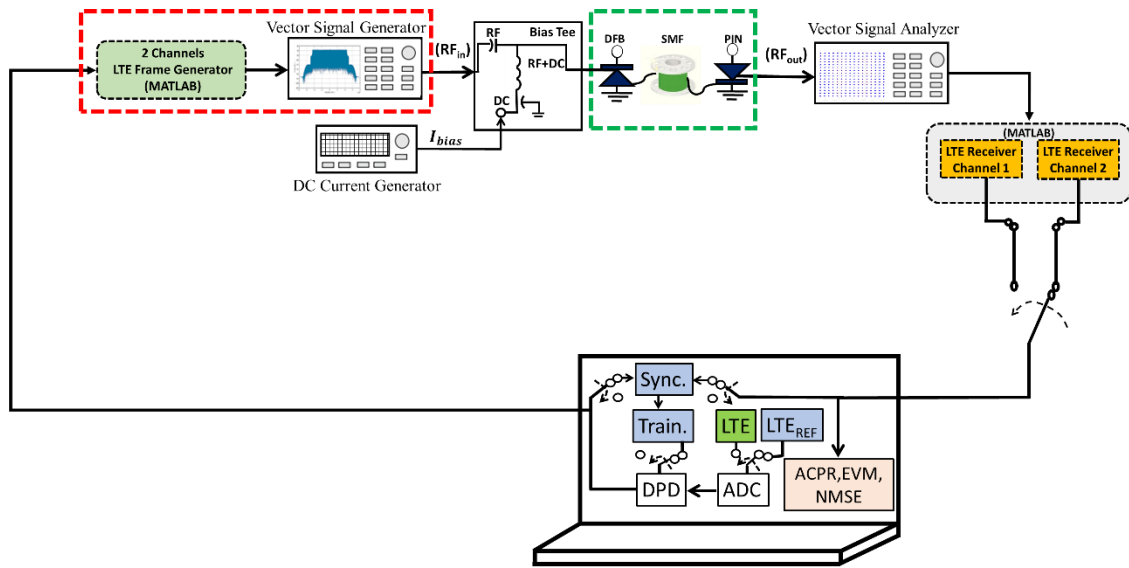


Figure 4.23: Experimental Setup for DFB based RoF link DPD (Training and Testing phase)

In order to study the DPD for multi-channel transmission, consider a two-band directly modulated DFB based RoF system. The multi-channel transmission is performed by using an inhouse MATLAB code that generates baseband samples of N independent Frequency Division Duplex (FDD) LTE channels before overlapping and then sending them to a Vector Signal Generator Agilent N5182B MXG X-Series Signal Generator for up-conversion and transmission

to RoF link. Two 256 quadrature amplitude modulation (256 QAM) RF signals both with 10 MHz bandwidth at 1 GHz and 1.2 GHz were then applied to the laser operating at 1310 nm wavelength. At the receiver side the signal is captured by a Vector Signal Analyzer and each channel is analyzed separately by the MATLAB code.

Both signal sequences were generated cyclically, therefore, the outputs of the RoF link were also cyclical. This enabled to use one VSA to record the baseband signals of the two bands in different cycles but regard them as the parallel outputs. The process of demultiplexing, down-conversion and ADC operation of the dual band RF signal is performed by VSA.

During the predistorter training, Both the channels of 10 MHz having 256 QAM modulation format at 1 GHz and 1.2 GHz without predistortion are fed in to the RoF system. The predistorter identification initiates with the coefficient estimation. The inputs, x_1 and x_2 (which are equals to u_1 and u_2 in this step) and outputs, z_1 and z_2 are applied.

Each signal received is passed through the DPD training phase. Firstly, the reference LTE frames are utilized for synchronizing the input and output sequences (Sync. block in Figure 4.23). The synchronization process is achieved through a local developed algorithm, which finds the cross-correlation for time delay estimation, by tapping the Primary and Secondary Synchronization Signals present in the LTE frame. Then, the DPD coefficients are obtained (Train. block in Figure 4.23) through MATLAB program.

For the DPD validation phase (all switches move to opposite direction in Figure 2), different LTE frames are sampled, predistorted, uploaded to the Signal Generator and transmitted through the optical link. It is noteworthy that the DPD is validated for general LTE frames.

At first, the proposed DPD technique for dual channel is experimentally investigated using GMP model by varying nonlinearity order ($K = 2, 3, 4, 5$) and memory length ($Q = 0, 1, 2, 3$). The RF input power in this case is fixed to a relative higher value of 0 dBm per band. The results are illustrated in Sec. 4.3.2.1.

4.3.2.1 Results and Discussion

Figure 4.24 in terms of effective improvement in ACPR. It can be seen in Figure 4.24(a) and Figure 4.24(b), there is a substantial improvement by employing GMP at higher K and Q in both channels. The nonlinearity orders up to 5 are required to be involved during DPD for better performance.

Taking into account higher nonlinearity orders only provides limited performance improvement, whereas the computational complexity increases. Similarly, by increasing the memory depth Q , distinct performance improvement occurs as the memory length increases. Finally, the DPD is evaluated with DVR method by varying the memory depth ($Q = 0, 1, 2, 3$) and ($K_{DVR} = 2, 3, 4, 5$) in Figure 4.24 (c) (channel 1) and Figure 4.24 (d) (channel 2). It can be appreciated that linearization is better with DVR as compared to GMP. DVR at $Q_{DVR} = 3, K_{DVR} = 5$ results in 14.52 dB and 15.49 dB of reduction in ACPR for 1st and 2nd channel respectively.

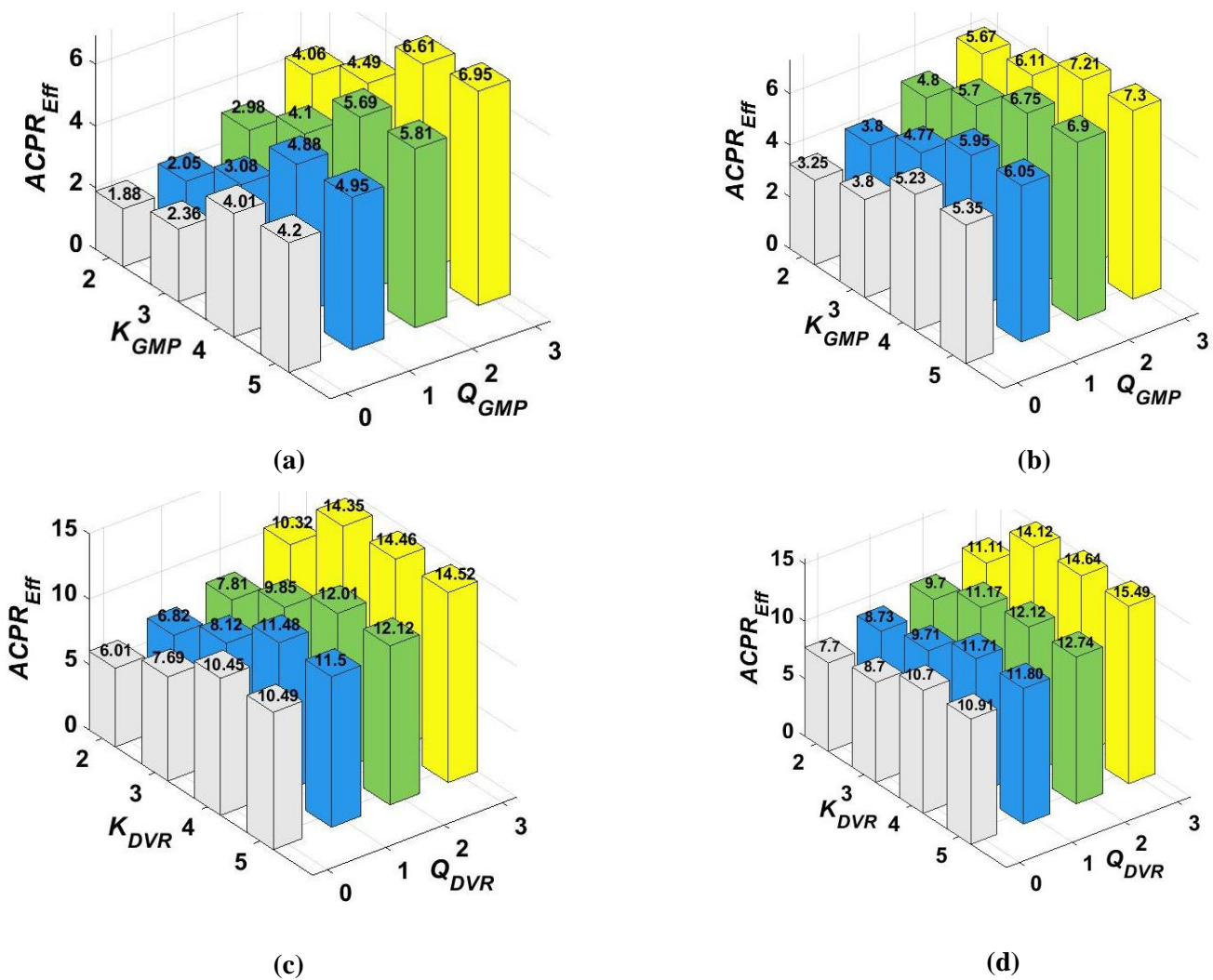


Figure 4.24: ACPR improvement for DFB in channel 1 and 2 with using GMP and DVR. (a) represents channel 1 with GMP. (b) represents channel 2 with GMP. (c) represents channel 1 with DVR and (d) represents DVR with channel 2.

For higher RF input power, the higher nonlinearity orders and memory depths are supposed to be considered. However, when the RF input power further increased to the level on which the performance was too bad to identify the impact of predistortion. In order to have a balance between the performance and the implementation complexity and to have fair comparison, $Q_{GMP} = Q_{DVR} = Q=3$ and $K_{DVR} = K_{GMP} = K = 4$ is chosen for the following investigations.

In Figure 4.25, the ACPR experimental results for several input powers (P_{in}) with and without DPD (GMP and DVR) for both channels are reported. The linearization performance proves better for DVR than GMP also in terms of reduction in the ACPR values.

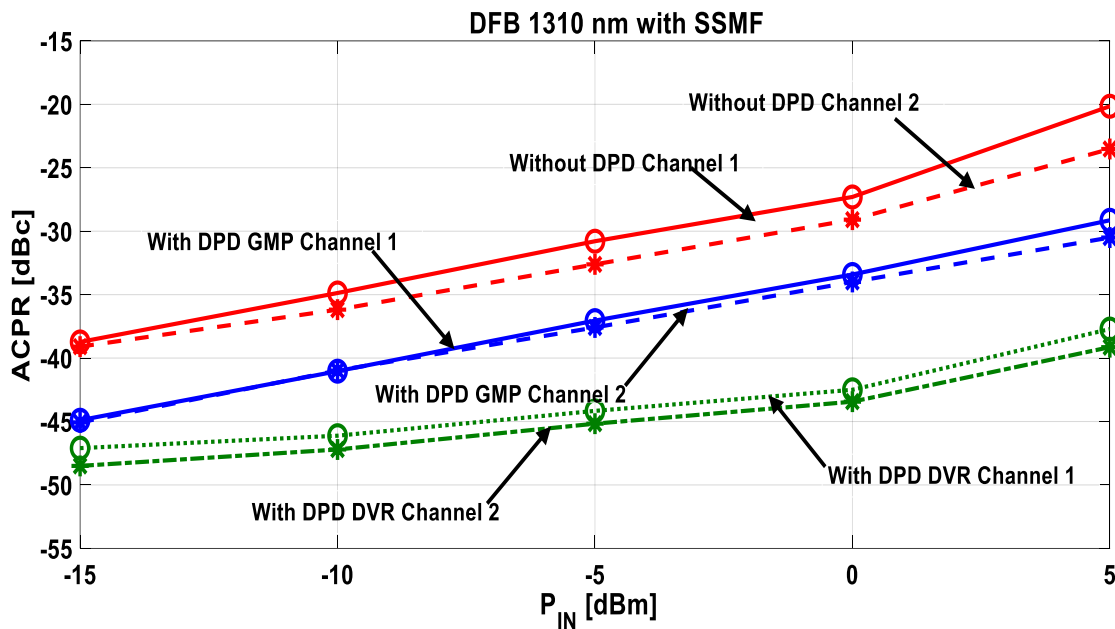


Figure 4.25: ACPR improvement for DFB in channel 1 and 2 with using GMP and DVR with varying RF input power

The summary of results with and without DPD at $P_{IN} = -15 \text{ dBm}$ and 5 dBm is given in following Table 4.6.

P_{IN} (dBm)	ACPR w/o DPD (dBc)	ACPR with GMP (dBc)	ACPR with DVR (dBc)
5	-21.84/-24.03	-30.53/-30.81	-39/-41.53
-15	-30.51/-31.2	-38.57/-40.88	-47/-50.91

Table 4-6: Linearization performance for DFB based directly- modulated RoF links

Now, the EVM with and without DPD for both channels is shown for varying RF input power in Figure 4.26. The performance behavior proves that DVR for both channels results in better realization than GMP method, e.g. at 0 dBm of P_{IN} , the EVM for both channels without DPD is 8.4/9.1 %, while with DPD-GMP it is 2.5/2.36 % and DVR results in 1.71/1.59 % respectively of EVM.

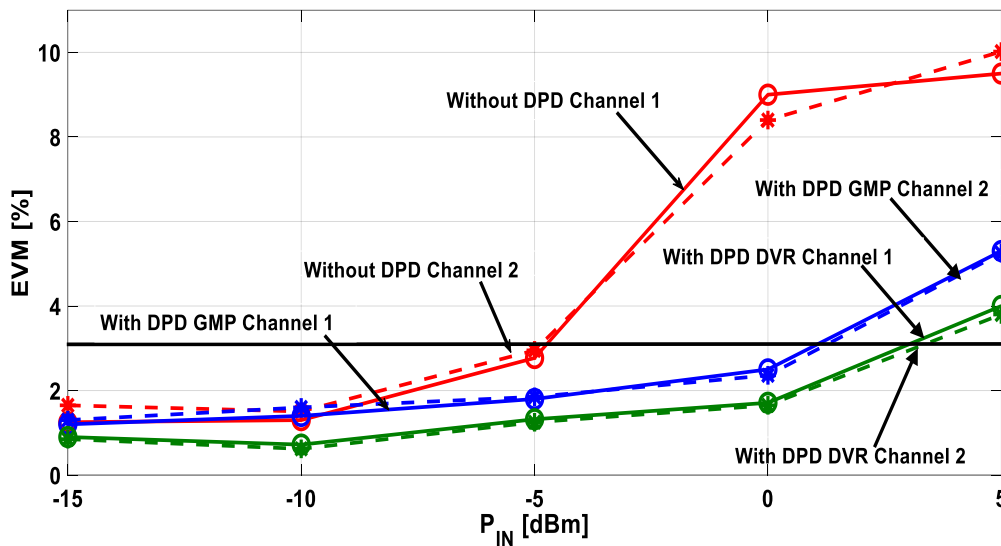


Figure 4.26: EVM improvement for DFB RoF link in channel 1 and 2 with using GMP and DVR with varying RF input power

By extending the length of the SSMF fiber span up to 1 km and applying the GMP-based DPD with $Q=1$, $K=3$ up to $P_{in} = 0 \text{ dBm}$, the ACPR remained below the reference level of -36 dBc given by the 3GPP Standard considered.

The power spectral density (PSD) for 0 dBm RF input power is shown in Figure 4.27. It can be seen that DVR results in better reduction than GMP.

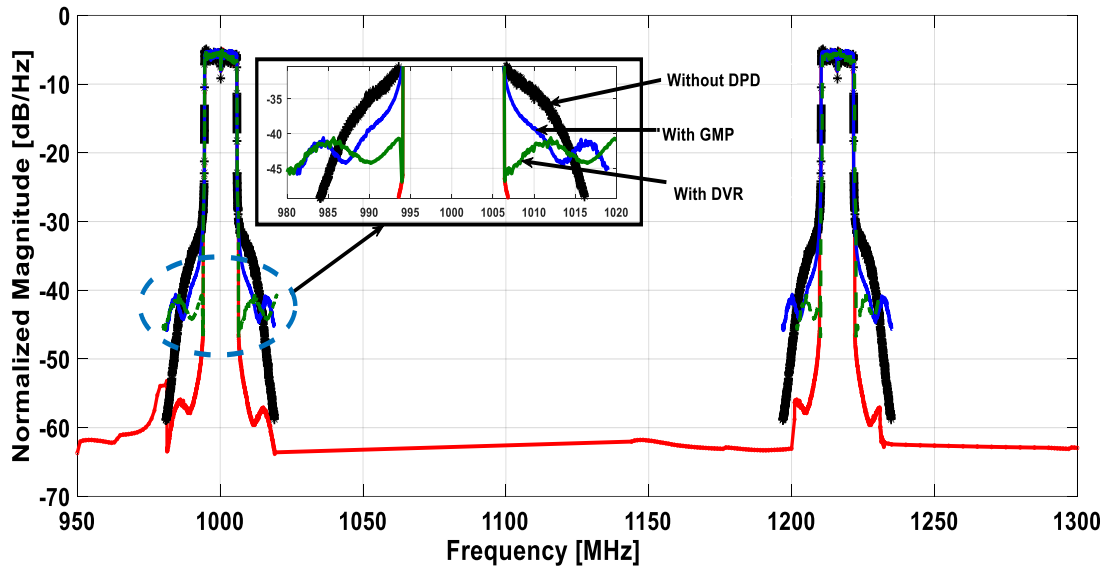


Figure 4.27: Spectral Regrowth of input, output and corrected channels for DFB based RoF link

4.3.3 Multi-Channel DPD for VCSEL based RoF System

In this section, like DFB, this section discusses the DPD approach for VCSEL based RoF links for dual channel case. VCSELs offer a cheaper solution for smaller transmission lengths up to 2 km. Applying DPD to such link lengths for multi-channel will be very beneficial. In all these cases, a cardinal issue is represented by the impairments of the opto-electronic devices and particularly the whole VCSEL based Radio over Fiber system. Such nonlinearities, that arise when high Peak-to-Average Power Ratio (PAPR) signals are transmitted and can have an important role especially for multi-channel transmission. They indeed can cause high in and out of band distortion, which leads to higher interference among near channels.

Like Figure 4.23, the experimental setup is shown in Figure 4.28. The only difference in this setup is presence of MM-VCSEL and MMF. A multi-mode VCSEL operating at 850-nm is utilized here with a MMF of length 75 meters. The PIN photodiode, having 2.5 GHz bandwidth and

responsivity factor of 0.6 A/W is used. The biasing current $I_{bias} = 4 \text{ mA}$ and $I_{th} = 0.8 \text{ mA}$ is fixed. The attenuation of MMF is 2.5 dB/Km .

The baseband LTE signal of 10-MHz with 256 QAM modulation format is emulated through a domestic software on MATLAB compliant with 3GPP release TS 36.104 V15.2.0 [4.22]. The signal is oversampled at 76.8 MSa/s. After this, the sampled sequence of signals passes through the DPD block, which is then RF transformed at 800 MHz by a Vector Signal Generator (VSG) (see Figure 3) and is then sent to the optical link.

The process of predistortion implied is similarly to one implied in Sec. 4.3.2.

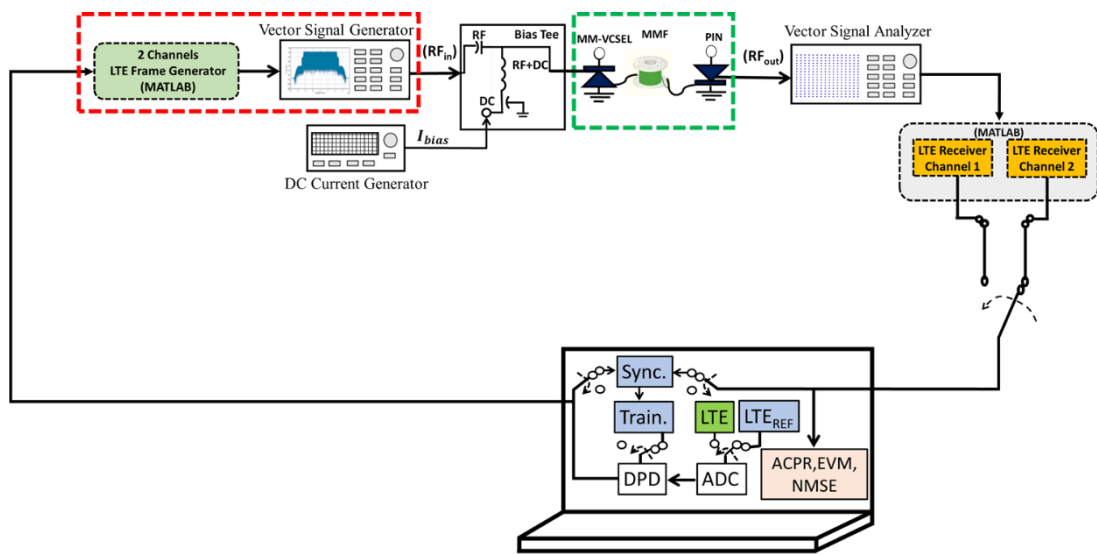


Figure 4.28: Experimental setup for MM-VCSEL based MMF for DPD training and testing phase

4.3.3.1 Results and Discussion

Figure 4.29 represents linearization performance in terms of effective improvement in ACPR. It can be seen in Figure 4.29(a) and Figure 4.29(b), there is a substantial improvement by employing GMP at higher K and Q in both channels. The nonlinearity orders up to 5 are required to be involved during DPD for better performance. The DPD is evaluated with DVR method by varying the memory depth ($Q = 0, 1, 2, 3$) and ($K_{DVR} = 2, 3, 4, 5$). It can be appreciated that linearization is better with DVR as compared to GMP. DVR at $Q_{DVR} = 3, K_{DVR} = 5$ results in 18.12 dB and 18.42 dB of reduction in ACPR for 1st and 2nd channel respectively.

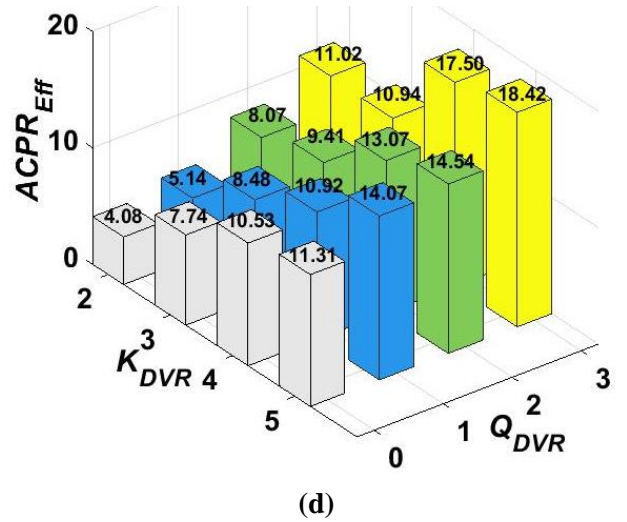
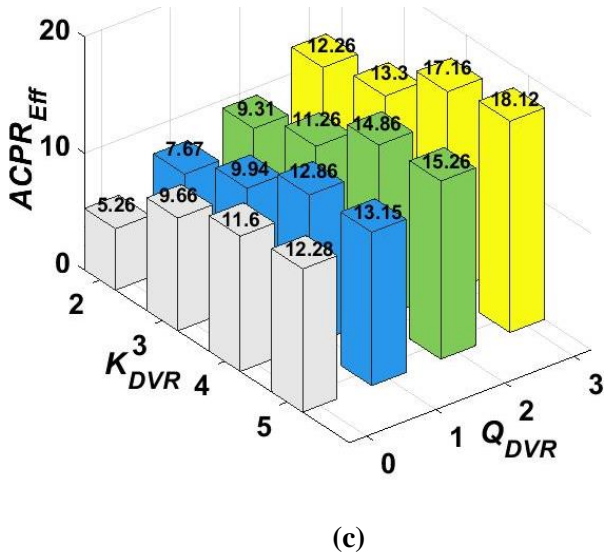
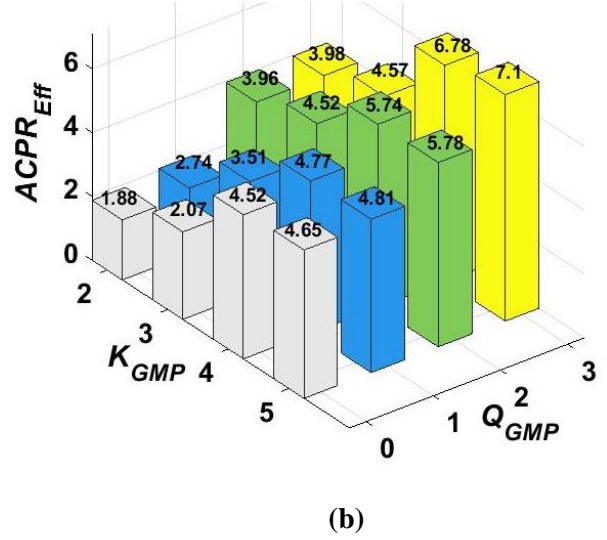
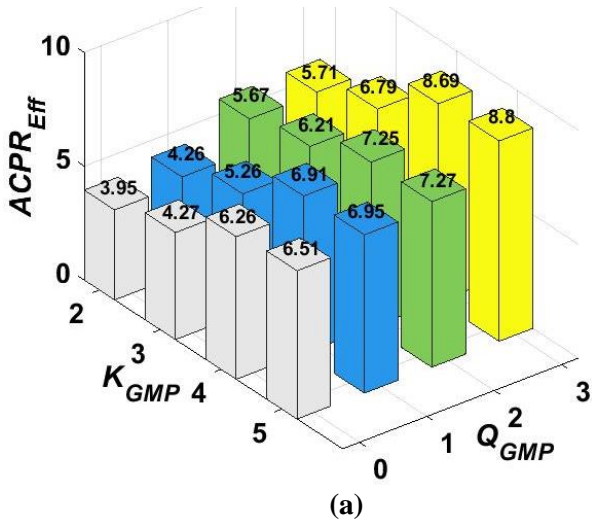


Figure 4.29: ACPR improvement for MM-VCSEL-MMF based RoF link in channel 1 and 2 with using GMP and DVR. (a) represents channel 1 with GMP. (b) represents channel 2 with GMP. (c) represents channel 1 with DVR and (d) represents DVR with channel 2.

In order to evaluate the efficacy of DPD with varying RF input power, Figure 4.30 reports the ACPR for both channels using GMP and DVR model. Indeed, as in SM-VCSEL, DVR results in better linearization than GMP. At 0 dBm, DVR results in 17 and 16 dBs of reduction with DVR and 5.4 and 5.6 dBs of reduction is observed with GMP model.

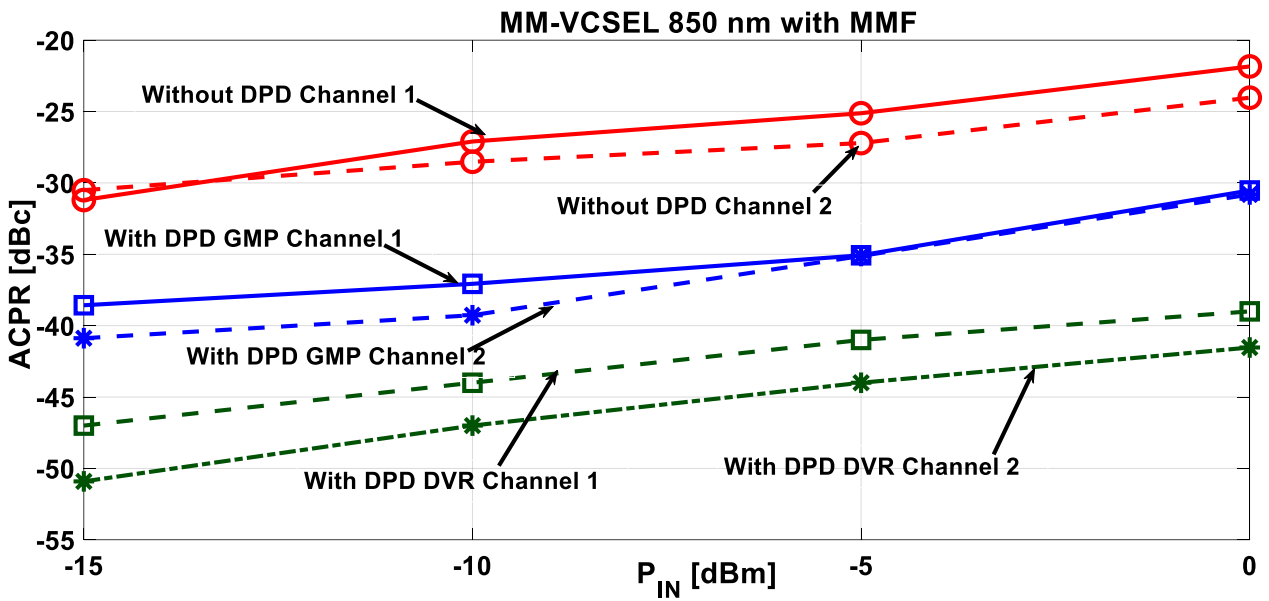


Figure 4.30: ACPR improvement for MM-VCSEL-MMF based RoF link in channel 1 and 2 with using GMP and DVR with varying RF input power

The power spectral density is shown in the Figure 4.31 for MM-VCSEL using GMP/DVR. It can be seen that PSD for both the channels is effected by the nonlinearities of VCSELs caused due to multichannel transmission.

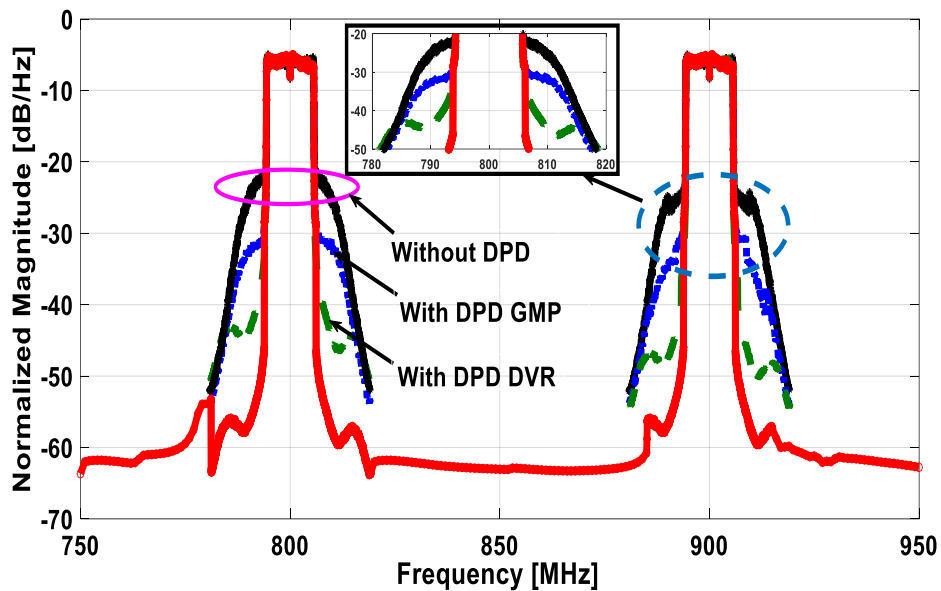


Figure 4.31: Spectral Regrowth for MM-VCSEL based MMF RoF link for both channels

The EVM characterization is done in order to consolidate the proposed architecture. With GMP and DVR, the uncompensated channels are linearized to 3.5% EVM limit set by 3GPP.

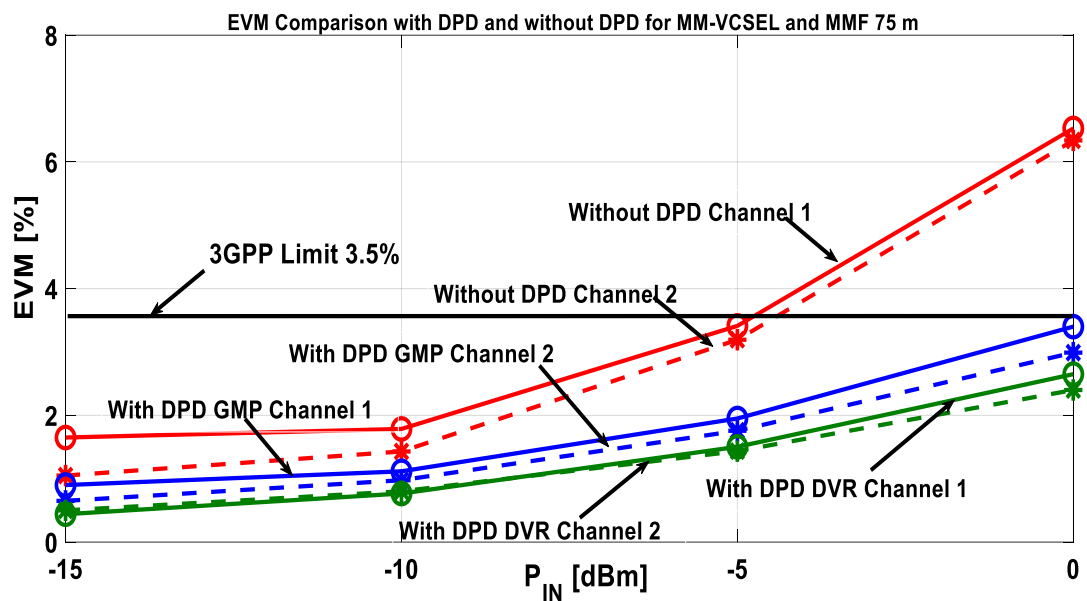


Figure 4.32: EVM performance for corrected and uncorrected both channels for DVR and GMP architectures

4.3.3.2 Conclusions

It has been shown that DPD is in good proportions for Multi channel VCSELs based RoF links. It is clear that like other cases, DVR results in better performance as compared to GMP. The proposed method is applicable for longer link distances, and/or higher values of RF input power are admitted, provided that the model is extracted with appropriate higher values of Q and/or K . Higher values of Q and/or K make also possible to apply the proposed DPD technique in the transmission of LTE signals, which exhibit higher bandwidth and/or modulation order with respect to the case considered.

4.4 REAL TIME SCENARIO

Digital Predistortion (DPD) has proven to be an effective technique to reduce the nonlinearities in RoF systems. From the applicative scenario, the process of DPD may be positioned at the Central Office (CO), e.g. where BBUs are placed and compensate the RoF Downlink nonlinearities. A periodical re-training of the Digital Predistortion system is in this case necessary,

requiring however a negligible time with respect to the time of normal operation of the RoF system. Various methods can be validated for enforcing the periodical training phase. Namely, if a RoF Uplink is applied, the nonlinearities in this case be compensated by a digital post distorter block located at a correspondent CO. By utilizing this method, the RoF downlink nonlinearities can be accumulated at BBU which will decrease the cost and complexity of remote antenna unit. In this section we will discuss some possible solutions that can be proposed for the applicative scenario.

It has been evidenced in previous discussions that Radio-over-Fiber (RoF) is an empowering technology for the upcoming 5G fronthaul networks due to its ability to carry broadband signals and provide high-speed connections and low latency due to advantages such as hardware costs saving, small footprint, low power loss, sharing resources and centralization.

The realization in Figure 4.33 below in principle is a possible implementation of a digital predistorter in adaptive form. This implementation has the advantage to put all the expensive processing of the signals at the Central Office / Base Transmit Station (CO-BTS), allowing to obtain a sharing of the cost among many users. In the figure, switches SW1, SW2 and SW3 are set to configuration (1) while switches SW4 and SW5 in configuration (2) and SW6, SW7 are not influent.

This corresponds to the “normal” operation of the bidirectional link. Indeed, the Digital Pre-Distorter (DPD) is assumed to be trained and to perform an appropriate processing of the digitized Base Band signal, which is subsequently brought back to analog form and modulated at radiofrequency (RF). After having passed through the Optical DL the signal enters a circulator (Ci) which allows to transmit the signal through a remote antenna unit (RAU). Conversely the signal which is received by the RAU, passes through (Ci) and is sent to the Optical UL up to the Central Office /Base Station. Here the signal is brought back to BB and processed by the CO-BTS (operation not show) in order to arrive to its final destination.

When switches SW4, SW6 and SW7, are set to configuration (3-A), and SW5 is connected to the ADC, a post-distortion operation is performed with reference to the UL.

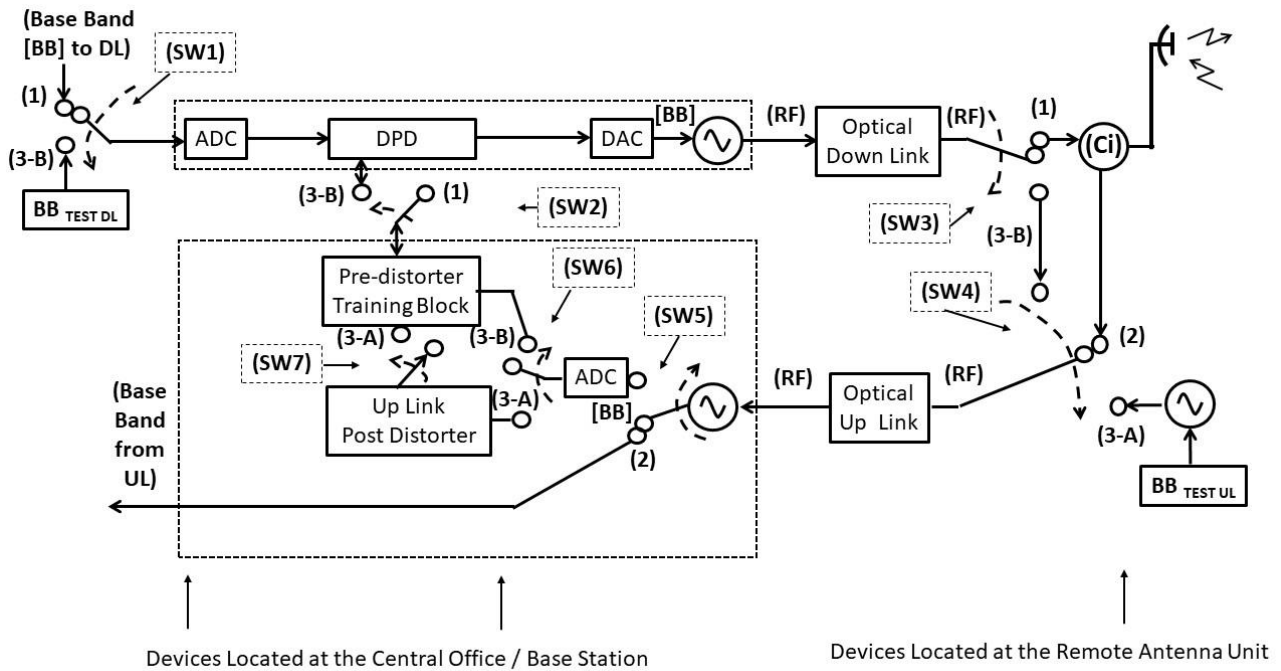


Figure 4.33: First possible realization of an adaptive predistortion scheme.

An RF test signal (which is known also at the (CO-BTS)) is sent through the Optical UL and arrives at the (RAU). Here, in a fashion similar to the one described in the submitted work, a Digital Post-Distortion is performed in order to counterbalance the nonlinearities of the UL.

The characteristic parameters of the memory polynomials determined through this operation are given to the Pre Distorter Controller Block. In principle, the Pre-Distorter Controller Block is in this way able to build the sampled version of the BB signal received at the RAU, as it would result if the operation of demodulation and sampling were performed at the RAU itself. It is expected that the nonlinear characteristics of the UL are rather stable with time, therefore, this operation is supposed to be seldom performed (namely, with the same frequency at which the training of the Digital Predistorter is realized). When switches SW1, SW2, SW3, SW4 and SW6 are set to configuration (3-B), SW5 is connected to the ADC (SW7 not influent), the training of the Digital Pre Distorter is performed.

It can be furtherly observed that performing a little change in the architecture reported in Fig 4.33, it is possible to exploit the post distortion of the Up Link not only to guarantee a reliable feedback to the Digital Predistortion system, but also to guarantee a higher quality of the signals received by the CO/BTS from the RAU during its normal operation. The one described is not the only

configuration possible for the implementation of a digital predistorter in adaptive form. Other possible alternative solutions are reported below.

Both proposals regard an alternative realization of the adaptive scheme for the Down Link. In both cases the price to pay is to set more signal processing devices at the Remote Antenna Unit. At the same time, the transmission of the feedback signal to the CO/BTS to realize the Digital Pre Distortion can be less demanding. Indeed, in both cases the information is digital, and at the same time it does not need to arrive in real time to the CO/BTS. It is then possible in this case to exploit even just an internet connection between RAU and BTS.

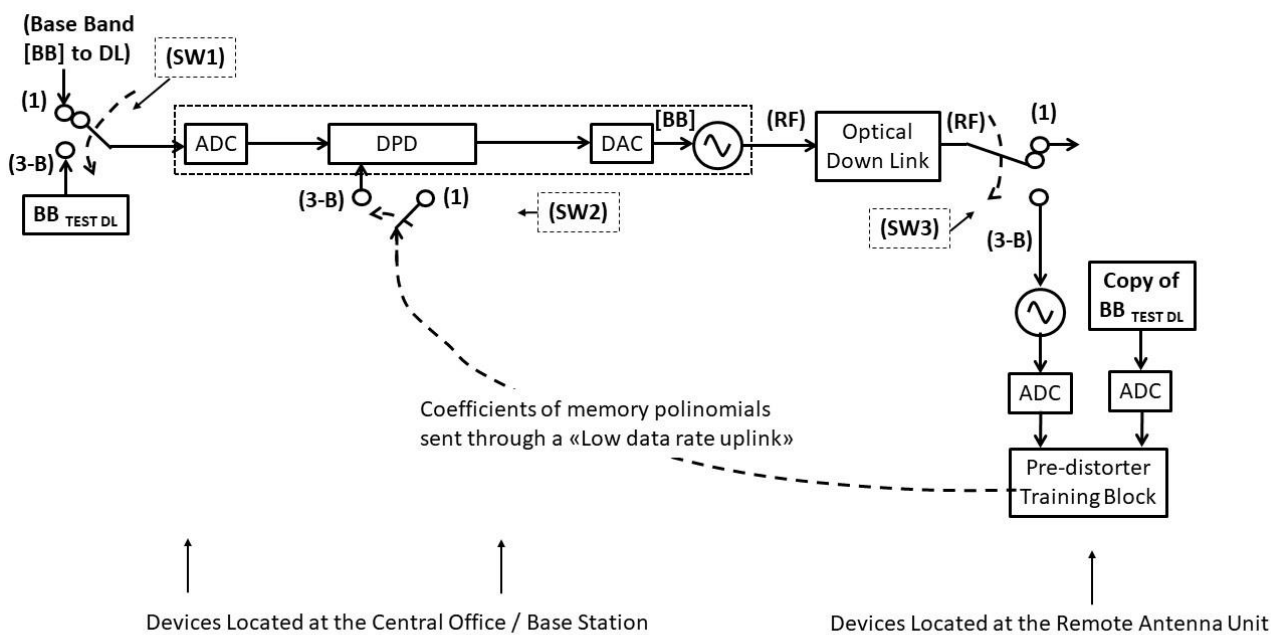


Figure 4.34: Second possible realization of an adaptive predistortion scheme.

In the following, we present a DPD methodology applied to Multi-Mode (MM) VCSEL-Multi mode fiber (MMF)-based RoF links where a simplifying approximation on the generation of the mentioned feedback signal is proposed. Indeed, this solution trains the pre-distorter taking a length of a few meters the output of a RoF link which shares the same VCSEL source of the system to be compensated. The feedback signal is in this way generated directly at the CO and is immediately available to the pre-distorter training block. This approach, which is based on the

fact that the nonlinearity of the RoF link is mainly induced by the directly modulated VCSEL, makes use of Generalized Memory Polynomial (GMP) model using ILA.

Its effectiveness will be evidenced in the remainder with reference to LTE standard signals, evaluating the transmission performance in terms of reduction of Normalized Mean Square Error (NMSE), Adjacent Channel Power Ratio (ACPR) and Error Vector Magnitude (EVM).

4.4.1 Modeling Approach

The indirect learning method used in this work (see Figure 4.35) estimates the DPD coefficients in a preliminary training phase. The baseband output of the RoF system converted into digital form $y(n)$ is fed as an input sequence to the Pre-Distorter Training block via the quantity $z(n)$, defined as $z(n) = y(n)/G$ where G is the gain of the RoF link. The estimation of coefficients can be done using any least-squares-based algorithm. Once the error function converges, the computed coefficients are applied to the predistorter (Digital Pre-Distorter block). The predistorter model used in this work is the Generalized Memory Polynomial (GMP).

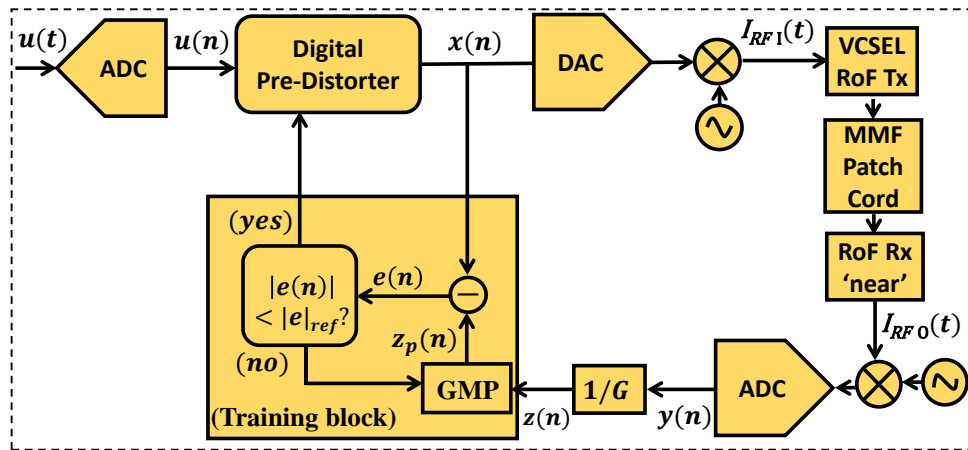


Figure 4.35: Block diagram of the training phase of the proposed DPD technique for a RoF system using Indirect Learning Architecture.

4.4.2 Experimental Setup

The schematic representation of the methodology implied is shown in Figure 4.36. The tests are performed by generating LTE signal of 10 MHz bandwidth having 256 QAM modulation format. The LTE signal is applied by Agilent N5182B MXG X-Series Vector Signal Generator (VSG) to the RoF link. The signal is modeled through in-house MATLAB software which

complies with the LTE standard (release 15.2 of the standard ETSI TS 136.211). This signal is modulated onto an RF carrier $f_c = 800$ MHz. The experimental RoF link consists of a MM VCSELS with a patch cord and a link length of MMF with 75 m and photodiode (PD), with responsivity of 0.22 A/W. The Relative Intensity Noise (RIN) of the MM VCSEL is -125 dB/Hz for $f_c = 800$ MHz. The VCSEL biasing current is $I_{bias} = 4$ mA, its threshold current is $I_{th} = 0.8$ mA and its maximum current is kept as $I_s = 8$ mA. Oversampling at a rate of 46.08 MHz is employed.

In the training phase of DPD, which corresponds to the positions of the symbolic switches represented in Figure 4.36, a link consisting of the same VCSEL of the RoF link to be linearized, a MMF patch cord and a photodiode of the same kind of the one utilized in the “far” receiver is utilized for giving the feedback signal to the predistorter training block. This configuration will be called as back-to-back (B2B) case. Reference LTE frames are utilized in this case where the input and output sequences have to be first synchronized in the time domain. This is accomplished through an in-house developed algorithm that calculates the cross-correlation for time delay estimation, by availing the Primary Synchronization Signals and Secondary Synchronization Signals present in the LTE frame. The DPD coefficients are then obtained (Train. block in Figure 3), again through a MATLAB program developed domestically.

In the testing phase, which is also represented by Figure 4.36, provided that all the symbolic switches are considered as set in the other position with respect to the depicted one, different LTE frames are sampled, predistorted, uploaded to the Signal Generator and transmitted through the optical link utilizing the zero-length case predistorter coefficients found in the training phase. ACPR, NMSE and EVM are then evaluated and compared to the corresponding case when no DPD is applied.

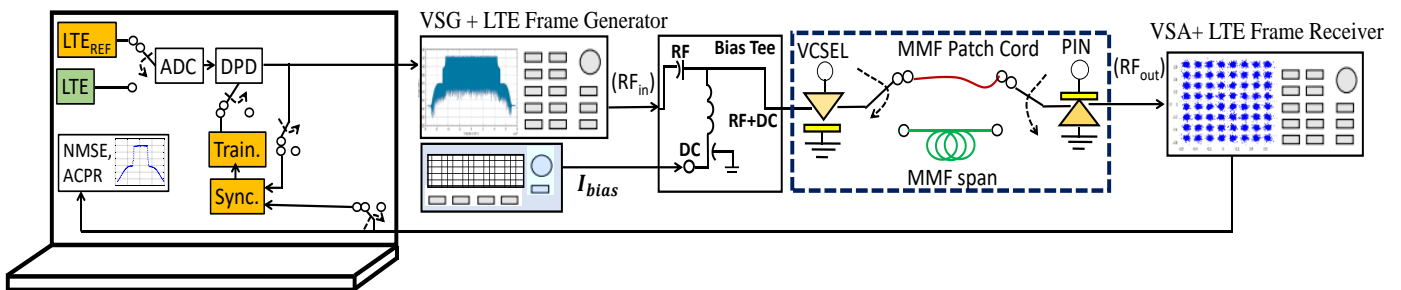


Figure 4.36: Block diagram of the experimental bench utilized for the proposed RoF system predistorter. VSG: Vector Signal Generator. VSA: Vector Signal Analyzer. The symbolic switches are represented in the positions corresponding to the training phase. The normal operation of the link is represented by the same figure where all the symbolic switches are set in the other position with respect to the represented one. VSG contains DAC and VSA contains ADC. MMF span represents the fiber length considered.

The DPD is tested not only for the reference signals that were used for training, but also for general LTE frames. It is worth mentioning the fact that the same training coefficients found during the B2B case are utilized, makes this solution straightforwardly feasible, as mentioned in the Introduction. Indeed, going back to Figure 4.36, the system enclosed by the dashed lines which performs both training and predistortion can be placed at the Central Office, allowing to reduce complexity and cost of the whole system.

4.4.3 Results and Discussion

In order to check the efficacy of methodology proposed, the laser is pushed to work near the threshold and compression points so that the regions have high Peak to Average Power Ratio (PAPR) and distortions. To see the effect of improvement of DPD in these high distortion critical regions, the biasing point (I_{bias}) is chosen as 2 mA. In this section, ACPR, EVM and NMSE are evaluated as a figure of merit.

Figure 4.37 presents the results of ACPR improvement in effective form with varying orders of K_{GMP} and Q_{GMP} keeping $R_{GMP} = 2$. It can be seen that after $K_{GMP} = 5$ and $Q_{GMP} = 3$, the increasing values of K_{GMP} and Q_{GMP} doesn't results in a very vast improvement. Hence, for the evaluations performed, the coefficients $K_{GMP} = 5$, $Q_{GMP} = 3$ and $R_{GMP} = 2$ are fixed.

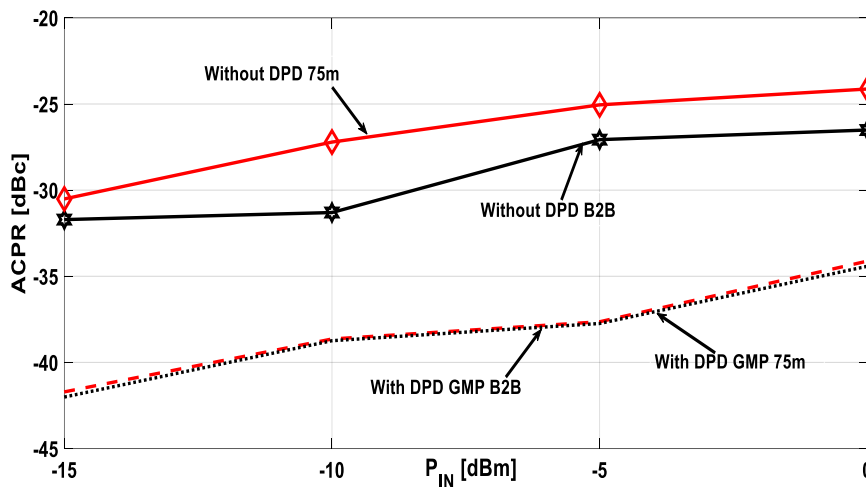


Figure 4.37: ACPR improvement with proposed DPD technique for varying orders of nonlinearity order (K_{GMP}) and memory depth (Q_{GMP}) at 0 dBm of input power.

In Figure 4.38, the behavior of ACPR is reported as a function of several input signal powers (P_{in}). Here, the orders of $K_{GMP} = 5$ and $Q_{GMP}=3$ are used keeping $R_{GMP} = 2$ as fixed quantity. The trend further signifies that improvement with DPD is in appreciable amount even for the crucial cases as well. It is evident that with the proposed approximation, the linearization for length cases is same as compared to back to back case. This is obvious that the nonlinearity of the RoF link is mainly induced by the laser as assumed in our proposed methodology. Indeed, the approximation makes the linearization straightforward without the additional complexity of feedback mechanism.

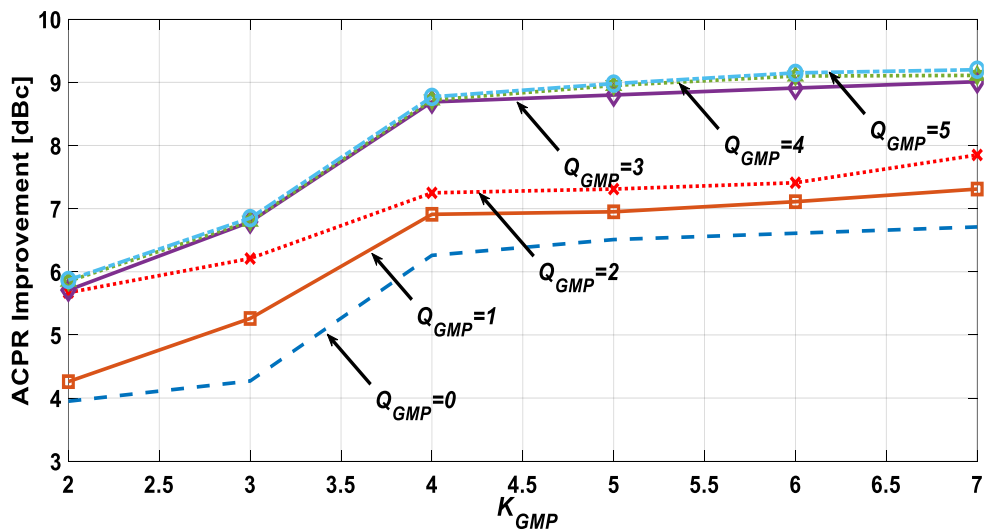


Figure 4.38: Comparison of Output signal without DPD and with DPD for back to back (0 m length) and 75 m MMF at 0 dBm input signal power

Figure 4.39 represents the spectral regrowth of applied methodology for $P_{IN} = 0 \text{ dBm}$. It can be seen that even with a signal having very high PAPR, working at a region close to threshold, high RF input power, the proposed method works well. The suppression of spectral growth due to linearization performed is in good proportions.

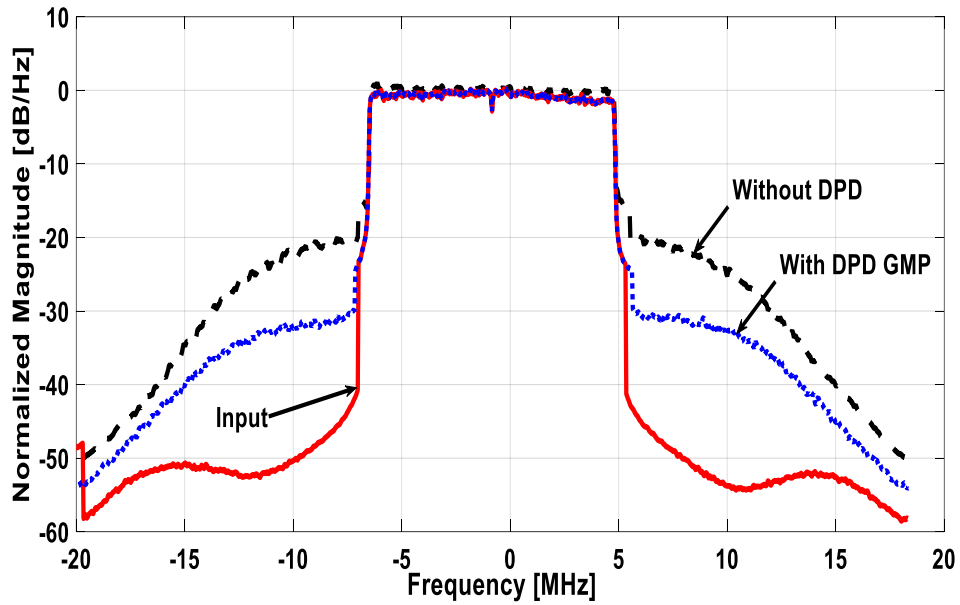


Figure 4.39: Comparison of Output signal without DPD and with DPD for back to back (0 m length) and 75 m length at 0 dBm input signal power

Figure 4.40 shows the EVM with and without DPD for varying P_{IN} . Indeed, with the presented DPD method, the 3.5% EVM limit set by 3GPP is met. This further confirms the effectiveness of the DPD since it results in correction within the limits.

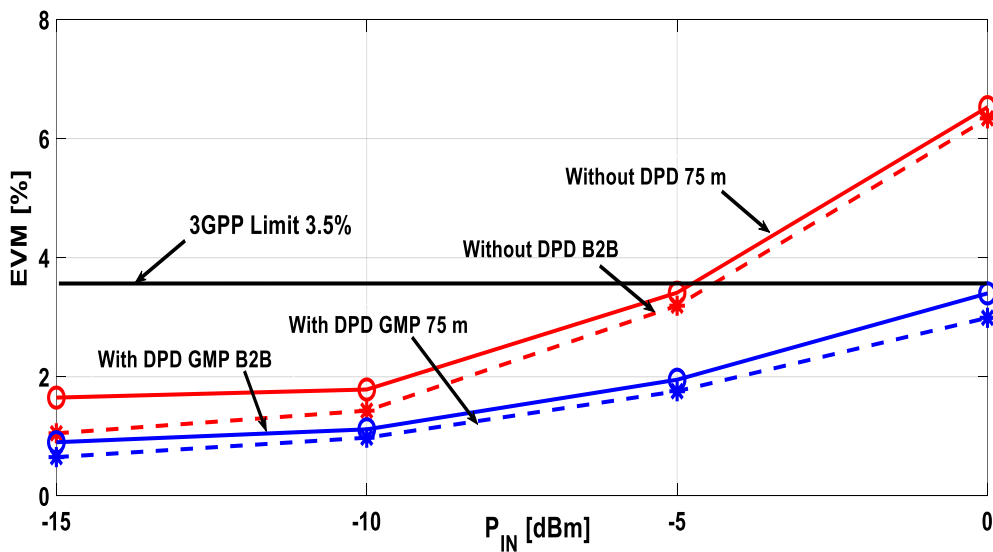


Figure 4.40: EVM comparison for DPD and without DPD for varying P_{IN}

Table 4.7 summarizes the results for with and without DPD. It can be seen that the proposed method linearizes the link in good proportions.

<i>Model</i>	<i>NMSE (dB)</i>	<i>ACPR (dBc)</i>	<i>EVM (%)</i>
No DPD	-24.10	-24.13	6.4
GMP-DPD	-36.14	-33.81	3.3

Table 4-7: Linearization performance for an input power of 0 dBm.

4.4.4 Discussion

This work reports the experimental evaluation of digital predistortion for RoF mobile fronthaul with feedback approximation for MM-VCSEL based RoF links. The experiments have been performed with MM-VCSEL based RoF link with an LTE 10 MHz signal having 256 QAM modulation format. The proposed feedback approximation does not only reduce the overall cost, but also removes the complexities required to carefully handle the own nonlinearities of feedback loop. Notable performance improvements have been obtained in terms of NMSE, ACPR and EVM. It has been shown that linearization with proposed feedback approximation is obtained in good proportions. The detailed evaluation with higher link lengths is envisaged for future work.

4.5 Conclusion

In this chapter, adaptive DPD based linearization methods were discussed. In Sec. 4.1, RoF links based on SM-VCSEL-SSMF and MM-VCSEL-MMF were discussed well in detail. In Sec. 4.2, DFB-SSMF based RoF link was linearized with improvement in the performance in terms of ACPR and EVM improvement. In Sec. 4.3, Multichannel based DPD was discussed for DFB-SSMF and MM-VCSEL-MMF based RoF links were linearized. Sec. 4.5 proposed a real time DPD approximation. In Table 4-8, Single channel DPD improvement is shown for SM-VCSEL-SSMF, MM-VCSEL-MMF and DFB-SSMF for NMSE, ACPR and EVM with and without DPD

using $K = 3$ and $Q = 2$. In Table-4.9, dual channel DPD is shown for DFB-SSMF and MMVCSEL-MMF RoF link cases.

<i>Model</i>	<i>SM-VCSEL-SSMF</i>			<i>MM-VCSEL-MMF</i>			<i>DFB-SSMF</i>		
	<i>NMSE (dB)</i>	<i>ACPR (dBc)</i>	<i>EVM (%)</i>	<i>NMSE (dB)</i>	<i>ACPR (dBc)</i>	<i>EVM (%)</i>	<i>NMSE (dB)</i>	<i>ACPR (dBc)</i>	<i>EVM (%)</i>
<i>Without DPD</i>	-19.86	-20	6.8	-17.63	-22.04	6.45	-19.10	-27.25	8.2
<i>With GMP</i>	-41.548	-44	4.7	-33.18	-36	2.1	-40.14	-47.62	1.9
<i>With MP</i>	-31.25	-35	3.4	-30.14	-29	3.4	-35.15	-44.56	2.36

Table 4-8: Linearization performance for an input power of 0 dBm for all cases (single channel)

<i>Model</i>	<i>DFB-SSMF</i>			<i>MM-VCSEL-MMF</i>		
	<i>NMSE (dB)</i>	<i>ACPR (dBc)</i>	<i>EVM (%)</i>	<i>NMSE (dB)</i>	<i>ACPR (dBc)</i>	<i>EVM (%)</i>
<i>W/O DPD</i>	-19.86	-21.84/-24.03	8.4/9.1	-17.63	--22/-25	7/7.1
<i>With GMP</i>	-41.548	-30.53/-30.81	2.5/3.6	-33.18	-30/-31	3.5/3.4
<i>With DVR</i>	-31.25	-39/-41.53	1.71/1.59	-30.14	-39/-41	2.3/2.4

Table 4-9: Linearization performance for an input power of 0 dBm for all cases (dual channel)

References

- 4.1 K. Y. Lau, "RF transport over optical fiber in urban wireless infrastructures," in IEEE/OSA Journal of Optical Communications and Networking, vol. 4, no. 4, pp. 326-335, April 2012.
- 4.2 Y. Shi ; D. Visani ; C.M. Okonkwo ; H. Yang ; H.P.A. van den Boom ; G. Tartarini ; E. Tangdiongga ; A.M.J. Koonen "First demonstration of HD video distribution over large-core POF employing UWB for in-home networks," 2011 Optical Fiber

- Communication Conference and Exposition and the National Fiber Optic Engineers Conference, pp 1-3 (2011)
- 4.3 Y. Shi et al., "Ultrawideband Signal Distribution Over Large-Core POF for In-Home Networks," in *Journal of Lightwave Technology*, vol. 30, no. 18, pp. 2995-3002, Sept.15, 2012.
- 4.4 D. Visani, G. Tartarini, M. N. Petersen, L. Tarlazzi and P. Faccin, "Link Design Rules for Cost-Effective Short-Range Radio Over Multimode Fiber Systems," in *IEEE Transactions on Microwave Theory and Techniques*, vol. 58, no. 11, pp. 3144-3153, Nov. 2010
- 4.5 J. Nanni et al., "Modal noise in 850nm VCSEL-based radio over fiber systems for manifold applications," *Proc. Fotonica AEIT Italian Conference on Photonics Technologies*, Turin, 2015, pp. 1-4.
- 4.6 J. Nanni et al., "VCSEL-Based Radio-Over-G652 Fiber System for Short-/Medium-Range MFH Solutions," *IEEE/OSA J. Lightw. Technol*, vol. 36, pp. 4430-4437, Oct.1, 2018.
- 4.7 D. Visani et al.: Wired and wireless multi-service transmission over 1mm-core GI-POF for in-home networks, *Electron. Lett.*, vol. 47, pp.203-205, Feb. 2011
- 4.8 D. Visani et al., "3×2N-QAM Constellation Formats for DMT Over 1-mm Core Diameter Plastic Optical Fiber", *IEEE Photonics Technology Letters*, 23, pp. 768-770 (2011).
- 4.9 J. Weiss, "Analog Optical RF-Links for Large Radio Telescopes,"*IEEE BiCMOS and Compound Semiconductor Integrated Circuits and Technology Symposium (BCICTS)*, San Diego, CA, 2018, pp. 24-27. doi: 10.1109/BCICTS.2018.8551058
- 4.10 J. A. Tatum et al., "VCSEL-based interconnects for current and future data centers," *J. Lightw. Technol.*, vol. 33, no. 4, pp. 727–732, Feb. 15, 2015

- 4.11 C. Wang et al., "Machine Learning Detection for DMT Modulated 112-Gbps VCSEL-MMF Optical Interconnection," Asia Communications and Photonics Conference (ACP), Hangzhou, 2018, pp. 1-3.
- 4.12 W. P. Ng, T. Kanesan, Z. Ghassemlooy and C. Lu, "Theoretical and Experimental Optimum System Design for LTE-RoF Over Varying Transmission Span and Identification of System Nonlinear Limit," in IEEE Photonics Journal, vol. 4, no. 5, pp. 1560-1571, Oct. 2012.
- 4.13 S. F. Yu, "Nonlinear dynamics of vertical-cavity surface-emitting lasers," in IEEE Journal of Quantum Electronics, vol. 35, no. 3, pp. 332-341, March 1999.
- 4.14 A. Hekkala et al., "Predistortion of Radio Over Fiber Links: Algorithms, Implementation, and Measurements," in IEEE Transactions on Circuits and Systems I: Regular Papers, vol. 59, no. 3, pp. 664-672, March 2012.
- 4.15 Mateo, C., Carro, P.L., Garca-Dcar, P., De Mingo, J., Salinas, I.: Radio-overfiber linearization with optimized genetic algorithm CPWL model. Opt. Express. 25(4). pp. 3694-3708, Feb. 2017.
- 4.16 M. U. Hadi, P. A. Traverso, G. Tartarini, O. Venard, G. Baudoin and J. Polleux, "Digital Predistortion for Linearity Improvement of VCSEL-SSMF-Based Radio-Over-Fiber Links," in IEEE Microwave and Wireless Components Letters, vol. 29, no. 2, pp. 155-157, Feb. 2019. doi: 10.1109/LMWC.2018.2889004
- 4.17 M. Abi Hussein, V. A. Bohara and O. Venard, "On the system level convergence of ILA and DLA for digital predistortion," 2012 International Symposium on Wireless Communication Systems (ISWCS), Paris, 2012, pp. 870-874.
- 4.18 D. Morgan, Z. Ma, J. Kim, M. Zierdt, and J. Pastalan, "A generalized memory polynomial model for digital predistortion of rf power amplifiers," Signal Processing, IEEE Transactions on, vol. 54, no. 10, pp. 3852–3860, Oct. 2006.
- 4.19 L. Ding, G. Zhou, D. Morgan, Z. Ma, J. Kenney, J. Kim, and C. Giardina, "A robust digital baseband predistorter constructed using memory polynomials," Communications, IEEE Transactions on, vol. 52, no. 1, pp. 159–165, Jan. 2004.

- 4.20 Hekkala, A., Lasanen, M.: ‘Performance of adaptive algorithms for compensation of radio over fiber links’. Proc. IEEE Wireless Telecommunication Symp., Prague, Czech Republic, April 2009, pp. 1–5
- 4.21 D. Morgan, Z. Ma, J. Kim, M. Zierdt, and J. Pastalan, “A generalized memory polynomial model for digital predistortion of rf power amplifiers,” *Signal Processing, IEEE Transactions on*, vol. 54, no. 10, pp. 3852–3860, Oct. 2006.
- 4.22 3GPP TS36.104 V15.2.0, Evolved Universal Terrestrial Radio Access (E-UTRA) User Equipment (UE) Radio Transmission and Reception (Release 15), March 2018.
- 4.23 L. C. Vieira and N. J. Gomes, "Experimental demonstration of digital predistortion for orthogonal frequency-division multiplexing-radio over fibre links near laser resonance," in *IET Optoelectronics*, vol. 9, no. 6, pp. 310-316, 12 2015. doi: 10.1049/iet-opt.2014.0160
- 4.24 Muhammad Usman Hadi, Hyun Jung, Salman Ghaffar, Pier Andrea Traverso, Giovanni Tartarini, Optimized digital radio over fiber system for medium range communication, *Optics Communications*, Volume 443, 2019, Pages 177-185, ISSN 0030-4018, <https://doi.org/10.1016/j.optcom.2019.03.037>.
- 4.25 Hadi, M., Hadi, M., Aslam, N., et al. (2019). Experimental Demonstration of MASH Based Sigma Delta Radio over Fiber System for 5G C-RAN Downlink. *Journal of Optical Communications*, 0(0), pp. -. Retrieved 23 Feb. 2019, from doi:10.1515/joc-2019-0011
- 4.26 P. M. Sevilá, V. Almenar, and J. L. Corral, “Transmission Over SSMF at 850 nm: Bimodal Propagation and Equalization,” *IEEE/OSA J. Lightw. Technol.*, vol. 35, no. 19, pp. 4125–4136, Oct 2017
- 4.27 G. Meslener, “Chromatic dispersion induced distortion of modulated monochromatic light employing direct detection,” *IEEE J. Quantum Electron.*, vol. QE-20, no. 10, pp. 1208–1216, Oct. 1984.

- 4.28 A. Zhu, Decomposed Vector Rotation-Based Behavioral Modeling for Digital Predistortion of RF Power Amplifiers. *IEEE Trans. Microw. Theory Tech.*, 63(2), 737-744, 2015
- 4.29 C. Kantana, et al., "Comparison of GMP and DVR models," 2018 INMMIC, Brive La Gaillarde, 2018, pp. 1-3
- 4.30 M.U. Hadi, J. Nanni, O. Venard, G. Baudoin, J. Polleux, P.A. Traverso, G. Tartarini "Linearity Improvement of VCSELs based Radio over Fiber Systems utilizing Digital Predistortion", *Advances in Science, Technology and Engineering Systems Journal*, vol. 4, no. 3, pp. 156-163 (2019).
- 4.31 Zhu, R., Zhang, X.: Broadband predistortion circuit design for electro-absorption modulator in radio over fiber system. In *Proceedings of the Optical Fiber Communications Conference and Exhibition(OFC)*, San Francisco, CA, USA (2014).
- 4.32 S. Bassam, "Advanced signal processing techniques for impairments compensation and linearization of SISO and MIMO transmitters," Doctor Dissertation, 2010.
- 4.33 S. A. Bassam, et al., "2-D digital predistortion (2-D-DPD) architecture for concurrent dual-band transmitters," *Microwave Theory and Techniques, IEEE Transactions on*, vol. 59, pp. 2547-2553, 2011.
- 4.34 S. A. Bassam, et al., "Linearization of concurrent dual-band power amplifier based on 2D-DPD technique," *Microwave and Wireless Components Letters, IEEE*, vol. 21, pp. 685-687, 2011. [6] H. Ku and J. S. Kenney, "Behavioral modeling
- 4.35 T. Eriksson and C. Fager, "Digital predistortion of concurrent multiband communication systems," 2014 *IEEE International Conference on Acoustics, Speech and Signal Processing (ICASSP)*, Florence, 2014, pp. 3918-3922.

Chapter 5

Experimental Evaluation of Digital Radio over Fiber

System

This chapter is based on the results published in journals [J3] and [J4].

The utilization of Analog Radio over Fiber System is prone to nonlinearities. In previous chapters it was discussed critically that how these links can be linearized. However, these linearization techniques have limitations. Therefore, as an example of the other possible solutions, Digital Radio over fiber system has been realized and discussed in detail.

5.1 Introduction

The use of Radio over Fiber technology has been growing to meet the demand of high bandwidth wireless services. Radio over Fiber has been regarded as an enabling technology for next generation networks, e.g. 5G. The primary aim of RoF is to provide a cost-effective efficient solution of distributing radio signals from a base station (BS) to remote antenna units (RAU). There have been many adaptations of RoF having their own advantages and disadvantages. Analog RoF (A-RoF) provides the least complex solution, however, it is susceptible to the nonlinearities coming from optical and microwave parts. It appears that intermodulation noises occur when sub-carrier multiplexing (SCM) is applied to A-RoF, both at the transmitter and receiver [5.1-5.3].

The recent technological advances in analog to digital converter (ADC) and digital to analog converter (DAC) have made it possible to push the functionalities of these converters closer to the base station, hence, enabling the receiver and transmitter functions to be performed in the digital domain. Figure 5.1 shows such a BS system architecture in which optical transmission of the analog signal is first digitized and then transporting it over the fiber.

In the digitized RoF link, firstly, the analog RF signal is converted to a digital signal through an ADC and is transmitted over the optical fiber. The optical signal is detected at the receiver side and is converted back to the analog domain using a digital to analog converter (DAC). When carrier frequencies and baud rates are high, the cost and power-hungry ADC/DAC requirements become prohibitively large. In addition, transmitting digital samples compared to an analog signal results in a lower spectral efficiency. However, digital transmission of data alleviates the detrimental effects of noise and non-linearities at transmitter and at receiver [5.2].

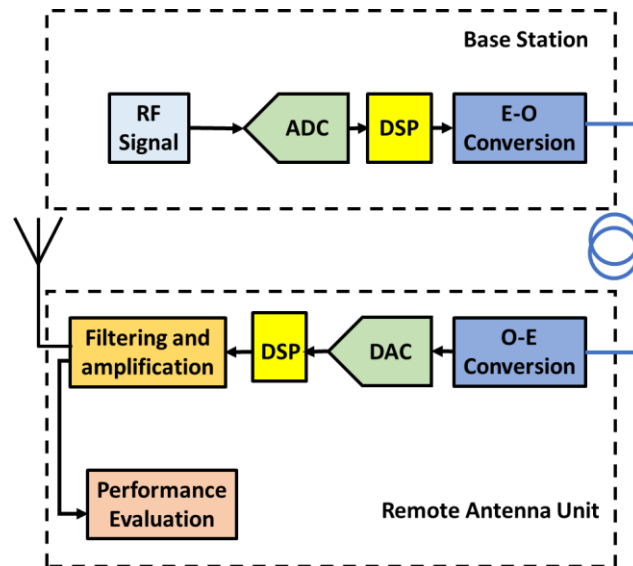


Figure 5.1: Block diagram of D-RoF system

5.2 Background-Digital Radio over Fiber

Digital Radio over Fiber has been evidenced primarily in [5.4] where a high-speed ADC was designed for the transmission of radio frequency signals over a digitally modulated optical fiber. As a part of literature review, the main contributions towards D-RoF are discussed below.

- **Wala et al.1993** In 1993, Wala et al. was a pioneer of implementing high speed ADC for digital transmission of radio frequency. The novel digital RF transport technology application was discussed, and performance was compared with A-RoF. Digital RoF demonstrated dynamic range better than their analog counterparts. It was shown that D-RoF has an insensitive BER to the fiber length up to 50 Km [5.4].

- **Gamage et al. 2009** Experimental analysis was presented for digitized RF transport over fiber link. Experimental results were presented for a digitized RF-over-fiber link using bandpass sampling for 6 MS/s 16 QAM modulation of an RF carrier of 1 GHz [5.5-5.6].
- **Yang et al. 2009** Novel evaluation of the link performance was done for different digitization resolutions, carrier frequencies, symbol rates and sampling frequencies. This was the first realistic demonstration on FPGA [5.7].
- **Yang et al. 2010** Unidirectional transmission of a digitized SCM RF signal composed of three QPSK modulated signals over an optical link using CW carrier is presented. It has been shown that the DAC may be used for recovering the digitized signal at different frequencies without a mixer and without a local oscillator [5.8].
- **D. Wake et al. 2010** It was shown that noise introduced by the RoF links does not have a significant impact on wireless range if the wireless system has uplink power control. It was shown that digitized radio transmission is the optimum choice from a cost perspective [5.9].
- **Ghafoor et al. 2012** Digitized duplex transmission for 64-QAM modulation was proposed. Bidirectional data transmission is achieved over a single 25 km optical fiber using a single optical pulsed source on VPI transmission maker [5.10].
- **Li et al. 2015** A new compression algorithm was proposed that is able to achieve 3 times higher spectral efficiency than CPRI. 30-35dB input dynamic range was demonstrated for 64 QAM 20 MHz LTE signal. This work also investigated the latency caused by the digital signal processing. It was shown that the delay is less than 2 microseconds on the FPGA boards to transmit and receive [5.11].

5.2.1 Band Pass Sampling

The principle of bandpass sampling is discussed in this section. The Nyquist sampling criteria suggests that in order to recover the analog signal from the sampled data, the sampling rate should at least be equal or higher than twice of the maximum frequency in the analog signal. This suggests that for RF signals having carrier frequencies in the GHz range, the nyquist criteria

suggests a sampling rates excessively high. This will result in very complex and expensive designs of the ADC/DAC which are not viable economically.

Since, the Nyquist/Shannon sampling criterion requires a very high sampling frequency for digitizing a modulated radio signal with a bandwidth B and a carrier frequency f_c in the GHz range. This would necessitate very high-speed electronics which should operate at least at twice $(f_c + \frac{B}{2})$ Hz. However, band-pass sampling, which relies on the pioneering work in [5.12], overcomes this practical issue, relaxing the constraints on the ADC/DAC performance in D-RoF systems [5.13].

The bandpass sampling technique has been proposed in [5.14-5.15] which solves the need of high sampling rate. Since most of the wireless signals have a limited bandwidth that is lower than the center frequency, the bandpass sampling technique ensures that the sampling rate is dependent on the bandwidth of the analog signal instead of its highest frequency. Sampling of an analogue signal generates a spectrum composed of spectral lobes at multiples of the sampling frequency [5.16]. If the sampling frequency is chosen by ensuring that the multiple copies of the original spectrum do not overlap in the frequency domain, then the original signal may be recovered by using a bandpass filter [5.14-5.15].

In Figure 5.2, the spectrum of the signal along its sampled version is depicted. It can be observed from Figure 5.2 that the sampled signal has a spectrum that contains the original signals spectrum repeated periodically at the multiples of the sampling frequency. The frequency spectrum is divided into multiple Nyquist zones, each having a width equal to half the sampling frequency. It may be observed from Figure 5.2 that in order to avoid overlapping among the different spectral, the sampling frequency has to be sufficiently high. In case the sampling frequency used is insufficiently high, the different spectral replicas will overlap, which gives rise to aliasing. In the next section, we derive the values of the sampling frequencies, which will allow us to avoid aliasing.

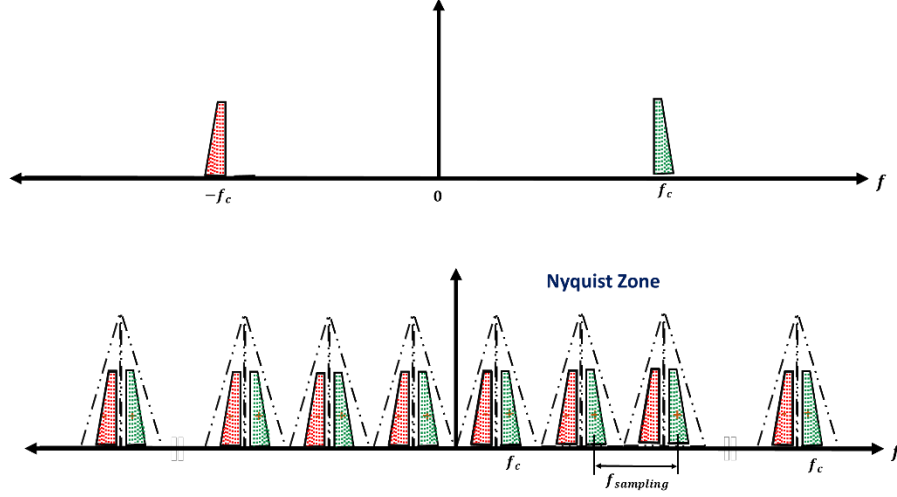


Figure 5.2: Spectrum of the signal along its sampled version

The Nyquist/Shannon sampling criterion requires a very high sampling frequency for digitizing a modulated radio signal with a bandwidth B and a carrier frequency f_c in the GHz range. This would necessitate very high-speed electronics which should operate at least at twice $(f_c + \frac{B}{2})$ Hz. However, band-pass sampling, which relies on the pioneering work in [5.14], overcomes this practical issue, relaxing the constraints on the ADC/DAC performance in D-RoF systems [5.15]. In Figure 5.2(a), the sampling requirements under bandpass sampling are depicted as per IEEE 802.16-2004 WiMAX (Worldwide Interoperability for Microwave Access) standard. The symbol rate is set to 16 MSymbols/s and carrier frequency f_c is 2.475 GHz with 20 MHz of bandwidth. In bandpass uniform sampling, the sampling frequency f_s must satisfy the following criteria in order to avoid spectral aliasing:

$$2 \frac{f_H}{N} \leq f_s \leq 2 \frac{f_L}{N-1} \quad (5.1)$$

$$1 \leq N \leq I_s \left[\frac{f_H}{f_H - f_L} \right] \quad (5.2)$$

where f_H is the highest and f_L is the lowest frequency of the band to be sampled. N is an integer, while $(f_H - f_L)$ is the bandpass signal bandwidth. I_s is the floor function which returns upper rounding to integer of the ratio $\left[\frac{f_H}{f_H - f_L} \right]$. By employing bandpass sampling, many replicas of bandpass signal can be obtained as shown in Figure 5.2(b). Since a 13 MHz wide guard-band

is kept on the both sides of the central frequency, ensuring to avoid spectral aliasing due to critical bandpass sampling, the total channel bandwidth becomes 46 MHz. Thus, the practical values to be considered for f_H and f_L are 2.498 GHz and 2.452 GHz respectively. The critical sampling frequency is $2 \times 46 = 92$ MSa/s. According to (5.2), and for the signal considered, N can take an integer value between 1 and 54. If N is chosen as 39, the bandpass sampling frequency f_S yields 128 MSa/s, which is a slightly higher rate than the critical sampling. Assuming the use of a low-cost, low-power 8-bit ADC the bit rate results to be 1.024 Gbps.

Note that a lower bit rate, i.e. a higher spectral efficiency, could be advantageously achieved through the introduction of appropriate signal processing stages (see e.g. the solution proposed in [5.13]). However, as specified in the Introduction, aim of this work is to demonstrate the capability of the proposed Digital Radio over Fiber system to cover lengths up to 70 km. In terms of spectral efficiency, this solution represents a slight improvement with respect to CPRI, which transmits the same 20 MHz LTE signal with 1.2288 Gbps instead of the 1.024 Gbps when utilized.

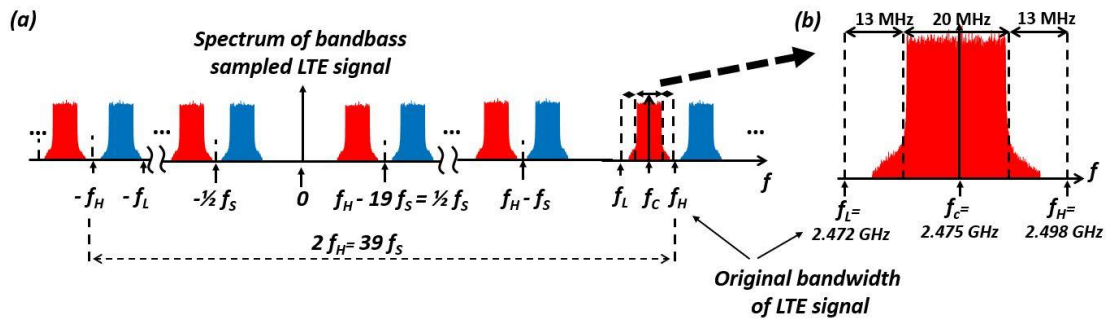


Figure 5.3: Schematic illustration of (a) Frequency spectrum of the bandpass sampled LTE signal (b) Original Bandwidth, of the same LTE signal, including guard bands.

5.3 Signal Impairments in D-RoF Link

There can be multiple components in a D-RoF link that can cause signal impairments. In this section, we will identify components wise the signal degradation that occurs in different stages of the D-RoF link.

5.3.1 Signal Impairments in ADC

Digital RoF systems utilizes bandpass sampling technique in order to reduce the over heads caused by high sampling rates. The ADC in such systems uses the bandpass sampling technique.

The important design consideration for the ADC is that they should effectively operate on the highest frequency component of the pass-band signal while sampling the pass-band signal at a sampling rate greater or twice the message bandwidth. Therefore, it is assumed that the analog bandwidth and sampling rate of the ADC used in our experiment satisfy both the criteria required for sampling a pass-band signal.

The main functionalities of ADC are shown in Figure 5.4. Indeed, the sampling rate is reduced by utilizing the band pass sampling technique, however, the sampling frequency has to be chosen smartly in order to avoid harmful spectral aliasing. Similarly, out of band noise can alias in to signal bandwidth and causes limitations to the ADC performance. Whenever a pass-band signal is subjected to bandpass sampling, the SNR of the sampled signal becomes degraded by at least the noise aliased from the bands between DC and the analog bandwidth of the ADC [5.16-5.17].

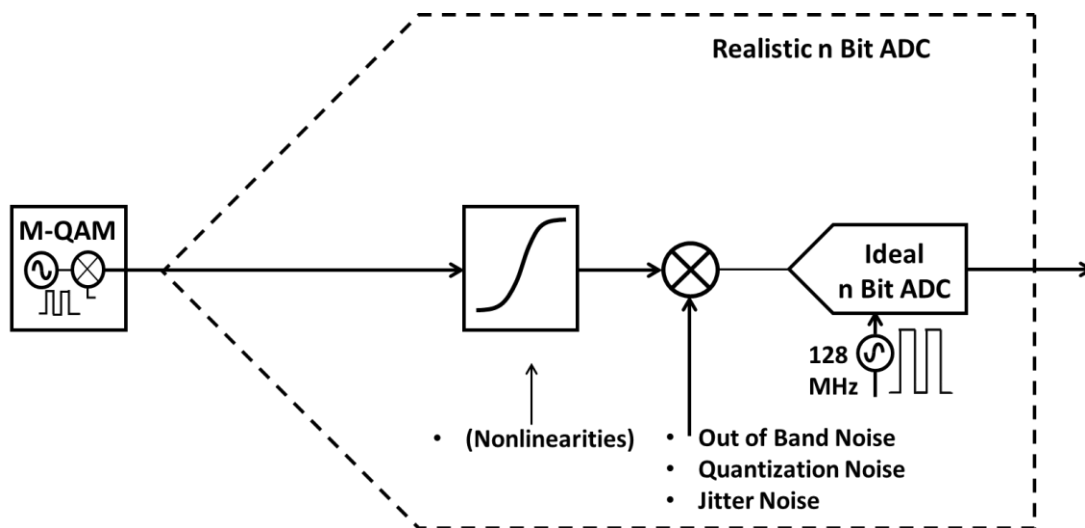


Figure 5.4: Schematic illustrating functions of the ADC

5.3.1.1 Signal to Noise Ratio (SNR) degradation in ADC

In this section, the SNR degradation in response to bandpass sampling is discussed. The bandpass filtering is done before digitization process. In this discussion, the noise is considered to be Additive White Gaussian Noise (AWGN).

5.3.1.2 Signal to Noise Ratio (SNR) degradation due to Quantization

The ADC output is a discrete function with a number of different states that are determined by the resolution of the device while its input is a continuous signal. Therefore, during this state conversion, it is possible that some information is lost and results in addition of distortion to the signal. This is regarded as quantization noise. The mean-square quantization noise power using single tone for an ideal quantizer is given by [5.18-5.19]:

$$Noise\ Power_{Quantization} = \frac{V_{peak}^2}{3 * L^2} \quad (5.3)$$

Here, V_{peak} represents the input peak voltage while L is the total number of quantization levels since $L = 2^n$ where n represents the resolution bits of ADC. The analog input mapping with respect to digital output code is shown below in Figure 5.5.

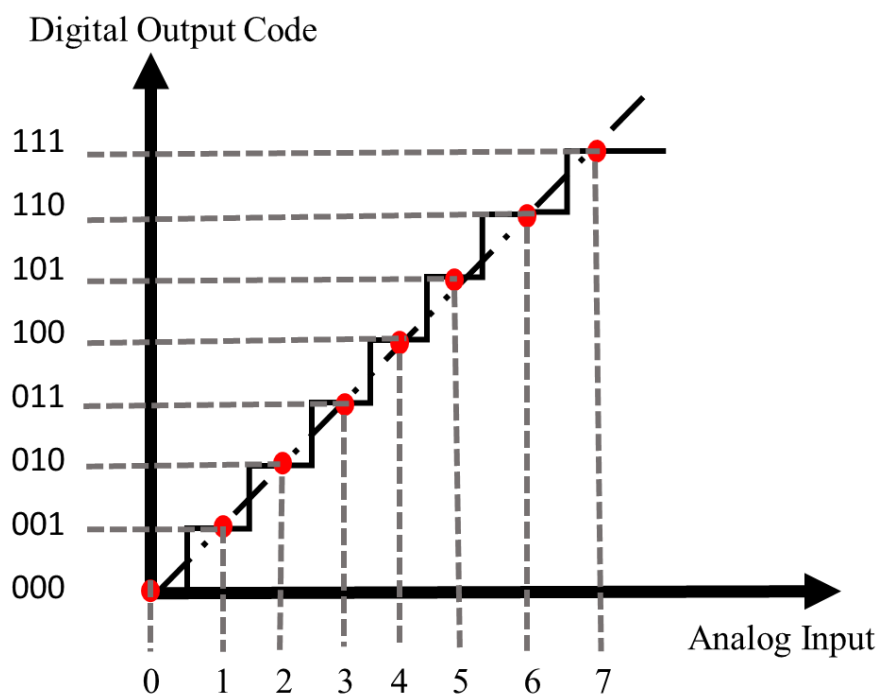


Figure 5.5: Schematic illustration of analog input mapping to digital output code

In general, signal to be quantized can be composed of many tones with different modulation formats. Since these modulation formats are multi levelled and can exhibit peak to average power ratio (PAPR), therefore, it is necessary to consider the PAPR of these signals. In the work done, we have used a QAM signal source with a particular modulation format, therefore, we write a general expression at this point for the reader understanding.

For M levels of QAM, PAPR can be written as:

$$PAPR = \frac{3(\sqrt{M} - 1)}{(\sqrt{M} + 1)} \quad (5.4)$$

where M -ary QAM signal has \sqrt{M} voltage levels. Assume that quantization errors are uniformly distributed and independent, SNR due to quantization noise can be written as follows:

$$SNR_{Quantization}(dB) = -10 \log_{10}(PAPR) + 6.02 * n + 10 \log_{10}(3) \quad (5.5)$$

where n represents the Number of Bits.

5.3.1.3 Signal to Noise Ratio (SNR) degradation due to out of band noise aliasing

In order to derive analytical formulation of SNR due to bandpass sampling, AWGN with zero mean is considered. It is assumed that with ideal bandpass filtering, ADC Resolution bits are high so out of band noise aliasing is due to thermal noise only. Total noise power is given as:

$$P_{Total-Noise-BPS} = P_{Noise-IN-BAND} + P_{Noise-Aliased} \quad (5.6)$$

where $P_{Noise-IN-BAND}$ is the in-band signal noise and $P_{Noise-Aliased}$ is aliased noise power.

$$P_{Noise-Aliased} = 2 \left(\frac{f_s}{2} \right) (N - 1) \left(\frac{N_{double-Thermal}}{2} \right) \quad (5.7)$$

where f_s is sampling frequency, N is integer and $N_{double-Thermal}$ is the noise power spectral density of double-sided thermal noise. $N_{double-Thermal}$ is given as:

$$N_{double-Thermal} = \frac{BT}{2} \quad (5.8)$$

Where B is the Boltzmann constant and T represents temperature in kelvin.

Therefore Eq. (5.6) becomes overall as:

$$P_{Total-Noise-BPS} = P_{Noise-IN-BAND} + (f_s)(N - 1) \left(\frac{BT}{4} \right) \quad (5.9)$$

Where $P_{Noise-IN-BAND}$ is given as:

$$P_{Noise-IN-BAND} = 2 \left(\frac{f_s}{2} \right) N * N_{double-Thermal} \quad (5.10)$$

$$P_{Noise-IN-BAND} = \left(\frac{f_s N B T}{2} \right) \quad (5.11)$$

Now Eq. (5.9) becomes:

$$P_{Total-Noise-BPS} = P_{Noise-IN-BAND} + P_{Noise-Aliased}$$

$$P_{Total-Noise-BPS} = \left(\frac{f_s B T}{2} \right) + \left(f_s * (N - 1) * \frac{B T}{4} \right) \quad (5.12)$$

SNR due to out of band pass sampling is given as:

$$SNR_{outofband} = \frac{P_{RF}}{P_{Total-Noise-BPS}} \quad (5.13)$$

Where P_{RF} represents signal power of the RF signal.

5.3.1.4 Signal to Noise Ratio (SNR) degradation due to Jitter Noise

Based on sampling theorems, it is expected to uniquely determine the input signal by the sampled data information. The effects of random errors on the nominal sampling time instant are commonly called timing jitter.

As explained before, there can be errors such as timing jitters that can arise due to band pass sampling. These timing jitters are caused by two main factors. They are enlisted as:

1. Aperture Jitter

2. Clock Jitter

Aperture jitter in the sample and hold circuit is the time delay between the sampled input and the actual time taken by the sampled analog input signal. Whereas, Clock Jitter is the random fluctuations in the period of clock [5.20-5.21].

Figure 5.6 depicts the effect of jitter. With the higher timing jitter, it will lead to higher voltage error in the sampled output version. It is clear from Figure 5.6 that this effect will be highly magnified with higher slew rates. There are three additional effects due to aperture and clock jitter listed below:

1. Increase in system noise floor.
2. Increase in the uncertainty in the actual sampled signal itself.
3. Inter-symbol interference [5.22-5.23].

In order to simplify the evaluation, let's assume that the aperture jitter and sampling clock jitter follow a Gaussian distribution with zero mean. The noise power due to jitter can be written as:

$$P_{jitter} = 2 \int \phi_s(f) \left[1 - e^{-\frac{(2\pi f)^2 \sigma_{jitter\ ADC}^2}{2}} \right] df \quad (5.14)$$

Here $\phi_s(f)$ represents power spectral density of signal while $\sigma_{jitter\ ADC}$ presents ADC jitter.

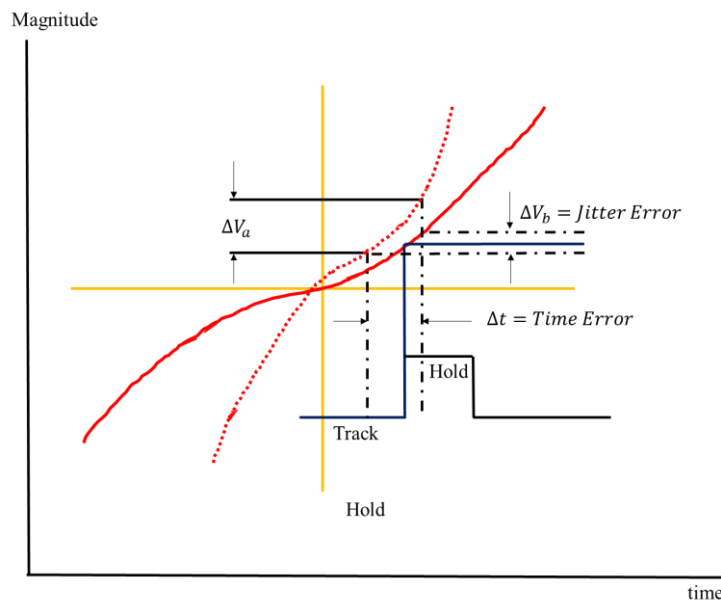


Figure 5.6: Schematic explaining the effect of jitter

SNR due to jitter is given as:

$$SNR_{ADC-jitter} = \frac{\int \phi_s(f) df}{2 \int \phi_s(f) \left[1 - e^{-\frac{(2\pi f)^2 \sigma_{jitter ADC}^2}{2}} \right] df} \quad (5.15)$$

In order to simplify this solution, it has been shown that modulated signal can be assumed to have a single carrier for the jitter noise calculations since it was shown in [30] that modulated carrier frequency is 10 times higher than the bandwidth signal i.e. $f_c > 10 * r_s(1 + \alpha)$. Since the magnitude change in the exponential term of the denominator of Eq. (5.15) is very small, therefore we can assume that $(2\pi f)^2 \sigma_{jitter ADC}^2 \ll 1$, hence the SNR due to jitter can be simplified to be:

$$SNR_{ADC Jitter}(dB) = -20 \log_{10}(2\pi f_c \sigma_{jitter ADC}) \quad (5.16)$$

5.3.2 Signal Impairments in DAC

Like ADC, DAC also has signal impairments that arise due to phase noise of the clock used in clocking the DAC. During this evaluation, the band pass modulated signal is treated as a single carrier for jitter calculations as given in [5.23,5.24]. Thus, the sampling clock jitter will follow a gaussian distribution with a zero mean. In order to derive the SNR degradation due to DAC, let's consider the block diagram of DAC in Figure 5.7. The simplified block diagram shown here first converts the streams of bits to sample values. These outputs are series of rectangular pulses with width equal to the inverse of the clock rate. That is the reason due to which DAC is mathematically modelled by a zero order hold (ZOH). ZOH is a circuit device whose response is a rectangular pulse with width equal to inverse of the sampling rate and its frequency spectrum is a sinc function. It was shown in P. Smith et al. [5.23] that the SNR of the DAC output is:

$$SNR_{DAC Jitter}(dB) = \frac{1}{\sigma_\theta^2} \left[\left(\frac{f_{clk}}{f_{sig}} \right) \right]^2 \quad (5.17)$$

where phase noise $\sigma_{\theta} = 2\pi f_{clk} \sigma_{jitter\ ADC}$, f_{clk} and f_{sig} represents clock and signal frequency respectively. Since the frequency response of the ZOH is a sinc function, it is attenuated due to jitter noise at higher frequencies and this effect will impart the expression given above in Eq. (5.17). Therefore, the new expression becomes:

$$SNR_{DAC\ Jitter} (dB) = \frac{1}{\sigma_{\theta}^2} \frac{\pi^2}{\left[\sin\left(\frac{\pi f_{sig}}{f_{clk}}\right) \right]^2} \quad (5.18)$$

$$SNR_{DAC\ Jitter} (dB) = -20 \log_{10} \left(2\pi f_c \sigma_{jitter\ DAC} \right)^{-2} \left[\text{sinc}\left(\frac{f_{sig}}{f_{clk}}\right) \right]^{-2} \quad (5.19)$$

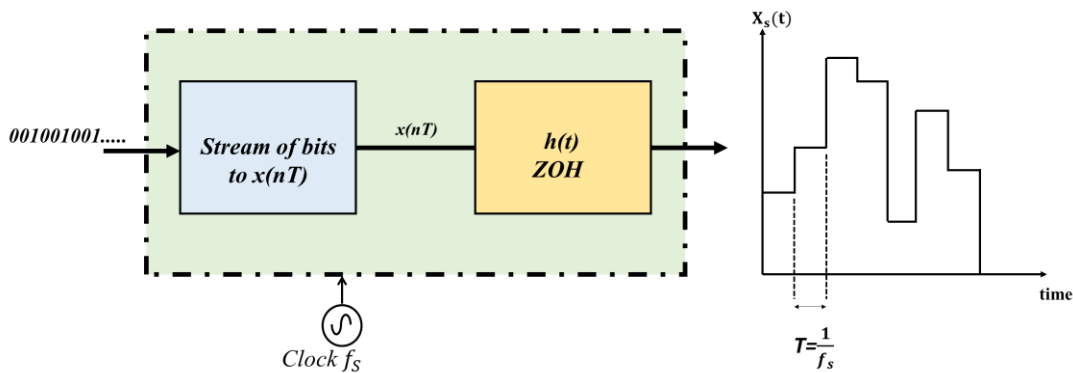


Figure 5.7: Schematic for DAC

5.3.3 Optical Link Noise

Apart from Noise sources in ADC and DAC, there are other noise sources like the one in optical link. These impairments arise due to optical channel noise. While deriving its expression, it is assumed that degradation is caused due to thermal noise. For such a receiver which is limited by the thermal noise, the Quality factor has been represented as:

$$Q = \left[\frac{1-r}{1+r} \right] \cdot \mathcal{R} * \frac{P_{avg}}{I_{thermalnoise}} \quad (5.20)$$

Where r represents the ratio between the received currents of two bits respectively, \mathcal{R} shows the responsivity of the photodiode, P_{avg} is the received optical power at the photodetector and $I_{thermalnoise}$ represents the current for the thermal noise. The Bit Error Rate (BER) is given as follows:

$$BER = \frac{e^{-\frac{Q^2}{2}}}{\sqrt{2\pi}(Q)} \quad (5.21)$$

The Bit errors that arise in the optical channel, they cause additional errors to analog signals during the reconstruction phase. Thus, adding noise to the reconstructed analog signal. Therefore, the optical BER named as $BER_{optical}$ becomes [5.25-5.26]:

$$BER_{Optical} = V_{peak}^2(L^2 - 1) * 4 * \frac{BER}{3 * L^2} \quad (5.22)$$

Therefore, the $SNR_{opticallink}$ becomes:

$$SNR_{opticallink} = \frac{P_s}{BER_{optical}} \quad (5.23)$$

5.3.4 Total Link Noise

In the discussion above, we have discussed in detail major components of noise that may arise in Digital RF optical link. The total link noise can therefore be expressed by summation of all these noise element by element. Figure 5.8 shows the noise sources in the digital link at each stage. The total SNR can be expressed as:

$$SNR_{LINK} = [SNR_{Quantization} + SNR_{outofband} + SNR_{ADCjitter}]_{ADC} + SNR_{opticallink} + SNR_{DACjitter} \quad (5.24)$$

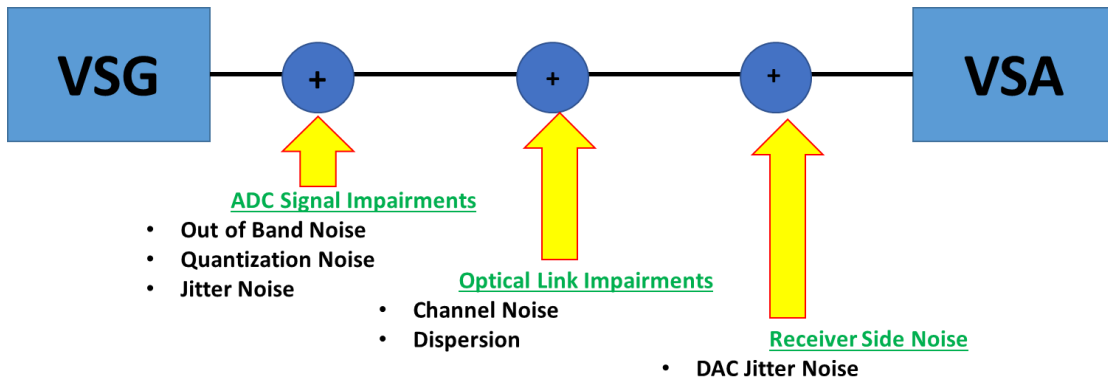


Figure 5.8: Block diagram of noise sources at different stages of the D-RoF link

Table 5.1 lists the mathematical expressions used for modelling the types of noise due to ADC and DAC. The values of the ADC and DAC RMS jitter, $\sigma_{jitter\ ADC}$ and $\sigma_{jitter\ DAC}$, respectively, are taken from the specifications of the Digital Sampling Oscilloscope utilized in the experimental part described in Section 5.6.

Table 5-1: Summary of different noise sources, with their expression and assumptions

<p>ADC: <i>Jitter Noise</i></p>	<p>$SNR_{ADC\ Jitter}(dB)$ $= -20 \log_{10}(2\pi f_c \sigma_{jitter\ ADC})$ where $f_c = 2.475\ GHz$; $\sigma_{jitter} = 0.8\ ps$</p>	<p>Assuming that: The ADC sampling clock Jitter has a zero mean with gaussian distribution.</p>
<p>ADC: <i>Quantization Noise</i></p>	<p>$SNR_{Quantization}(dB)$ $= -10 \log_{10}(PAPR)$ $+ 6.02 * n + 10 \log_{10}(3)$ where $PAPR = \frac{3(\sqrt{M}-1)}{\sqrt{M+1}}$; $M = 64$; $n =$ <i>Number of Bits</i></p>	<p>Assuming that: Quantization errors are: a) Uniformly Distributed. b) Independent</p>
<p>ADC: <i>Out of Band Noise Aliasing</i></p>	<p>$SNR_{OB-NoiseAliasing}(dB) = \frac{2P_s}{Nf_sKT}$ where $P_s =$ output power of RF modulated signal; $N =$ integer referred to Nyquist zones; $f_s =$ Sampling Frequency ; $K =$ Boltzman constant; $T =$ Temperature in Kelvin</p>	<p>Assuming that: ADC Resolution bits are high so out of band noise aliasing is due to thermal noise only.</p>
<p>DAC: <i>Signal Degradation due to DAC jitter noise</i></p>	<p>$SNR_{DAC\ Jitter}(dB)$ $= -20 \log_{10}(2\pi f_c \sigma_{jitter\ DAC})^{-2}$ $* \left[\text{sinc} \left(\frac{f_c}{f_s} \right) \right]^{-2}$</p>	<p>Assuming that: The band pass modulated signal is treated as a single carrier for jitter calculations.</p>

	where $f_c = 2.475 \text{ GHz}$; $f_s = 128 \text{ MHz}$; $\sigma_{\text{jitter ADC}} = 0.8 \text{ ps}$	
--	--------------------------------------------------------------------------------------------------------------	--

5.4 Analytical model for D-RoF systems

The D-RoF link proposed has been realized by means of VPI Transmission Maker. Figure 5.9 presents the block diagram of the system, where the main functionalities of the different blocks are specified, together with the list of the non-idealities taken into account.

The 64 QAM RF signal is fed into the ADC with n bits of resolution which performs the digitization using the bandpass uniform sampling technique. Quantization, and coding functions are performed by this block. Through quantization, the discretization of the continuous signal is performed with respect to ADC resolution giving it a new representation in discrete-time and amplitude domain.

The quantized signal is then converted to a binary sequence and subsequently encoded using a NRZ (non-return to zero) encoder. Then, this stream of bits modulates a Distributed Feed Back (DFB) laser diode. The modulated optical carrier is transported over an optical channel of standard single mode fiber (SSMF) and is then detected by a photoreceiver, based on a PIN photodetector. The output data received are then fed into a digital signal processor (DSP) that recovers the digital data stream, which in turn goes to the DAC for normalization, decoding and signal reconstruction operations. Finally, this reconstructed signal is fed to a Performance Evaluator block, which computes SNR, EVM and Eye Opening Penalty (EOP).

Different kinds of noise are generated in the ADC. First of all, whenever a bandpass signal is bandpass sampled out of the band, noise aliases into the Nyquist zones [5.26-5.29]. Moreover, the ADC can introduce quantization and jitter noise into the link. The quantization noise is determined by the resolution bits of the ADC while jitter noise can be due both to the ADC itself

(aperture jitter) and to the sampling clock. Considering the receiver side, the DAC is in turn subject to jitter noise which is due to the phase noise of the clock utilized.

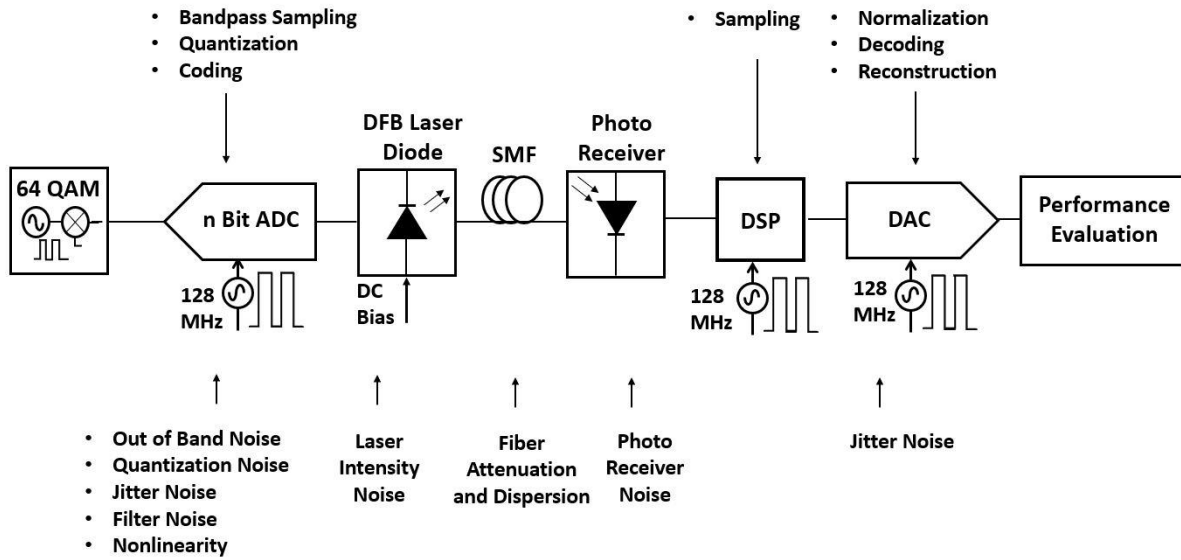


Figure 5.9: Block Diagram of the D-RoF link considered, evidencing the main functionalities of the signal-processing components and the non-idealities taken into account in the model.

Signal Degradation that arises due to bandpass sampling, clock jitter noise and quantization noise are weakly correlated, and these noise sources can then be assumed to be independent [5.27]. Mean of the bandpass sampling, jitter and quantization noises are zero. Furthermore, DAC jitter noise is due to the clock jitter can be assumed to be independent of both optical link and ADC.

The resolution of the ADC should ensure that quantization error is uniformly distributed. This means that SNR due to quantization noise should be higher than SNR due to jitter noise [5.12]:

$$SNR_{Quantization} > SNR_{jitter} \tag{5.25}$$

Equation (5.25) can be expanded in the following form:

$$-10 \log_{10}(PAPR) + 6.02 * n + 10 \log_{10}(3) > -20 \log_{10}(2\pi f_c \sigma_{jitter}) \tag{5.26}$$

In (5.26), **PAPR** is the Peak to Average Power Ratio and amounts to 8.1 dB while f_c is 2.475 GHz and σ_{jitter} that represents the ADC RMS jitter is 0.8 psec. By considering these values in (5.26), we selected $n = 8$, as the optimal resolution for the ADC.

The impairments associated with the Analog to Digital Conversion operation include also the introduction of nonlinearities. These are taken into account by assuming the ADC as composed by an ideal device to which the different noise contributions are added, and which is preceded by a nonlinear block accounting for the distortion introduced by the real ADC. Such nonlinear block has been set in the model in the form of a truth table, extrapolated from the behavior of the real ADC utilized for the experimental test. The causes of non-ideal behavior introduced in the D-RoF system by the optical link which were taken into account in the model consist in the Intensity Noise of the DFB laser, in the attenuation and chromatic dispersion of the optical fiber, and in the presence of shot and thermal noise at the photodetector. The corresponding characteristics are listed in Table 5-2.

Table 5-2: Parameters utilized in the simulation of the Optical Link

Optical Link Component	Parameters Values
Laser	Wave Length= 1550 nm Average Power= 10 mW Line Width= 16e6 Hz $I_{Bias} = 40 \text{ mA}$ $I_{Threshold} = 10 \text{ mA}$ RIN = -130 dB/Hz
Fiber	Dispersion= $16 \frac{ps}{nm \cdot km}$ Length= up to 70 km Attenuation= $0.2 \frac{dB}{km}$
Photo-detector	Responsivity 0.6 A/W Shot Noise (computed assuming $I_{Dark} \sim 0 \text{ mA}$) Thermal Noise (Computed assuming= 290°K)

5.4.1 Performance Results

In the present section, the performance of the D-RoF system proposed will be compared with the performance of an A-RoF system. The A-RoF system considered is practically composed by the block diagram represented in Figure 5.1 once the ADC, DSP and DAC blocks are removed. This means that the 64 QAM RF signal directly modulates the DFB laser diode, and that the Performance Evaluator block is placed immediately after the photo receiver.

Figure 5.10 evaluates the EVM performance of the two RoF methodologies with respect to fiber length. Input Power P_{IN} is set at level 0 dBm. The trend of the A-RoF curve shows that with the increase in the fiber length, there is a significant rise in the value of EVM for A-RoF. Indeed, for lengths greater than 60 km the A-RoF link exceeds the 3GPP threshold of EVM=8%, while the D-RoF link maintains a value of EVM lower than 3% over the whole range of lengths considered, which is well below the 3GPP limit. Figure 5.10 also shows the 64-QAM received constellations in both architectures for $L=70$ km, allowing to appreciate that the received symbols are more scattered in the A-RoF case with respect to the D-RoF one, and confirming that the latter is less affected by the causes of impairments present in the system.

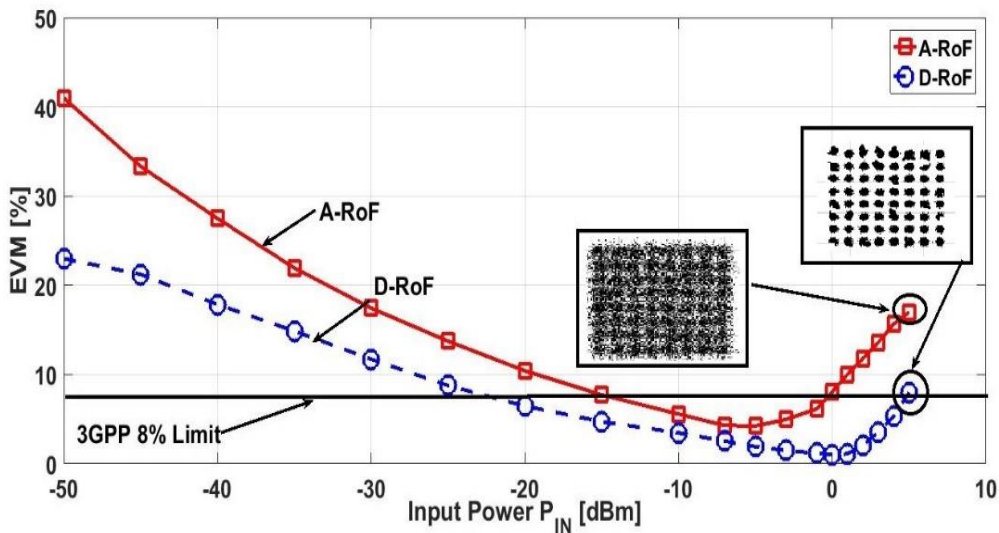


Figure 5.10: Values of EVM vs RF input power are illustrated for both the Analog and the Digital RoF systems analyzed. PDSCH (Physical Downlink Shared Channel) constellations at $P_{IN} = 5$ dBm are shown as well.

In order to evaluate the dynamic range of the two architectures, the EVM performance is evaluated with varying input powers. Since, in Figure 5.10, the EVM for 0 dBm input power for 60 km is equal or less than 8% for both, A-RoF and D-RoF, the length is fixed to 60 km. Figure 5.11 shows then for this value of the link length the EVM estimation for varying input powers.

With reference to both systems a qualitatively similar behaviour can be observed. Initially, for increasing values of the input RF power, the values of EVM tend to decrease, since the power of the useful signal increases with respect to the power of the noise contributions. Once a minimum value of EVM is reached (for $P_{IN} \sim -5\text{dBm}$ and for $P_{IN} \sim 0\text{dBm}$ in the A-RoF and D-RoF cases, respectively), the value of EVM starts to exhibit a positive slope with respect to increasing values of P_{IN} . This last behaviour is due to the insurgence of distortion terms generated within either of the two systems.

In the case of the A-RoF link the spurious terms which determine an increase of EVM for $P_{IN} > -5\text{dBm}$ are due to the fact that relatively high PAPR of the modulating signal causes the DFB laser to go below threshold determining a distortion in the signal transmitted over the optical carrier.

In the case of the D-RoF link, the increase of EVM for $P_{IN} > 0\text{dBm}$ are caused by the nonlinearities of the ADC, which, as mentioned above, are taken into account through the introduction of an appropriate nonlinear block realized in the form of truth table, which precedes an ideal ADC.

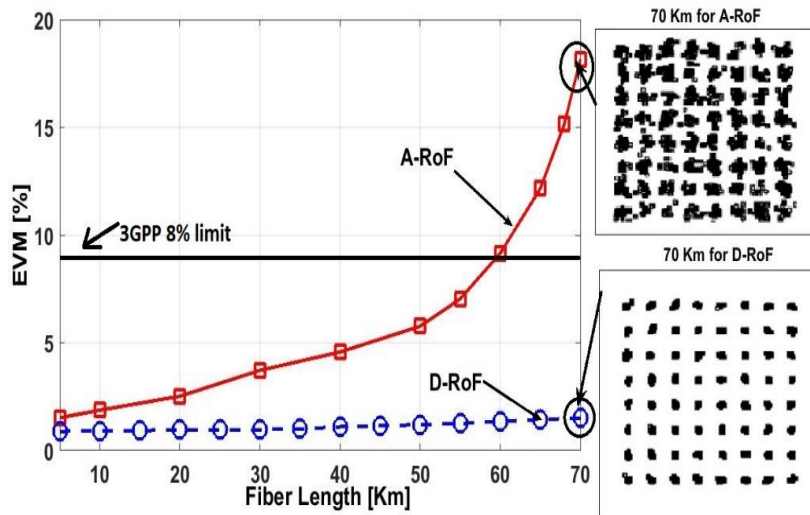


Figure 5.11: Values of EVM vs fiber length L are illustrated for both the Analog and the Digital RoF systems analyzed. PDSCH constellations at $L = 70\text{ km}$ are shown as well.

From Figure 5.11, it can be appreciated that the dynamic range of the A-RoF lies between -15 dBm and 0 dBm , adding up to 15 dB , while in the D-RoF link, it ranges from -22 dBm to 5 dBm , adding up to 27 dB . The accepted dynamic range in accordance to 3GPP limit for Analog RoF link is then almost half as compared to Digital RoF link. The constellation chart shows the symbols received at the D-RoF boundary of the 3GPP 8% limit ($P_{IN}=5\text{ dBm}$). It is evident that the Analog RoF symbols reception is noisier than that of Digital RoF link in correspondence to the same value of P_{IN} .

The comparison between Analog and Digital RoF is further performed by evaluating the signal to noise ratio (SNR). Figure 5.12 represents the comparison of SNR for varying fiber lengths at 0 dBm of input power. Also, in this case D-RoF outperforms A-RoF.

In case of D-RoF, the SNR maintains a constant value for $L < 35\text{ km}$. This is determined by the fact that the quantization noise of the ADC given by (5.25) prevails over all the other contributions, which practically do not influence the value of the SNR. However, for higher lengths, the noise collected at the optical receiver section starts to dominate over the quantization noise as a result of the increased fiber loss, limiting the overall link performance. In case of A-RoF, the signal attenuation is the main cause of the monothonical reduction of the SNR which is observed for increasing values of the link length.

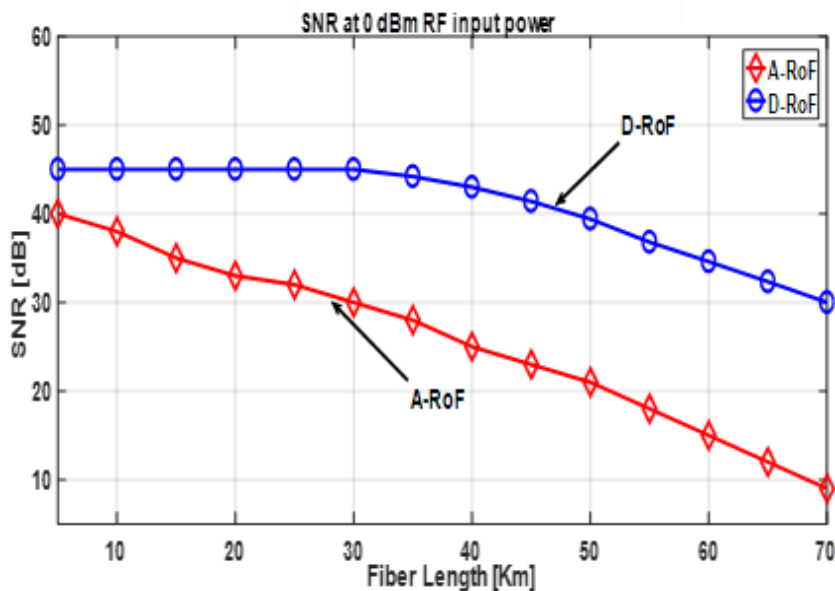


Figure 5.12: Results for SNR vs. Fiber Length

Figure 5.13 highlights the influence of the number of bits chosen for the ADC resolution on the values SNR and EVM for the D-RoF Link. The selected Input optical power P_{IN} is 0 dBm and length of the link is fixed to 60 km. It can be appreciated that the number of 8 bits chosen for the ADC resolution represents a correct choice, since the value of the EVM would only very slightly increase while the value of the SNR would not even increase at all if $n=9$ or $n=10$ were chosen for the ADC resolution.

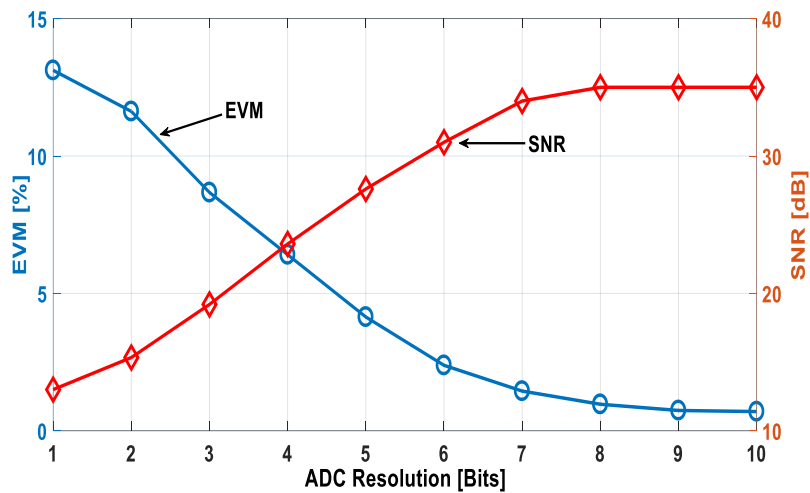


Figure 5.13: Results for EVM and SNR as a function of ADC Resolution

The transmission performance of A-RoF and D-RoF systems is further investigated by analysing the Eye diagrams of the transmitted signals. Figure 5.14 allows to appreciate that for both systems EOP increases with the increasing fiber length. EOH in the A-RoF case closes after a distance of 45 km, in line with the fact that EOP approaches infinity. In the D-RoF case, the EOH remains open within all the considered fiber length range. For a distance of 70 km EOP shows a value of 7.4 dB. Although there is not, in general, a direct relation between EOP and more quantitative parameters like the EVM, its evaluation allows to have an immediate idea of the quality of the received signal.

In addition, the evaluation of the EOP will constitute in the next section one of the benchmark utilized for the experimental validation of the proposed D-RoF system.

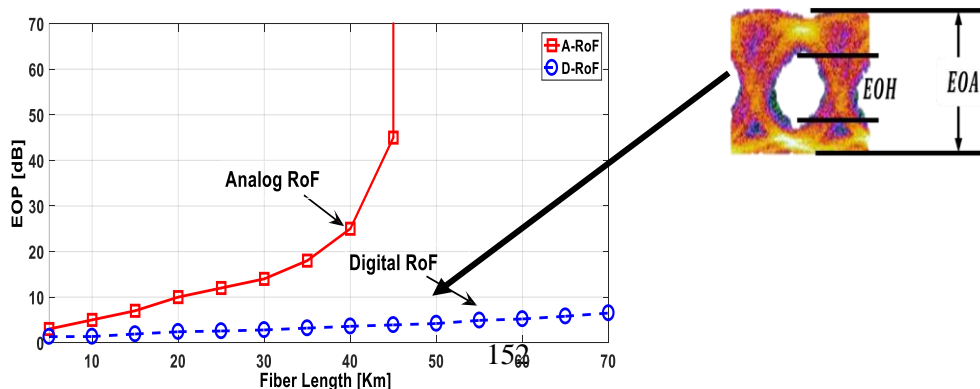


Figure 5.14: Eye Opening Penalty versus Fiber length. The inset shows the EOP for D-RoF at 50 km.

5.5 D-RoF Experimental Setup and Analytical Model Results Validation

In order to verify the proposed analytical model, the digitized radio over fiber link has been demonstrated through an experimental setup, whose schematic is shown in Figure 5.15. The RF signal is generated by a Vector Signal Generator (VSG). A 20 MHz LTE signal having 64 QAM modulation is used to modulate a carrier frequency of 2.475 GHz. The bandpass sampling is carried out at 128 MSamples/s. For emulating the ADC, the Digital Sampling Oscilloscope (DSO) Keysight Technologies DSOX1102G is utilized, which captures more than 50000 samples/s and whose maximum resolution is 8 bits. The coder and the quantizer are implemented by a software code. The time window captured using the DSO was 500 μ s. The samples processing is done offline. Note that this practical implementation is very similar to the one proposed in [5.28], two primary differences being the use of a Distributed Feedback (DFB) laser (instead of a VCSEL), and the distance covered by the optical link, which in this experimental case is 30 km (instead of 20 km).

At first, the samples are coded and appended with a preamble of optimum binary sequences having lowest probability of failure as given in [5.29]. The chosen preamble was (+ 1, + 1, + 1, + 1, + 1, + 1, - 1, - 1, - 1, - 1, - 1, - 1, + 1, +1, - 1, - 1). The preamble can in principle lead to additional over heads, however, the selected preamble has negligible effect since it has 16 bits leading to a bit rate of 1.024 Gbps. The resultant binary digital stream is obtained through Keysight 81134A pulse pattern generator (PPG).

Before this stream is used to directly modulate the Opti Lab 1550 nm Distributed Feedback (DFB) Laser, it is necessary to attenuate the peak to peak output voltage of the PPG so that the DFB laser is biased at 40 mA with an extinction ratio of 0.07. This operation guarantees that the DFB laser always operates above threshold. The possible nonlinear effects that may arise in the evaluation of the system performance must be ascribed to the non-ideal behavior of the ADC included in the DSO. The DC bias current is unified with the attenuated signal using a bias tee. This resultant signal modulates the laser and transmits it over 30 km of fiber length. The received optical signal is photo detected using a photodiode having 0.6 A/W of responsivity.

The received signal is fed into the data recovery block that consist of a DSO and a correlator. The photodiode output is captured by the DSO and is then sent to the correlator block

(implemented through a software code) which compares the captured output data stream with the preamble in order to identify the starting bit.

The DAC consists of a decoder, a zero-order hold (ZOH) and signal reconstruction block clocked at 128 MHz. The decoder and the ZOH are implemented by a software code while the signal reconstruction is employed using an arbitrary waveform generator (AWG). The output of the correlator data stream is decoded off-line in the decoder block of DAC and decoded samples were generated electrically using the AWG. This reconstructed signal is then fed to the VSA. In Figure 5.15 (a), (b) and (c), the signal is shown at different stages. In Figure 5.15 (a), the quantized signal containing 50,000 samples converted to 400,000 bits after coding is shown. Figure 5.15(b) and 5.15(c) show respectively the photodiode output captured by the DSO in the data recovery block and its spectrum in the frequency domain.

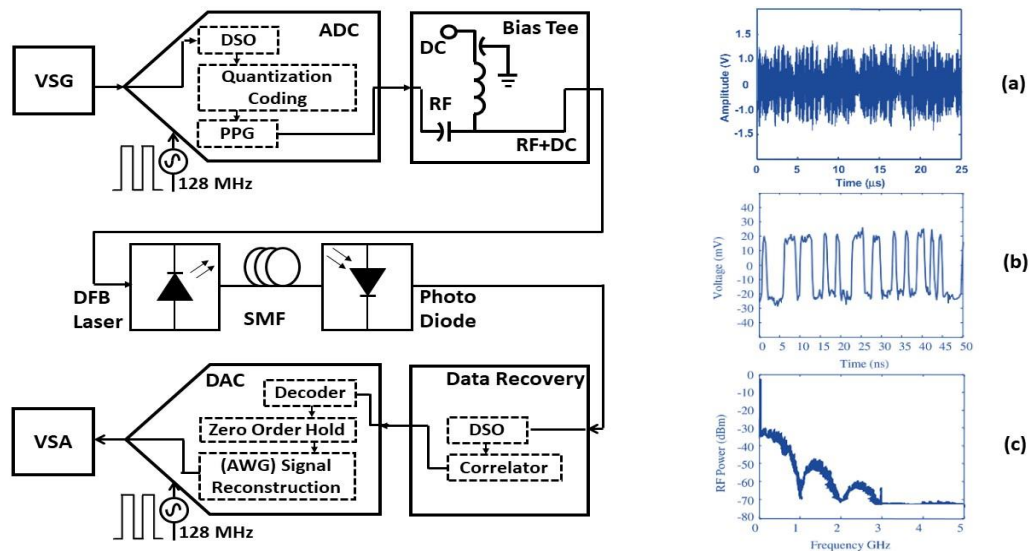


Figure 5.15: Experimental setup for D-RoF transmission. VSG: Vector Signal Generator. DSO: Digital Signal Oscilloscope. PPG: Pulse Pattern Generator. SMF: Single Mode Fiber. AWG: Arbitrary Waveform Generator. VSA: Vector Signal Analyzer. The inset (a) represents the quantized signal at the output of the DSO. Inset (b) and (c) represents the photodiode output signal and spectrum captured by the DSO.

5.5.1 Results and Discussion

In order to validate the experimental bench, a comparison between measured and modelled data is performed, referred to the experimental setup described, where the length of the fiber is set to 30 km. Figure 5.16 shows the behaviours of SNR resulting from the described analytical model ($SNR_{ANALYTIC}$) and from the experimental measurement (SNR_{EXP}) as a function of the number of ADC resolution bits. A difference between about 5 dB (for $n=3$) and about 9 dB (for $n=8$) can be observed between $SNR_{ANALYTIC}$ and SNR_{EXP} , when considered with a RF carrier frequency of 2.475 GHz.

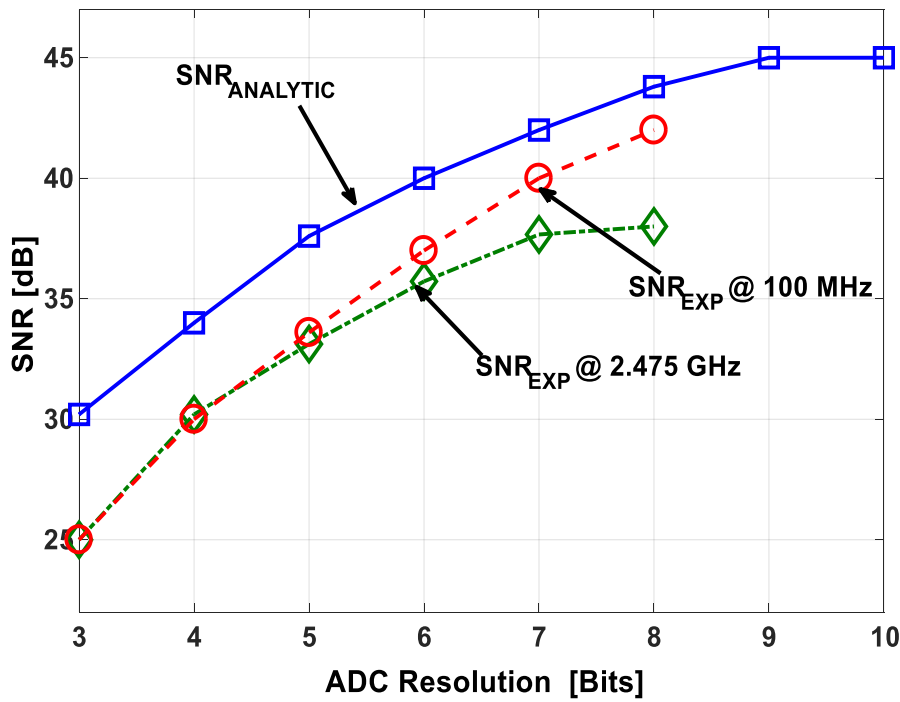


Figure 5.16: Theoretical vs Experimental SNR for varying ADC resolution bits

However, the behaviors of modelled and measured EVM ($EVM_{ANALYTIC}$ and EVM_{EXP} , respectively) again as function of the number of ADC resolution bits, which is reported in Figure 5.17 shows only a slight difference between the two curves, indicating that the simulation model developed can be a useful tool for predicting the system performance.

As an additional test, SNR_{EXP} and EVM_{EXP} , have been measured also considering, after bandpass sampling, the spectral replica of the transmitted signal at 100 MHz (and not at 2.475 GHz). The computed behavior coming from the theoretical simulation does not vary in this case, but it can be appreciated that SNR_{EXP} and EVM_{EXP} are both in good agreement with the

theoretical values of $SNR_{ANALYTIC}$. It appears that the lower agreement exhibited at 2.475 GHz is due to a sort of higher “insertion loss” which is performed by the instrumentation at higher order Nyquist zones. This can be possibly included in the parameters of the model utilized numerical simulation, which results validated by the measurements performed on the considered experimental bench. Similarly, it can be concluded based on our theoretical and experimental observations that an ADC with 8 resolution bits is sufficient to achieve optimum SNR and EVM performance.

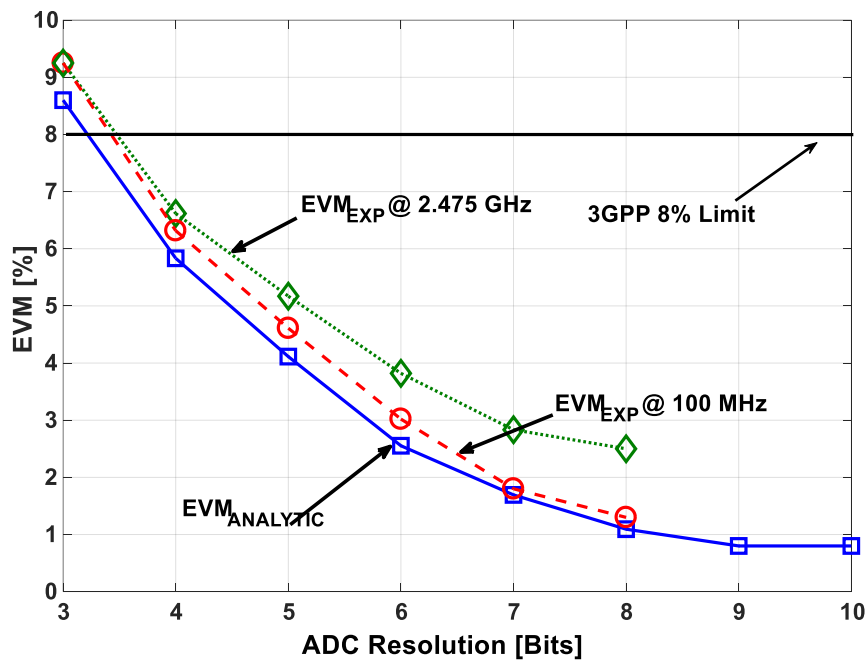


Figure 5.17: Theoretical versus experimental EVM for different numbers of ADC bits

As an additional comparison, Figure 5.18 presents the behaviour of EVM for changing values of the RF input power. The link length is again fixed to 30 km for both theoretical/ analytical $EVM_{ANALYTIC}$ and Experimental EVM_{EXP} . The trend in Figure 5.18 confirms the consideration expressed above, namely that the EVM_{EXP} for the 2.475 GHz spectral replica undergoes higher insertion losses compared to the spectral replicas at lower order zones [5.30]. The experimental results EVM_{EXP} @ 100 MHz are very close to $EVM_{ANALYTIC}$ curve. The slight difference can be attributed to experimental errors.

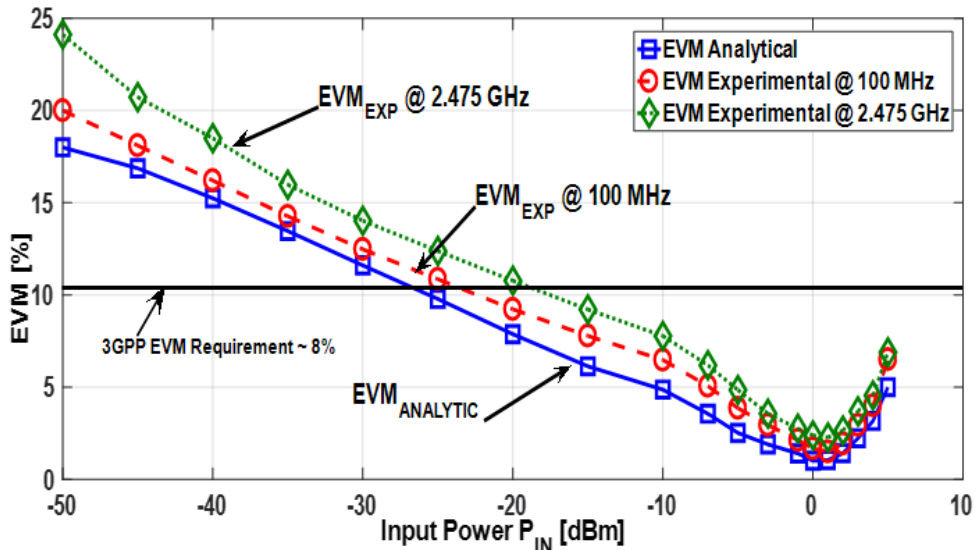


Figure 5.18: Theoretical versus experimental EVM for varying RF input power at 30 Km.

The Eye-Opening Penalty (EOP) defines the deterioration in the eye diagrams. EOP is the ratio of the non-distorted reference eye called Eye Opening Amplitude (EOA) to the eye opening of the distorted eye, i.e. the Eye Opening Height (EOH) [5.31]. Finally, Figure 5.19 shows the comparison of the Eye-opening penalty computed with the analytical model ($EOP_{ANALYTIC}$) with the one measured in the experimental (EOP_{EXP}) for RF spectral replicas at 100 MHz and 2.475 GHz respectively. In line with the previous observations, it can be appreciated that the both computed EOP_{EXP} exhibit values very similar to the $EOP_{ANALYTIC}$ which is a further validation of the analytical model.

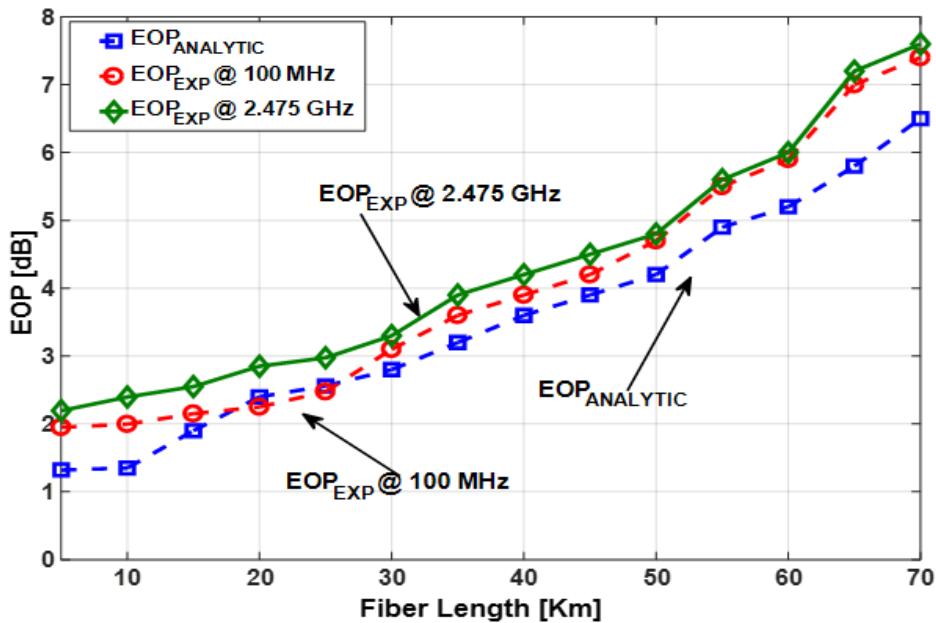


Figure 5.19: Theoretical versus experimental EOP for varying fiber lengths.

Table 5.3 presents the summary of the performance parameters for experimental and analytical D-RoF link. The link length is 30 km, 8 bits of resolution and 0 dBm of RF input power. It can be seen that model results are very much in accordance with the experimental results.

Table 5-3: Summary of the analytical and experimental bench for D-RoF

Parameter	D-RoF Experimental		D-RoF Analytical
	@ 100 MHz	@ 2.475 GHz	
EVM (%)	1.3	2.2	1.1
EOP (dB)	3.1	3.3	2.8
SNR (dB)	38	40	43

5.6 Conclusions

A comprehensive analysis has been presented on the performance of Digital and Analog RoF systems. It has been demonstrated that the use of D-RoF system for broadband wireless signal transportation and distribution applications employing bandpass sampling for 20 MHz LTE signal having 64 QAM modulation format. The proposed technique has demonstrated the increase of the reach of the fiber distance up to 70 km with an optimized value of resolution bits. Moreover, the analytical model utilized for D-RoF has been validated experimentally for 30 km of fiber length. The results obtained for experimental bench are in accordance with the D-RoF analytical model. It's also evident that the performance of the D-RoF is predominantly determined by the performance of the ADC. By employing bandpass sampling, indeed, ADC complexity and overheads of sampling at giga samples can be relaxed. Indeed A-RoF link has less good performance than D-RoF link, one still may prefer usage of A-RoF over D-RoF for short distances keeping in mind the throughput and losses versus cost of deploying D-RoF system. Real time implementation of the above proposed system and multichannel propagation using D-RoF is envisaged for the future work.

References

- 5.1 L. Breyne, G. Torfs, X. Yin, P. Demeester and J. Bauwelinck, "Comparison Between Analog Radio-Over-Fiber and Sigma Delta Modulated Radio-Over-Fiber," in *IEEE Photonics Technology Letters*, vol. 29, no. 21, pp. 1808-1811, 1 Nov. 1, 2017. doi: 10.1109/LPT.2017.2752284
- 5.2 G. Tartarini, P. Faccin, "Efficient characterization of harmonic and intermodulation distortion effects in dispersive radio over fiber systems with direct laser modulation", *Microwave and Optical Technology Letters* 46 (2), 114-117
- 5.3 G. Alcaro, D. Visani, L. Tarlazzi, P. Faccin, G. Tartarini, "Distortion mechanisms originating from modal noise in radio over multimode fiber links", *IEEE Transactions on Microwave Theory and Techniques* Volume 60, Issue 1, January 2012, Pages 185-194
- 5.4 P. M. Wala, "A new microcell architecture using digital optical transport," in *Proc. 43rd IEEE Vehicular Technology Conf.*, 1993.
- 5.5 Prasanna A. Gamage, A. Nirmalathas, C. Lim, M. Bakaul, D. Novak, and R. Waterhouse, "Efficient Transmission Scheme for AWG-based DWDM Millimetre-Wave Fibre-Radio Systems", *IEEE Photon. Technol. Lett.*, vol. 19, no. 4, pp. 206 – 208, 2007.
- 5.6 D. Novak, "Hybrid Fiber Radio - The Application of Photonic Links in Wireless Communication Systems," *OFC 2009 Short Course 217*, 2009.
- 5.7 Y. Yang, C. Lim, A. Nirmalathas, "Multichannel Digitized RF-Over-Fiber Transmission based on Bandpass Sampling", *IEEE Trans. Microwave Theory Tech.* 58(11), 3181-3188 (2010)
- 5.8 Y. Yang, C. Lim, A. Nirmalathas, "Investigation on Transport Schemes for Efficient High-Frequency Broadband OFDM transmission in Fibre-Wireless Links", *IEEE J. Lightw. Technol.*, vol. 32, pp. 267-274, January 2014.
- 5.9 Y. Yang, C. Lim, and A. Nirmalathas, "Experimental demonstration of multi-service hybrid fiber-radio system using digitized RF-over-fiber technique," *IEEE J. Lightw. Technol.*, vol. 29, pp. 2131–2137, July 2011.

- 5.10 Y. Yang, C. Lim, A. Nirmalathas, "A full-duplex digitized RoF system for millimeter-wave OFDM transmission", 38th European Conference and Exhibition on Optical Communications, P3.12, 2012
- 5.11 D. Wake, M. Webster, G. Wimpenny, K. Beacham and L. Crawford, "Radio Over Fiber for Mobile Communications," October 2004, pp. 157–160
- 5.12 S. Ghafoor and L. Hanzo, "Sub-Carrier-Multiplexed Duplex 64-QAM Radio-over-Fiber Transmission for Distributed Antennas", IEEE Communications Letters, vol. 15, No. 12, pp. 1368-1371, 2011.
- 5.13 T. Li, R. V. Penty and I. H. White, "Novel digital radio over fibre for 4G-LTE," 2015 IEEE International Conference on Communication Workshop (ICCW), London, 2015, pp. 312-317. doi: 10.1109/ICCW.2015.7247197
- 5.14 Vaughan RG, Scott NL, White DR (1991) The theory of bandpass sampling. IEEE Trans Acoust Speech Signal Process 39(9):1973–1984
- 5.15 A. Nirmalathas, P. A. Gamage, C. Lim, D. Novak, R. Waterhouse and Y. Yang, "Digitized RF transmission over fiber," in IEEE Microwave Magazine, vol. 10, no. 4, pp. 75-81, June 2009.
- 5.16 Christina Lim, Ampalavanapillai (Thas) Nirmalathas, Ka-Lun Lee, Dalma Novak, and Rod Waterhouse, "Intermodulation Distortion Improvement for Fiber–Radio Applications Incorporating OSSB+C Modulation in an Optical Integrated-Access Environment," J. Lightwave Technol. 25, 1602-1612 (2007)
- 5.17 Y. Sun, "Nonuniform Bandpass Sampling in Radio Receivers," Microelectronics and Information Technology, 2004.
- 5.18 B. Brannon, Basics of Designing a Digital Radio receiver (Radio 101), Analog Devices.
- 5.19 L. Chang, P. S. Huang and T. -M. Tu, "Aperture Jitter of Sampling System in AWGN and Fading Channels," IEEE. Trans. Instrum. Meas., vol. 56, no. 3, pp. 831-839, 2007.
- 5.20 H. Kobayashi, M. Morimura, K. Kobayashi, and Y. A. -O. Onaya, "Aperture jitter effects in wideband ADC systems," in Proc. IEEE Int. IECE Conf., 1999.

- 5.21 H. Kobayashi, M. Morimura, K. Kobayashi, and Y. A. -O. Onaya, "Aperture jitter effects in wideband sampling systems," in 16th IEEE Proc. Instrumentation and Measurement Technology (IMTC '99), 1999.
- 5.22 J. G. Proakis, *Digital Communication*, 4th ed., pp. 205.
- 5.23 P. Smith, "Little known characteristics of phase noise," AN - 741, Analog Devices.
- 5.24 ADC083000 8-Bit, 3 GSPS, High Performance, Low Power A/D Converter, National Semiconductors.
- 5.25 Viterbi, "Lower bounds on maximum signal-to-noise ratios for digital communication over the Gaussian channel," *IEEE Tans. Commun.*, vol. 12, no. 1, pp. 10-17, 1964.
- 5.26 J. K. Cavers and S. P. Stapleton, "A DSP-based alternative to direct conversion receivers for digital mobile communications," in *IEEE Conf. Global Telecommunications Conference (GLOBECOM '90)*, 1990.
- 5.27 AVR120: Characterization and Calibration of the ADC on an AVR
- 5.28 Y. Yang, C. Lim, A. Nirmalathas, "High performance fiber-radio link: Digitized radio-over-fiber", 2012 Asia Communications and Photonics Conference (ACP), Guangzhou, 2012, pp. 1-3.
- 5.29 M. Grayson, and M. Darnell, "Optimum synchronisation preamble design," *Electron. Lett.*, vol. 27, no. 1, pp. 36-38, 1991
- 5.30 M. C. Lawton, "Sensitivity analysis of radio architectures employing sample and hold techniques," in *Proc. 6th Int. Conf. on Radio Receivers Associated Systems*, 1995, pp. 52-56.
- 5.31 Cordeiro RF, Oliveira ASR, Vieira J, Silva TOE. Wideband all-digital transmitter based on multicore DSM. *IEEE MTT-S International Microwave Symposium (IMS) 2016*.

Chapter 6

Sigma Delta Radio over Fiber Systems as a New Candidate for Fronthaul Applications

The findings of this chapter have been published as journal articles [J5], [J6] and [J7] while another article [A2] has been submitted.

This chapter discusses another class of RoF system which is called as Sigma Digital Radio over Fiber (S-DRoF) system. The chapter introduces the need and importance of Sigma delta RoF system, an auxiliary method that amalgamates the advantages of A-RoF and D-RoF. It discusses the basics of sigma delta modulator ($\Sigma \Delta M$). The need of power hungry and high-speed digital to analog converter (DAC) required in D-RoF is replaced by a $\Sigma \Delta M$. It describes the different architectures that have been proposed. The analytical model with simulation is shown and then experimental setup is discussed.

6.1 Introduction

In recent years, the continuous demand for delivering gigabits of data rate has become crucial. Next-generation networks such as 5G require high speed data rate, cost effective and low latency solutions [6.1]. In order to support such networks, a worthwhile and greener optical transport solution will be needed. Radio over Fiber (RoF) systems have been looked upon as a capacitive technology to cope with the on growing demand of these next generation networks.

The techniques adapted for RoF can be either in analog or digital form. A-RoF and D-RoF have been discussed comprehensively in previous chapters. Digital RoF (D-RoF) can overcome the nonlinear effects arising in A-RoF [6.2-6.3]. It has been regarded as a robust solution in terms of performance. However, the cost of D-RoF increases as the requirement of high precision analog to digital and digital to analog converters adds up to it. Similarly, the phase relation

between many RRHs doesn't remain steady and spectral efficiency decreases [6.4]. Therefore, the existence of an alternative solution which can fix these bottlenecks would be desirable.

An auxiliary methodology is Sigma Delta Modulated Radio over Fiber (S-DRoF) that amalgamates the advantages of A-RoF and D-RoF [6.5-6.8]. This is a power efficient and robust technique eliminating the need for high-speed digital circuitry. The need of power hungry and high-speed digital to analog converter (DAC) required in D-RoF is replaced by a sigma delta modulator ($\Sigma \Delta M$). The same RRH can be used for ARoF and S-DRoF. However, similar to D-RoF, the digital signal transmitted over the link is highly resistant to nonlinearities.

In this chapter, we discuss the basics of Sigma delta $\Sigma \Delta M$, its' different forms and novel robust solution for the implementation of 5G CRAN downlink applications are proposed. This chapter is organized as follows. Section 6.2 summarizes the RoF architectures. Section 6.3 briefly proposes a novel digitization interface based on Sigma Delta Radio over Fiber (S-DRoF) that employs the SDM to RF signal. Section 6.4 describes the system description where different architectures are used. Firstly, simulation is shown, and experimental setup is discussed. In Section 6.5, performance analysis of S-DRoF is presented in terms of Error Vector Magnitude (EVM) and Signal to Noise Ratio (SNR) while Section 6.5 concludes the chapter.

6.2 Review of Sigma Delta Radio over Fiber System

There are three different methods utilized for mobile fronthauling as shown in Figure 6.1 (a)-(c). It shows the mobile front haul with three different implementation techniques. 6.1 (a) shows an analog mobile front haul architecture based on RoF techniques. The baseband signal is upconverted to RF signal which is then converted to an optical signal in electrical to optical (E-O) conversion block and transmitted through the optical link. At the receiver, optical to electrical (O-E) block retrieves the received RF signal back to electrical domain. This signal is then transmitted through the antenna after performing filtering and amplification.

However, this solution is susceptible to nonlinearities coming from its microwave and optical parts [6.9-6.15]. In order to subdue these nonlinearities, various solutions have been proposed for the linearization of A-RoF links that were discussed in detail in Chapter 2.

Since the linearization methods implied to A-RoF links are limited to narrow bandwidth and require feedback which is a tedious process. Similarly, for 5G networks, it would be challenging to dynamically track and compensate the nonlinear channel response, especially given the fact of broadband time varying data traffic from multiple RATs.

On the other hand, Digital mobile fronthaul (D-MBFH) based on Digital-Radio over Fiber (D-RoF) is not affected by the nonlinear effects arising in A-RoF [6.16-6.18]. Figure 6.1 (b) represents the D-RoF architecture. The common public radio interface (CPRI) that was proposed by the CPRI cooperation, Nokia, Bell Labs, Ericsson, Huawei, Orange and NEC, was adopted as the D-MBFH interface [6.19]. However, when CPRI was employed as a digitization interface developed for narrowband radio access technologies (RATs), such as UMTS (CPRI version 1 and 2), WiMAX (version 3), LTE (version 4) and GSM (version 5), due to its limited spectral efficiency, it had limited scalability. Moreover, it also required tremendous data traffic in the fronthaul network segment. Similarly, the cost of D-RoF increases as the requirement of high-performance analog-to-digital and digital-to-analog converters adds to it. Similarly, the phase relation between many RRHs does not remain steady and spectral efficiency decreases [6.20]. Therefore, an alternative solution, which can overcome these bottlenecks, would be desirable.

The CPRI bottleneck can be outmaneuvered by employing Sigma-Delta Modulation (SDM). An auxiliary methodology is Sigma-Delta Radio over Fiber (S-DRoF) that combines the advantages of both A-RoF and D-RoF. It is a simpler and power efficient solution that eliminates the need for high-power of the 1-bit quantization noise is very high, its spectral density is shaped for the most part out of the band of interest.

The digital signal transmission is highly immune to non-linearities, as in the case of D-RoF. At the receiver end, a band-pass filter (BPF) guarantees the correct digital-to-analogue conversion of the signal and the spectral emission requirements by filtering the out-of-band quantization noise. Figure 6.1 (c) shows the general scheme of S-DRoF. The power-hungry multi-bit DAC and the subsequent linear driver at the D-RoF transmitter are replaced by a sigma delta (SD) modulator.

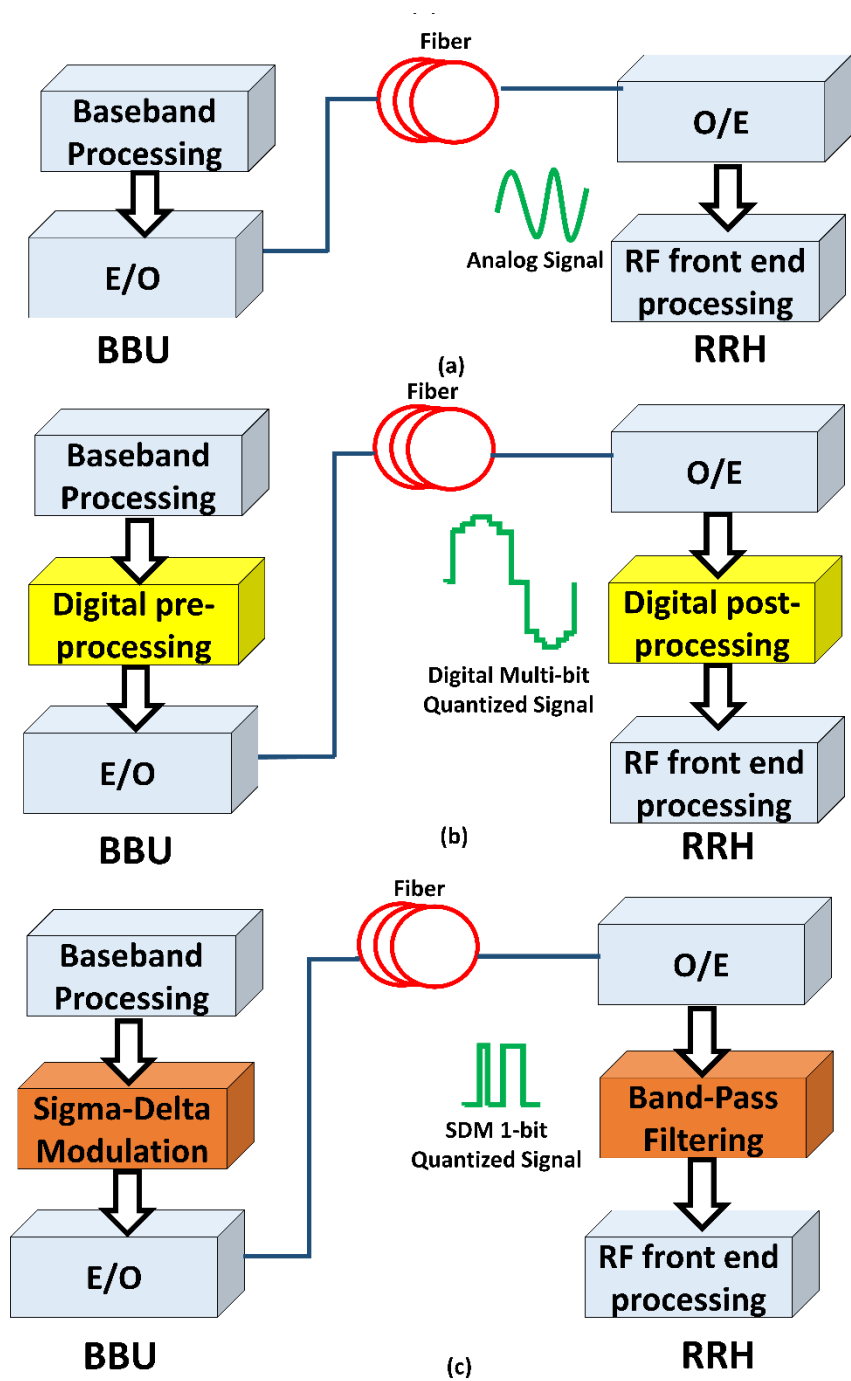


Figure 6.1: Schematic illustration of (a) A-RoF, (b) D-RoF and (c) S-DRoF. ADC: Analog to Digital Converter; DSP: Digital Signal Processor; E-O: Electrical-to-Optical; SMF: Single Model Fibre; O-E: Optical-to-Electrical; DAC: Digital to Analog Converter; SDM: Sigma Delta Modulation; BPF: Band Pass Filtering.

6.3 Operation Principle

The sigma-delta modulation ($\Sigma \Delta M$) utilizes oversampling of an input signal at a rate several times higher than the Nyquist rate. In $\Sigma \Delta M$, the number of quantization bits are limited due to which Nyquist sampling results in significant quantization noise. However, in order to deal with this quantization, the oversampling extends the Nyquist zones which can be spread over a wide range of frequency that leads to in-band noise reduction. Therefore, the unwanted and relatively high quantization noise can be refiltered then to reduce it in the useful band.

A very basic difference between conventional ADC and $\Sigma \Delta M$ is aliasing. $\Sigma \Delta M$ samples the signal at many times its bandwidth. Therefore, it does not require a complex high order anti-aliasing filter. Aliasing occurs when sampled, a signal is reproduced, in the frequency domain, at multiples of the sampling frequency, as band-limited signals. When Nyquist rate is used, these signal reproductions appear to be close together as shown in Figure 6.2(a). This can result in aliasing issues as shown in the Figure 6.2(b). When oversampling is employed, since signal images are distant, this overlapping issue does not occur as shown in Figure 6.2(c).

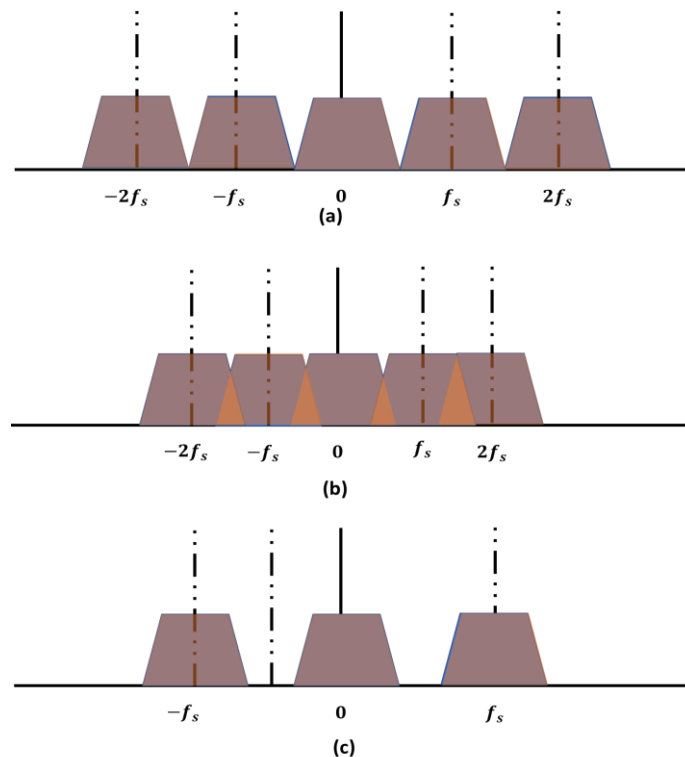


Figure 6.2: Frequency domain for (a) Nyquist rate ADC, (b) the aliasing effect, and (c) oversampling ADC ($\Sigma \Delta M$ concept).

The quantization operation can be performed with very low resolution with a sampling rate higher than the Nyquist criteria. The limited number of quantization bits results in a considerable amount of quantization noise. Therefore, the unwanted and relatively high quantization noise can be re-filtered in order to reduce it in the useful band. The use of BPF not only eliminates the need of expensive and power-hungry DACs, but also circumvents the data-rate bottleneck linked with CPRI.

Different from Nyquist ADC, SDM trades quantization bit for sampling rate, using high sampling rate and only few (1-bit generally) quantization bits. After baseband processing, digital baseband signal is upconverted to radio frequency, then a bandpass delta-sigma modulation encodes the discrete-time multibit RF signal into a one-bit data stream. In Figure 6.3(a), (b), (c) and (d) shows the behavior of Nyquist ADC generally utilized. It can be seen that it utilizes Nyquist sampling followed by multi bit quantization. In contrast to this, Figure 6.3(a*), (b*), (c*) and (d*) shows the operation principle of bandpass SDM.

In Figure 6.3(b*), the Oversampling extends the Nyquist zone, so that quantization noise can be spread over a wide frequency range. In Figure 6.3(c*), the noise shaping technique pushes the quantization noise out of the signal band that separates the noise from the signal in frequency domain. In Figure 6.3(d*), at RRH, a BPF takes out the desired signal eliminating the out of band noise and retrieving the analog waveform.

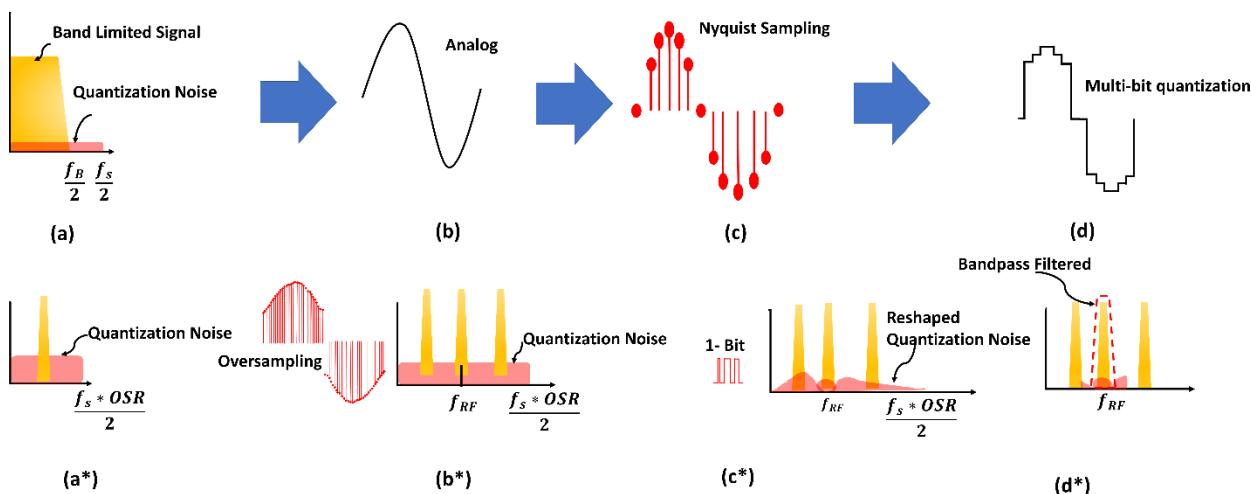


Figure 6.3: Operation principles of: (a)-(d) shows Nyquist ADC and (a*)-(d*) shows sigma delta modulation concept. (a*) Quantization noise mapped. (b*) Oversampling extends the range of quantization noise. (c*) Noise shaping. (d*) BPF.

6.4 Structures of Sigma Delta Modulator ($\Sigma \Delta M$)

In this section, the structure of $\Sigma \Delta M$ utilized in our work are discussed. There are two main structures that have been exploited in the work performed. The first structure discussed is Second Order Sigma Delta Modulator and the other one is Multi-stAge-noise-SHaping (MASH) based Sigma Delta Modulator.

6.4.1 Second Order Sigma-Delta Modulator

The significance of $\Sigma \Delta M$ is the quantization of the baseband signal. This operation is performed with a very low resolution and at a sampling rate much higher than the Nyquist criteria. Since, the quantization bits are limited, Nyquist sampling leads to a significant quantization noise. Therefore, the relatively high quantization noise can be reshaped in frequency domain so that the noise in the useful band can be reduced. This operation leads to a very high Signal to Noise Ratio (SNR) [6.21].

At the receiver end, the bandpass filtering (BPF) of the reshaped spectrum suppresses the quantization noise that results in retrieving of the original signal. Figure 6.4 shows the schematic of the second order with the combination of A_1 and A_2 yields a second order $\Sigma \Delta M$. The input amplitude of $\Sigma \Delta M$ is expressed with respect to this full-scale range. To simplify the computational analysis, let's consider that quantizer has been replaced with a linear approximation, i.e. removal of the quantizer and adding (white) quantization noise [6.21]. Therefore, signal transfer function (STF) is the transfer function of the input x to the output y when the quantizer is neglected.

Similarly, the noise transfer function (NTF) is the transfer function from the quantization noise input to the output y when the input is zero. Therefore, it can be represented as follows in Eq. (6.1):

$$\begin{aligned} y(z) &= STF(z) + x(z) + NTF(z)Q_e(z) \\ &= z^{-1}x(z) + (1 - z^{-1})^2 Q_e(z) \end{aligned} \quad (6.1)$$

where $y(z)$ is the output, $x(z)$ is the input and $Q_e(z)$ is the quantization error. The integrators A_1 and A_2 are expressed as follows in Eq. (6.2) and (6.3):

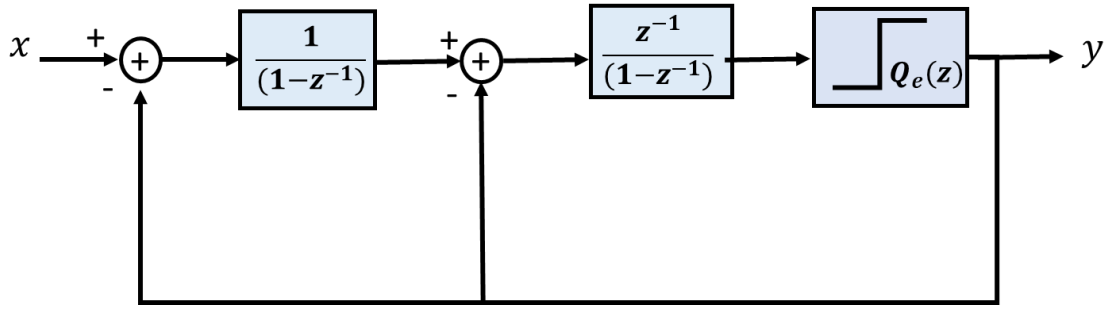


Figure 6.4: Frequency domain model of Second order $\Sigma \Delta M$ structure

$$A_1 = \frac{1}{(1-z^{-1})} \quad (6.2)$$

and

$$A_2 = \frac{z^{-1}}{(1-z^{-1})} \quad (6.3)$$

The magnitude of the *NTF* is evaluated as follows:

$$|NTF(e^{j2\pi f})|^2 = (2 \sin(\pi f))^4 \approx (2\pi f)^4, \text{ for } f \ll 1 \quad (6.4)$$

In order to evaluate the behavior of the proposed SDM, the absolute values of *STF* and *NTF* are plotted in Figure 6.5 [6.22]. The signal is unaffected, and its quantization noise is immensely boosted in high, out-of-band frequencies, and highly attenuated in the signal band, around 0. This means that the total quantization noise is greater, but since it is located out of the signal bandwidth, therefore, it can be easily band pass filtered at the output.

The *SNR* of the Second order SDM is given in Eq. (6.5) when sin wave is considered as an input signal with power $P_u = \frac{A^2}{2}$, where A is the peak amplitude.

$$SNR = 15 A^2 \frac{(OSR)^5}{2\pi^4} \quad (6.5)$$

where *OSR* is Over Sampling Ratio.

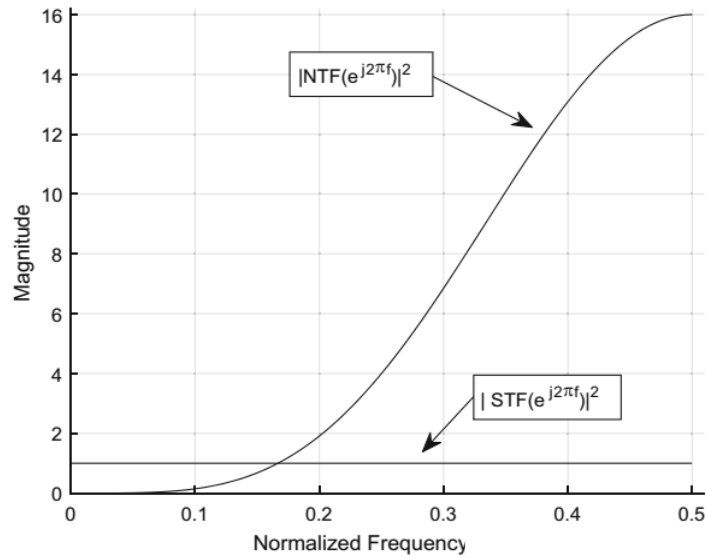


Figure 6.5: Frequency response of Second order $\Sigma \Delta M$ structure

6.4.1.1 System Description

The experimental setup is shown in Figure 6.6. The RF signal is generated at digital signal processor (DSP) which is emulated by MATLAB. Then, this signal is sigma delta modulated by 2nd order SDM implemented on MATLAB. The sigma delta modulated stream is then sent to Pulse Pattern Generation (PPG) block which is implemented in MATLAB. As far as, optical fronthaul link is concerned, it is implemented in the VPI Transmission Maker.

The pulse generated pattern is then used to directly modulate the 1550 nm Distributed Feedback (DFB) Laser. The Standard Single Mode Fiber (SSMF) of different lengths is utilized for comparison. The photodiode is followed by a BPF to filter the optical signal. This is followed by down conversion to baseband and further it is processed in evaluation block. The RF signal digitized by 1 bit 2nd order SDM is a 64 QAM modulated LTE signal of 20 MHz. The carrier frequency f_c is 1.14 GHz. The details of the parameters utilized are given in Table 6.1.

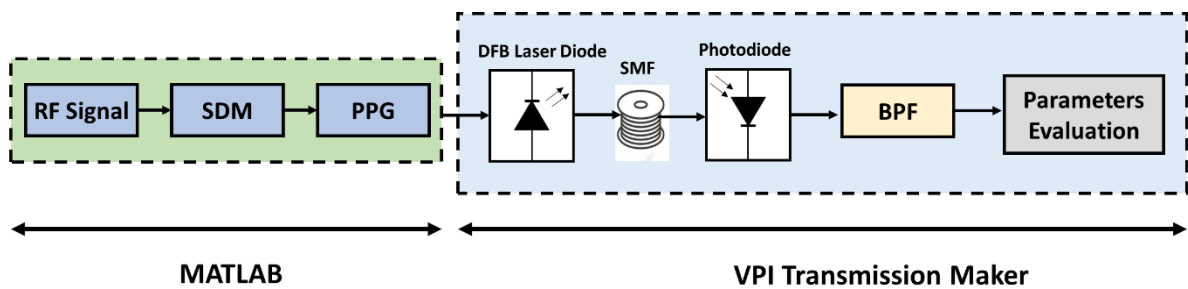


Figure 6.6: Simulation setup for Sigma Delta Radio over Fiber system. SDM: Sigma Delta Modulation. PPG: Pulse Pattern Generation, BPF: Band Pass Filtering.

Table 6-1: Parameters Value

Parameter		Value
RF Signal		Carrier frequency = 1.14 GHz Constellation format= 64 QAM
Optical Link	Laser	Wave Length= 1550 nm Average Power= 10 mW Line Width= 16e6 Hz
	Fiber	Fiber Dispersion= $16 \frac{ps}{nmkm}$ Fiber Distance= 20 Km Attenuation= $0.2 \frac{dB}{Km}$
	Photo detector	Responsivity 0.9 A/W Bandwidth: 4 GHz
Bandpass Filtering		Band Pass Bandwidth=190 MHz Conversion gain (Complete Receiver (PD+BPF))=220 V/W

6.4.1.1.1 Experimental Results and Discussion

In this section, the performances of the proposed S-DRoF are evaluated. At first, the performance of S-DRoF is evaluated by the Error Vector Magnitude (EVM). The 3GPP has set an EVM limit for LTE signals modulated by 64 QAM modulation format to be 8% [6.23]. The performance is measured for various symbol rates up to 100 MBd and for different fiber lengths up to 20 km. The results are shown in Figure 6.7. The degradation in EVM performance is observed for all the fiber lengths. It is observable that 20 km SSMF link degrades faster than others. The degradation is that the received signal has low power due to the path loss. However, 6% of EVM at 20 km is good enough to receive a 64-QAM modulated signal.

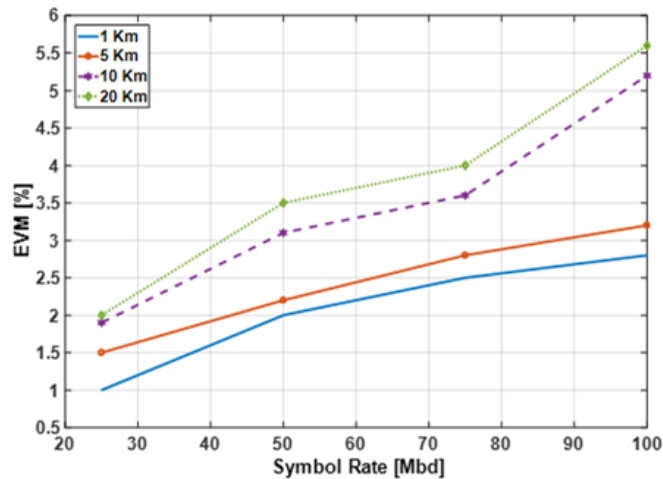


Figure 6.7: EVM performance for varying symbol rate for varying fiber lengths.

Similarly, in Figure 6.8, constellation diagram is reported for 20 km case for 25 and 100 Mbd respectively. This signifies that EVM is poorer with higher baud rate.

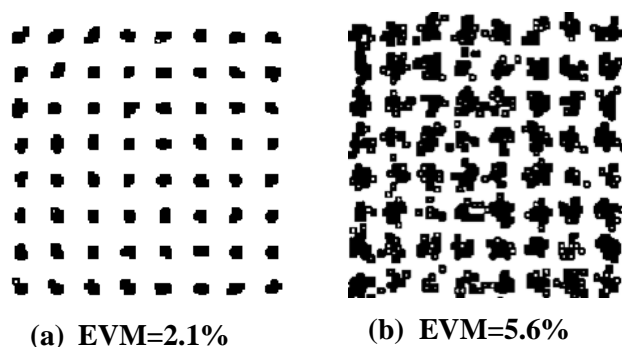


Figure 6.8: EVM performance for 20 km at (a) 25 Mbd and (b) 100Mbd

Moreover, to evaluate the dynamic range of the proposed system, the EVM performance is evaluated in Figure 6.9 with varying RF input power for 20 km link. For this evaluation, the utilized symbol rate was 16 M Symbols/sec in order to ensure that there is no loss of synchronization and 8% limit of EVM for 3GPP standard is not violated.

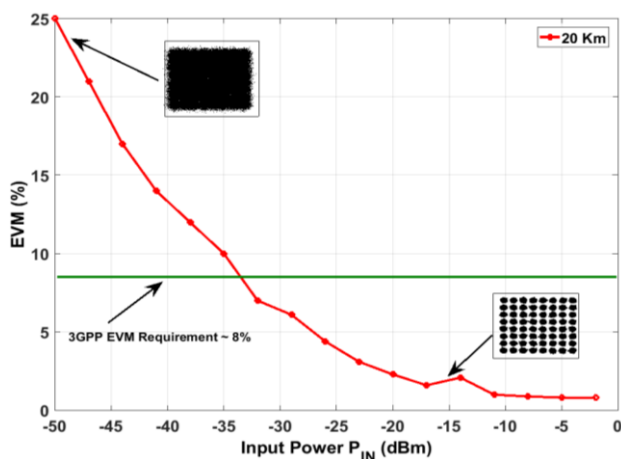


Figure 6.9: EVM performance for varying symbol rate for varying fiber lengths.

Now, the performance of the proposed S-DRoF is evaluated by finding the adjacent power ratio (ACPR). The ACPR is evaluated for three different lengths from 10 up to 20 km. The RF input power is varied from -10 dBm to 0 dBm. It can be seen in Figure 6.10 that the value of ACPR for every length is increasing with increasing RF input power. If we consider the case when RF

input power is -5 dBm , the $ACPR$ for 10, 15 and 20 km is -32 , -38.14 and -35.23 dBc respectively which are still within the standard's specifications.

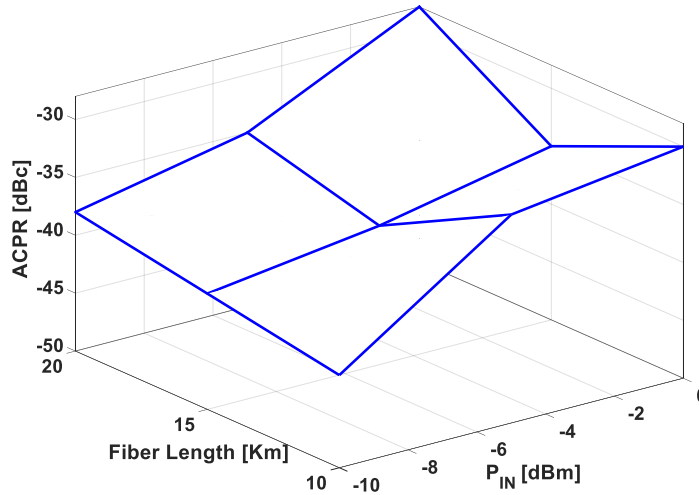


Figure 6.10: $ACPR$ performance for varying RF input power and varying fiber lengths.

Table 6.2 reports the evaluated parameters when RF input power is -5 dBm at 20 km.

Table 6-2: Performance Evaluation for 20 km at -5 dBm

Length (Km)	EVM (%)	$ACPR$ (dBc)
10	0.98	-32.12
20	1.3	-35.23

6.4.2 Multi-stage-noise-Shaping (MASH) based $\Sigma \Delta M$

Figure 6.11 shows the schematic of the proposed $\Sigma \Delta M$ known as Multi stage noise SHaping (MASH). It is designed using stages, where the next stage input is the quantization error introduced by the quantizer of the current stage, which is the difference between its output and input. The individual outputs are digitally filtered and combined in a way that the quantization noise of each stage, excluding the last, is canceled at the overall output of the structure.

Similarly, the input of the second stage is the quantization error of the first stage. The output of second stage becomes:

$$y_2(z) = STF_1(z) * Q_{e_1}(z) + NTF_1(z)Q_{e_2}(z) \tag{6.6}$$

Moreover, the digital filters A_1 and A_2 must be designed at respective stages in order to cancel the quantization errors. The condition becomes:

$$A_1 \cdot NTF_1 + A_2 \cdot STF_2 = 0 \quad (6.7)$$

The overall output becomes:

$$\begin{aligned} y &= A_1 y_1 - A_2 y_2 \\ &= STF_1 \cdot STF_2 \cdot x - NTF_1 \cdot NTF_2 \cdot Q_{e_2} \end{aligned} \quad (6.8)$$

By considering the first order $\Sigma \Delta M$ where $STF = z^{-1}$ and $NTF = 1 - z^{-1}$ as given in [6.19], we can write (6.4) as:

$$y(z) = z^{-2}x(z) - Q_{e_2}(z)[1 - z^{-1}]^2 \quad (6.9)$$

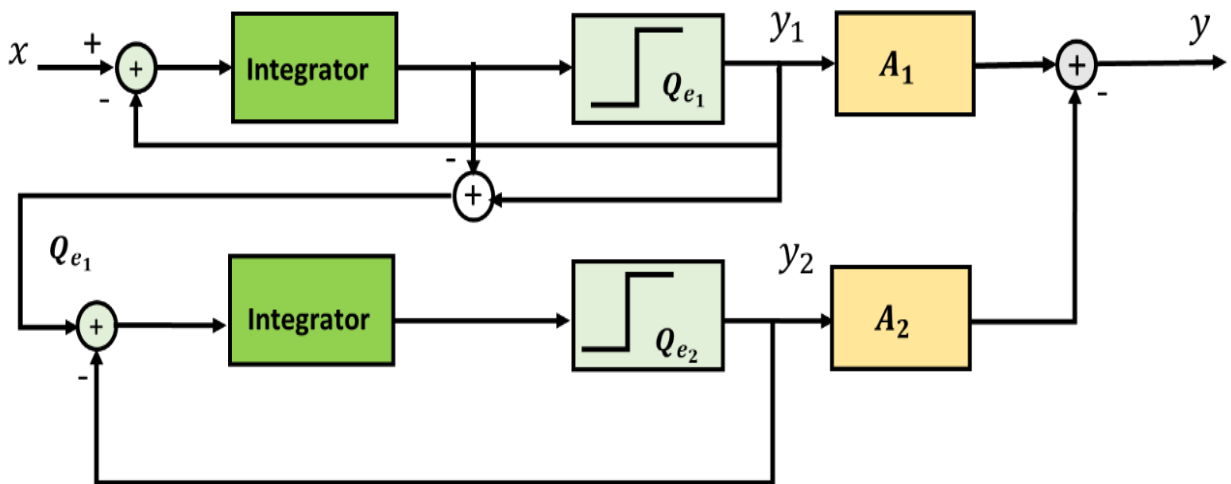


Figure 6.11: 2 stage MASH based $\Sigma \Delta M$ structure

Eq. 6.9 shows that the second order structure has noise shaping performance of fourth order modulator. Stability of the structure is determined by the order of modulators used. Stability becomes a less important issue due to simplicity of the design stages since we utilize first order $\Sigma \Delta M$ in each stage of MASH.

Similarly, quantization error is employed as an input which is very close to true white noise reducing the need of dithering. Likewise, there is no harmonic distortion of the signal generated in these stages. Consequently, the MASH structure permits the use of multi-bit quantizer in the higher stages without requiring the need of correction of the DAC nonlinearity. The reason is that

it is high-pass filtered by the *NTF* of the previous stage, suppressing it at the baseband. In the section below, the details of experimental bench utilized are shown.

6.4.2.1 System Description

The schematic of the experimental bench is shown in Figure 6.12. The RF signal is generated at digital signal processor (DSP) through MATLAB code. This RF signal is converted to 1-bit sigma delta modulation signal by MASH $\Sigma \Delta M$ implemented in MATLAB. The sigma delta modulated stream is then sent to Keysight 81134A Pulse Pattern Generator which directly modulates the Distributed Feedback (DFB) laser having 1550 nm wavelength. Single Mode Fiber (SSMF) of length up to 5 km is utilized in this experimental evaluation. The optical stream of transmitted data is converted into electrical domain by photodiode having 9.3 GHz of bandwidth. The photodiode output is fed to a low noise amplifier (LNA) followed by a BPF to filter the optical signal. This is followed by down conversion to baseband and further it is processed in evaluation block. The RF signal digitized by 1-bit MASH $\Sigma \Delta M$ is a 256 QAM modulated LTE signal of 20 MHz. The carrier frequency f_c is 3.5 GHz. The details of the parameters utilized are given in Table 6.3.

Table 6-3: Performance Evaluation Parameters

Parameter		Value
RF Signal		Carrier frequency = 3.5 GHz Constellation = 256QAM
Optical Link	Laser	Wavelength= 1550 nm Average Power= 10 mW Line Width= 16e6 Hz
	Fiber	Fiber Dispersion= $16 \frac{ps}{nmkm}$ Distance=0.1, 1, 2, 5 km Attenuation= $0.5 \frac{dB}{km}$
	Photo-detector (PD)	Responsivity 0.9 A/W Bandwidth: 9.3 GHz
Bandpass Filtering		Band Pass Bandwidth=190 MHz Conversion gain (Complete Receiver (PD+BPF))=220 V/W

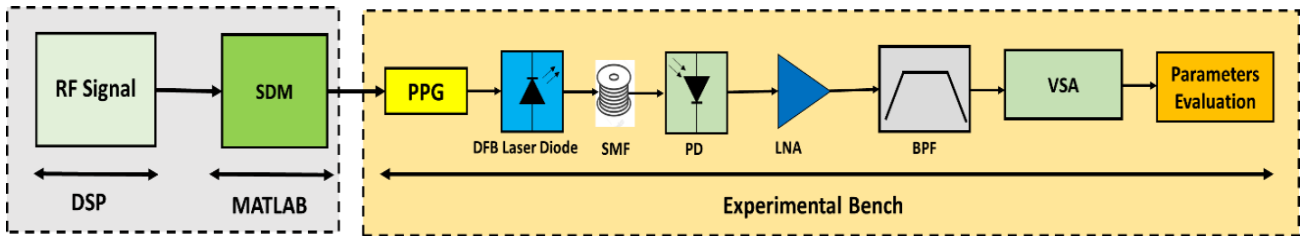


Figure 6.12: Experimental Bench for Sigma Delta Radio over Fiber system. SDM: Sigma Delta Modulation. SMF: Single Mode Fiber. PPG: Pulse Pattern Generation. BPF: Band Pass Filtering. LNA: Low Noise Amplifier. VSA: Vector Signal Analyzer

6.4.2.1.1 Experimental Results and Discussion

In this section, the performances of the proposed S-DRoF are evaluated. Firstly, the performance of S-DRoF is firstly evaluated by the error vector magnitude (EVM). The 3GPP has set an EVM limit of 3.5% for LTE signals modulated by 256 QAM modulation format [6.23]. The performance is measured for various symbol rates up to 400 Mbd and for different fiber lengths up to 5 km at 0 dBm of RF input power. The results are shown in Figure 6.13. The degradation in EVM performance is observed for all the fiber lengths. The reason for the degradation is that the received signal has low power due to the path loss.

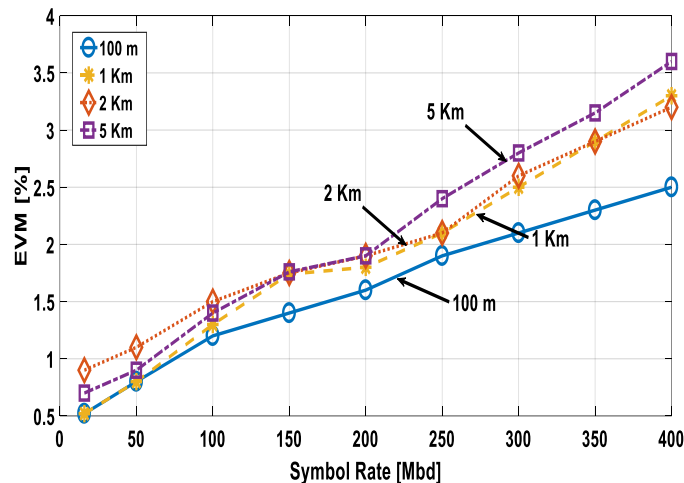


Figure 6.13: EVM performance for varying symbol rates and fiber lengths.

In Figure 6.14, the performance is expressed by varying the distance length up to 5 km for varying input RF powers keeping in mind the fact that front haul lengths are generally in this order. It is observable that from -15 dBm of RF input power, EVM is in the limits for all the link lengths set by the 3GPP for 256 QAM.

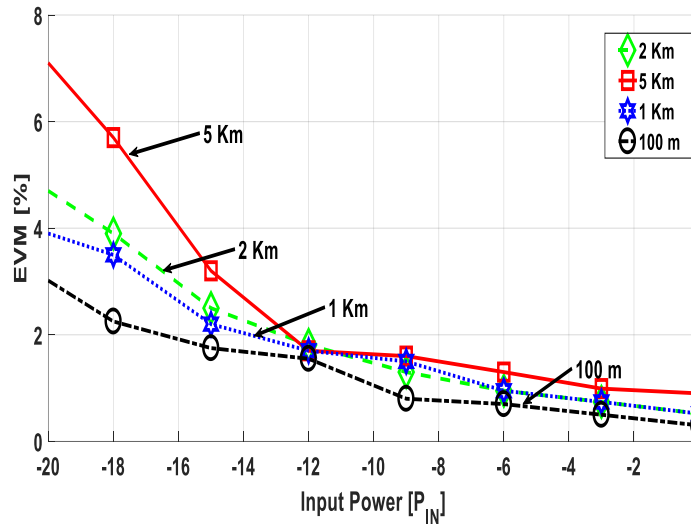


Figure 6.14: EVM performance for varying input powers and fiber lengths.

Now, the performance of the proposed S-DRoF is evaluated by measuring the adjacent leakage ratio (ACLR). The ACLR is evaluated by changing the fiber length up to 5 km. The RF input power is varied from -15 dBm to 0 dBm . The behavior is shown in Figure 6.15. Since higher input power leads to higher order of distortions in the adjacent channels, therefore ACLR rises.

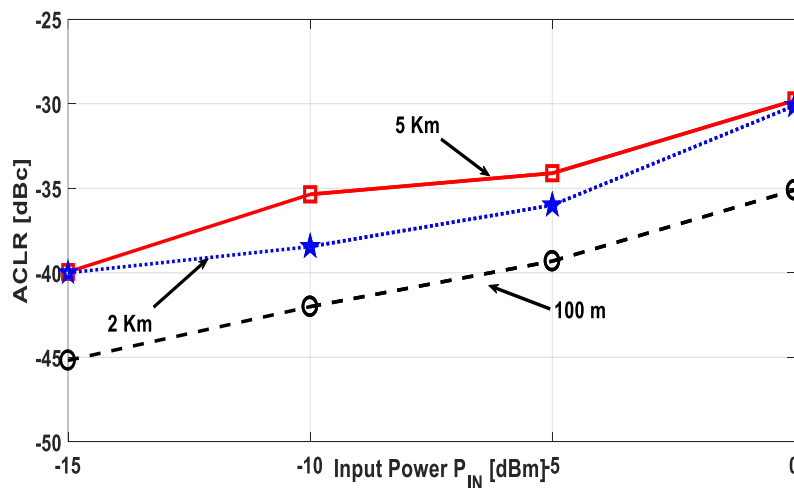


Figure 6.15: ACLR performance for varying RF input power and varying fiber lengths.

The transmission performance of the proposed S-DRoF is investigated by Eye diagrams of the transmitted signal systems. Figure 6.16 reports the EOP versus fiber length. It shows that the EOP stays constant with the increasing fiber length. In the S-DRoF case, the EOH does not closes. Also, by looking at the inset at 5 km, the eye remains clean and wide open.

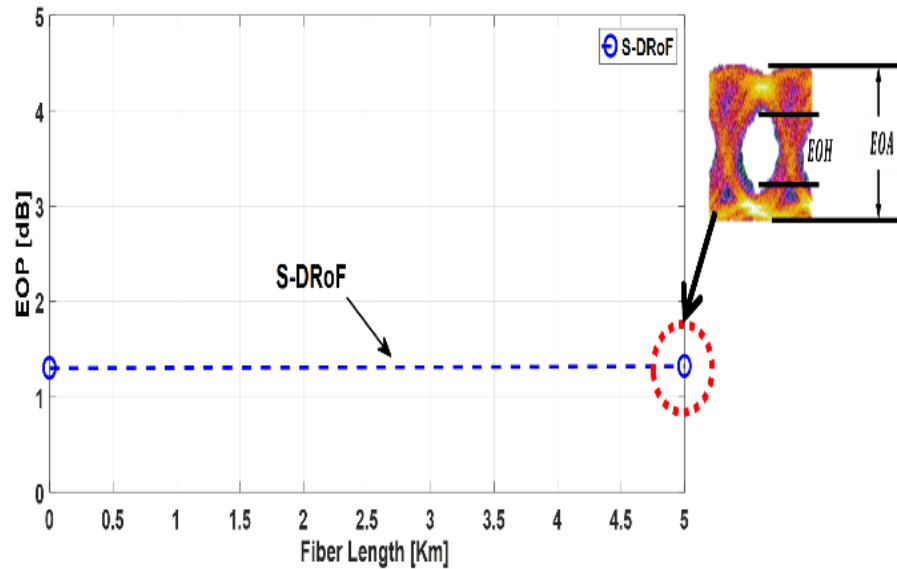


Figure 6.16: EOP versus Fiber length for 0 dBm of input power

The summary of the comparative overview of the parameters evaluated is given in Table 6.4 for the maximum and minimum length utilized for -5 dBm of input power at 400 Mbd.

Table 6-4: Performance Summary at -5 dBm for 400 Mbd

Length (Km)	<i>EVM</i> (%)	<i>ACPR</i> (dBc)
0.1	2.5	-39.31
5	3.55	-34.11

Since this technique is meant to be utilized for 5G sub-6GHz band fronthaul applications, its cost analysis is important factor. Since SDM trades quantization bit for sampling rate, using high sampling rate and only few (1-bit generally) quantization bits, the need of very expensive and high-speed digital circuitry is not required. In case of CPRI, D-RoF systems at the remote antenna units (RAU) require a DAC which needs to be high speed and efficient enough to handle the operations. In case of S-DRoF, the deployment of DAC is replaced by a band pass filter which further decreases the cost. DSP kit is required for both, D-RoF and S-DRoF, so, the cost of DSP kit remains constant. However, one major challenge to both D-RoF and S-DRoF is the need of high processing speed.

Sigma delta modulation requires high oversampling ratio to achieve the performance. To overcome the speed limit of existing FPGA, several parallel processing techniques have been

reported, including polyphase decomposition [6.24] and look-ahead time-interleaving [6.25-6.26]. This means that by employing these techniques, even a simple FPGA kit can be deployed for the S-DRoF. This methodology greatly reduces the cost of S-DRoF to some thousands of euros as compared to D-RoF that will cost tens of thousands of euros for the same parameters and application. On basis of these facts, it can be proposed that S-DRoF is much cheaper solution than D-RoF systems.

In this section, we have performed a novel demonstration experimentally for MASH based Sigma Delta Radio over Fiber for 5G sub-6GHz band fronthaul applications. By employing MASH, the second order SDM performance can be obtained. Utilization of proposed system eliminates the need for high-speed ADCs and DACs required in D-RoF systems. The experimental workbench has been evaluated for LTE signal of 20 MHz bandwidth having 256 QAM modulation which is modulated on a 3.5 GHz carrier frequency at 1550 nm. The measurement results show that this methodology is suitable for transmitting LTE signals. The real time implementation of MASH based S-DRoF is achievable with FPGA which will be discussed in the next section.

6.4.3 Real time Implementation of Sigma Delta Radio over Fiber System for Fronthaul Applications

In this section, we present the real time implementation of $\Sigma \Delta M$ on FPGA. 2nd order $\Sigma \Delta M$ discussed previously in Sec. 6.4.1 is chosen to demonstrate the realistic experimental setup. The section includes the implementation based on demonstration of 4 lane proof of real time sigma delta radio over fiber system.

6.4.3.1 Experimental Setup

Figure 6.17 shows the experimental test bed utilized for this work. Let us consider four pairs of an in-phase and quadrature baseband signals. This pair of baseband signals are sigma delta modulated by SD modulator at 6 GSa/s. We employ 2nd order SD-modulator to evaluate the performance. Moreover, the parallel multistage scheme can result in desired sampling rate [6.27]. The unwanted and relatively high quantization noise can be filtered out in order to reduce it in the useful band.

The sigma delta modulated baseband signals (both 1 bit) are up converted to a single bit binary signal. This binary signal has sampling rate of 12 GSps and carrier frequency f_c of 3 GHz. This is followed by the electrical optical conversion. The optical converted signals are transmitted over Standard Single Mode Fibers (SSMFs). At each receiver, the photodiode converts the optical signal back to electrical domain followed by a bandpass filter (BPF) which filters the quantization noise. The module has a capacity to implement 4x parallel transmitters. However, for simplicity, only one lane proof is shown. To bring the optical signal to the respective RRHs, MTP breakout SMF fiber is used.

The RF signal generation (baseband signal generation, up-sampling and up-conversion) and SDMs (1st order and 2nd order) shown in Figure 6.17 are implemented on Xilinx Virtex Ultrascale VCU108 FPGA Evaluation Kit. After the FPGA performs sigma delta modulation, the 1-bit sigma delta modulated stream is fed to Module QSFP28-PIR4-100G (1310 nm Distributed Feed-back laser) is employed for the electrical optical conversion to transmit over SSMF. The received signals are then fed to respective RRH units having low noise amplifier (LNA) that amplifies the signal followed by analog band pass filter which filters the out of band noise. The band pass filtered signals are fed to UXR1004A Infiniium UXR real time oscilloscope having vector analysis software for post processing of data and parameters evaluation. The noise current spectral density around f_c is $16 \frac{pA}{\sqrt{Hz}}$. The module QSFP28-PIR4-100G has 4 transmitters in which each transmitter has a clock data recovery (CDR) to resample the data if needed.

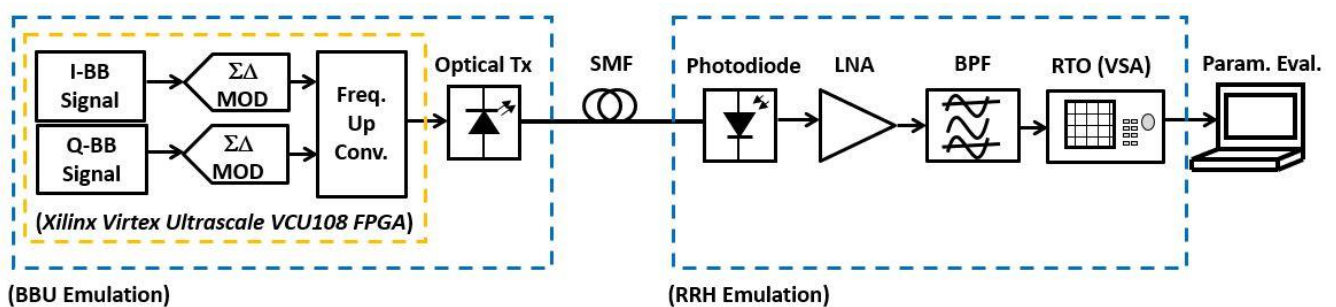


Figure 6.17: Experimental test bed for real time implementation of Sigma Delta Radio over Fibre system. I-BB, Q-BB: In-Phase and Quadrature Baseband, respectively; $\Sigma\Delta$ MOD: Sigma Delta Modulator; Optical Tx: Optical Transmitter; SMF: Single Mode Fibre; LNA: Low Noise Amplifier; BPF: Band Pass Filtering; RTO: Real Time Oscilloscope; VSA: Vector Signal Analyzer; Param. Eval.: Parameters Evaluation.

The parameters and values are given in Table 6.5.

Table 6-5: System parameters

Parameter	Value
RF Signal	Carrier frequency = 3 GHz Constellation format= 256 QAM
Laser	Wavelength= 1310 nm Transmitter Type= 4x DFB Cable Type= SMF Connect Type= MTP
Optical Fibre	Fibre Dispersion= $16 \frac{ps}{nmkm}$ Fibre Distance= 0.1, 1, 2, 5, 10 km Attenuation= $0.42 \frac{dB}{km}$
Photodiode	Responsivity 0.6 A/W Bandwidth: 5 GHz
Bandpass Filtering	Band Pass Bandwidth=180 MHz Conversion gain (Complete Receiver (PD+BPF) = 210 V/W

6.4.3.2 Experimental Results and Discussion

The performance of S-DRoF is calculated by the Error Vector Magnitude (EVM). Firstly, we calculate the EVM performance of 1 km and 10 km link length for all the 4 channels by varying RF input powers. This will clarify the performance variations of 4 channels with respect to each other. Figure 6.18 reports EVM for the input powers with 100 Mbd for 10 km and 0.1 km. Since Channel 4 is the worst effected case, therefore all the evaluations from this point onwards will be shown for channel 4.

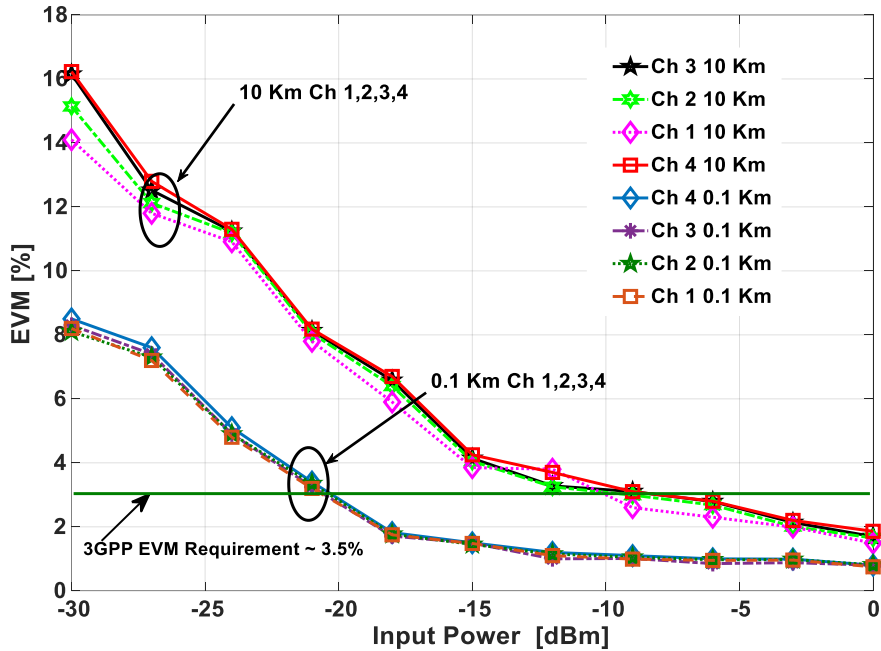


Figure 6.18: EVM performance for varying input powers for all channels with minimum and maximum link length

Figure 6.19(a) reports the EVM for varying symbol rates up to 400 MBd for different fiber lengths at 0 dBm of input power. The increase in EVM is observable for all the fiber lengths. It is observable that EVM for 10 km is higher since the low power of received signal is due to the path loss. Similarly, a higher baudrate will result in a higher total noise power in the signal band and thus it leads to an increased EVM. Similarly, in Figure 6.19 (b) and (c), the constellation diagram is observed for the minimum length and minimum baud rate with respect to maximum length case and maximum baud rate respectively. It is observable that for 100 MBd, EVM for 100 m length is less than 1% and received constellation diagram is clean. However, for the 400 MBd, 10 Km length case, the received constellation is rather noisier and EVM is around 3%. Though, it is below the threshold of 3.5% set by 3GPP, it is acceptable. This signifies that EVM increases with higher baud rate as it leads to higher total noise power in the signal band.

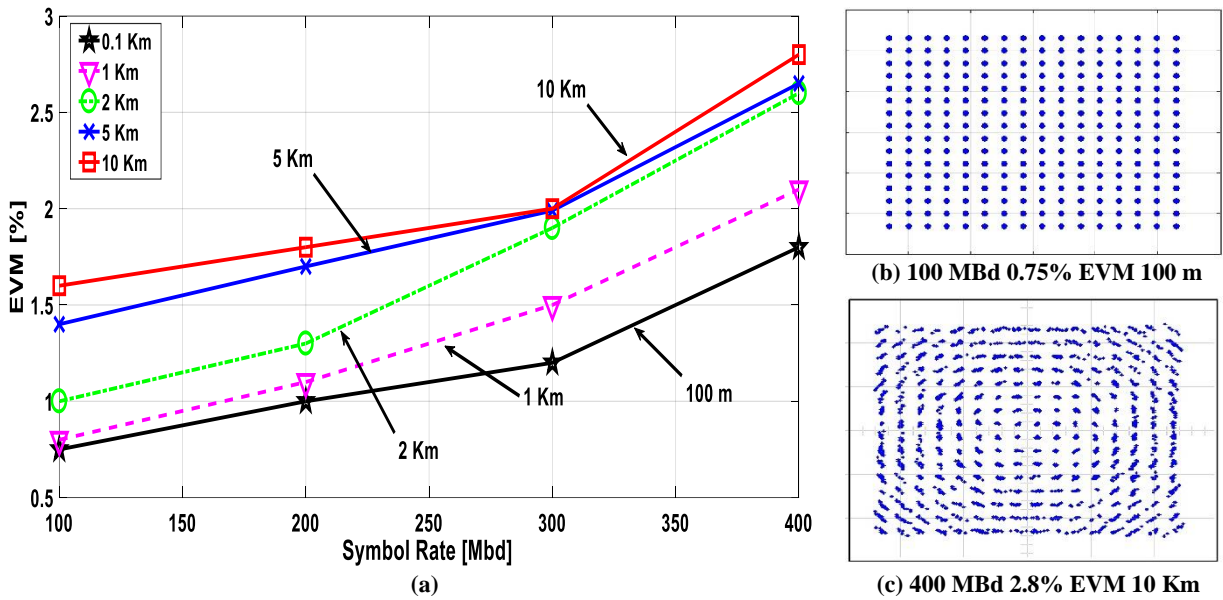


Figure 6.19: (a) EVM performance for varying symbol rate for different SMF lengths. (b)-(c) Constellation diagrams for minimum and maximum baud rate and fiber lengths at input power $P_{IN} = 0 \text{ dBm}$.

In order to evaluate the dynamic range of the system under test, the EVM is evaluated for varying values of input power in Figure 6.20 (a). For this evaluation, the symbol rate was set to 100 MBd. It can be seen that with increasing values of the input powers, the EVM falls in the acceptable 3.5 % range. The received optical power for varying distances is shown in measures of EVM degradation. Figure 6.20 (b) shows that EVM for 0.1, 5 and 10 km of distances are satisfying the 3.5% requirements of 3GPP. The trend validates that it can be a promising candidate for future mobile front haul applications.

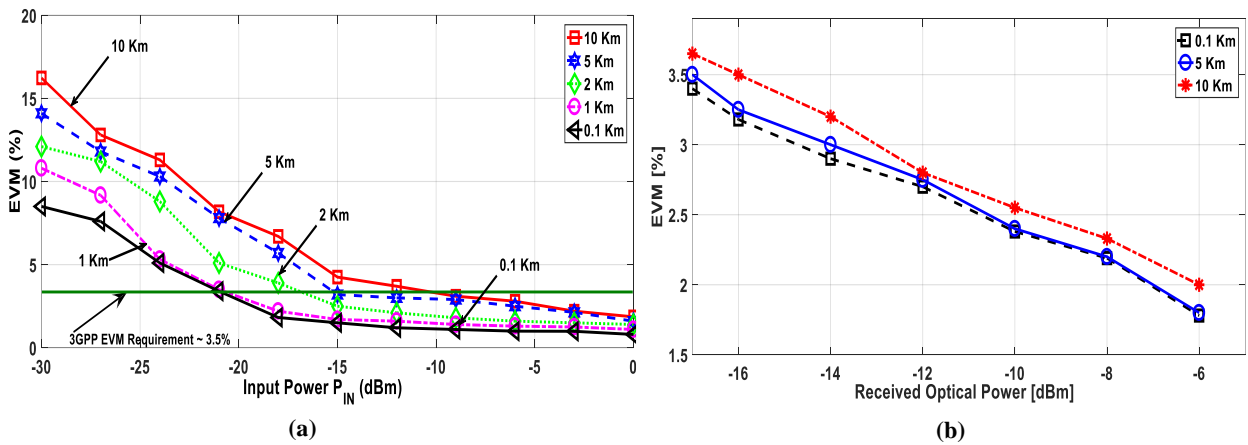


Figure 6.20: (a) EVM performance for varying input powers for varying link lengths. (b) EVMs vs received optical power for 0.1 km (black squared), 5 km (blue circular) and 10 km (red star).

Figure 6.21 represents the experimental evaluation of ACLR value with respect to changing input RF power and fiber length respectively. The trend signifies that ACLR increases with increasing fiber length and higher input power as it leads to higher order of distortions in the adjacent channels. It can be seen that ACLR for 0 dBm at 10 km is -29.91 dBc.

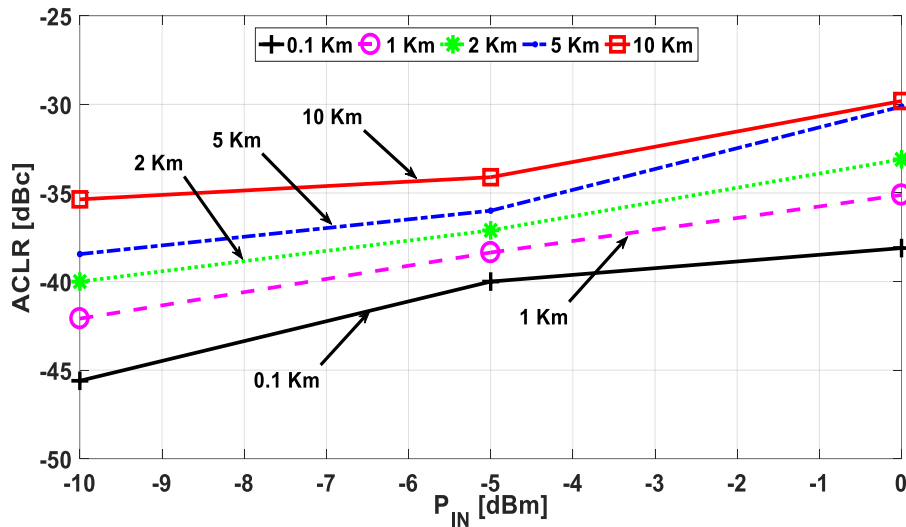


Figure 6.21: ACLR vs input power for varying lengths.

Figure 6.22 reports the EVM for 10 km link length with symbol rates ranging from 100 MBd to 400 MBd, at different values of input power P_{IN} . It is visible that performing an increase from the value $P_{IN} = -16$ dBm, for which it is $EVM > 3.5\%$ for all the symbol rates considered, the EVM monotonically decreases and, starting with the 100 MBd and ending with the 400 MBd case, the transmission is gradually attainable while respecting the EVM limit.

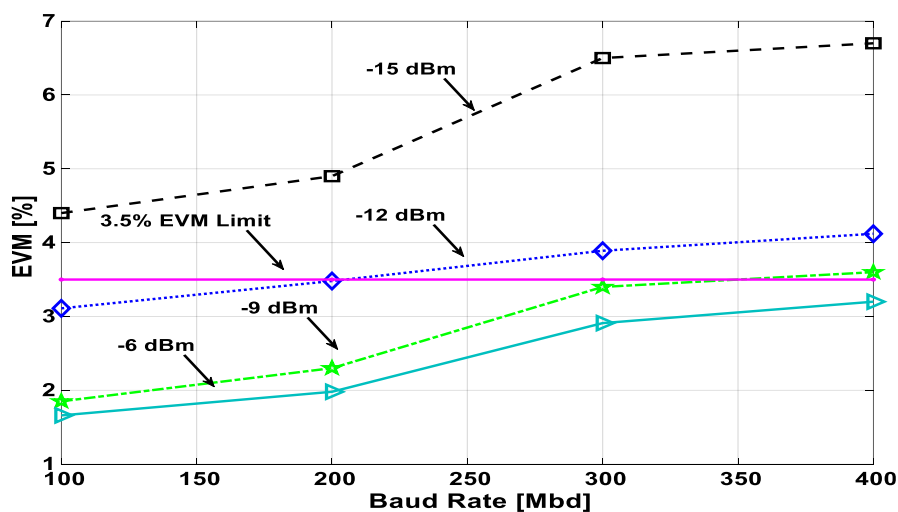


Figure 6.22: EVM for different RF input powers with different baud rates for 10 km fiber length.

A behaviour similar to the one reported in Figure 6.23 is also observable for the other values of link length considered. In order to summarize all the measured performances, Figure 6.23, reports, for each considered value of L value minimum value $P_{IN,min,EVM<3.5\%}$ below which P_{IN} cannot fall in order to guarantee $EVM < 3.5\%$. It can be appreciated that when transmitting at 400 Mbd it is $P_{IN,min,EVM<3.5\%} = -18 \text{ dBm}$ for $L = 0.1 \text{ km}$, while it is $P_{IN,min,EVM<3.5\%} = -6 \text{ dBm}$ for $z = 10 \text{ km}$. In line with the considerations developed above, the values of $P_{IN,min,EVM<3.5\%}$ can be identified as the optimized ones, since they maintain the ACLR at the lowest possible value, while allowing the received EVM to accomplish the 3GPP requirement.

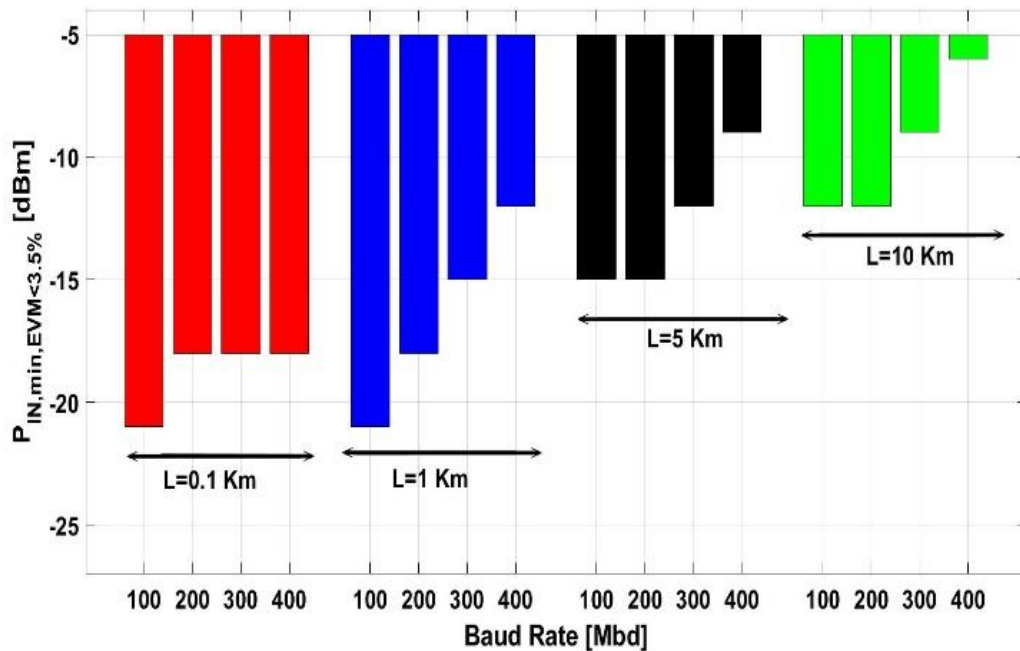


Figure 6.23: Minimum RF input required to achieve a determined baud rate for different link lengths.

The summary of the comparative overview of the parameters evaluated is given in Table 6.6 for the maximum and minimum length utilized for 0 dBm of input power at 100 MBd.

Table 6-6: Performance Evaluation at 0 dBm for 100 MBd

Length (km)	EVM (%)	$ACPR$ (dBc)
0.1	0.8	-38.45
10	1.6	-29.81

In this section, we have proposed and demonstrated the implementation of S-DRoF link for the fronthaul applications with length up to 10 km. Utilization of such links eliminate the need for high-speed ADCs and DACs required in D-RoF systems. The experimental workbench has been evaluated for LTE signal of 20 MHz bandwidth having 256 QAM modulation which is modulated on a 3 GHz carrier frequency at 1310 nm. The 12 GSps sigma delta modulators are realized on FPGA. The results show an EVM of less than 3% per lane for a 3 Gbps (400 MBd 256-QAM modulation) for 10 km SSMF using DFB at 0 *dBm*. The demonstrated real time S-DRoF link can cover the desired range of the 5G C-RAN fronthaul networks.

6.5 Conclusion

In this chapter, we have demonstrated and experimentally characterized a Sigma Delta RoF link for fronthaul applications with length up to 10 km. The workbench has been evaluated for LTE signal of 20 MHz bandwidth having 256 QAM modulation, which is upconverted by a 3 GHz carrier frequency at 1310 nm. Starting from simulation analytical model, the technique has been realized through experimental bench. Then, 6x2 GSa/s sigma delta modulators are realized on FPGA. The results show an EVM of less than 3% per lane for a 3 Gbps (400 MBd 256-QAM modulation) for 10 km SSMF using DFB at 0 *dBm*. Optimized values of the RF input power which maintain the ACLR at the lowest possible value, while allowing the received EVM to accomplish the 3GPP requirements have been identified for different possible values of the link length, with a maximum value of -6 *dBm* for a length of 10 km. The demonstrated real time $\Sigma\Delta$ -RoF link can cover the desired range of the 5G C-RAN fronthaul networks.

References

- 6.1 C. Ranaweera, E. Wong, A. Nirmalathas, C. Jayasundara and C. Lim, "5G C-RAN With Optical Fronthaul: An Analysis From a Deployment Perspective," in *Journal of Lightwave Technology*, vol. 36, no. 11, pp. 2059-2068, 1 June1, 2018.
- 6.2 China Mobile, "C-RAN the road towards green RAN (version 2.5)," White Paper, Oct 2011

- 6.3 Christina Lim, Ampalavanapillai (Thas) Nirmalathas, Ka-Lun Lee, Dalma Novak, Rod Waterhouse, Waterhouse intermodulation distortion improvement for fiber–radio applications incorporating OSSB+C modulation in an optical integrated-access environment, *J. Lightwave Technol.* 25 (2007) 1602–1612.
- 6.4 A. Haddad and M. Gagnaire, “Radio-over-Fiber (RoF) for mobile backhauling: A technical and economic comparison between analog and digitized RoF,” in *Proc. Int. Conf. Opt. Netw. Design Modeling*, May 2014, pp. 132–137
- 6.5 L. Breyne, G. Torfs, X. Yin, P. Demeester and J. Bauwelinck, "Comparison Between Analog Radio-Over-Fiber and Sigma Delta Modulated Radio-Over-Fiber," in *IEEE Photonics Technology Letters*, vol. 29, no. 21, pp. 1808-1811, 1 Nov.1, 2017. doi: 10.1109/LPT.2017.2752284
- 6.6 I. C. Sezgin, J. Gustavsson, T. Lengyel, T. Eriksson, Z. S. He and C. Fager, "Effect of VCSEL Characteristics on Ultra-High Speed Sigma-Delta-Over-Fiber Communication Links," in *Journal of Lightwave Technology*, vol. 37, no. 9, pp. 2109-2119, 1 May1, 2019. doi: 10.1109/JLT.2019.2898270.
- 6.7 M.U..Hadi, P..A.Traverso, G.Tartarini, H. Jung, “Experimental characterization of Sigma Delta Radio over fiber system for 5G C-RAN downlink”, *ICT Express* available online 21 June 2019
- 6.8 Luis M. Pessoa, Joana S. Tavares, Diogo Coelho, and Henrique M. Salgado, "Experimental evaluation of a digitized fiber-wireless system employing sigma delta modulation," *Opt. Express* 22, 17508-17523 (2014)
- 6.9 A. Pizzinat, P. Chanclou, F. Saliou, T. Diallo, "Things you should know about fronthaul," *IEEE Journal of Lightwave Technology*, vol.33, no.5, pp.1077-1083, 2015
- 6.10 M.C. Parker, et al. "Radio-over-fibre technologies arising from the Building the future Optical Network in Europe (BONE) project," *IET Optoelectronics*, 4(6),. 247 – 259, 2010
- 6.11 D. Visani et al., “ 3×2N-QAM Constellation Formats for DMT Over 1-mm Core Diameter Plastic Optical Fiber”, *IEEE Photonics Technology Letters*, 23, pp. 768-770 , 2011

- 6.12 M. Morant, R. Llorente, "Performance analysis of multiple radio-access provision in a multicore-fibre optical fronthaul", *Optics Communications* 436 (2019) 161–167
- 6.13 Y. Shi et al., "Ultrawideband Signal Distribution Over Large-Core POF for In-Home Networks," *IEEE/OSA J. Lightw. Technol.*, vol. 30, pp. 2995-3002, Sept. 2012.
- 6.14 G. Meslener, "Chromatic dispersion induced distortion of modulated monochromatic light employing direct detection," *IEEE J. Quantum Electron.*, vol. QE-20, no. 10, pp. 1208–1216, Oct. 1984.
- 6.15 T. Kurniawan, A. Nirmalathas, C. Lim, D. Novak and R. Waterhouse, "Performance analysis of optimized millimeter-wave fiber radio links," in *IEEE Transactions on Microwave Theory and Techniques*, vol. 54, no. 2, pp. 921-928, Feb. 2006.
- 6.16 T. Pfeiffer, "Next generation mobile fronthaul architectures," *Optical Fiber Communications Conference (OFC) 2015*, paper M2J.7.
- 6.17 G. Alcaro, D. Visani, L. Tarlazzi, P. Faccin and G. Tartarini, "Distortion Mechanisms Originating From Modal Noise in Radio Over Multimode Fiber Links," in *IEEE Transactions on Microwave Theory and Techniques*, vol. 60, no. 1, pp. 185-194, Jan. 2012. doi: 10.1109/TMTT.2011.2171982
- 6.18 J. Wang et al., "Digital mobile fronthaul based on delta-sigma modulation for 32 LTE carrier aggregation and FBMC signals," in *IEEE/OSA Journal of Optical Communications and Networking*, vol. 9, no. 2, pp. A233-A244, Feb. 2017.
- 6.19 Muhammad Usman Hadi, Hyun Jung, Salman Ghaffar, Pier Andrea Traverso, Giovanni Tartarini, "Optimized digital radio over fiber system for medium range communication," *Optics Communications*, Volume 443, 2019, Pages 177-185, ISSN 0030-4018, <https://doi.org/10.1016/j.optcom.2019.03.037>
- 6.20 Hadi, M., Jung, H., Traverso, P., et al. (2019). Digital Radio Frequency Transport over Optical Fiber for 5G Fronthaul Links . *Journal of Optical Communications*, 0(0), 2019, doi:10.1515/joc-2019-0051

- 6.21 David Fouto, Nuno Paulino, Design of Low Power and Low Area Passive Sigma Delta Modulators for Audio Applications, 2017, Springer, ISSN 2191-8112 ISSN 2191-8120 (electronic) Springer Briefs in Electrical and Computer Engineering. ISBN 978-3-319-57032-7
- 6.22 M. U. Hadi et al., “Performance Appraisal of Sigma Delta Modulated Radio over Fiber System”, Journal of Optical Communications, 0(0), pp. Jan. 2019, from doi:10.1515/joc-2018-0227, (2019).
- 6.23 3GPP, “Base Station (BS) transmission and reception,” Technical Specification ETSI TS136.104 V13.3.0, 2016.
- 6.24 Cordeiro RF, Oliveira ASR, Vieira J, Silva TOE. Wideband all-digital transmitter based on multicore DSM. IEEE MTT-S International Microwave Symposium (IMS) 2016.
- 6.25 Tanio M, Hori S, Tawa N, Yamase T, Kunihiro K, An FPGA-based all-digital transmitter with 28-GHz time-interleaved delta-sigma modulation. IEEE MTT-S International Microwave Symposium (IMS) 2016.
- 6.26 Tanio M, Hori S, Tawa N, Kunihiro K, An FPGA-based all-digital transmitter with 9.6-GHz 2nd order time-interleaved delta-sigma modulation for 500-MHz bandwidth. IEEE MTT-S International Microwave Symposium (IMS) 2017:149–52.
- 6.27 R. Hossain et al., “Parallel MASH $\Delta\Sigma$ modulator,” US Patent US8203475B2 [Online] (Available: <https://patents.google.com/patent/US8203475>) (2012)

Chapter 7

Conclusions/Final Remarks and Future Directions

7.1 Summary and Final Remarks

This thesis dissertation has discussed the linearization methodologies for Analog Radio over fiber systems and proposed Digital and Sigma Delta class of radio over fiber links. In the first part of the dissertation (mainly Chapter 2,3 & 4), Analog class of Radio over Fiber links were discussed in context of compensating the nonlinearities issues. In chapter 3, a proposed technique and its implementation were discussed. The predistortion is applied firstly to sinusoidal signals and then to LTE standard signals. It is shown that proposed technique is able to compensate the link impairments in good proportions for long RoF links.

Then, the dissertation discussed linearization techniques based on indirect learning architecture. Two class of links are linearized i.e. Vertical Capacity Surface Emitting Lasers (VCSELs) and Distributed Feedback Laser (DFB) based RoF links. Volterra polynomial structures such as memory polynomial (MP) and generalized memory polynomial (GMP) methods are proposed for linearizing Radio over fiber links. Then, a comparison is shown for linearization of DFB based RoF links with Volterra methods (MP and GMP) with Decomposed Vector Rotation (DVR) method. Similarly, a novel demonstration is shown for dual channel transmission where each channel nonlinearities are reduced with the DPD models proposed in this chapter. Finally, a feedback approximation methodology is proposed which is a possible implementation of a digital predistorter in adaptive form.

The second half of dissertation stresses upon the other possible methods that can be used for front haul applications. With this approach, instead of compensating the Analog Radio over Fiber links, Digital and Sigma Delta Radio over Fiber Links are discussed.

Chapter 5 introduces the need and importance of digital RoF system. It is discussed that why Digital RoF is a good option to switch from Analog RoF to Digital RoF. Analytical model is proposed and it is shown that a better error free transmission is obtained for digital RoF as compared to Analog RoF. Then, an experimental validation of this analytical model is presented which proves that the proposed digital radio over fiber system is an optimized version that uses less number of ADC resolution bits.

Finally, in Chapter 6, Sigma Digital Radio over Fiber (S-DRoF) system is studied. The chapter introduces the need and importance of Sigma delta RoF system, an auxiliary method that amalgamates the advantages of A-RoF and D-RoF. It discusses the basics of sigma delta modulator ($\Sigma \Delta M$). The need of power hungry and high-speed digital to analog converter (DAC) required in D-RoF is replaced by a $\Sigma \Delta M$. It describes the different architectures that have been proposed. The analytical model with simulation is shown and then experimental setup is validated. Finally, a real time S-DRoF is proposed that can be used for fronthaul applications. The summary of all the methodologies implied in this dissertation are summarized in the following Table 7-1.

Table 7-1: Summary of RoF Transmission Topics Discussed in this Dissertation

Sr. No.	Methodology	System Characteristics	Evaluated Quantities
1	Behavioral Direct Digital Predistortion Methodology for Analog Radio over Fiber System (Chapter 3)	<ul style="list-style-type: none">• DFB laser 1550 nm with Standard Single Mode Fiber (SSMF) of 50 km length.	ACLR, EVM
2	Digital Predistortion Methodology for Analog Radio over Fiber System (Chapter 4)	<ul style="list-style-type: none">• Single Mode VCSEL 850 nm with SSMF of 1.5 km.➤ Single Channel LTE 5, 10 MHz signal Bandwidth.➤ Dual channel 20 MHz LTE signal.	ACLR, NMSE and AM/AM, AM/PM ACLR, NMSE, EVM and AM/AM, AM/PM

3	Digital Predistortion Methodology for Analog Radio over Fiber System (Chapter 4)	<ul style="list-style-type: none"> • Multi Mode-VCSEL 850 nm with SSMF of 1.5 km. ➤ Single Channel LTE 5, 10 MHz signal Bandwidth. ➤ Dual channel 20 MHz LTE signal. 	ACLR, NMSE, EVM and AM/AM, AM/PM ACLR, NMSE, EVM and AM/AM, AM/PM
4	Digital Predistortion Methodology for Analog Radio over Fiber System (Chapter 4)	<ul style="list-style-type: none"> • DFB-MQW Laser 1310 nm with SSMF of 1.5 km. ➤ Single Channel LTE 10 MHz signal Bandwidth. ➤ Dual channel 20 MHz LTE signal. 	NMSE, EVM and AM/AM, AM/PM NMSE, EVM and AM/AM, AM/PM
5	Optimized Digital Radio over Fiber System (Chapter 5)	<ul style="list-style-type: none"> • DFB 1550 nm with SSMF of 70 km with 20 MHz LTE signal bandwidth. ADC Resolution is 8 bits. (Analytical and Experimental Validation) ➤ Single Channel LTE 20 MHz signal Bandwidth. 	ACLR, EVM, EOP

6

Sigma Delta Radio over Fiber
System
(Chapter 6)

- DFB 1550 nm with SSMF of 10 km with 20 MHz LTE signal bandwidth (Analytical and Experimental Validation). MASH and 2nd order SD modulator used.
- Single Channel LTE 20 MHz signal Bandwidth.
- Real Time Experimental bench for 4x channel Sigma Delta Radio over Fiber links

ACLR, EVM, EOP

ACLR, EVM, EOP

7.2 Future Perspective of the work

The work presented in the first part of dissertation establishes a foundation for analyzing problems involving modeling and compensation for Radio over Fiber Links. The motivation of this work was the provision of efficient digital signal processing (DSP) techniques, in order to eliminate the unavoidable distortions and nonlinearities of A-RoF links and improve the overall system performance.

Thus, the presented behavior model technique Direct Digital Predistortion Technique (DPDT) discussed in Chapter 3 and developed digital compensation techniques based on Indirect Learning Architecture (ILA) provides a better understanding of the impact of different types of distortions and nonlinearities associated and give better tools to compensate for their effects on the system performance. Future directions of this work should focus on extending DSP techniques to incorporate the distortions and nonlinearities of the wireless channel and the receiver. The real time implementation of this setup with 5G NR signals will be interesting upgrade from LTE and LTE-A signals.

The algorithm developed for extraction of the DPD coefficients uses Least Squares Method (LMS). It can be extended for real-time implementation of DPD coefficients extraction that should improve the performance and update the model more precisely.

Similarly, the linearization method for Analog RoF systems can be mitigated with the help of Machine Learning techniques such as Machine learning based classifiers such as Support Vector Magnitude (SVM), KNN (K nearest neighbor) algorithms and many other techniques. These methods should be implemented, and a study should be carried out in order to see the potential of linearization implied with the help of this methodology. The important factors to be considered are time consumed for the training, resources allocation and realistic implementation of the approach. Similarly, adapting this work to compensate for all the distortions in the system requires extensive further investigation and analysis.

Moving on, for the Digital Radio over Fiber system, the link length achieved with optimized resolution bits can be increased for higher carrier frequencies as well. This possible increase in

potential reach can be achieved if careful design considerations are made. Similarly, the proposed system in Chapter 5 can be implied for multi-channel cases as well. This case should be further investigated.

Furthermore, with regards to Sigma Delta Radio over Fiber Systems, wider signal bandwidth and higher carrier frequency of 5G signals, more efficient time-interleaving pipeline processing architecture need to be investigated to relax the FPGA speed. Moreover, higher-order delta-sigma modulator with advanced noise shaping techniques, such as multiband operations for non-contiguous carrier aggregation should be investigated as well.

Appendix A

List of Publications

Journal Publications [published]

- J1. Muhammad Usman Hadi, Pier Andrea Traverso, Giovanni Tartarini, Hyun Jung, Experimental characterization of Sigma Delta Radio over fiber system for 5G C-RAN downlink, *ICT Express, Special Issue on Next Generation (5G/6G) Mobile Communications*, 2019, ISSN 2405-9595, <https://doi.org/10.1016/j.ict.2019.06.002>.
- J2. Hadi, M.U., Nanni, J., Polleux, J.L., Traverso, P.A., Tartarini, G. Direct digital predistortion technique for the compensation of laser chirp and fiber dispersion in long haul radio over fiber links, «*Opt Quant Electron*», *Nature* (2019) 51: 205. <https://doi.org/10.1007/s11082-019-1923-8>
- J3. M.U. Hadi, J. Nanni, O. Venard, G. Baudoin, J. Polleux, P.A. Traverso, G. Tartarini "Linearity Improvement of VCSELs based Radio over Fiber Systems utilizing Digital Predistortion", «*Advances in Science, Technology and Engineering Systems Journal*», vol. 4, no. 3, pp. 156-163 (2019), doi:<http://dx.doi.org/10.25046/aj040321>
- J4. Hadi, M.U., Jung, H., Traverso, P., et al. (2019). Digital Radio Frequency Transport over Optical Fiber for 5G Fronthaul Links . «*Optical Communications*», 0(0), pp. 2019, from doi:10.1515/joc-2019-0051.
- J5. Muhammad Usman Hadi, Hyun Jung, Salman Ghaffar, Pier Andrea Traverso, Giovanni Tartarini, Optimized digital radio over fiber system for medium range communication,«*Optics Communications*», Volume 443, 2019, Pages 177-185, ISSN 0030-4018, <https://doi.org/10.1016/j.optcom.2019.03.037>.
- J6. M.U. Hadi et al. "Experimental Demonstration of MASH Based Sigma Delta Radio over Fiber System for 5G C-RAN Downlink". «*Journal of Optical Communications*», (2019).
- J7. M.U. Hadi et al ." Performance Appraisal of Sigma Delta Modulated Radio over Fiber System", «*Journal of Optical Communications*», (2019). [article]

- J8. M. U. Hadi, P. A. Traverso, G. Tartarini, O. Venard, G. Baudoin, and J. Polleux, "Digital Predistortion for Linearity Improvement of VCSEL-SSMF-Based Radio-Over-Fiber Links," in «*IEEE Microwave and Wireless Components Letters*», (2019). [article]
- J9. M. U. Hadi, C. Kantana, P. A. Traverso, G. Tartarini, O. Venard, G. Baudoin, and J. Polleux, "Assessment of Digital Predistortion Methods for DFB-SSMF-Radio-over-Fiber Links Linearization," in «*Microwave and Optical Technology Letters* », (2019). [article]
- J10. N. Aslam, K. Xia and M. U. Hadi, "Optimal Wireless Charging Inclusive of Intellectual Routing based on SARSA Learning in Renewable Wireless Sensor Networks," in «*IEEE Sensors Journal*». doi: 10.1109/JSEN.2019.2918865 (2019) [article]
- J11. Aslam, N.; Xia, K.; Haider, M.T.; Hadi, M.U. Energy-Aware Adaptive Weighted Grid Clustering Algorithm for Renewable Wireless Sensor Networks. «*Future Internet*»2017, 9, 54. [article]
- J12. Khurshid, K., Khan, A., Siddiqui, H., Rashid, I., & Hadi, M.U (2019). Big Data Assisted CRAN Enabled 5G SON Architecture. *Journal of ICT Research And Applications*, 13(2), 93-106. doi:10.5614/itbj.ict.res.appl.2019.13.2.1 [article]

Conferences

- C1. MU Hadi et al ., "Experimental evaluation of digital predistortion for VCSEL-SSMF-based Radio-over-Fiber link," 2018 IEEE International Topical Meeting on Microwave Photonics (MWP), Toulouse, 2018, pp. 1-4. [Contribution to conference proceedings]
- C2. Fuochi, F.; Hadi, MU; Nanni, J.; Traverse, PA; Tartarini, G., Digital Predistortion Technique for the Compensation of Nonlinear Effects in Radio over Fiber Links, in: Proceeding on Forum on Research and Technologies for Society and Industry (RTSI), 2016, pp. 1 - 6 (proceedings of: 2nd International Forum on Research and Technologies for Society and Industry (RTSI 2016), Bologna, 6 - 8 September) [Contribution to conference proceedings]
- C3. Fuochi, Filippo; Hadi, Muhammad Usman; Nanni, Jacopo; Traverso, Pier Andrea; Tartarini, Giovanni, Reduction of harmonic distortion in radio over fiber links through digital preprocessing, in: XXI RiNEm - National Meeting of Electromagnetism, 2016, pp. 1 - 4 (proceedings of: XXI RiNEm - National Meeting of Electromagnetism, Parma, 12 - 14 September 2016) [Contribution to conference proceedings]

C4.J. Nanni, L. Fernandez, M.U. Hadi., et.al., "Multi-Channel LTE-over-Fiber System Based on 850 nm VCSEL and SSMF for Low Cost, Low Consumption Fronthauls," 2019 21st International Conference on Transparent Optical Networks (ICTON), Angers, France, 2019, pp. 1-4.

Journal Publications [Accepted/ Submitted]

A1. M. U. Hadi, O. Venard, G. Baudoin, J. Polleux and G. Tartarini, "Practically feasible closed-loop Digital Predistortion for VCSEL-MMF-based Radio-over-Fiber links," in «*Radio Engineering Journal* », (2019).

A2. M.U. Hadi, Hyun Jung, Pier Andrea Traverso, Giovanni Tartarini, "Experimental Demonstration of Real-Time Sigma-Delta Radio over Fibre System for Fronthaul Applications", in «*IET-OptoElectronics*», (2019)